Sandwich Steels for Crash Energy Absorption Applications

Submitted for the degree of

Doctor of Philosophy in Engineering

October 2014

Sanjeev Sharma, MEng.

THE UNIVERSITY OF WARWICK

Abstract

This thesis has examined the applicability of steel–polypropylene–steel sandwich materials for the role of axial energy absorbers, an application previously undescribed in the literature. The results show that energy absorption performance of steel–polypropylene–steel sandwich materials can be predicted to within –2% and +8%, as well as highlighting the potential for their use in automotive applications.

The work has demonstrated that the deformation modes in the steel–polypropylene–steel sandwich mimic the monolithic metal crash structure, however, with smaller fold radii, hypothesised to be due to shear in the polypropylene core. It was observed that increasing the core thickness increased the radius of the folds in the structure when undergoing collapse. Though due to the variability in the folding patterns of sandwich material in the crash structures seen in this work, it could not be stated with certainty.

From the physical testing, the effect of core thickness for a fixed skin thickness is also defined. The physical tests showed a linear relationship between increasing core thickness and mean crush force. Further, the effectiveness of increasing the core thickness on the specific energy absorption was identified. The testing also showed an unprecedented >60% increase in energy absorption from quasi–static to dynamic for all three thicknesses of Steelite sandwich material, a level not seen in monolithic metal crash structures. Hence, suggesting an increased strain rate sensitivity of steel in MPM sandwich materials over the monolithic steel, a property which has been suggested in the literature for tensile tests but unknown in axial crash deformation.

The testing demonstrated the potential for the crushing mode to change from a desirable progressive crushing mode to an undesirable and difficult to predict progressive failure. This occurred with a 7:1 core to skin thickness ratio, though failure of the steel skin is seen at all ratios. A 70%:30% ratio of thickness for the polypropylene core to steel skin is shown to minimise steel skin failure, i.e. the individual steel skin thickness should be no less than 15% of the total sandwich thickness.

Finite element analysis presented in this thesis shows a single shell element model with laminated shell theory invoked can be used in LS–DYNA to predict the performance of the steel–polypropylene–steel sandwich materials. However, there is a potential thickness limit for which the model is applicable for the single hat and backplate crash structure considered; further research would be required to increase the confidence in the model. The single shell element model was accurate to within +8% of the physical test results.

An analytical solution fitted the LS–DYNA single shell element model well and showed increasing the core thickness is more effective at increasing the specific energy absorption than increasing the skin thickness. The analytical solution also shows the potential for a steel–polypropylene–steel sandwich with a core to skin ratio of 70%:30% ratio by thickness to equal the performance of high strength aluminium alloys.

Declaration of authorship

This thesis is submitted in partial fulfilment of the requirements for the degree of Doctor of Philosophy. It described work carried out from October 2010 to September 2014. Unless otherwise indicated the research described is my own and not the product of collaboration. No part of this thesis has been submitted to any other university, or as any part of any other submission to the University of Warwick.

Signed,

Date:

Acknowledgements

I would like to acknowledge:

- The University of Warwick and EPSRC for their financial contribution and the opportunity to undertake this research;
- Tata Steel for their financial contribution and the use of their facilities in Walsall, UK, Shotton, UK and IJmuiden, Netherlands for sandwich material production and testing;
- Professor Richard Dashwood, Dr Darren Hughes and Dr Iain McGregor for their excellent supervision;
- Those in WMG, University of Warwick who made this research possible: Dr Richard (Cash Rules Everything Around Me) Beaumont, Dr Dezhi Li, Zac Parkinson, Neil Reynolds, Darren (Inappropriate Fridays) Stewardson, David Williams and Martyn Wilkins.
- Roel Boesenkool, Tata Steel, IJmuiden for his guidance and assistance through my PhD, as well as providing me with steel at über short notice;
- All the friends I have made at the University of Warwick over the past few years;
- My mum, dad, sister and Annie for putting up with me.

Contents

Abbreviations

AHSS	Advanced high strength steel
AKDQ	Aluminium–killed drawing quality steel
APA	Aluminium–polymer–aluminium
BIW	Body–in–white
CNC	Computer numerically controlled
CFRP	Carbon fibre reinforced plastic
DC	Double core
DP	Dual phase
DPSW	DP600 sandwich
ECCS	Electrolytically chrome coated steel
ELV	End of life vehicle directive
FEA	Finite element analysis
FMVSS	Federal Motor Vehicle Safety Standards
FRP	Fibre reinforced plastic
FSV	Future Steel Vehicle
GFRP	Glass fibre reinforced plastic
GMT	Glass mat thermo composite
IIHS	Insurance Institute for Highway Safety
IPA	Iso propyl alcohol
ISO	International Standards Organisation
LCVTP	Low Carbon Vehicle Technology Project
LST	Laminated Shell Theory
MCM	Metal–composite–metal
MCF	Mean crush force
MEK	Methyl ethyl ketone

ML	Metal laminate
MPM	Metal–polymer–metal
NCAP	New Car Assessment Programme
OEM	Original Equipment Manufacturer
PEEK	Polyether ether ketone
PET	Polyethylene terephthalate
PMT	Peak metal temperature
PP	Polypropylene
PVC	Poly vinyl chloride
RSW	Resistance spot weld
RTM	Resin transfer moulding
SC	Single core
SEA	Specific energy absorption
SPR	Self–pierced rivet
SPS	Steel–polypropylene–steel
TC	Triple core
TRIP	Transformation induced plasticity
TWB	Tailor welded blank
UHSS	Ultra high strength steel
UTS	Ultimate tensile strength
WFT	Wet film thickness
WHO	World Health Organisation

Units

N	Newtons
kN	Kilo Newtons
MN	Mega Newtons
J	Joules
kJ	Kilo Joules
MJ	Mega Joules
m	Metres
mm	Millimetres
µm	Micrometre or micron
°	Degrees
min	Minute
s	Seconds
kg	Kilograms
g	Grams
kHz	Kilo Hertz
mph	Miles per hour
kph	Kilometres per hour

Nomenclature

D	Cowper–Symonds coefficient	s^{-1}
E	Elastic modulus	$N.m^{-2}$
E_a	Absorbed energy	J
$E_{a,max}$	Maximum absorbed energy	J
I	2nd moment of area	m^4
KE	Kinetic energy	J
M_o	Plastic bending moment	N.m
P	Force	N
P_m	Mean crush force	N
PE	Potential energy	J
SE	Spring energy	J
T	Overall material thickness	m
V	Impact velocity	$m.s^{-1}$
β_σ	Plastic bending moment correction factor	
d	Distance of skin from the neutral axis	M
ε	Strain	
$\dot{\varepsilon}$	Strain rate	s^{-1}
g	Gravitational acceleration	$m.s^{-2}$
h	Drop height	m
k	Spring constant	$N.m^{-1}$
m	Drop weight mass	kg
p	Effective width of crash structure	m
q	Cowper–Symonds exponent	
r	Radius of gyration	M
s	Displacement	m

s_{max}	Maximum displacement	m
σ_f	Flow stress of skin material	Pa
σ_c	Flow stress of core material	Pa
σ_o	Flow stress	Pa
σ_{UTS}	Ultimate tensile strength	Pa
σ_y	Yield strength	Pa
t_f	Face or skin thickness	m
t_c	Core thickness	m
x	Spring displacement	m

1 Introduction

The perceived future of the automotive industry is to produce lightweight vehicles to achieve improved fuel economy and reduce carbon dioxide emissions both in use and in production, whilst also adhering to the End of Life Vehicle (ELV) directive set out by the European Commission [1]. The ELV states that as of January 2015, 95% of a vehicle is to be reused and/or recovered at the end of its useful life.

Therefore, the use of not readily recyclable materials in the automotive structure will become more difficult in the future but vehicle weight must still be reduced. Further, the challenge of vehicle mass reduction must be met whilst also keeping pace with the increasing occupant and pedestrian protection regulations [2].

There is also further impetus to decrease vehicle mass since the introduction of hybrid and electric powertrains in vehicles. The introduction of this new type of powertrain has come with a substantial increase in vehicle mass largely due to battery mass. For example, a current Toyota Auris hybrid is 15% heavier than the conventional petrol model [3].

There are a number of methods available to the automotive industry for light–weighting of the vehicle structure. These include the use of ultra–high strength steel (UHSS) and advanced high strength steel (AHSS) to down–gauge components [4]–[6]. Composite materials such as glass (GFRP) or carbon fibre reinforced plastics (CFRP) can be used to great effect in mass reduction where stiffness is the main requirement from the material [7]. Polymers and plastics also provide a route to light–weighting due to their low density (approximately 1/8 of steel). However, there are issues with their environmental stability, heat resistance, creep and most importantly strength. Hence, the use of plastics and polymers is

currently limited to non–structural, cosmetic panels such as bumper covers and trim panels.

Using steel–polymer–steel (SPS) sandwich materials [8]–[10] could provide a lightweight solution which meets or exceeds the energy absorption performance of the current state of the art materials used in the automotive body–in–white, whilst meeting the legislative requirements for vehicle crashworthiness [11].

This project performs underpinning research to establish whether SPS materials are appropriate for automotive crash applications.

1.1 Crash safety legislation

This research concerns the energy absorption of the motor vehicle, therefore the legislative requirements for such are described.

The performance requirement of the front end crash structure is set out in vehicle crashworthiness legislation by various bodies worldwide; the Federal Motor Vehicle Safety Standards (FMVSS) and the World Health Organisation (WHO) are examples of such organisations. However, the largest driver tends to be consumer driven companies, the most noted of these being the Global New Car Assessment Programme (Global NCAP). Most new cars are purchased and tested by NCAP bodies around the world, the exceptions being limited edition and particularly expensive models.

Most full vehicle front–end impact requirements from the different authorities around the world can be summarised into either partial overlap or full overlap impacts with either a deformable or rigid barrier. Tests speeds vary from regulation to regulation, however, since motor vehicles are in general sold throughout the world, they are designed to meet the most stringent standard.

With regards to front impact assessment the most difficult tests to pass are highest speed tests and smallest overlap tests. The highest speed is the 64 km/h (40 mph) European NCAP 40% overlap into a deformable barrier [12]. The test with the least overlap is the Insurance Institute for Highway Safety's (IIHS) latest test, the small overlap front test where only 25% of the vehicle front end is impacted into a barrier at 48 km/h (30 mph) [13].

Figure 1.1 shows the Euro NCAP 64 km/h test on a 2014 Mercedes C–class with a deformable barrier (blue). A 'crash test dummy' can be seen inside the vehicle. The force and acceleration data from sensors throughout the vehicle and on the

crash test dummy are used to assess vehicle performance in crash and give the vehicle it's rating. Physical attributes of the vehicle in crash, such as successful airbag deployment, pedals and steering wheel intrusion into the passenger compartment and the extent of the damage to the occupant safety cell are also considered [2].

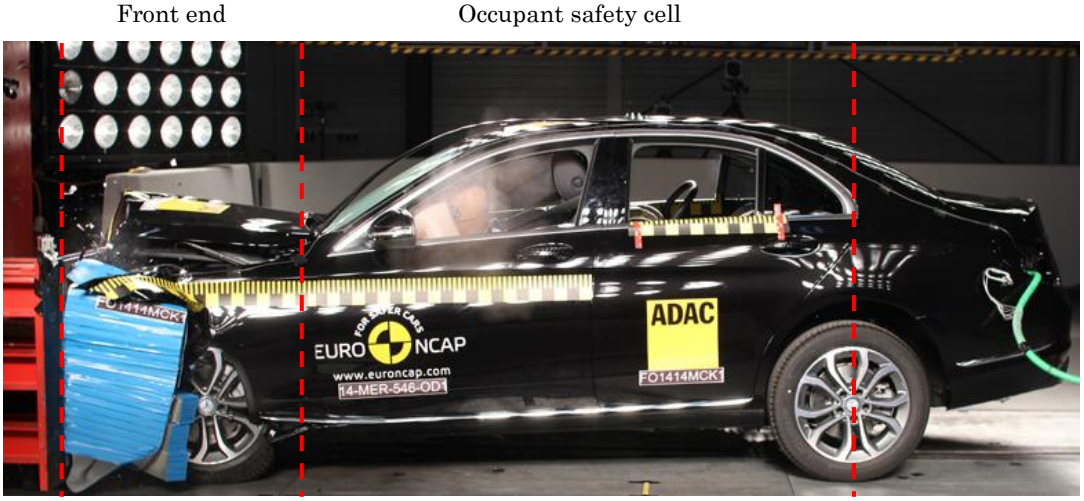

Figure 1.1 – European NCAP front impact test at 64 km/h. Image taken from euroncap.com [14].

The crash test in Figure 1.1 shows the deformation to the front–end of the vehicle. The front–end crash structure is designed to absorb the impact energy, hence large scale deformation occurs to the front–end in order to reduce the forces experienced by the occupant safety cell.

The focus of this research is to explore suitable alternative materials to conventional steel and aluminium alloys currently used to produce automotive crash structures. The intention is to maintain existing performance whilst reducing crash structure mass.

1.2 Current automotive body–in–white crash structures

The body–in–white (BIW) is a term used in the automotive industry which refers to the basic structure of the vehicle. This does not include the powertrain, doors or interior fittings. The current mainstream automotive BIW is referred to as the unitized body (uni–body) structure [15], which is shown in Figure 1.2. The conventional automotive uni–body is a single shell made up almost exclusively of pressed sheet steel panels, which are welded together. The strength, stiffness and load transfer paths are provided by all the panels joined together.

The function of the front longitudinal members highlighted in blue in Figure 1.2 is to absorb impact energy from a front–end collision. Additionally, a bolt–on structure, called a crash box, is added onto the end of the longitudinal member; collectively they are known as crush tubes or crush cans. The success of these members is dependent on whether they reduce the crash forces experienced by the vehicle occupants.

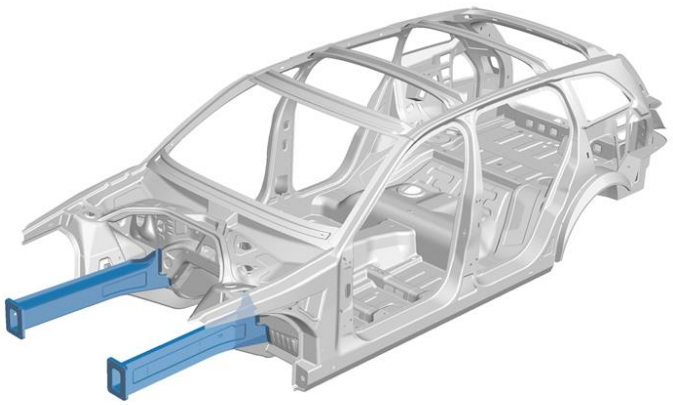

Figure 1.2 – Representative automotive body–in–white [16] made up of pressed sheet metal. Shown in blue are the front longitudinal members.

The likelihood of occupant injury is decreased as the energy absorbing members reduce the deceleration or pulse experienced by the occupants [11]. Furthermore,

the energy absorption of the front longitudinal members reduces intrusion into the occupant region of the vehicle, lowering the chance of physical injury [2].

The typical construction of the front longitudinal member is the top hat and backplate, shown in Figure 1.3. The top hat and backplate are most commonly joined together at the flanges using resistance spot welds (RSW) though these members are also produced from aluminium extrusions in premium applications. In this work only the top hat and backplate type members are tested.

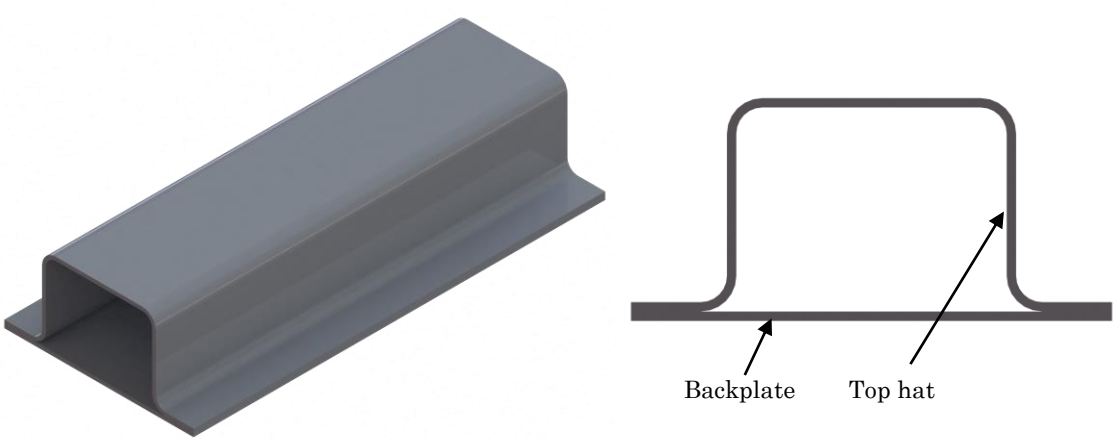

Figure 1.3 – Representation of the top hat and backplate structure commonly used for the front longitudinal member.

During impact, the front longitudinal member deforms along its length, absorbing energy. The mechanism of energy absorption is described in Section 1.5.

The front longitudinal members are large structural components of the vehicle, which makes their mass reduction, whilst maintaining energy absorption performance of academic and commercial interest, and will form the topic of research in this PhD.

1.3 Body–in–white mass reduction

There are a number of parties working on light–weighting the BIW. These are the automotive Original Equipment Manufacturers (OEMs), material manufacturers/ suppliers (steel, aluminium and composite producers) and research organisations. There are different methods currently employed and considered by automotive OEMs, these will be described in the next section.

1.3.1 Down–gauging

Down–gauging is the process of reducing the thickness of a part to reduce its weight, which usually involves increasing the strength of the thinner metal to compensate [2], [4].

The state of the art steel body–in–white is now being produced using a higher percentage of higher strength steels than ever before, which allows for the down–gauging of components [17]. Figure 1.4 shows the use of boron steels and other ultra–high strength steels (UHSS) in a Ford Taurus BIW, reducing the thickness of the heaviest components.

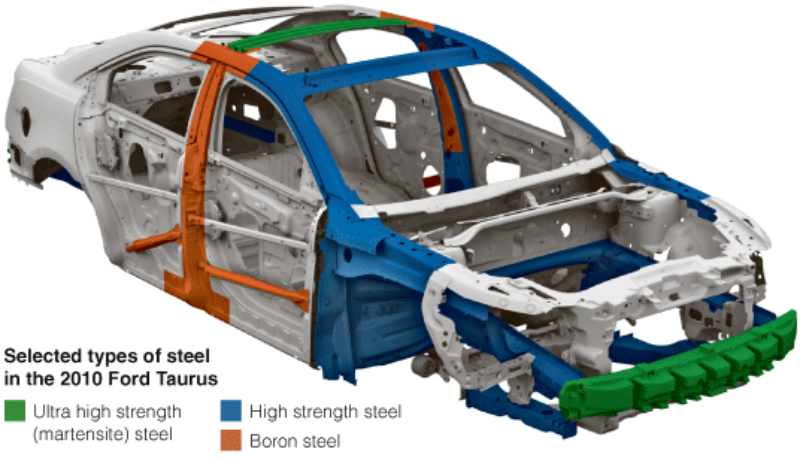

Figure 1.4 – Use of high strength steels to down gauge the automotive body–in–white [18].

However, down–gauging decreases the bending stiffness of the part since the material's elastic modulus does not change with increasing strength and hence, is

not necessarily the correct solution in all cases. For example, where intrusion is an issue the deflection of the part is limited by not only strength but bending stiffness. An example of an intrusion critical part is the B–pillar, shown in Figure 1.4 as the vertical orange part.

1.3.2 Tailor welded blanks

A tailor welded blank (TWB) is a part which is pressed from a sheet made up of multiple thicknesses and grades of steel (in all production examples). The individual sheets are seam welded or brazed together, and the joined sheet is then pressed into shape [19], [20].

Figure 1.5 shows the use of the tailor welded blank. A thinner gauge steel is used for the front of the crash structure to reduce the peak impact force and thicker gauge steel towards the rear to increase crushing force. This softens the impact at first and increases the force gradually. Therefore, the impulse felt by vehicle occupants is reduced whilst the mean crushing force hence, energy absorption, is maintained. This is typical of the steel industry's current solutions to light–weighting, with the use of thinner gauge and higher strength steels where possible and tailor welded blanks to join to thicker or different grades of steel. Tailor welded blanks do have disadvantages, including issues such as welding two grades of steel of different strength and ductility [20]–[26]; furthermore, formability and crushing response differs depending on weld position [22], [26].

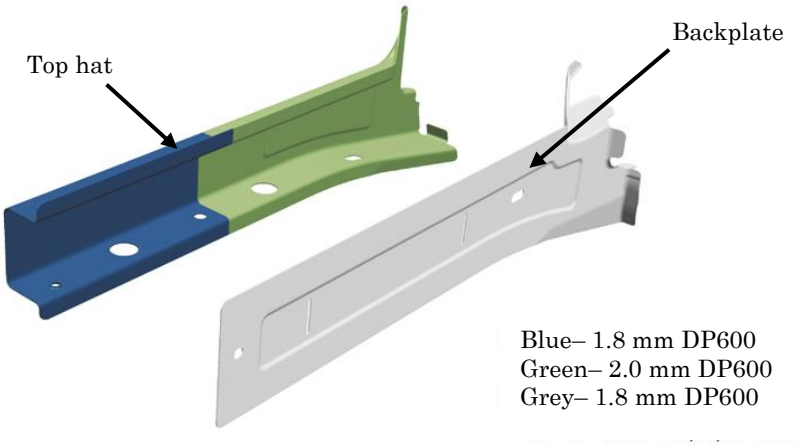

Figure 1.5 – Representative of a tailor welded top hat. The blue part is a thinner steel than the green part, both are seam welded or brazed together and pressed into shape [16].

The techniques of light–weighting described above highlight the complexity in body–in–white design. Where different load cases and criteria must be met by the same part, hence strength increase and down–gauging may not always be the solution.

1.3.3 Lightweight materials substitution

Lightweight materials substitution uses aluminium alloys, Fibre Reinforced Plastic composites (usually with glass (GFRPs) or carbon (CFRPs) as the reinforcement), magnesium alloys, titanium alloys and foams in place of steel.

Using lightweight alloys such as aluminium or magnesium has an advantage over steels since the use of low–density materials allows the use of thicker parts. Therefore, the bending stiffness of the steel part may be matched whilst reducing component mass.

Jaguar Land Rover and Mercedes–Benz currently produce a conventional uni–body which is predominantly, if not completely made from aluminium alloys. Figure 1.6 shows a Mercedes SLS aluminium uni–body and closures. Hence, material substitution performs light–weighting by producing the conventional automotive

uni–body using a lower density material, with Jaguar claiming a 40% reduction in BIW mass by replacing steel with aluminium in their XJ (X350) model [27].

Figure 1.6 – Mercedes–Benz SLS body–in–white [28] produced entirely using aluminium alloys.

However, the disadvantages of using aluminium are the reduced formability of aluminium alloys, the reduction in material strength, stiffness and hardness [29]. Additionally, since it is currently not conventional to resistance spot weld aluminium alloys [30] and some are un–weldable [29], [31], the common joining method in the BIW is the steel self–pierced rivets (SPRs), as well as SPRs combined with an adhesive [32]. Conversely, SPRs are an expensive and mass increasing joint. Additionally, introducing their own galvanic corrosion issues, as the steel rivet and aluminium sheet are in close proximity [33].

1.3.4 Body–in–white redesign

Another method of weight reduction employed by automotive OEMs is the redesign of the body–in–white or components of it. Audi and Jaguar Land Rover mass–produce vehicles with aluminium castings in place of stamped steel sheet; this is shown in Figure 1.7 and Figure 1.8.

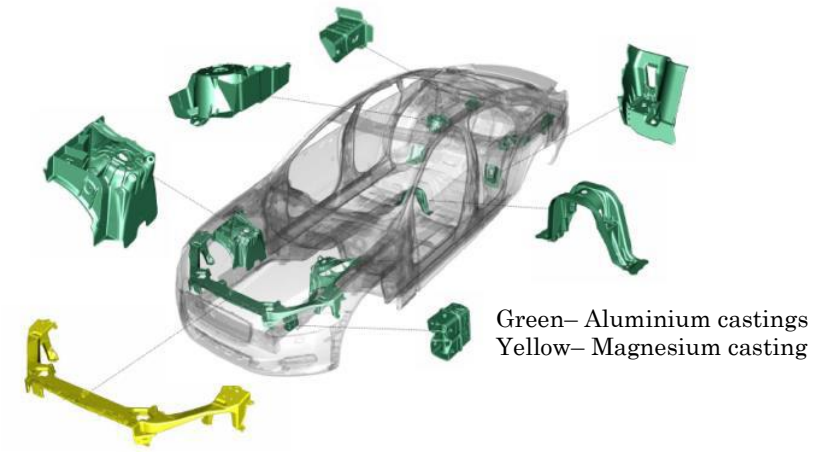

Figure 1.7 – Aluminium castings in green and magnesium casting in yellow used to produce a Jaguar X351 body–in–white.

Figure 1.8 also shows the Audi A2 model, where the BIW employs a space frame structure as opposed to the conventional uni–body. The space frame chassis uses struts connected at nodes to produce the basic structure of the vehicle as opposed to the conventional BIW, which is produced using joined sheet metal where the sheet metal is a stressed part of the vehicle structure. Audi use a combination of castings, extrusions and pressed sheet metal, all aluminium, to produce its space frame BIW.

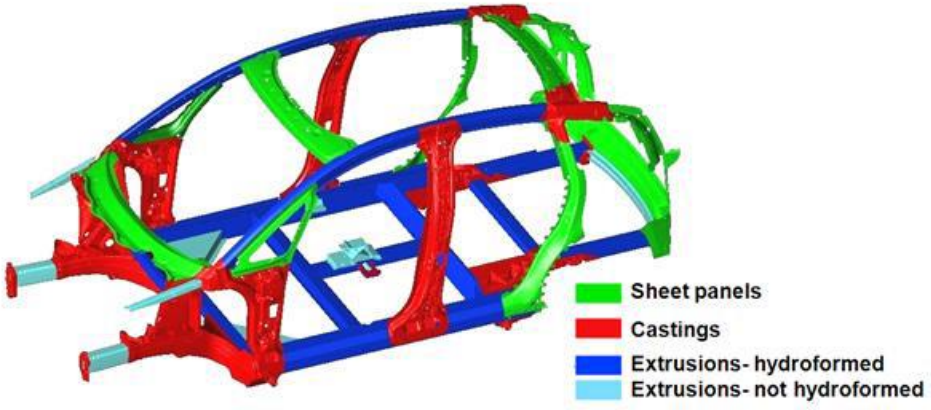

Figure 1.8 – Audi A2 which uses an aluminium space frame type structure as opposed to the conventional body–in–white.

Another more drastic change to the design of the body–in–white is the approach BMW have taken with the i–series models (launched in November 2013). The i–

series vehicles utilise a hybrid electric powertrain incorporating an internal combustion engine, electric motor and battery power; the body–in–white is separated to what could be considered the "original" car design, the chassis and coach [34], see Figure 1.9. The chassis holds the powertrain, suspension and ancillaries; the coach holds the occupants and interior fittings. The coach employs CFRP composites to produce a lightweight structure; the chassis uses the battery pack as a structural module of the vehicle and exploits aluminium alloys for the sheet metal pressings to further lower vehicle mass.

Figure 1.9 – BMW i–series BIW consists of a chassis and coach. Image adapted from [35].

1.4 Alternatives to monolithic sheet materials

Section 1.2 and 1.3 described the current automotive body–in–white structure and the latest advancements such as the aluminium uni–body. However, steel remains the predominant material used in the BIW, albeit with a progression toward the use of higher strength grades and thinner gauges to reduce vehicle weight. Not considered is the use of titanium or magnesium alloys as their use in structural components in the BIW is not deemed suitable. This section therefore, considers the alternatives to using monolithic sheet metals in further detail.

1.4.1 Composite materials

Composite materials are receiving more interest in the body–in–white because of their high specific strength and directional properties. A composite material in this instance, regardless of manufacturing route, refers to a fibre reinforced material. The matrix may be either a thermoset polymer such as an epoxy resin, or a thermoplastic polymer such as a polyamide. The reinforcement is predominantly glass or carbon fibre. However, there are other reinforcements available, for example natural fibres and polymer fibres [36] though these materials are not currently used in the automotive sector.

Current uses and research in composite materials for automotive applications vary widely from outer panels and carriers with no structural requirements to structural members and crash energy absorbers. Research into the use of composite materials in the BIW to replace conventional metals is expansive.

Examples of composite use in the mainstream BIW includes the Land Rover Evoque composite tailgate which is produced using resin transfer moulding (RTM) and glass mat thermo–composite (GMT) [37], which has led to a 30% reduction in its weight compared to a steel tailgate.

Currently, the most common use of composite materials is the front end carrier module [38], [39], a complex but non–structural part which holds many ancillaries for the engine and cooling systems. The carrier requires stiffness but not particular strength therefore in steel it tends to be very thick and heavy hence, has been replace with glass fibre reinforced plastic (GFRP). An example being the Mazda 6 which has employed a glass fibre polypropylene matrix front end carrier since 2002 [40].

There are also some uses of carbon fibre reinforced plastics (CFRP) in the body–in–white of low production volume vehicles. The BMW M–series cars have CFRP roofs reducing the mass and also lowering the centre of gravity over the standard vehicle [41].

More commonly CFRP is implemented for the full BIW of super cars such as Ferraris and Lamborghinis. In these applications the entire BIW is made in one piece from CFRP [42], an example is shown in Figure 1.10. However, it is noteworthy that even in these instances metallic energy absorbers are still employed. The avoidance of fibre reinforced plastics in the automotive crash structure is due to the method of energy absorption for these materials, which involves large scale fracture and failure [43]. This failure mechanism is avoided in the automotive mass market due to customer concerns and the difficulty in predicting performance. Figure 1.10 shows the front aluminium extrusion crash tubes of the McLaren MP4–12C super car.

Figure 1.10 – A state of the art super car (McLaren MP4–12C) using a carbon fibre tub for occupants and aluminium extrusions front and rear for crash protection [44].

1.4.2 Sandwich materials

Sandwich materials have discrete layers bonded together. The stiff materials are placed on the outer surfaces whilst a low density core maintains the separation between the stiff layers without increasing the weight of the part. Therefore, sandwich materials exhibit high specific bending stiffness and are advantageous in applications where elastic bending or deflection are the greatest consideration.

Sandwich materials are often confused or grouped with laminate materials; the difference being the proportion of polymer and adhesive in the layup and the intended function. Figure 1.11 shows a schematic of a metal–laminate panel, where the adhesive core (in red) bonds two metal skins, which may or may not be the same grade or thickness.

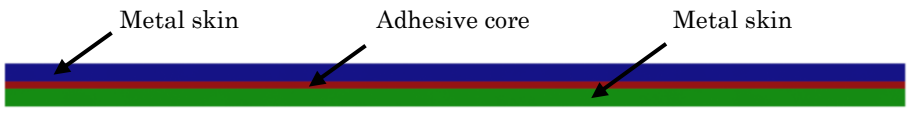

Figure 1.11 – Metal–laminate panel, with two steel skins bonded with an adhesive.

A sandwich material on the other hand has a considerably thicker core, which is bonded between the two metal skins (Figure 1.12).

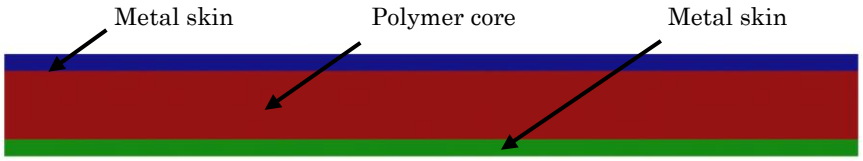

Figure 1.12 – Representation of a metal–polymer–metal (MPM) sandwich panel.

Sandwich panel cores are not limited to polymers or adhesives; bonded honeycombs and composite materials such as fibre–reinforced plastics (FRPs) have been used as core materials [8].

The laminates and sandwich materials considered are metal skinned since these are by far the most common in engineering applications, due to the metal's stiffness, ductility, and comparative ease of manufacturing. Metal–laminates are generally intended for noise and vibration reduction whereas sandwich panels are designed for their stiffness properties [9], [16], [45]–[48]. The overall material thickness of a laminate is essentially the same as the monolithic panel it replaces assuming equal stiffness. In other words, a 1.0 mm steel panel would be replaced with a 0.5/0.05/0.5 mm (steel/adhesive/steel) laminate, which has the same stiffness and essentially the same weight, so no weight reduction is gained in this component. However, due to the addition of an adhesive core, the vibration characteristics are dramatically changed, with the loss factor of the panel increased providing enhanced damping properties [49], [50]. In the automotive sector where noise, vibration and harshness are important in BIW design, metal–laminates allow weight reduction by decreasing the amount of additional sound deadening material required.

The MPM sandwich panel with a thicker core may well have improved dampening properties [51], but the increase in core thickness provides a bending stiffness increase for little weight increase, due to the low density of the core (this will be explained in more detail in Section 1.6).

The core of the MPM sandwich material can be any polymer, either engineering polymers such as polyamide (Nylon) or commodity polymers such as polypropylene or polyethylene, or even polymer foams. The purpose of the core in the MPM sandwich is to act as a low density filler to maintain a fixed distance between the metal layers and to transmit shear stresses through the layers [52].

Currently, industry and academic researchers are concentrating their efforts on employing MPM sandwich materials for the outer panels of the automotive body to reduce their weight. In general these panels are non–structural parts such as door outer panels, bonnet and tailgate outer panels and spare tyre wells [53], [54].

An example of MPM sandwich materials in automotive applications is the use of a commercially available product, Hylite. This is a 1.2 mm thick aluminium/ polypropylene/aluminium (0.2/0.8/0.2 mm) sandwich [54], [55]. This research was conducted in the 1990s by Hoogovens B.V. (now part of Tata Steel Europe). There are a few published examples of work done on this material, including a pressing trial of a Volkswagen Polo hood (or bonnet) in the material [54] (shown in Figure 1.13), and hem flanging processes attempted on the material to allow mass part production using sandwich materials [56].

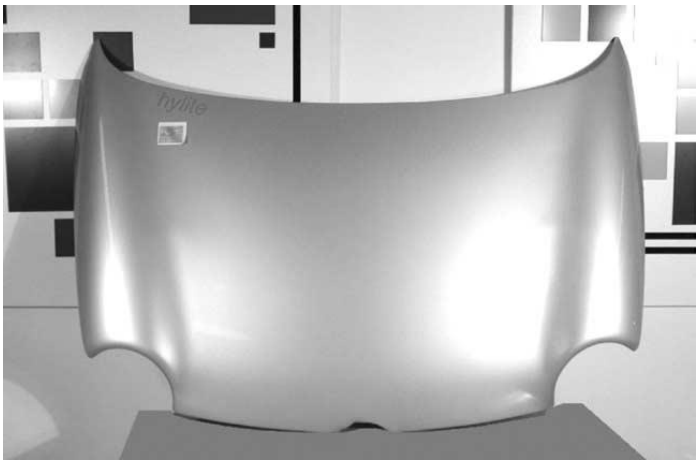

Figure 1.13 – Volkswagen Polo bonnet/hood panel made from Hylite sandwich panel, an aluminium–polypropylene–aluminium sandwich panel [54].

The concept of using sandwich materials for the automotive body–in–white has been attempted by Inrekor. The sandwich material used has a polypropylene foam core with aluminium skins. The chassis (Figure 1.14) is made from flat sandwich panels, which are bolted together, and a body is bolted on top, unlike the current BIW, which brings the two together in the uni–body construction to save weight. Even so, Inrekor claim a weight saving of 30–40% [57]. However, this chassis concept has not been used for any production vehicles.

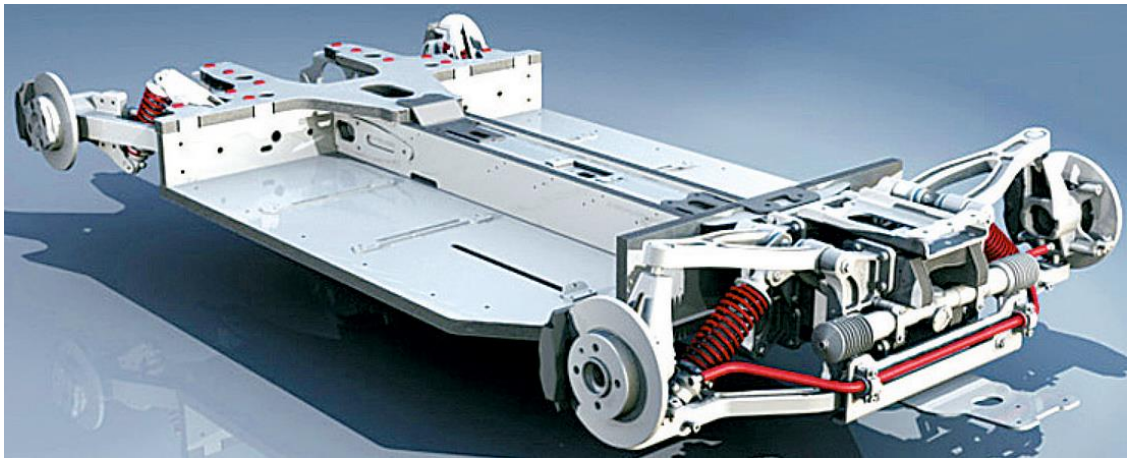

Figure 1.14 – Inrekor sandwich panel chassis concept [57].

1.5 Mechanism of energy absorption

The method of energy absorption of the front longitudinal member is the axial collapse of the crash tube, shown in Figure 1.15. The axial collapse of the material is a predictable phenomenon hence the energy absorption of the structure once determined can be readily repeated. This is shown by the large body of testing in this field [58]–[68]. Furthermore, a relatively high stroke efficiency can be achieved, with the common assumption in this field that a crash tube is able to collapse 73% of its original length [69]. After this point, the tube self–contacts and the crushing force increases markedly, this is known as "bottoming out".

The collapse of the crash tube is defined as a local buckling of a length of the tube with a toroidal fold in the corners and an Euler type buckle along the straight sections [70]. This is usually described as the asymmetric folding pattern.

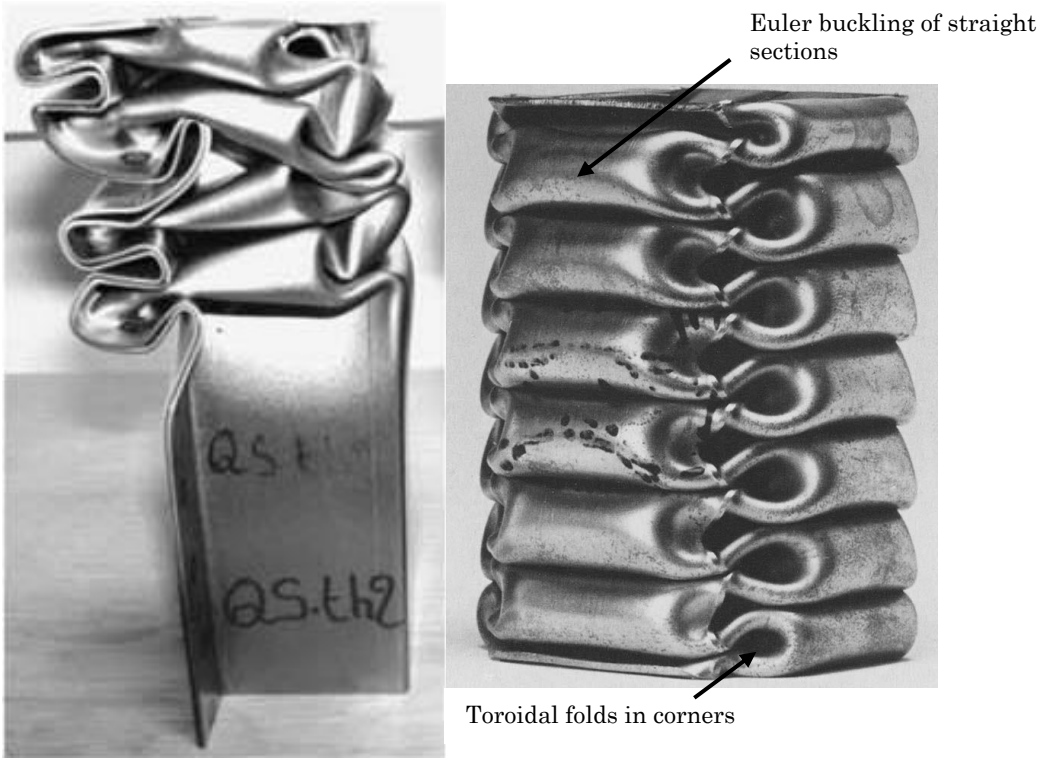

Figure 1.15 – Left shows the axial collapse of a top hat and backplate crash tube (60 × 60 mm section) [71] and right shows a rectangular section (37 × 37 mm) such as welded tube or extrusion. Folding is predictable and repetitive. Scale bar is not provided by the author.

The cross section of the crash tube can be considered to be made up of a series of corner elements, where each corner element folds with a bending and rolling deformation [72]. A fold wavelength is created therefore, a repeating unit is produced along the length of the structure.

For each fold, the initial energy absorption is due to the bending of the material to produce the fold or horizontal hinge line, (Figure 1.16). The remainder of the energy absorption is rolling of the horizontal hinge line as it collapses further. The energy absorption mechanisms are therefore resistance to bending and resistance to rolling of the folded material. Once a cross section has fully collapsed it essentially becomes rigid and the next length of material folds in the same manner. Overall, multiple folds make up the collapse of the crash tube, hence energy is absorbed progressively over length of the tube.

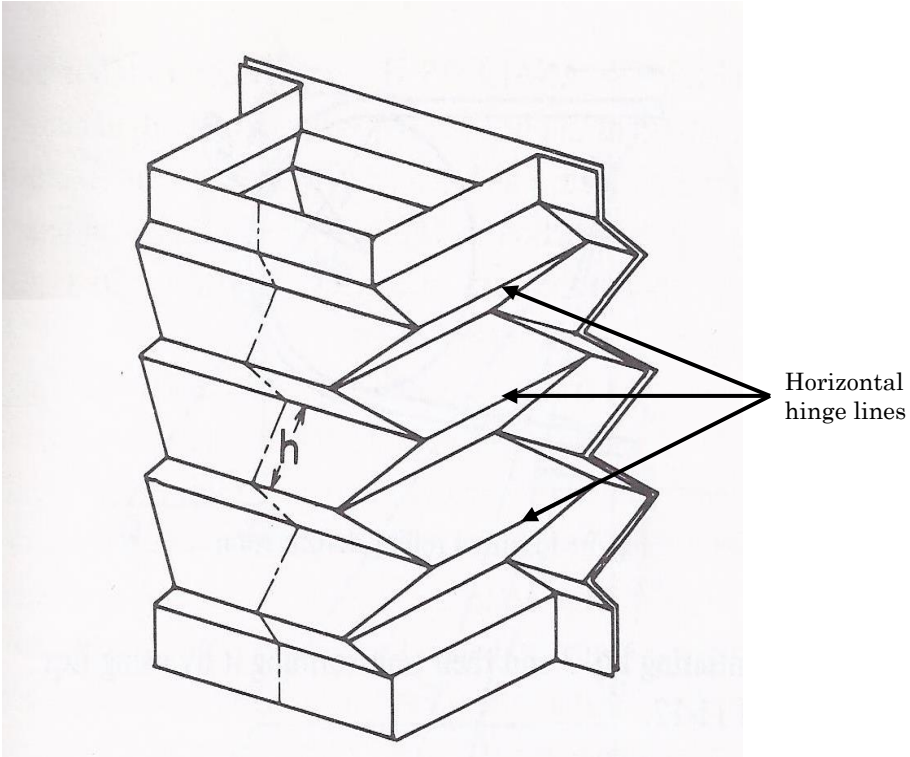

Figure 1.16 – The idealised deformation of a top hat and backplate crash structure, image taken from [72].

The characteristic force–displacement response of a crushed metal tube is shown in Figure 1.17. The crushing force can be seen along with the crushing distance of the tube and the fold wavelength and the response of the tube at each portion of the fold is also evident. The maxima in the force are indicators of the onset of a fold, the minima are the points at which the folds have completed. The large initial peak is the resistance to the initial fold in the material. Subsequent folds form with lower force. The horizontal dashed line indicates the average or mean crush force (P_m) over the entire crushing distance.

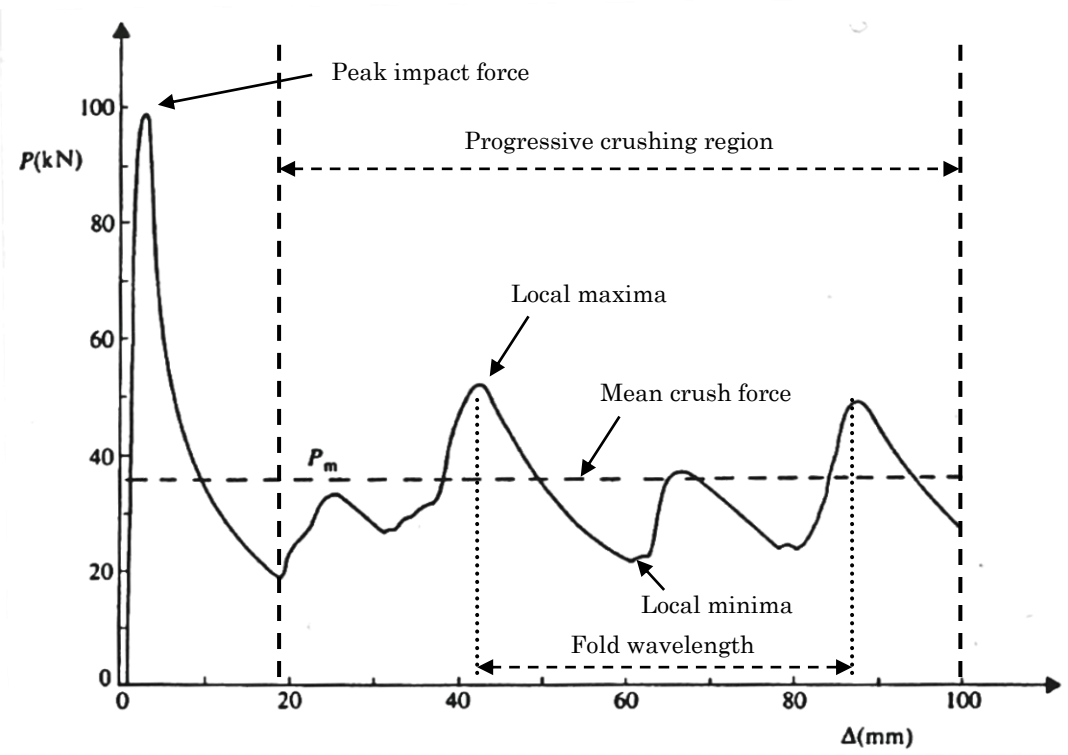

Figure 1.17 – Characteristic force–displacement output from a steel crash structure impact test, image taken from [70].

The peak impact force is important to consider as the initial deceleration in an impact must be minimised to reduce injury risk to the occupants [11], but also the peak impact force must be high enough to withstand low speed impacts without damage. A ratio of the peak impact force to the mean crush force can also be calculated and this determines the significance of the undesirable peak impact

force in the total energy absorption. The ideal material should be designed to minimise the peak impact force whilst maximising the mean crush force. In other words, the difference between the peak impact force and the mean crush force should be small.

Furthermore, from the force–displacement curve, the energy absorption is calculated using the method in Equation 1.1 and the mean crush force for the impact is defined using Equation 1.2.

$$E_a = \int_0^{max} P \cdot ds \qquad \text{Equation 1.1}$$

Where, E_a = Energy absorbed (J)

P = Force at any given point (m)

ds = Displacement at a given point (m)

Integrating P with respect to ds and rearranging gives the following:

$$P_m = {}^{E_{a,max}}/_{s_{max}} \qquad \text{Equation 1.2}$$

$E_{a,max}$ = Maximum energy absorbed (J)

P_m = Mean crush force (N)

s_{max} = Displacement at maximum energy (m)

To compare the performance of a crash structure to another, the specific energy absorption (SEA) is a commonly used parameter [73]. The SEA is defined in Equation 1.3.

$$SEA = {}^{E_{a,max}}/_{m_{deformed}} \qquad \text{Equation 1.3}$$

SEA =Specific energy absorption (J/g)

$m_{deformed}$ = Mass of deformed length (g)

1.6 Sandwich theory

Stiffness can be considered in two ways, intrinsically as the modulus (predominantly elastic modulus) of a material, or extrinsically as the stiffness of a part or component due its geometry, usually thickness. Therefore, to increase the force for a given deflection one can either increase the elastic modulus of the material or increase the thickness of the material. In general, both of these methods will increase the mass of the component. This is shown readily by Equation 1.4, which is the elastic deflection equation from classical mechanics for a component in bending [74].

To ascertain a certain value of M (the bending moment), with a fixed r, either the elastic modulus, E (intrinsic stiffness) or the 2nd moment of area, I (component thickness) can be increased.

$$M = \frac{E \cdot I}{r} \qquad \text{Equation 1.4}$$

Where, M = bending moment (N.m)

E = Elastic modulus of the material ($N.m^{-2}$)

r = Radius of gyration (m)

I = 2nd moment of area (m^4)

The 2nd moment of area, I is of particular interest since this shows the relationship between the stiffness of a component and the thickness of the material. The 2nd moment relates to thickness as shown in Equation 1.5. Since the 2nd moment of area is proportional to the cube of the thickness (for a rectangular section), a small

increase in thickness leads to a significant increase in stiffness. However, the weight increases linearly with thickness.

$$I = \frac{bT^3}{12} \qquad \text{Equation 1.5}$$

Where, b = width of part (m)

T = thickness of the material (m)

Applying this methodology to MPM sandwich materials in bending, an increase in stiffness can be achieved without significant mass increase. The use of a low density core allows the thickness of the component to be increased without a linear increase in mass. This stiffness increase due to increased thickness is subverted somewhat by the elastic modulus reduction of a sandwich material; since a low density core has a low modulus which reduces the average modulus of the sandwich material.

This is quantified by parallel axis theorem modified for a sandwich panel (Equation 1.6). The cores properties other than its thickness are ignored as the core is assumed to provide separation and not stiffness.

$$I = 2 \cdot \left(\frac{b{t_f}^3}{12} + \mathrm{b} \cdot t_f \cdot \mathrm{d}^2 \right) \qquad \text{Equation 1.6}$$

Where, b = width of part (m)

t_f = thickness of skin material (m)

d = distance of skin from the neutral axis (m)

From parallel axis theorem it can be seen how MPM sandwich materials can have a high specific bending stiffness and plastic bending stiffness [75], [76]. The total

amount of material used in the skin, $2t_f$ can be less than the thickness of the solid material, T it replaces due to the addition of the separation, d in the sandwich increasing the material stiffness. This allows components to be produced which meet the stiffness requirement of the monolithic structures replaced whilst having a reduced mass.

For energy absorption in crash structures, another parameter is also important, the plastic bending moment. This moment (defined in Equation 1.7) is the resistance to plasticity through the entire section of the material during bending. Therefore, the greater the plastic bending moment, M_p, the greater the resistance to bending, which essentially increases the energy required to bend the section.

$$M_p = \frac{\sigma_y \cdot T^2}{4} \qquad \text{Equation 1.7}$$

Where, σ_y = Yield strength (Pa)

T = thickness of the material (m)

Equation 1.7 shows that the plastic bending moment is proportional to the square of the thickness. Hence, increasing the material thickness significantly increases the plastic bending moment and the potential for energy absorption.

The second factor in the plastic bending moment is the yield strength, σ_y. An MPM sandwich material with a polymer core will invariably have a lower strength than the monolithic metal. Since the plastic bending moment is proportional to yield strength, the polymer core's low strength will reduce the positive effect of the thickness.

Thus from classical mechanics, the statement "an increase in thickness of a material increases the energy absorbed" may be true for monolithic metals, this

relationship between energy absorption and thickness is not known for sandwich materials. Therefore, the use of an MPM sandwich material for an energy absorber in automotive crash structures warrants investigation.

1.7 A case for MPM sandwich materials?

The aim of this PhD is to develop fundamental understanding into the performance of MPM sandwich materials for use in automotive crash structures.

Section 1.3.3 shows that aluminium alloys are a suitable lightweight alternative to steels for automotive crash structures; however, aluminium alloys are significantly more expensive than steels, in terms of raw material cost and overall manufacturing cost. For this reason, steel is still the predominant material used to produce the body–in–white of high volume production vehicles.

Therefore, this research will explore the possibility of MPM sandwich materials competing with the mass specific energy absorption of aluminium alloys. The potential for MPMs to be manufactured at lower cost than aluminium alloys and their ease of recyclability could strengthen the resolve to employ them in crash structures in the body–in–white.

The crash performance will be compared to state of the art crash structure materials currently used. This allows the light–weighting performance of the sandwich materials to be easily identified and any advantages to their use highlighted.

Steel–polypropylene–steel will be used as the model to assess the performance of MPM sandwich materials. The interest in steel originates from its high elastic modulus, availability in various strength and thickness grades and low cost. Whilst PP may not be the ideal core, it is a convenient and adequate core for the concept study of MPM sandwich materials. Therefore, steel–polypropylene–steel provides a model for assessing MPM sandwich materials in crash structures.

The contribution to knowledge of this project is the fundamental research into the use of steel–polypropylene–steel sandwich materials for automotive crash structures. The research conducted allows the production of lightweight automotive crash structures, which maintain the performance of the current state of the art materials, with a reduced mass.

1.7.1 Objectives

To gain an understanding into the performance of steel–polypropylene–steel sandwich materials when used for automotive crash structures, the following objectives were set:

- State of the art monolithic metals are to be impact tested in order to provide a performance target in terms of specific energy absorption, mean crush force and deformation modes.
- Production of steel–polypropylene–steel sandwich materials which have sufficient bond strength to resist forming strains imparted on the adhesive layer.
- Quasi–static and dynamic (impact) testing of sandwich materials is to be performed to compare material performance to state of the art monolithic metals and to determine their deformation modes.
- Determine the optimal joint for crash structures in each material tested (both monolithic metals and steel–polypropylene–steel sandwich materials.
- Define a method of predicting the crash performance of steel–polypropylene–steel sandwich materials using finite element analysis.

1.8 Thesis structure

This chapter discussed the background to the project, the theory of the potential MPM sandwich materials advantage in energy absorption and the aspirations of the research. The following includes the scope of work undertaken in order to assess the crash performance of MPM sandwich materials.

Chapter 2 details the relevant literature on energy absorption methods and materials in the automotive crash structure.

Chapter 3 states the methodology by which the physical testing was performed. This includes all of the test methods for quasi–static and dynamic testing (quasi–static crush and crash testing respectively). The methods of sandwich material production used and the performance testing on the sandwich materials to enable production of crash structures such as T–peel testing to ensure a sufficient bond. The method of crash structure production is also discussed.

Chapter 4 details the results of the sandwich material manufacture optimisation as well as observations during the manufacture of sandwich materials and crash structures.

Chapter 5 describes the results of the quasi–static crush and dynamic (crash) testing. The crushing forces and energy absorbed are calculated for the three repeat tests on each sandwich material construction produced. The difference in deformation and energy absorption performance quasi–statically and dynamically is considered. Monolithic materials are tested for comparison to the sandwich materials. Images of the deformed crash structures are also shown for the sandwich materials to show the deformation progression of sandwich materials.

Chapter 6 defines the methodology for finite element (FE) modelling in LS–DYNA using MPM sandwich materials. The methodology for modelling sandwich materials is compared to monolithic material modelling best practice along with relevant literature on the topic of material modelling.

Chapter 7 validates the finite element simulation results against the physical crash testing (Chapter 4). The differences between the physical testing and the simulations are also discussed and accounted for.

Chapter 8 studies the effect of the polypropylene core thickness and the steel skin thickness on the energy absorbed by the sandwich material crash structures. Two methods are used for this purpose. Firstly, a full–factorial analysis is performed using the validated finite element model from Chapter 6. An analytical solution is then proposed, this solution is modified from a model in the literature, which predicts the performance of monolithic metal crash structures. The analytical solution is validated against the finite element analysis solutions.

Chapter 9 provides a summation of the work done, concluding remarks and further work required to make the use of MPM sandwich materials a viable option for automotive crash structures.

1.9 References

[1] European Commission, “End of Life Vehicles,” 2014. [Online]. Available: http://ec.europa.eu/environment/waste/elv_index.htm. [Accessed: 05-May-2014].

[2] G. Davies, *Materials for Automobile Bodies*. Elsevier, 2012.

[3] Toyota Motor Corporation, “Toyota Auris specifications,” 2014. [Online]. Available: http://www.toyota.co.uk/new-cars/auris-specs-prices. [Accessed: 05-May-2014].

[4] X. M. Chen, M. F. Shi, G. Chen, M. Kamura, K. Watanabe, and Y. Omiya, “Crash Performances of Advanced High Strength Steels of DP780, TRIP780 and DP980,” *Soc. Automot. Eng. Tech. Pap.*, no. 2005–01–0354, 2005.

[5] Z. G. Hu, P. Zhu, and J. Meng, “Fatigue properties of transformation-induced plasticity and dual-phase steels for auto-body lightweight: Experiment, modeling and application,” *Mater. Des.*, vol. 31, no. 6, pp. 2884–2890, 2010.

[6] N. Abedrabbo, R. Mayer, A. Thompson, C. Salisbury, M. Worswick, and I. van Riemsdijk, “Crash response of advanced high-strength steel tubes: Experiment and model,” *Int. J. Impact Eng.*, vol. 36, no. 8, pp. 1044–1057, 2009.

[7] A. Mamalis, M. Robinson, D. Manolakos, G. Demosthenous, M. Ioannidis, and J. Carruthers, “Crashworthy capability of composite material structures,” *Compos. Struct.*, vol. 37, no. 2, pp. 109–134, Feb. 1997.

[8] A. Carradò, J. Faerber, S. Niemeyer, G. Ziegmann, and H. Palkowski, “Metal/polymer/metal hybrid systems: Towards potential formability applications,” *Compos. Struct.*, vol. 93, no. 2, pp. 715–721, Jan. 2011.

[9] M. Weiss, B. F. Rolfe, M. Dingle, and J. L. Duncan, “Elastic Bending of Steel-Polymer-Steel (SPS) Laminates to a Constant Curvature,” *J. Appl. Mech.*, vol. 73, no. 4, pp. 574–579, 2006.

[10] M. Grujicic, V. Sellappan, S. Kotrika, G. Arakere, A. Obieglo, M. Erdmann, and J. Holzleitner, “Suitability analysis of a polymer-metal hybrid technology based on high-strength steels and direct polymer-to-metal adhesion for use in load-bearing automotive body-in-white applications,” *J. Mater. Process. Technol.*, vol. 209, no. 4, pp. 1877–1890, 2009.

[11] Office of Vehicle Safety Research, “NHTSA FMVSS 208,” 1999.

[12] EuroNCAP, “EuroNCAP Frontal impact,” 2014. [Online]. Available: http://www.euroncap.com/tests/frontimpact.aspx. [Accessed: 04-Mar-2014].

[13] Insurance Institute for Highway Safety, “Small overlap frontal test.” [Online]. Available: http://www.iihs.org/iihs/ratings-info/frontal-crash-tests. [Accessed: 30-Jun-2014].

[14] EuroNCAP, “Mercedes Benz C-class NCAP rating report,” *2014*. [Online]. Available: http://www.euroncap.com/results/mercedes_benz/c_class/546.aspx. [Accessed: 03-May-2014].

[15] R. B. GmbH, *Automotive handbook*. Wiley, 2004.

[16] ThyssenKrupp, “Reference longitudinal member made of DP-W 600.” [Online]. Available: http://incar.thyssenkrupp.com/4_04_020_LT01_Referenz.html?lang=de. [Accessed: 17-Feb-2013].

[17] World Auto Steel, “FutureSteelVehicle Project.” [Online]. Available: http://www.worldautosteel.org/projects/future-steel-vehicle/. [Accessed: 19-Apr-2014].

[18] “Many Faces, and Phases, of Steel in Cars.” [Online]. Available: http://www.kleanindustries.com/s/environmental_market_industry_news.asp?ReportID=364972. [Accessed: 12-Mar-2014].

[19] T. Nakagawa, “Recent Developments in Auto Body Panel Forming Technology,” *CIRP Ann. - Manuf. Technol.*, vol. 42, no. 2, pp. 717–722, Jan. 1993.

[20] J. Rojek, M. Hyrcza-Michalska, A. Bokota, and W. Piekarska, “Determination of mechanical properties of the weld zone in tailor-welded blanks,” *Arch. Civ. Mech. Eng.*, vol. 12, no. 2, pp. 156–162, Jun. 2012.

[21] M. Abbasi, M. Ketabchi, T. Labudde, U. Prahl, and W. Bleck, “New attempt to wrinkling behavior analysis of tailor welded blanks during the deep drawing process,” *Mater. Des.*, vol. 40, pp. 407–414, Sep. 2012.

[22] F. Xu, G. Sun, G. Li, and Q. Li, “Experimental study on crashworthiness of tailor-welded blank (TWB) thin-walled high-strength steel (HSS) tubular structures,” *Thin-Walled Struct.*, vol. 74, pp. 12–27, Jan. 2014.

[23] S. K. Panda and D. R. Kumar, “Improvement in formability of tailor welded blanks by application of counter pressure in biaxial stretch forming,” *J. Mater. Process. Technol.*, vol. 204, no. 1–3, pp. 70–79, Aug. 2008.

[24] S. Gaied, J.-M. Roelandt, F. Pinard, F. Schmit, and M. Balabane, “Experimental and numerical assessment of Tailor-Welded Blanks formability,” *J. Mater. Process. Technol.*, vol. 209, no. 1, pp. 387–395, Jan. 2009.

[25] R. Safdarian Korouyeh, H. Moslemi Naeini, M. J. Torkamany, and G. Liaghat, “Experimental and theoretical investigation of thickness ratio effect on the formability of tailor welded blank,” *Opt. Laser Technol.*, vol. 51, pp. 24–31, Oct. 2013.

[26] K. Veera Babu, R. Ganesh Narayanan, and G. Saravana Kumar, “An expert system for predicting the deep drawing behavior of tailor welded blanks,” *Expert Syst. Appl.*, vol. 37, no. 12, pp. 7802–7812, Dec. 2010.

[27] Jaguar Land Rover, “World Leaders in Aluminium.” [Online]. Available: http://www.jaguarlandrover.com/gl/en/innovation/world-leaders-in-aluminium/.

[28] Altair Engineering Incorporated, “Novelis Supplies Aluminum Body for New 2012 Mercedes SL Saving 140kg,” 2012. [Online]. Available: http://altairenlighten.com/2012/05/novelis-supplies-aluminum-body-for-new-2012-mercedes-sl-saving-140kg/. [Accessed: 20-Feb-2014].

[29] J. E. Hatch, A. Association, and A. S. Metals, *Aluminum: Properties and Physical Metallurgy*. American Society for Metals, 1984.

[30] L. Han, M. Thornton, D. Boomer, and M. Shergold, “A correlation study of mechanical strength of resistance spot welding of AA5754 aluminium alloy,” *J. Mater. Process. Technol.*, vol. 211, no. 3, pp. 513–521, Mar. 2011.

[31] J. C. Benedyk, *Materials, Design and Manufacturing for Lightweight Vehicles*. Elsevier, 2010.

[32] G. Di Franco, L. Fratini, and A. Pasta, “Influence of the distance between rivets in self-piercing riveting bonded joints made of carbon fiber panels and AA2024 blanks,” *Mater. Des.*, vol. 35, pp. 342–349, Mar. 2012.

[33] A. Chrysanthou, “Corrosion behaviour of self-piercing riveted joints,” *Self-Piercing Riveting*, pp. 41–55, 2014.

[34] G. Genta and L. Morello, *The Automotive Chassis: Volume 1: Components Design*. Springer, 2008.

[35] BMW Group, “The future of urban mobility. BMW i.,” 2014. [Online]. Available: http://www.bmw.co.uk/en_GB/new-vehicles/bmw-i/bmw-i/concept.html. [Accessed: 07-Jul-2014].

[36] I. Verpoest, S. Lomov, Y. Swolfs, P. Jacquet, V. Michaud, J.-A. Manson, J. Hobdell, P. Hine, P. Marquette, H. Herten, and H. Vasiliadis, “Advanced Materials Enabling High-Volume Road Transport Applications of Lightweight Structural Composite Parts,” *SAMPE J.*, vol. 50, no. 3, pp. 30–37, 2014.

[37] Plastic Omnium, “Business Review 2012,” 2013. [Online]. Available: http://www.plasticomnium.com/24h/en/innovation.html. [Accessed: 05-Sep-2013].

[38] M. Chaturvedi, W. Schijve, and M. Marks, “Advanced Thermoplastic Composites for Automotive Semi-Structural Applications,” *Soc. Automot. Eng. Tech. Pap.*, no. 2009–26–0086, Jan. 2009.

[39] S. Kulkarni and W. Schijve, “Glass-Reinforced Thermoplastic Composites for Front End Module Applications,” *Soc. Automot. Eng. Tech. Pap.*, no. 2011–26–0053, Jan. 2011.

[40] T. Tochioka, C. Kawamoto, M. Ogawa, and K. Sugimoto, “Development of Module Carriers by Injection Molding with Long Glass-Fiber Reinforced

Polypropylene," *Soc. Automot. Eng. Tech. Pap.*, no. 2003–01–0791, Mar. 2003.

[41] BMW Group, "BMW M6 Coupe - Carbon roof." [Online]. Available: http://www.bmw.com/com/en/newvehicles/mseries/m6coupe/2012/showroom/design/carbontop.html.

[42] A. Jacob, "Built in Italy: the Lamborghini Avendator," *Reinf. Plast.*, vol. 57, no. 5, pp. 29–31, Sep. 2013.

[43] A. Mamalis, D. Manolakos, M. Ioannidis, and D. Papapostolou, "Crashworthy characteristics of axially statically compressed thin-walled square CFRP composite tubes: experimental," *Compos. Struct.*, vol. 63, no. 3–4, pp. 347–360, Feb. 2004.

[44] McLaren Automotive, "MP4-12C carbon fibre chassis," 2011. [Online]. Available: http://media.mclarenautomotive.com/. [Accessed: 02-May-2014].

[45] J.-K. Kim and T.-X. Yu, "Forming and failure behaviour of coated, laminated and sandwiched sheet metals: a review," *J. Mater. Process. Technol.*, vol. 63, no. 1–3, pp. 33–42, 1997.

[46] H. S. Cheng, J. Cao, H. Yao, S. D. Liu, and B. Kinsey, "Wrinkling behavior of laminated steel sheets," *J. Mater. Process. Technol.*, vol. 151, no. 1–3, pp. 133–140, 2004.

[47] J. K. Kim and P. F. Thomson, "Forming behaviour of sheet steel laminate," *J. Mater. Process. Technol.*, vol. 22, no. 1, pp. 45–64, 1990.

[48] ThyssenKrupp, "BONDAL® makes engines quieter," *Sep. 19, 2006*, 2006. [Online]. Available: http://www.thyssenkrupp.com/en/presse/art_detail.html&eid=TKBase_1158243329937_216795425.

[49] T. E. Welch and J. R. Schwaegler, "Cost and Performance Benefits for Laminated Steel Body," *Soc. Automot. Eng. Tech. Pap.*, no. 1999–01–1784, May 1999.

[50] L. A. Mignery, "Designing Automotive Dash Panels with Laminated Metal," *Soc. Automot. Eng. Tech. Pap.*, no. 1999–01–3201, Sep. 1999.

[51] M. Dunand and J.-N. Gacel, "USILIGHT: A Cost-Effective Solution to Lighten Cars," *Soc. Automot. Eng. Tech. Pap.*, no. 2006–01–1216, Apr. 2006.

[52] D. Mohr and T. Wierzbicki, "Crushing of soft-core sandwich profiles: experiments and analysis," *Int. J. Mech. Sci.*, vol. 45, no. 2, pp. 253–271, 2003.

[53] T. M. Link, "Formability and Performance of Steel-Plastic-Steel Laminated Sheet Materials," *Soc. Automot. Eng. Tech. Pap.*, no. 2001–01–0079, Mar. 2001.

[54] I. Burchitz, R. Boesenkool, S. van der Zwaag, and M. Tassoul, "Highlights of designing with Hylite - a new material concept," *Mater. Des.*, vol. 26, no. 4, pp. 271–279, 2005.

[55] W. Hufenbach, J. Jaschinski, T. Weber, and D. Weck, "Numerical and experimental investigations on HYLITE sandwich sheets as an alternative sheet metal," *Arch. Civ. Mech. Eng.*, vol. 8, no. 2, pp. 67–80, 2008.

[56] W. T. M. Buters, T. Retter, and W. Stall, "Hem Flanging Hylite Sandwich Sheet for Mass Production," *Soc. Automot. Eng. Tech. Pap.*, no. 982330, Sep. 1998.

[57] inrekor TM Ltd, "Inrekor chassis." [Online]. Available: http://www.inrekor.com/. [Accessed: 03-Sep-2013].

[58] Ø. Jensen, M. Langseth, and O. S. Hopperstad, "Experimental investigations on the behaviour of short to long square aluminium tubes subjected to axial loading," *Int. J. Impact Eng.*, vol. 30, no. 8–9, pp. 973–1003, Sep. 2004.

[59] A. G. Hanssen, M. Langseth, and O. S. Hopperstad, "Static and dynamic crushing of circular aluminium extrusions with aluminium foam filler," *Int. J. Impact Eng.*, vol. 24, no. 5, pp. 475–507, May 2000.

[60] O.-G. Lademo, T. Berstad, M. Eriksson, T. Tryland, T. Furu, O. S. Hopperstad, and M. Langseth, "A model for process-based crash simulation," *Int. J. Impact Eng.*, vol. 35, no. 5, pp. 376–388, May 2008.

[61] W. Abramowicz and N. Jones, "Dynamic axial crushing of square tubes," *Int. J. Impact Eng.*, vol. 2, no. 2, pp. 179–208, 1984.

[62] L. Durrenberger, X. Lemoine, and A. Molinari, "Effects of pre-strain and bake-hardening on the crash properties of a top-hat section," *J. Mater. Process. Technol.*, vol. 211, no. 12, pp. 1937–1947, 2011.

[63] F. Schneider and N. Jones, "Observations on the design and modelling of some joined thin-walled structural sections," *Thin-Walled Struct.*, vol. 46, no. 7–9, pp. 887–897, 2008.

[64] F. Schneider and N. Jones, "Influence of spot-weld failure on crushing of thin-walled structural sections," *Int. J. Mech. Sci.*, vol. 45, no. 12, pp. 2061–2081, 2003.

[65] M. Tani and A. Funahashi, "Energy Absorption by the Plastic Deformation of Body Structural Members," *Soc. Automot. Eng. Tech. Pap.*, no. 780368, 1978.

[66] M. D. White and N. Jones, "Experimental quasi-static axial crushing of top-hat and double-hat thin-walled sections," *Int. J. Mech. Sci.*, vol. 41, no. 2, pp. 179–208, 1999.

[67] N. Jones, "Energy-absorbing effectiveness factor," *Int. J. Impact Eng.*, vol. 37, no. 6, pp. 754–765, 2010.

[68] S. S. Hsu and N. Jones, “Quasi-static and dynamic axial crushing of thin-walled circular stainless steel, mild steel and aluminium alloy tubes,” *Int. J. Crashworthiness*, vol. 9, no. 2, pp. 195–217, Mar. 2004.

[69] W. Abramowicz, “The effective crushing distance in axially compressed thin-walled metal columns,” *Int. J. Impact Eng.*, vol. 1, no. 3, pp. 309–317, 1983.

[70] N. Jones, *Structural Impact*. Cambridge University Press, 2011.

[71] V. Tarigopula, M. Langseth, O. S. Hopperstad, and A. H. Clausen, “Axial crushing of thin-walled high-strength steel sections,” *Int. J. Impact Eng.*, vol. 32, no. 5, pp. 847–882, May 2006.

[72] T. Ohkubo, K. Shirasawa, and Y. Akamatsu, “Mean Crushing Strength of Closed-Hat Section Members,” *Trans. Soc. Automot. Eng. Japan*, no. 740040, 1974.

[73] N. Jones, *Structural Impact*. .

[74] R. C. Hibbeler and S. C. Fan, *Statics and Mechanics of Materials Si*. Pearson Prentice Hall, 2004.

[75] ArcelorMittal, “ArcelorMittal Sollight brochure.” [Online]. Available: http://www.arcelormittal.com/fce/repository/Brochures/Sollight_usermanual_EN.pdf. [Accessed: 20-Jun-2012].

[76] K. C. Shin, J. J. Lee, K. H. Kim, M. C. Song, and J. S. Huh, “Axial crush and bending collapse of an aluminum/GFRP hybrid square tube and its energy absorption capability,” *Compos. Struct.*, vol. 57, no. 1–4, pp. 279–287, 2002.

2 Literature review

This chapter details the current knowledge relevant to the improvement of axial impact energy absorbers. There is a wide variety of materials which could possibly be used for the purpose of energy absorption. However, the choices are limited to metals, composites, sandwich panels and hybrids as being appropriate for the automotive crash energy absorber. Foams and honeycombs are considered but only as a reinforcement for an existing structure as their use alone in the automotive sector is not appropriate, due to the multi–purpose nature of the body–in–white.

The first section considers the crash testing and structural response of monolithic metals and the current state of the art in the field. Second, the use of composites is considered and their energy absorption potential is discussed as well as the deformation characteristics of composites in crash situations. The latest work on the use of sandwich materials in other fields is considered, although some of the work is not necessarily directly related to crash testing, the work is relevant to understanding the performance of sandwich materials in crash structures. Finally, the relatively limited research already undertaken using sandwich materials for energy absorption is examined, and the opportunity for research is identified.

Not considered in this review is the energy absorption mechanisms for ballistic impacts and the materials used for these applications since the loading and mechanisms of energy absorption are not applicable. Ballistic impacts are carried out at much higher strain rates (over 1000 s^{-1}) and in general point impacts with the aim being to prevent penetration. Hence, not applicable in the field of axial energy absorption.

There are a number of areas that are not considered in depth in the review due to being outside of the primary project goals. These include defining the bending stiffness of the material, the formability of the material (unless relevant to the production of crash structures) and detailed analysis of the bond between metal and polymer; therefore, these topics will not be considered within this literature survey.

2.1 Metallic energy absorbers

The most common method of front–end energy absorption in the automotive body–in–white (BIW) is the axially impacted crush tube, the structure that is considered in this thesis. The use of a metal tube, whether a top–hat and closure plate, seam welded tube or an extrusion as an energy absorber has seen much research since the 1970s [1], [2]. Detailed reviews of this work through to the current day are available [3], [4]. The mechanism of energy absorption in the tube has already been described in Chapter 1 – Introduction.

2.1.1 Material thickness

It has been previously shown by Reid [5] that for square steel tubes, a 10% increase in material thickness (hence mass) results in a 14% increase in energy absorption; an increase in material thickness will always lead to greater specific energy absorption (SEA). This is an important fact when comparing SEA values for different crash structures. The SEA for steels in automotive impacts is for example quoted to be around 8–12 $J.g^{-1}$ [6], whereas the rail locomotive crash structure designed to absorb significantly more energy is quoted as 50 $J.g^{-1}$ [7]. The claimed energy absorption ranges for rail and automotive structures are in different orders of magnitude [8]. Thus, context is required and will be provided in this literature survey by also comparing the mean crush force in addition to the SEA.

The increase in material thickness has been shown to increase the radius of the fold in the crash structure [9], Figure 2.1. Schneider & Jones [9] tested two top hat and closure plate crash structures in steel. The observed difference in fold radius is clear, with thicker steel on the left compared to the right.

Figure 2.1 – Top–hat crash structures made from thick (left) and thin (right) steels. The larger fold radius in the thicker material can be seen [9]. Scale bar is not provided by the author.

The disadvantage of the increased thickness and fold radius is the decrease in effective folding length due to the reduction in the number of possible folds. It is noteworthy to mention that an increase in the thickness of the metal is also accompanied with an increase in the peak impact force [10], [11], which is an important factor when designing crash structures.

2.1.2 Material strength and ductility

An increase in material strength is directly correlated to the energy absorbed [10]. Reid [5] has shown for square steel tubes that a 10% increase in material strength results in a 7% increase in energy absorption.

Hence, higher strength steels, which have higher ultimate tensile strength (UTS), will invariably attain a higher strength in the material (higher flow stress) compared to mild steels, and can therefore, be used to decrease the mass of the crash structure. This was demonstrated by ThyssenKrupp, when they replaced a high strength DP600 steel with an even higher strength TRIP780 (UTS increase from 600 to 780 MPa nominally). They were able to reduce component mass by 14% [12]. However, the disadvantage of this is a potential increase in peak impact force with increasing material strength [10], [11].

Although higher ultimate tensile strength (UTS) increases the energy absorbed, Jones [13] suggests that the flow stress of the metal rather than its UTS is more important. The flow stress being the stress attained in the material. In general, the failure strain is not reached by a crash tube in steel or aluminium alloys, therefore, the peak stress is not attained as the metal undergoes collapse. Hence, materials that undergo a rapid strain hardening (higher strain hardening exponent) can be more effective than materials of an equivalent strength but lower strain hardening exponent, since more of the "*strength capacity*" is utilised. Schneider & Jones [14] suggest an average strain of only 10% is reached through the entire crash tube in progressive folding, hence much of the strength of a monolithic metal is never utilised.

2.1.3 Strain rate

The difference in performance of crash structures statically and dynamically has been investigated for monolithic materials [15], [16]. Hsu *et al.* [11] and Bambach *et al.* [17] show the use of strain rate sensitivity of a material is an effective method of increasing the energy absorption The flow stress of a material can increase significantly (up to double for mild steels [11], [17]) at higher strain rates producing the same effect as using a higher strength material. This effect is commonly seen in steels, and to a lesser extent in aluminium alloys [11].

The static crush strength to the dynamic crush strength ratio is therefore of interest. It is well known for mild steels [11], however, relatively unknown for most aluminium alloys [18]. Little research has been performed for most fibre–reinforced composite materials, although both aluminium alloys and composites are commonly assumed to have little sensitivity [19].

In the context of this project, strain rate sensitivity has the ability to reduce the gauge of a steel used as skin material for a sandwich.

2.1.4 Increasing the number of corners – quantify single, double and circular

Increasing the number of corners in a crush tube has been shown analytically and experimentally to increase the crushing force required to deform a metal tube [20]–[22]. Figure 2.2 shows a four corner single hat and closure plate (left) *versus* an eight corner double hat (right). Double hats absorb more energy and have a higher specific energy absorption [13] for a given volume of material. However, the folding of the single hat is seen to be more regular than the double hat [14]. This ensures a stable and repeatable performance, hence limiting the adoption of the double hat, as repeatability is important in the safety critical structures of the vehicle.

Figure 2.2 – Increasing from 4 corners (left) with a single hat to 8 corners (right) with a double hat. Image adapted from [22]. Scale bar is not provided by the author.

Closed hat sections such as those shown in Figure 2.2 are conventional structures used as front longitudinal members, even though circular crush tubes have a higher SEA. A circular tube will absorb approximately 29% more energy than a top–hat crash structure [11], [13], [15]. However, joining circular tubes to the body–in–white is a difficult and expensive process. Various numerical simulations have been performed using multi–corner tubes [23]–[27] in axial impacts. Figure 2.3 shows the predicted deformation of various tubes of increasing numbers of corners [24]. The comparative crushing force or energy absorption of these structures is not described. Yamashita *et al.* [25], however, suggests increasing the

number of corners beyond eleven provides no advantage, and show in their work that the increase in corners is more effective for thinner metals.

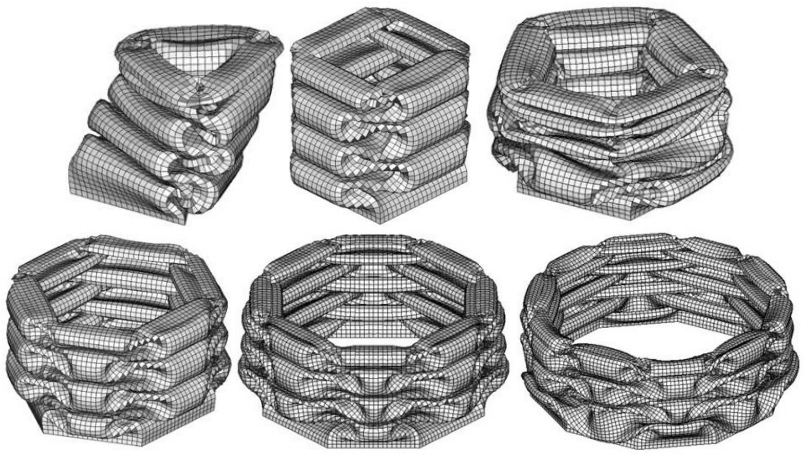

Figure 2.3 – Numerical analysis of impacts on tubes with increasing numbers of corners. Image modified from [24]. Scale bar is not provided by the author.

Tang *et al.* [23] modelled the effect increasing the number of corners in a crash structure had on the specific energy absorption. The mass of 6060–T4 aluminium alloy used was fixed Figure 2.4. The folding modes are the same as those in conventional crash tubes; however, the increased number of corners produced more toroidal folds than buckling straight sections which as a result increases the energy absorbed [3].

The relative energy absorption between the structures is 1:2.2:3.5, showing the effectiveness of increasing the number of corners. The structure Figure 2.4c produces an SEA of 20.2 $J.g^{-1}$ for a 23.9 kN mean crush force, this is an SEA value usually attained by square section structures designed for 50 kN impacts.

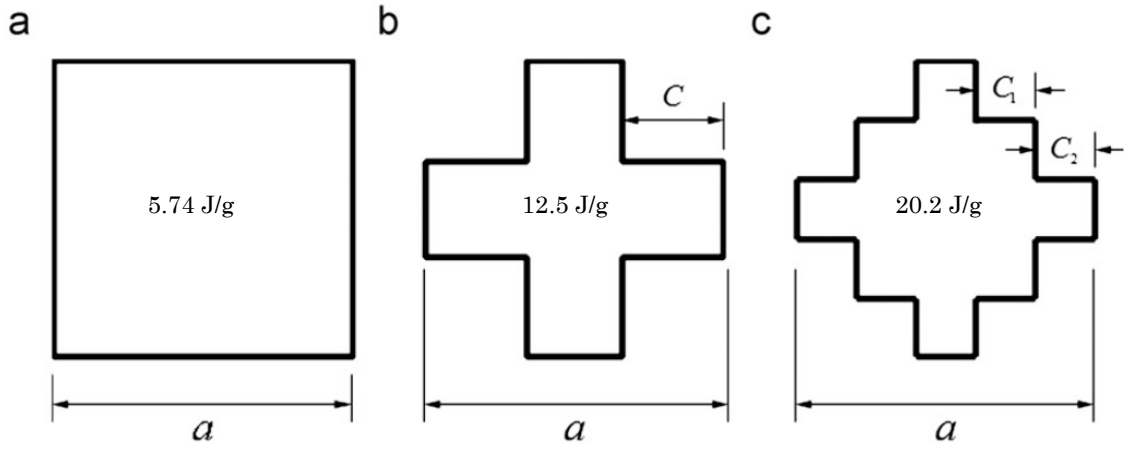

Figure 2.4 – Increasing the number of corners for a fixed amount of material to increase energy absorption. The specific energy absorption values are superimposed into the middle of the structures to show their effectiveness. Image modified from [23]. C = 30 mm, $C_1 = C_2 = 16$ mm.

A common theme in the studies of multi–corner tube methods of increasing energy absorption is the application of finite element modelling to show their efficacy, physical testing has not been performed. This is due to the difficulty in producing complex structures, and therefore suggests that even though these are effective methods of increasing performance they are not realistically producible, especially in high volume production. Additionally, as with circular crash tubes the practicality of attaching a multi–corner crash tube to the rest of the body–in–white is in question.

2.1.5 Use of cells

Zhang & co–workers and many others [24], [26], [28]–[31] have contributed significantly towards the improvement of metallic crash structures using cells within the crush tube. Multi–cell columns have been employed to increase the crushing force of circular tubes, Figure 2.5. The mean crush force for the un–stiffened tube (Figure 2.5 – image 1) is 8.33 kN, with a 77% increase for the stiffened three cell tube (Figure 2.5 – image 2) and a 112% increase in mean crush force for the stiffened four cell tube (Figure 2.5 – image 3) over the un–stiffened tube (Figure 2.5 – image 1). However, the SEA increase for (Figure 2.5 – image 3)

over (Figure 2.5 – image 1) is only 23% and the three cell tube (Figure 2.5 – image 2) has a very similar SEA to the four cell tube (Figure 2.5 – image 3). The use of cells in the crush tube has a two–fold effect, the use of more material as well as the interaction between the cells and the tube wall both increase the resistance of the structure to axial deformation hence increase the energy absorbed.

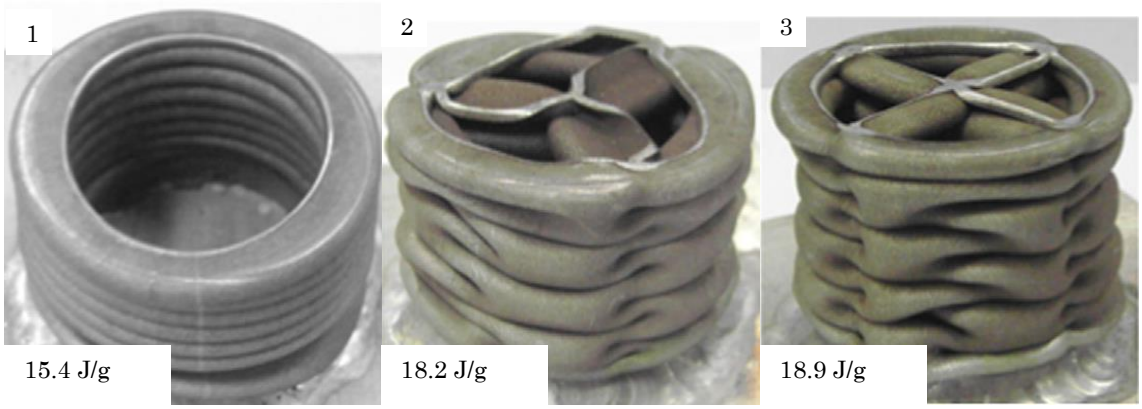

Figure 2.5 – Multi–cell columns to increase the crushing force of a simple circular tube [28]. (a) – un–stiffened tube, (b) – 3 cells and (c) – 4 cells. Scale bar is not provided by author.

Kim [32] has run an optimisation process on a square aluminium tube which resulted in a multi–cell profiled tube, shown in Figure 2.6. The design optimisation produced a complex geometry, essentially joining four small square tubes together. The square geometry achieved 10 $J.g^{-1}$ whereas the optimised geometry reached 18.8 $J.g^{-1}$ for the same mass of aluminium used, showing a 90% increase in SEA. The energy absorption increase is due to there being more corners in the structure for the fixed amount of material, the corners requiring a greater force to collapse than the straight sections. Kim [32] also analytically compared the specific energy absorption of the optimised square tube with the cell reinforced square tubes (such as seen in Figure 2.5), claiming an improvement over these structures as well [28].

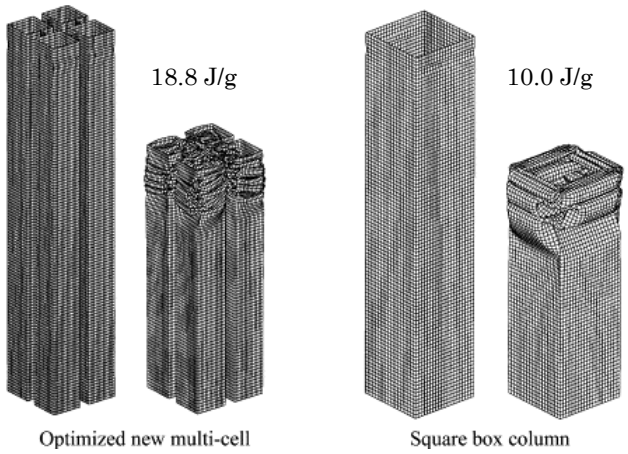

Figure 2.6 – Multi–cell rectangular tube (left) increases energy absorption 1.9 times over square tube (right), image taken from [32]. Nominal width of columns are 60 mm.

Cells are currently used in the automotive body–in–white crash structure however, only one dividing wall is common practice. The use of multiple walled cells would be difficult to produce economically, and extrusion would be the obvious method of manufacture. These methods would be effective at increasing energy absorption when there is space limitation in the automotive structure, but restrictions in the manufacturing routes, production costs, cycle times, as well as the limited choice of aluminium grades suited to extrusion make this undesirable.

2.1.6 Cavity fillings

The use of metal foams, polymer foams, solid polymers, honeycombs and even cork to fill the cavity of the metal crash structure in order to increase the energy absorbed by the structure has been researched extensively [18], [33]–[39]. Most commonly, the foam or honeycomb material used is an aluminium alloy. A large body of work by Langseth, Hopperstad and co–workers study the effect of aluminium foam–filled aluminium tubes [18], [39]–[45]. The work involves static and dynamic testing of aluminium extrusions with foams of differing strengths and densities, differing aluminium extrusion grades and thicknesses, and the effect of adhesively bonding the foam to the cavity. The folding mode was found to be the same asymmetric folding in the foam–filled sections as in the empty crash

structures, Figure 2.7. However, the folding wavelength is seen to decrease in the foam–filled sections and more folds are therefore produced [34].

Costas *et al.* [36] filled the void of a steel crash box with a polyethylene terephthalate (PET) foam core (the core was not bonded to the crash box). Quasi–static crush testing showed a 20% improvement in SEA when filling the core with a PET foam. Santosa *et al.* [46] showed a near 50% SEA increase when bonding the aluminium core into the void over merely placing it within the void. This is due to the un–bonded core having no shear resistance, therefore not increasing the shear strength of the material combination. The un–bonded core only conforms to the crushing of the crash box, whereas the bonded core increases the stiffness of the crash box as well as crushing. Additionally, the SEA increase was greater using an aluminium honeycomb rather than an aluminium foam. Santosa *et al.* [46] also predicted that the use of a foam or honeycomb is more effective than simply increasing the crush tube wall thickness.

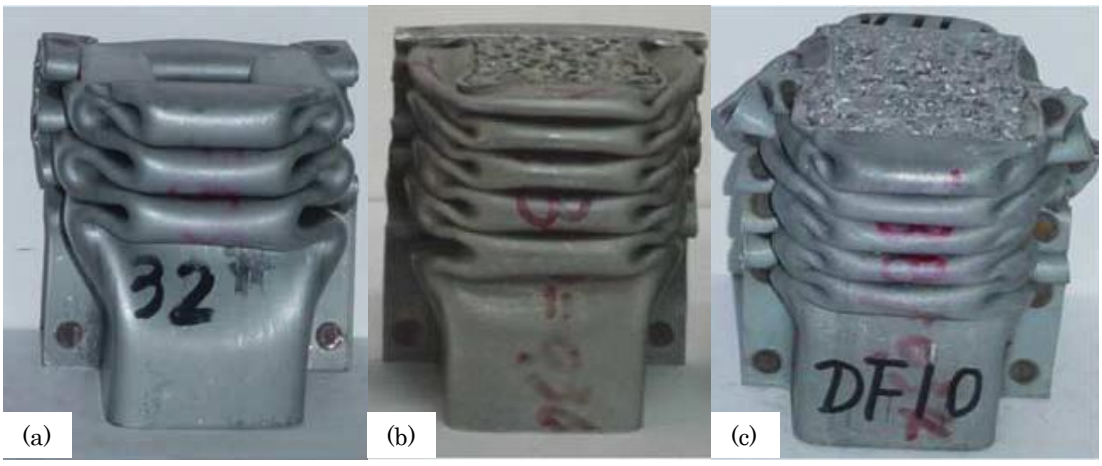

Figure 2.7 – (a) shows an un–filled single top hat, (b) shows a filled single top hat, (c) shows an filled double hat [34]. Scale bar not provided by the author.

The research into cavity filling of crash structures shows the use of a metal foam is an effective method of increasing the energy absorption, the use of polymer foam fillers may also be appropriate. However, the inclusion of a filler would invariably lead to a thinner metal crash structure with the remainder of the energy

absorption provided by the polymer. This may have adverse effects on the stability and stiffness of the crash structure in other loading conditions it must be designed to encounter, such as bending and fatigue. Further, the manufacturability of the foam–filled structure concerning not only physical volumes but also factors such as repeatability and predictability of performance may also be an issue. However, foam filling has been shown to be an effective method of increasing the specific energy absorption.

2.2 Composite materials

Composite materials are candidates for energy absorption in the mainstream automotive sector as a result of their proven history in motorsport, exhibiting high SEA due to high strength and brittle failure modes [47]. Meredith *et al.* [48] tested carbon fibre reinforced polymer (CFRP) cones, a representative of a single–seat race car crash structure, Figure 2.8, achieving 34 $J.g^{-1}$ for a 4 kJ impact.

The energy absorption mechanism of fibre reinforced composites is different to metals and can be considered a progressive failure as opposed to a progressive crush [47].

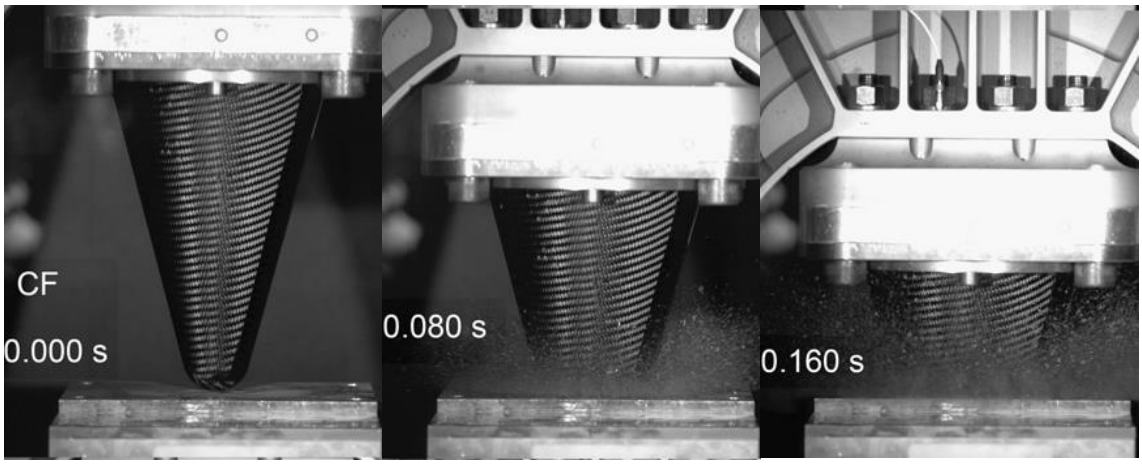

Figure 2.8 – 4 kJ impact on CFRP cone, showing the pulverising deformation to absorb energy, image modified from [48]. Scale bar is not provided by the author.

The energy absorption mechanisms seen in FRP composites are: fibre splitting and cracking, de–bonding of the fibres from the matrix, and brittle failure of the fibres and the matrix [49], [50]. Figure 2.8 shows the typical failure of epoxy resin composite materials aptly.

Mamalis & co–workers [49] quasi–statically compressed CFRP square tubes to show their effectiveness in energy absorption scenarios. The mean crush force was significantly higher (150 kN) than that designed for automotive crash structures

(around 50–60 kN) and consequently the SEA is high at 38.1 $J.g^{-1}$. The deformation of the CFRP statically is shown in Figure 2.9. In comparison to dynamic testing there is less brittle fracture observed (comparing Figure 2.8 to Figure 2.9). The SEA achieved by Mamalis [49] is lower than that reported by Meredith [49], who also carried out tests at a lower crush force range. The relatively poor performance of Mamalis' crush tubes could be due to many factors: the strength and orientation of the fibres and the composite system being the most pertinent.

The composite system has many variables: such as pre–impregnated or resin infused material. Whether the fibres are a woven material or uni–directional plies, and the matrix material, which could be a plethora of either thermoset or thermoplastic materials.

The geometry of the crash structure is also important whether using square tubes or conical frustra (cones). The difference in specific energy absorption may be due to fibre orientation, Mahdi *et al.* [51] showed that ±45° fibres produced the highest mean crush force over the entire length of the circular tube of GFRP.

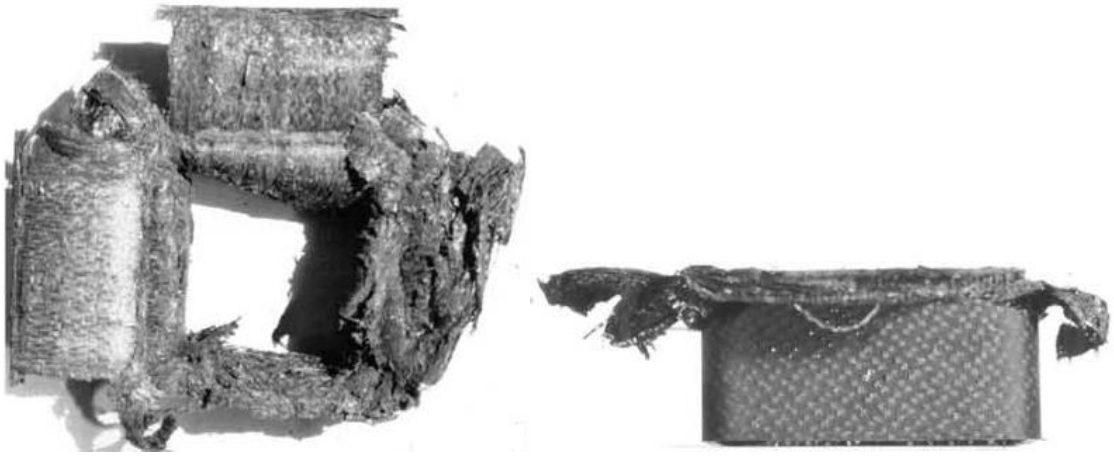

Figure 2.9 – CFRP composite crash structure showing progressive failure to absorb energy. Image from [49]. Crash structures are 100 × 100 mm square tubes.

Glass fibre reinforced composites (GFRP) are also a candidate for automotive front–end crash structures due to their lower cost than CFRP; however, in general

they are lower strength materials, hence resulting in a lower SEA. Mamalis *et al.* [52] produced GFRP front longitudinal members achieving a range of specific energy absorptions from 40–70 $J.g^{-1}$ for approximately 140 kN impacts. Mamalis *et al.* [7] also worked with the Advanced Railway Research Centre, Sheffield to review the applicability of composite materials. The field of railway locomotives is an area where considerable mass reduction is possible, due to the current use of heavy gauge steels. The review article showed uni–directional carbon fibre reinforced polyether ether ketone (PEEK) matrix could nearly quadruple the performance of steel at values approaching 200 $J.g^{-1}$. The SEA values are skewed as the required energy absorption range impact for rolling stock is in the mega–Joule range as opposed to the kilo–Joule range required for automotive crash structures [8]. The mean crush force of a rail crash energy absorber is in the order of 700 kN. However, the review article shows the potential of fibre reinforced composite crash structures for axial impact energy absorbers.

For the mainstream automotive range of impact energies, the Low Carbon Vehicle Technology Project (LCVTP) explored the use of thermoplastic composites for mass production of structural components [53]. The LCVTP performed impact tests on glass fibre reinforced polyamide composite crash structures. The results showed the GFRP structures (27 $J.g^{-1}$) performed better than AA5754 aluminium alloy (16 $J.g^{-1}$) and DP600 steel (12.5 $J.g^{-1}$), where all structures had the same geometry [6], [54]. The impacted composite structure with its progressive failure as opposed to progressive crushing is shown in Figure 2.10 – b, a comparison to the progressive crushing of the AA5754 structure (Figure 2.10 – a) can be seen.

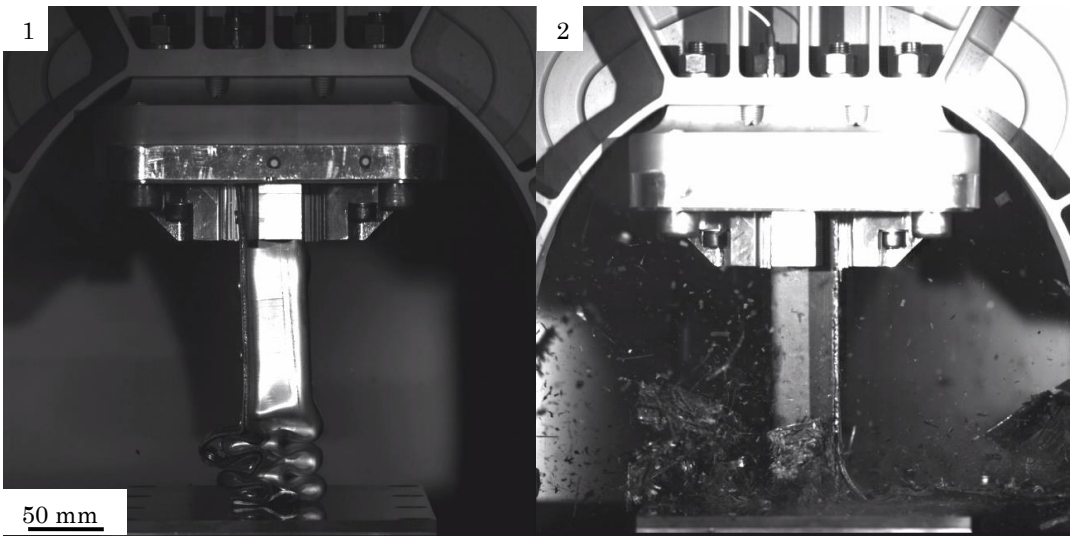

Figure 2.10 – Materials crash tested in the LCVTP project. Image 1 – AA5754 aluminium alloy, image 2 – all polyamide–glass fibre reinforced composite. Adapted from [53].

Brittle collapse type failure seen in Figure 2.8, Figure 2.9 and Figure 2.10 is not preferred in the mainstream automotive sector. There is a possibility of separation of the composite material from the rest of the body structure, which could alter the load path to the rest of the body–in–white. Additionally, simulation of fibre reinforced composite materials is in its infancy. Therefore, there is little confidence in the deployment of composite materials in the crash critical areas of the automotive BIW.

Nevertheless, the issue of these progressive failure mechanisms is currently being addressed. Composites research has moved into the modification of the matrix materials to increase ductile behaviour and is considering the hybridisation of the reinforcement fibres. Hybridisation involves adding flexible fibres into the composite to reduce the brittleness of carbon or glass epoxy composites [55].

Further limitations in the adoption of composites in the automotive BIW are the cycle times for production of parts. LCVTP showed that for 50,000 parts per annum, the use of GFRP composite maybe possible, but for more than 50,000 parts, aluminium and particularly steel are considerably cheaper. Further increases to

the cost of composites in the BIW are the use of high pressure and high temperature processes such as resin transfer moulding and autoclaving [56].

Another difficulty is the joining of composites in the high volumes common in the automotive sector. Composite joining methods are currently in their infancy; however, there are joining technologies available for the attachment of composite materials together and to metals. Methods such as laser welding for joining thermoplastics together [57] and more importantly thermoplastics to metals [58] are currently being researched as well as other methods such as ultrasonic welding [59]. However, the most promising research is in the use of adhesive bonds, mechanical fastening and combination joints where mechanical fasteners (such as rivets and screws) are used in conjunction with adhesives [60]. Composites are a diverse and vastly researched material sector for crash structure applications, hence manufacturing methods and applicability will move forward. Nevertheless, in order to be successful they must become cost competitive.

2.3 Hybrid materials

Hybrid materials, general combine metals, composites and/or foams with the intention of further improving performance of energy absorbers will be discussed in this section.

In a similar method to metallic crash structure improvement (earlier discussed in Section 2.1.6), foams have been used to fill the vacant space in composite tubes [61], [62]. In general, there was little improvement in performance (25.5 to 28.8 $J.g^{-1}$), and in some instances a reduction in performance due to global failure of the composite instead of progressive crushing. Therefore, these hybrid materials are not considered suitable and not discussed further.

2.3.1 Composite wrapping of metallic structures

The hybrid materials discussed in this section are metal tubes adhesively bonded with fibre reinforced plastics on the exterior surface. Initially, this field of hybrid materials was aimed at reinforcement of metallic structures for civil engineering applications. The primary purpose being to prevent elephants foot failure commonly seen in pressure vessels after earthquakes [63], [64], see Figure 2.11.

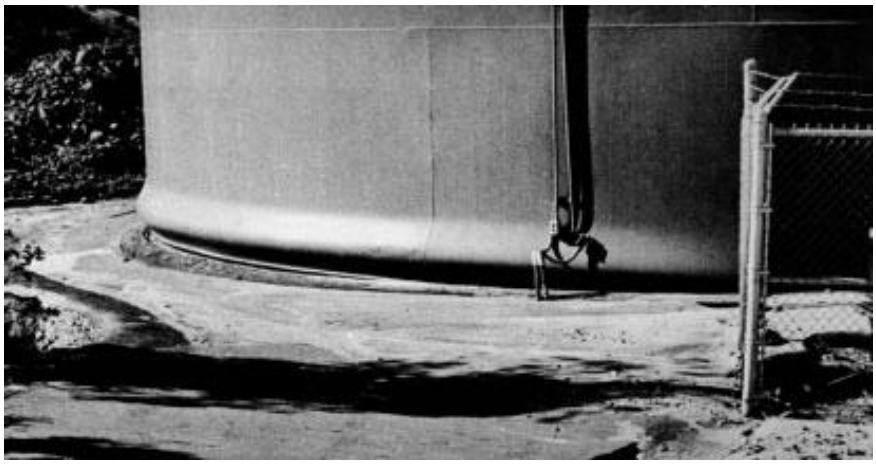

Figure 2.11 – Elephants foot buckling seen in elastically buckled civil structures [64]. Scale bar is not provided by the author.

Bambach, Elchalakani, Teng and others [64]–[73] have extensively researched the composite wrapped metal tubes for reinforcement and are able to double the peak buckling load to reduce the risk of pressure vessel failure [72], [73]. An increase in the peak buckling load would result in an increased crushing load in progressive crushing scenarios. Therefore, the research has naturally progressed into impact testing.

Shin *et al.* [74] examine axial impacts in 6xxx series aluminium alloy square tubes wrapped with GFRP composite. The hybrid tubes were quasi–statically crushed (5 mm/min for 90 mm displacement). The effect of the GFRP layup orientation on the crushing mode was considered. Figure 2.12 concisely shows the deformation modes. Figure 2.12 – images 1, 2 & 3 shows 0° fibres, 90° fibres, 0°/90° cross plies respectively and Figure 2.12 – image 4 shows the –45°/+45° cross plies, where the 0° fibre direction is in the loading direction.

Figure 2.12 shows that the aluminium tube deforms under progressive crushing in all cases [3]; in other words its deformation mode is unaffected by the composite wrapping. The composite material in Figure 2.12 – images 1, 3 & 4 deformed in modes commonly observed in the crushing of FRPs, namely cracking, frond bending and axial splitting [49], [74]. The exception is the composite plies wrapped at 90°, shown in Figure 2.12 – image 2, which became constrained in the folds of the aluminium as it progressively crushed. The increase in crushing force is most likely due to the resistance to deformation of each fold by the fibres and increase in overall material thickness. Any further analysis such as the mean crushing force or specific energy absorption was not provided. However, published work [74] does confirm that the hybrid composite is more effective than either the aluminium or GFRP alone.

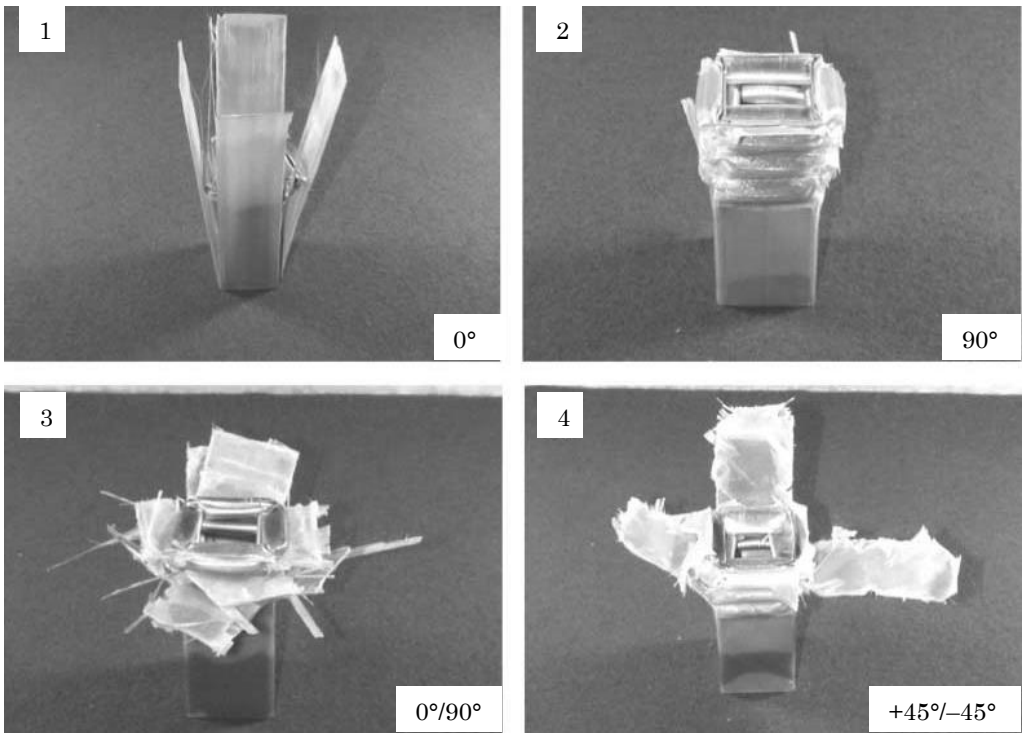

Figure 2.12 – Different deformation modes seen with differing ply orientation, modified from [74]. Tubes are 30 × 30 mm square section.

Kim *et al.* [68] and Bambach *et al.* [75] considered the effect of increase ply thickness of the CFRP composite wrap. Kim *et al.* [68] showed that the use of two composite plies increased the SEA by 30% and the addition of anothertwo plies only further increased the SEA by 8%. Bambach *et al.* [75] showed that the energy absorption of a combination of CFRP and aluminium tubes was better than the structures individually.

Bambach *et al.* [67], [76] reinforced steel tubes with a CFRP woven material as opposed to uni–directional layers. The work highlights the effect of geometry of the metal tube and wrapping thickness and showed that the woven composite in 0°/90° layers deformed around the steel tube much like the 90° uni–directional layers presented by Shin *et al.* [74] (see Figure 2.13). Bambach [67] also added multiple layers of woven CFRP showing a 23% SEA increase for two layers and a further 24% increase for a further two layers of composite.

Figure 2.13 – Steel tube (left) and composite reinforced steel tube (right) shown side by side [67]. Scale bar is not provided by the author.

Similar work was conducted by Song *et al.* [77] on circular tubes as opposed to square tubes, using aluminium alloys of different thicknesses, as well as steel and copper tubes. Again, the 90° fibre direction was found to be the most suitable. The work looked at both dynamic impact events and comparative quasi–static crush tests. No deformation difference was seen between the two impact types; however, the dynamic impacts had a higher energy absorption. The steel wrapped with composite had a doubling of the absorbed energy between static and dynamic which cannot be accounted for in the strain rate sensitivity of the steel alone [11]. Even a doubling of the strength of the material due to strain rate sensitivity would only produce a 50% increase in specific energy absorption. Therefore, either the matrix must be a strain rate sensitive polymer or indeed fibre breakage at high speed requires greater force.

Bambach [17] also showed the importance of steel crash structure geometry on the effectiveness of the composite wrap. For 70.7 mm square steel structures, the CFRP wrapping gave no improvement in SEA whereas the larger 99.1 mm square steel improved the SEA by up to 59%.

There is not a strong case for the wrapping of automotive crash structures with composite materials, though, some large performance increases were shown. The

gain in performance is however, geometry dependent. The folding modes are heavily dependent on fibre orientation and fibre/matrix combination. Additionally, the production of these structures would be labour intensive and most probably impractical in the mass manufacturing environment of the automobile BIW. The ability to meet production volumes for automobiles economically is doubtful for such methods, both in cost and cycle times.

2.4 MPM Sandwich research

This section considers the existing research applicable to metal–polymer–metal (MPM) sandwich materials not necessarily crash related. However, the performance of sandwich materials in crash may be inferred, such as material stiffness or local bending behaviour.

2.4.1 Formability

MPM sandwich (see definitions in Chapter 1) panel forming is of particular interest due to the intended use as automotive skin panels [78]–[80].

Link (US Steel), Burchitz (Hoogovens R,D&T, now Tata Steel) and Dunand (Arcelor Auto now Arcelor–Mittal) [80]–[82] have all performed research on the dent resistance of steel–polypropylene–steel (SPS) and aluminium–polypropylene–aluminium (APA) sandwich panels. Dent resistance defines how much energy is required to dent an exterior automotive panel such as a door panel, to maintain the aesthetics of the vehicle outer. The general result being the sandwich panel with around 60% of the weight (and equal stiffness) will perform as well as the monolithic panel it replaces [80]–[82]. Additionally, increasing the core thickness increased the static dent resistance for little weight penalty in all cases. This shows the potential of MPM sandwich panels in elastic bending energy absorption, that under impact they do not collapse or fold in a manner significantly different to monolithic panels. Asnafi *et al.* [83] explored the use of Metal–Composite–Metal sandwich panels for dent resistance. The panels tested had a glass fibre reinforced polypropylene core and 0.2 mm stainless steel skins. The advantage of their use is not clearly established; results showed the 1.0 mm thick MCM panels had a greater dent resistance than a 1 mm aluminium alloy panel. Nonetheless, the MCM panels were 46% heavier than the aluminium alloy panels. The use of stiff

materials for the core offers no benefit since they do little to increase the bending stiffness of the material.

Jackson *et al.* [84] performed incremental forming tests on various commercially available sandwich panels; both solid polymer core panels with steel and aluminium alloy skins, an all–steel fibre cored and an all–aluminium foam cored sandwich. They showed the solid polymer cored materials form successfully whereas, the foam and fibre cored materials do not (Figure 2.14).

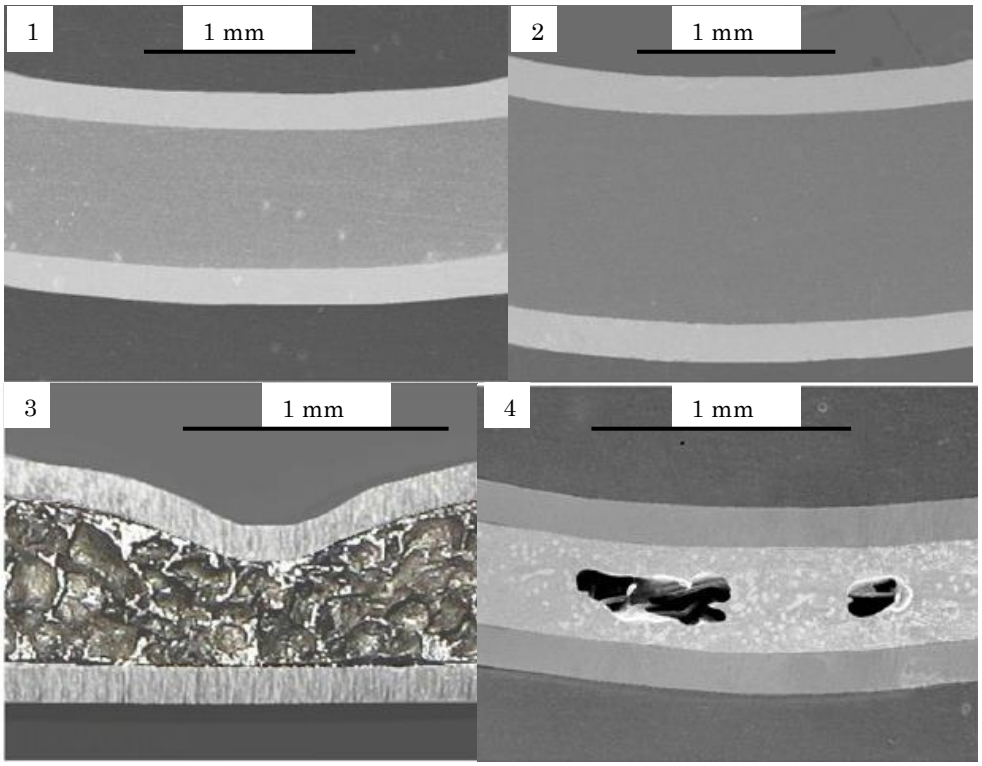

Figure 2.14 – Image 1 – SPS, image 2 – APA, image 3 – Al–Al foam–Al, image 4 – Steel–steel fibre–steel sandwich panels undergoing incremental forming, adapted from [84].

The poor formability seen in the non–solid cored sandwich panels was due to extensive core crushing in the soft cores which are not able to transfer the force imparted on the top surface to the bottom surface. Crushing of the core leads to a significant reduction in their bending strength and hence a reduction in the plastic bending moment. This will reduce their effectiveness in Euler buckling of crash structures. Additionally, forming of crash structures would reduce the material

thickness in particular in the corners, which further reduces the ability of the formed crash structure to outperform monolithic materials.

Carrado *et al.* [85] manufactured steel–polypropylene–steel and steel–glass reinforced polypropylene–steel sandwiches, performing cup draw tests for the purpose of deep drawing evaluation. They showed the MPM materials with fibre reinforcement all delaminated completely, and none of the MPM panels performed better than the same volume of monolithic steel alone. Carrado *et al.* showed the adhesive bond between the layers of the sandwich material is critical to its performance.

Gresham [86] performed hemispherical punch tests on aluminium skinned sandwich panels with either a glass fibre reinforced core or a self–reinforced polypropylene (PP) core. They showed the self–reinforced PP sandwich performed better than the glass–reinforced sandwich, drawing much further, however, reasons for such were not discussed. This could be due to the stiffness increase of the glass fibre core, which is less ductile and less compliant than the polypropylene core. Therefore, an over–stiff core may not be as effective as a lower strength polymer core due to high strength and lack of ductility, as well as requirement for a higher bond strength with a higher core strength as shown by Mohr [87].

Strain rate testing on APA sandwich panels by Kim *et al.* [88] shows the sandwich had a higher positive strain rate dependency than the aluminium alloy alone. The strain rate effect on the APA panel could be due to the polypropylene in the sandwich, a material shown to have a significant strain rate dependency [89]. Since the aluminium alloy is of relatively low strength, the effect of the polypropylene core may be seen, even though the metal skin is the main component. Positive strain rate sensitivity is advantageous, increasing the strength of the material under high strain deformation hence, increasing crash energy absorption.

However, with steel skins the effect of the polymer may not be significant, due to the positive strain rate dependency and high strength commonly associated with steels.

The formability work shows the potential of MPM sandwich panels. The dent resistance performance suggests the local stiffness behaviour of MPM sandwich materials mimics that of monolithic metals, with little core crush. The use of a low density core also seems more advantageous than attempting to increase the sandwich strength by using fibre reinforced plastics (FRPs) for the core. The complete delamination of these materials shows the bond strength is proportional to the core strength. Additionally, the polymer ductility does not alter the forming modes of the sandwich if perfectly bonded, whereas, the brittle nature of FRPs alters the performance of the sandwich panel significantly.

2.4.2 Buckling and plastic bending moment

Plastic bending moment is an important material property when considering a materials resistance to bending. Buckling behaviour defines how a material will behave when axially impacted. Therefore, these characteristics are important in crash.

Plastic bending moment testing and analytical modelling on the bending of sandwich materials was performed by Mohr & Wierzbicki and co–authors [90], [91]. Figure 2.15 shows a sandwich material undergoing an Euler buckle due to end–on compression. Figure 2.15 (left) shows a rigid cored sandwich response and Figure 2.15 (right) shows a soft core sandwich, where the core undergoes significant shear. The former is shown to be preferred due to the increase in force, P required to fully bend the material.

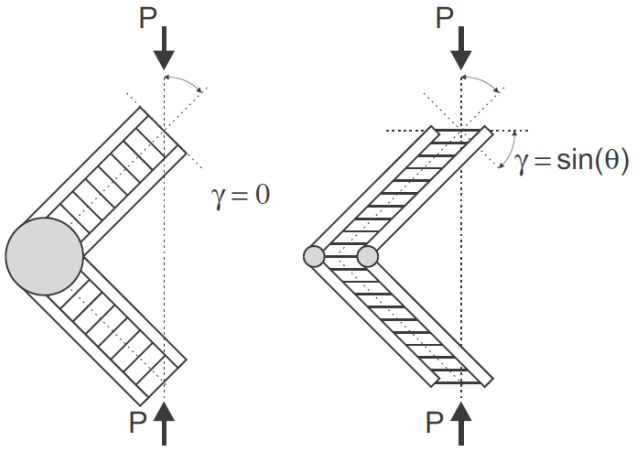

Figure 2.15 – Plastic bending of a sandwich material with a rigid core (left) and a soft core which shears in bending (right) [90].

The analytical modelling of a perforated core sandwich [90] showed that for a given thickness, a solid steel core contributed 66% of the energy absorption of the entire structure. Whilst with a core of 25% solidity, only 37% of the energy is absorbed by the core. Additionally, for the lower solidity core there is a reduction in the energy absorbed by the skin. Therefore, Mohr & Wierzbicki [90], [91] showed the positive effect a stiff core had on both the overall energy absorbed but also the stress transfer to the skin and hence the energy absorbed by the skin. This modelling was performed using a metal core, a core which even when perforated is much stiffer than a polymer core. What therefore remains unanswered is how effective will a polymer core be, such as in an MPM sandwich material when end–on compressed. Inherently the core itself will absorb little energy; this is anticipated due to its low strength, stiffness and placement along the neutral axis in bending. However, the cores' role is to transfer forces from one skin to another in order to allow the stiff skins to deform. If the core cannot fulfil this role the entire sandwich becomes ineffective at energy absorption.

End–on compression testing has been researched on metal skinned sandwich panels [35] as well as GFRP skinned sandwich panels [92], both using a PVC foam core. Fleck & Sridhar [92] changed the core density to show the effect of core

stiffening on the buckling behaviour. Core shear, Figure 2.16 – b, was seen in the lower density foams, whereas Euler buckling, Figure 2.16 – a, was seen in the highest density foam. Micro–buckling, Figure 2.16 – c, was also seen in the skin of the highest density core. Face sheet wrinkling, Figure 2.16 – d, was reported by Zenkert & Olson [35] in steel skins of the sandwich but not in the Fleck & Sridhar's [92] GFRP skins. This is most likely due to the lack of plasticity in GFRP. Zenkert & Olson [35] also reported Euler buckling of the sandwich panel before the onset of face sheet wrinkling.

Therefore, a rigid core material allows the global or Euler type buckling to occur in the sheet material rather than failure of the skin or core. This in turn means the plastic bending moment principle can be applied to MPM sandwich panels. Whereas a low density foam core is most likely too soft to ensure Euler buckling.

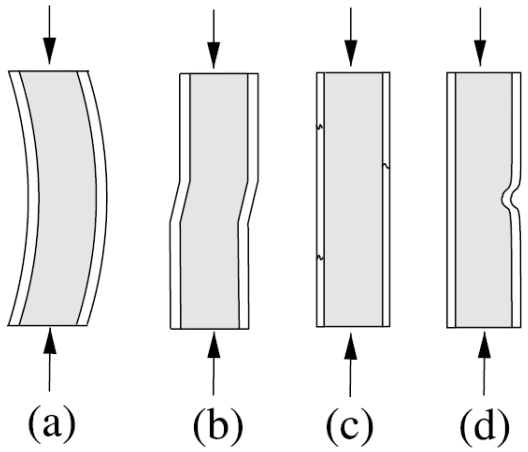

Figure 2.16 – Failure modes exhibited in the GFRP sandwich panel, (a) – Euler macro–buckling; (b) – core shear macro–buckling; (c) – face sheet micro–buckling and (d) – face sheet wrinkling [92].

The studies of Euler buckling and plastic bending moment of sandwich materials shed light on the end on compression of sandwich materials and suggests that with a high density foam or solid core they may be suitable for crash tubes and could yield a higher SEA than monolithic materials.

The stiffer and less compressible the core is, the greater the plastic bending moment of the material undergoing buckling hence leading to a significant increase in specific energy absorption.

2.5 Energy absorption using sandwich materials

This section details the available literature on the use of metal–skinned sandwich materials in axial impact scenarios.

Zenkert & Olsson [35] considered the axial performance of closed–cell PVC foam cored sandwich panels with high strength steel skins. The crushing performance of a sandwich column in both quasi–static and impact testing was explored. Results are reported for both an unfilled and filled column (where the vacant section of the column is filled with a PVC foam). The deformation modes are the same as those of monolithic metals, showing the asymmetric crushing modes [35], Figure 2.17.

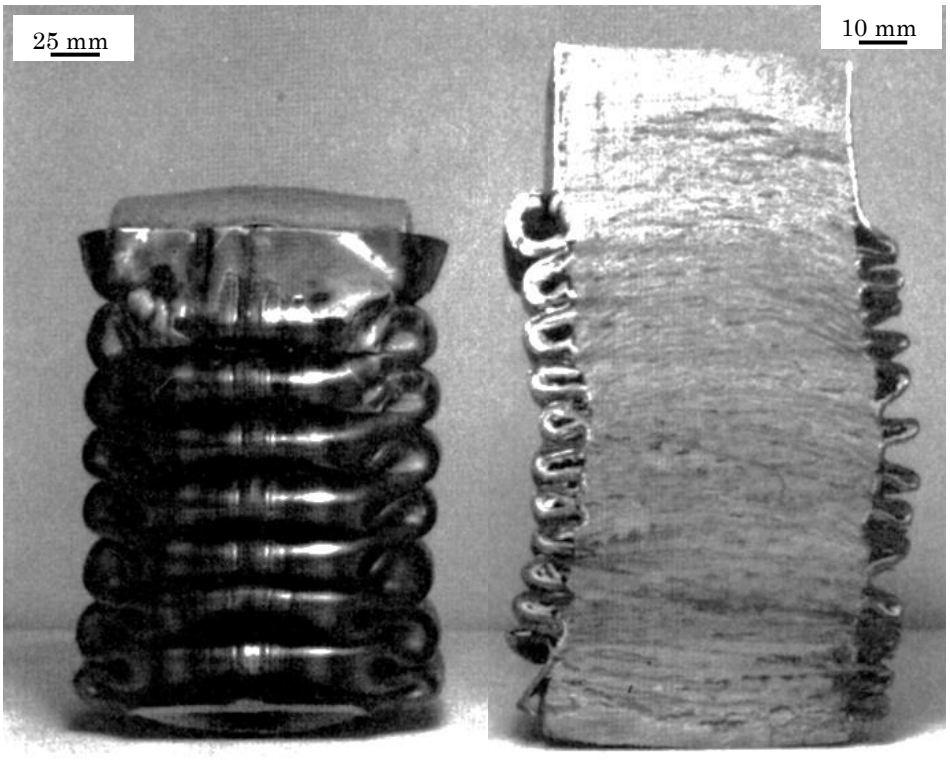

Figure 2.17 – Crush tube made from steel/PVC foam/steel sandwich, filled with PVC foam. Deformed tube (left), cut section (right), image taken from [35].

The deformation of the unfilled column is not shown in the published literature however, is reported to be similar, although with longer fold wavelengths. The deformation seen is consistent with foam filled steel and aluminium crash tubes [34], showing the foam filling of the vacant space in the crush box reduces the

folding lengths, producing a large number of small wavelength folds. The method of fabrication of the column from the foam cored sandwich is unclear. The SEA for the unfilled columns is up to 9.3 $J.g^{-1}$, a value easily achievable in steel [6], [93] when considering the crushing forces they are testing at are around 100 kN. In comparison, the foam filled structures reach up to 17.8 $J.g^{-1}$ a value more in the realms of what would be defined to show light–weighting potential. However, aluminium alloys are commonly seen to perform around the 20 $J.g^{-1}$ mark for a much lower mean crush force [6], [93]. Therefore, Zenkert & Olsson [35] showed the advantage of the use of a cavity filling, which is shown previously for metallic crash structures [18], [33]–[39]. However, the research did not exploit the sandwich concept to increase the performance of the axial crush tube. This could be due to the use of a PVC foam core which does not transmit shear as effectively as a solid core [87], [91], as discussed previously.

Mohr & Wierzbicki [90], [94] produced light–weight crash structures using a commercially available all stainless steel sandwich panel (trade name Lamera Hybrix) [95] [96]. The crash structures were double hats joined using blind rivets with an internal wall to produce two cells, shown in Figure 2.18.

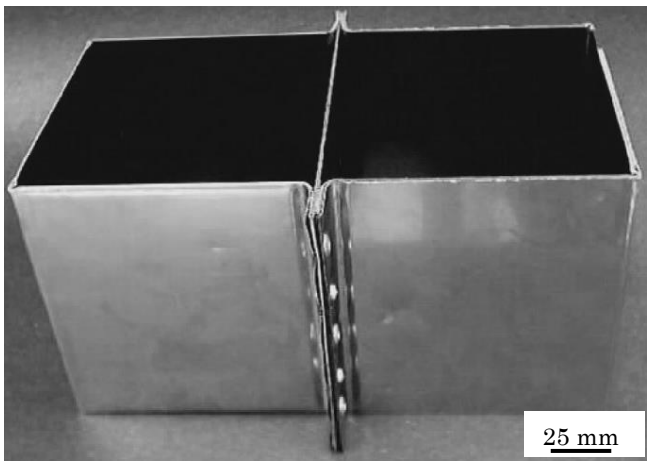

Figure 2.18 – Crash structure produced using an all stainless steel sandwich material [90].

This gives the sandwich material an equivalent density of around 3700 kgm^{-3}, approximately half that of steel. Figure 2.19 shows microscopy of the magnetically aligned stainless steel fibres on the left and a schematic diagram of the sandwich on the right.

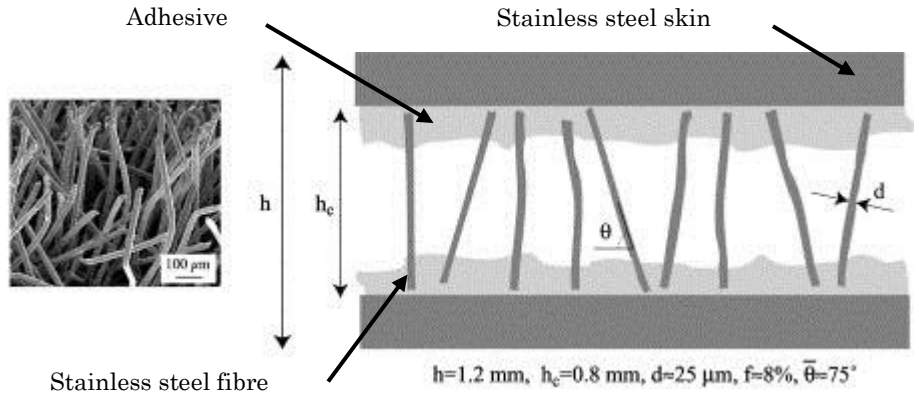

Figure 2.19 – Stainless steel sandwich with stainless steel fibre core, image shows fibre orientation. Image taken from [96].

Crush testing showed the material deformation of the steel panel is similar to a monolithic metal, Figure 2.20 – image 1. The folds were seen to have a small wavelength (value not given by author) and there is considerable core crushing, Figure 2.20 – image 2. Core crushing reduces the effectiveness of the sandwich panel in bending hence reducing the plastic bending moment of the material. The force–displacement results showed a similar crushing response in the sandwich as a monolithic steel of the total skin thickness, i.e. 0.4 mm thick. However, Lamera hybrix achieved an SEA of 4 $J.g^{-1}$ compared to the 0.4 mm thick monolithic steel's 2.2 $J.g^{-1}$, showing the potential of the sandwich material. Doubling of the SEA may not occur when a more appropriate crash structure geometry is used (a smaller effective width). Since in the larger geometry tested, the thickness of the crash structure is critical in ensuring asymmetric folds as opposed to unstable collapse occurs. Mohr and Wierzbicki [90], [94] showed the potential of the Lamera Hybrix sandwich material even with a collapsible core. As well as showing the difference

in the deformation to monolithic metals, the sandwich material exhibiting corners folds which transition between short and long, Figure 2.20 – image 3. Whereas, in monolithic metals, this would not occur, compare Figure 2.20 – image 3 to Figure 2.1.

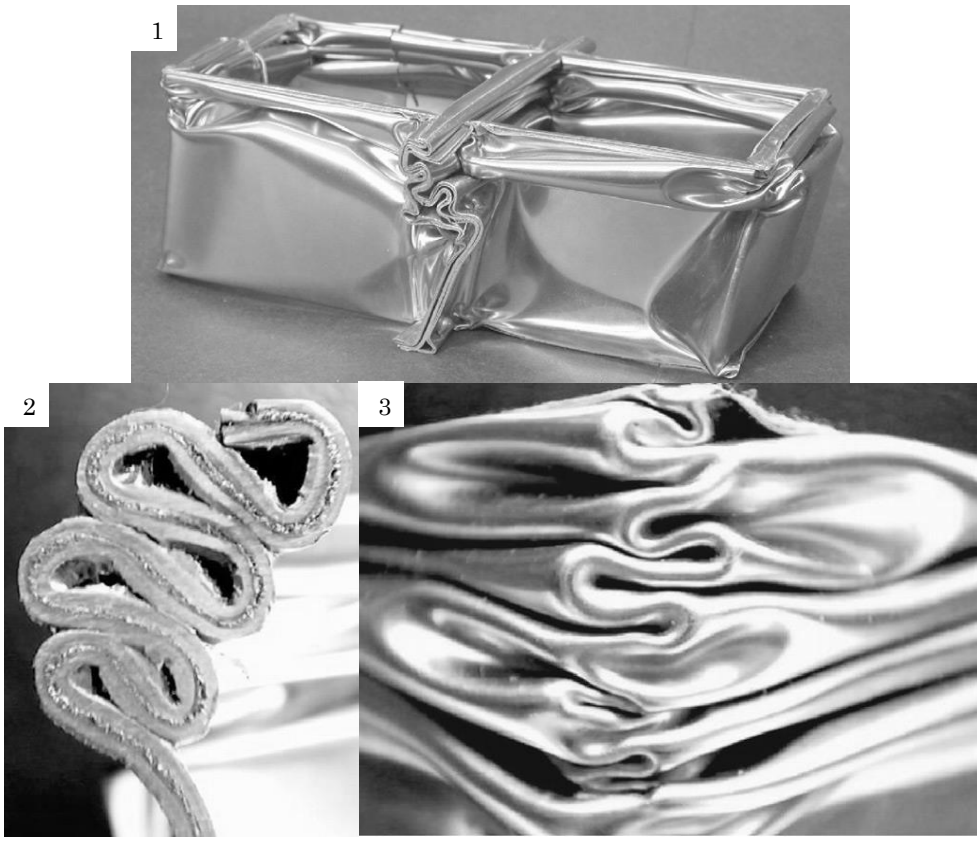

Figure 2.20 – Image 1 – deformation of the double hat structure, image 2 – buckling of the sandwich material and image 3 – folding in the corners. Adapted from [90]. Author did not provide scale bars.

Mohr & Wierzbicki [91], when modelling an all–steel perforated core sandwich, showed the effect of core solidity on the energy absorption of the crash structure, changing perforations in the core 0% to 75%. All perforated core structures absorbed significantly less energy than the solid material, but the SEA for all structures remained essentially the same (range of 13 to 13.7 $J.g^{-1}$). In order to maintain the same mean crush force, the modelling showed a thicker core was required; this also led to a 50% increase in SEA. However, it was postulated that the increased core thickness would lead to a greater chance of the skin steel failing.

Dunand & Gacel [81] suggested uses for an aluminium–killed drawing quality (AKDQ) steel sandwich panel produced by Arcelor–Mittal (trade name USILIGHT). Single hat crash structures were produced and drop tested. Little data is provided, although the authors suggest an SEA increase of 50% over monolithic steel of 1.5 mm thick with a 2 mm sandwich (0.25/1.5/0.25 mm layup). The deformation is shown in Figure 2.21. No further explanation is given, but visually the crash structures can be seen to deform in a similar manner to monolithic steels, Figure 2.1 as is also seen in Zenkert & Olsson [35] and Mohr & Wierzbicki's work [90] discussed previously.

Figure 2.21 – USILIGHT sandwich material crash structures, image modified from [81]. Crushed distance is 150 mm.

2.6 Conclusions of Literature review

This chapter has shown that MPM sandwich materials have been researched for axial impact absorbers and the idea is shown to have potential. The technology to produce MPM sandwich materials is already available and widely used in fields such as architecture for building facades and graphic design for stiff mounting boards with a metallic surface [97]. Formability of automotive structures has also been researched and shown sandwich materials to be formable using current metals pressing equipment [82], [88], [98]–[100]. Joining solutions have also been suggested for joining MPM sandwich materials to metals using self–pierced rivets (SPRs) [101] and to other sandwich materials using SPRs, clinching and laser brazing [81], [102].

However, up until now the effectiveness of metal–polymer–metal sandwich panels has not been fully quantified. Deformation modes have not been considered with changing skin thickness, core thickness or material strength. The literature shows MPM sandwich materials could yield an increased energy absorption performance, but it does not explore the limits of their performance in axial impact scenarios, nor does it compare these materials definitively to their monolithic metal counterparts to categorically judge their performance.

2.7 Summary of Literature review

There is a considerable drive to reduce the mass of the automotive body–in–white. Metal–polymer–metal sandwich panels have been predominantly researched for use in automotive skin panels (outer cosmetic skin panels of the vehicle). Published work on the forming limits and modelling of forming of sandwich panels is broad, but little work has been done on the use of metal–polymer–metal sandwich panels for structural panels with the exception of the investigation of the bending performance. Less still has been published on the use of metal–polymer–metal sandwich materials in automotive crash structures.

The literature review shows the ideal and repeatable crushing response of the monolithic metallic crash structure and the extensive research in this area. Higher strength steels and lower density aluminium alloys have been shown to give significant increases in the specific energy absorption. The disadvantage of the use of high strength steels and aluminium alloys is their low ductility and in some instances difficulty in joining. However, lower ductility is not necessarily a problem in monolithic materials. Common press–forming methods are also not always available for these advanced grades; therefore, complex forming processes have to be used, such as warm forming, hot forming, hydroforming and super–plastic forming.

Fibre reinforced composites have been shown to achieve high specific energy absorption, via progressive failure of the material. This method of energy absorption is undesirable in front impact crash structures due to the potential of an unpredictable loading path through the rest of the body–in–white. For stiffness limited components, composites will inevitably be used in the pursuit of a lighter body–in–white. This is appropriate in components where large scale deformation does not occur. Metal–composite hybrids may be a better choice than composites

for the front longitudinal member and bolt–on crash structure. The progressive crushing mode seen in the metal crash structure can be maintained by suitable fibre orientation, and the performance of the metallic structure can be improved upon. The disadvantage of the metal–composite hybrid is the metal crash structure has to be formed, then wrapped and post bonded in composite. This requires multiple processes for a part, which is conventionally two stamped steel sheets spot–welded together. The additional cost and process time would be significant and prohibitive for mass manufacture.

The use of metal–polymer–metal sandwich panels has the potential to not only outperform steel but also aluminium alloys with the correct balance of steel skin thickness and strength and core thickness in the sandwich.

The metal–polymer–metal sandwich material has been shown to press much like the metal sheet it replaces, and the lower strength of the sandwich will require lower cost press equipment. The reduced ductility due to the reduction in steel thickness may not cause a problem in forming or crash due to sandwich materials retaining good formability. In the crash structure, reduced thickness of the metal will increase the stress in the skin. However, it has been shown the ultimate strength of sheet metals is rarely reached in crash structures; hence, this may not pose a problem.

A final point from the literature review is the difficulty in comparing results of different crash structure geometries due to shape, thickness and stability of the deformation of the crash structure. As well as the lack of finite element modelling to fill in gaps in knowledge.

2.8 References

[1] C. L. Magee and P. H. Thornton, "Design Considerations in Energy Absorption by Structural Collapse," *Soc. Automot. Eng. Tech. Pap.*, no. 780434, Feb. 1978.

[2] T. Ohkubo, K. Shirasawa, and Y. Akamatsu, "Mean Crushing Strength of Closed-Hat Section Members," *Trans. Soc. Automot. Eng. Japan*, no. 740040, 1974.

[3] N. Jones, *Structural Impact*. Cambridge University Press, 2011.

[4] G. Lu and T. Yu, *Energy Absorption of Structures and Materials*. CRC Press, 2003.

[5] J. D. Reid, "Towards the understanding of material property influence on automotive crash structures," *Thin-Walled Struct.*, vol. 24, no. 4, pp. 285–313, Jan. 1996.

[6] N. Reynolds, *Advanced Composite Materials for Automotive Applications: Structural Integrity and Crashworthiness*. Wiley, 2013.

[7] A. Mamalis, M. Robinson, D. Manolakos, G. Demosthenous, M. Ioannidis, and J. Carruthers, "Crashworthy capability of composite material structures," *Compos. Struct.*, vol. 37, no. 2, pp. 109–134, Feb. 1997.

[8] Oleo International, "Rail Products and Services Brochure." [Online]. Available: http://www.oleo.co.uk/media/media_uploads/Rail-series-brochure-EN.pdf.

[9] F. Schneider and N. Jones, "Observations on the design and modelling of some joined thin-walled structural sections," *Thin-Walled Struct.*, vol. 46, no. 7–9, pp. 887–897, 2008.

[10] X. M. Chen, M. F. Shi, G. Chen, M. Kamura, K. Watanabe, and Y. Omiya, "Crash Performances of Advanced High Strength Steels of DP780, TRIP780 and DP980," *Soc. Automot. Eng. Tech. Pap.*, no. 2005–01–0354, 2005.

[11] S. S. Hsu and N. Jones, "Quasi-static and dynamic axial crushing of thin-walled circular stainless steel, mild steel and aluminium alloy tubes," *Int. J. Crashworthiness*, vol. 9, no. 2, pp. 195–217, Mar. 2004.

[12] ThyssenKrupp, "Reference longitudinal member made of DP-W 600." [Online]. Available: http://incar.thyssenkrupp.com/4_04_020_LT01_Referenz.html?lang=de. [Accessed: 17-Feb-2013].

[13] N. Jones, "Energy-absorbing effectiveness factor," *Int. J. Impact Eng.*, vol. 37, no. 6, pp. 754–765, 2010.

[14] F. Schneider and N. Jones, “Influence of spot-weld failure on crushing of thin-walled structural sections,” *Int. J. Mech. Sci.*, vol. 45, no. 12, pp. 2061–2081, 2003.

[15] W. Abramowicz and N. Jones, “Dynamic progressive buckling of circular and square tubes,” *Int. J. Impact Eng.*, vol. 4, no. 4, pp. 243–270, 1986.

[16] M. Langseth and O. S. Hopperstad, “Static and dynamic axial crushing of square thin-walled aluminium extrusions,” *Int. J. Impact Eng.*, vol. 18, no. 7–8, pp. 949–968, Oct. 1996.

[17] M. R. Bambach, H. H. Jama, and M. Elchalakani, “Static and dynamic axial crushing of spot-welded thin-walled composite steel–CFRP square tubes,” *Int. J. Impact Eng.*, vol. 36, no. 9, pp. 1083–1094, Sep. 2009.

[18] M. Langseth, O. S. Hopperstad, and A. G. Hanssen, “Crash behaviour of thin-walled aluminium members,” *Thin-Walled Struct.*, vol. 32, no. 1–3, pp. 127–150, Sep. 1998.

[19] D. Kecman, “An engineering approach to crashworthiness of thin-walled beams and joints in vehicle structures,” *Thin-Walled Struct.*, vol. 28, no. 3–4, pp. 309–320, Jul. 1997.

[20] R. J. Hayduk and T. Wierzbicki, “Extensional collapse modes of structural members,” *Comput. Struct.*, vol. 18, no. 3, pp. 447–458, 1984.

[21] M. Tani and A. Funahashi, “Energy Absorption by the Plastic Deformation of Body Structural Members,” *Soc. Automot. Eng. Tech. Pap.*, no. 780368, 1978.

[22] M. D. White, N. Jones, and W. Abramowicz, “A theoretical analysis for the quasi-static axial crushing of top-hat and double-hat thin-walled sections,” *Int. J. Mech. Sci.*, vol. 41, no. 2, pp. 209–233, 1999.

[23] Z. Tang, S. Liu, and Z. Zhang, “Energy absorption properties of non-convex multi-corner thin-walled columns,” *Thin-Walled Struct.*, vol. 51, pp. 112–120, Feb. 2012.

[24] X. Zhang and H. Huh, “Crushing analysis of polygonal columns and angle elements,” *Int. J. Impact Eng.*, vol. 37, no. 4, pp. 441–451, Apr. 2010.

[25] M. Yamashita, M. Gotoh, and Y. Sawairi, “Axial crush of hollow cylindrical structures with various polygonal cross-sections,” *J. Mater. Process. Technol.*, vol. 140, no. 1–3, pp. 59–64, Sep. 2003.

[26] A. Najafi and M. Rais-Rohani, “Mechanics of axial plastic collapse in multi-cell, multi-corner crush tubes,” *Thin-Walled Struct.*, vol. 49, no. 1, pp. 1–12, 2011.

[27] T. Tran, S. Hou, X. Han, W. Tan, and N. Nguyen, “Theoretical prediction and crashworthiness optimization of multi-cell triangular tubes,” *Thin-Walled Struct.*, vol. 82, pp. 183–195, Sep. 2014.

[28] X. Zhang and H. Zhang, “Axial crushing of circular multi-cell columns,” *Int. J. Impact Eng.*, vol. 65, pp. 110–125, Mar. 2014.

[29] C. Graciano, G. Martínez, and A. Gutiérrez, “Failure mechanism of expanded metal tubes under axial crushing,” *Thin-Walled Struct.*, vol. 51, pp. 20–24, Feb. 2012.

[30] G. Martínez, C. Graciano, and P. Teixeira, “Energy absorption of axially crushed expanded metal tubes,” *Thin-Walled Struct.*, vol. 71, pp. 134–146, Oct. 2013.

[31] A. Alavi Nia and M. Parsapour, “Comparative analysis of energy absorption capacity of simple and multi-cell thin-walled tubes with triangular, square, hexagonal and octagonal sections,” *Thin-Walled Struct.*, vol. 74, pp. 155–165, Jan. 2014.

[32] H.-S. Kim, “New extruded multi-cell aluminum profile for maximum crash energy absorption and weight efficiency,” *Thin-Walled Struct.*, vol. 40, no. 4, pp. 311–327, Apr. 2002.

[33] S. P. Santosa, T. Wierzbicki, A. G. Hanssen, and M. Langseth, “Experimental and numerical studies of foam-filled sections,” *Int. J. Impact Eng.*, vol. 24, no. 5, pp. 509–534, 2000.

[34] H.-W. Song, Z.-J. Fan, G. Yu, Q.-C. Wang, and A. Tobota, “Partition energy absorption of axially crushed aluminum foam-filled hat sections,” *Int. J. Solids Struct.*, vol. 42, no. 9–10, pp. 2575–2600, May 2005.

[35] D. Zenkert and K.-A. Olsson, “DP-Sandwich—The utilization of thin high-strength steel sheets in compression,” *Thin-Walled Struct.*, vol. 7, no. 2, pp. 99–117, Jan. 1989.

[36] M. Costas, J. Díaz, L. E. Romera, S. Hernández, and A. Tielas, “Static and dynamic axial crushing analysis of car frontal impact hybrid absorbers,” *Int. J. Impact Eng.*, vol. 62, pp. 166–181, Dec. 2013.

[37] T. Y. Reddy and R. J. Wall, “Axial compression of foam-filled thin-walled circular tubes,” *Int. J. Impact Eng.*, vol. 7, no. 2, pp. 151–166, Jan. 1988.

[38] V. S. Deshpande and N. A. Fleck, “High strain rate compressive behaviour of aluminium alloy foams,” *Int. J. Impact Eng.*, vol. 24, no. 3, pp. 277–298, 2000.

[39] A. G. Hanssen, M. Langseth, and O. S. Hopperstad, “Static and dynamic crushing of square aluminium extrusions with aluminium foam filler,” *Int. J. Impact Eng.*, vol. 24, no. 4, pp. 347–383, Apr. 2000.

[40] A. G. Hanssen, M. Langseth, and O. S. Hopperstad, “Static and dynamic crushing of circular aluminium extrusions with aluminium foam filler,” *Int. J. Impact Eng.*, vol. 24, no. 5, pp. 475–507, May 2000.

[41] A. G. Hanssen, M. Langseth, and O. . Hopperstad, “Optimum design for energy absorption of square aluminium columns with aluminium foam filler,” *Int. J. Mech. Sci.*, vol. 43, no. 1, pp. 153–176, Jan. 2001.

[42] A. Reyes, O. S. Hopperstad, A. G. Hanssen, and M. Langseth, "Modeling of material failure in foam-based components," *Int. J. Impact Eng.*, vol. 30, no. 7, pp. 805–834, Aug. 2004.

[43] A. G. Hanssen, M. Langseth, and O. S. Hopperstad, "Static crushing of square aluminium extrusions with aluminium foam filler," *Int. J. Mech. Sci.*, vol. 41, no. 8, pp. 967–993, Aug. 1999.

[44] A. Reyes, O. S. Hopperstad, and M. Langseth, "Aluminum foam-filled extrusions subjected to oblique loading: experimental and numerical study," *Int. J. Solids Struct.*, vol. 41, no. 5–6, pp. 1645–1675, Mar. 2004.

[45] A. G. Hanssen, O. S. Hopperstad, M. Langseth, and H. Ilstad, "Validation of constitutive models applicable to aluminium foams," *Int. J. Mech. Sci.*, vol. 44, no. 2, pp. 359–406, Feb. 2002.

[46] S. Santosa and T. Wierzbicki, "On the modeling of crush behavior of a closed-cell aluminum foam structure," *J. Mech. Phys. Solids*, vol. 46, no. 4, pp. 645–669, 1998.

[47] G. Savage, "Formula 1 Composites Engineering," *Eng. Fail. Anal.*, vol. 17, no. 1, pp. 92–115, Jan. 2010.

[48] J. Meredith, S. Cozien-Cazuc, E. Collings, S. Carter, S. Alsop, J. Lever, S. R. Coles, B. M. Wood, and K. Kirwan, "Recycled carbon fibre for high performance energy absorption," *Compos. Sci. Technol.*, vol. 72, no. 6, pp. 688–695, Mar. 2012.

[49] A. Mamalis, D. Manolakos, M. Ioannidis, and D. Papapostolou, "Crashworthy characteristics of axially statically compressed thin-walled square CFRP composite tubes: experimental," *Compos. Struct.*, vol. 63, no. 3–4, pp. 347–360, Feb. 2004.

[50] A. G. Caliskan, "Crashworthiness of Composite Materials & Structures for Vehicle Applications," Nov. 2000.

[51] E. Mahdi, A. M. S. Hamouda, and T. A. Sebaey, "The effect of fiber orientation on the energy absorption capability of axially crushed composite tubes," *Mater. Des.*, vol. 56, pp. 923–928, Apr. 2014.

[52] A. G. Mamalis, D. E. Manolakos, G. A. Demosthenous, and M. B. Ioannidis, "The static and dynamic axial collapse of fibreglass composite automotive frame rails," *Compos. Struct.*, vol. 34, no. 1, pp. 77–90, Jan. 1996.

[53] University of Warwick, "Low Carbon Vehicle Technology Project." [Online]. Available: http://www2.warwick.ac.uk/fac/sci/wmg/mediacentre/wmgcorporatebrochures/lcvtp_brochure_final.pdf.

[54] D. Emerson, D. Almond, N. Reynolds, D. Hughes, M. Pharaoh, and G. Williams, "Energy Absorption Characteristics of Automotive-Type Beam Structures in High-Speed Crush Testing," in *45th International SAMPE Technical Conference (ISTC); 2013 October 24, 2013; : SAMPE Tech Journal.*, 2013.

[55] E. Cates and S. Jacques, “Hybrid Reinforcement Yarns for Impact-Resistant Composite Structures,” in *JEC Europe, Composites show & Conferences*, 2014.

[56] A. Jacob, “Built in Italy: the Lamborghini Avendator,” *Reinf. Plast.*, vol. 57, no. 5, pp. 29–31, Sep. 2013.

[57] W. Knapp, S. Clement, C. Franz, M. Oumarou, and J. Renard, “Laser-bonding of long fiber thermoplastic composites for structural assemblies,” *Phys. Procedia*, vol. 5, pp. 163–171, Jan. 2010.

[58] P. Amend, S. Pfindel, and M. Schmidt, “Thermal Joining of Thermoplastic Metal Hybrids by Means Of Mono- and Polychromatic Radiation,” *Phys. Procedia*, vol. 41, pp. 98–105, Jan. 2013.

[59] F. Balle, S. Huxhold, G. Wagner, and D. Eifler, “Damage Monitoring of Ultrasonically Welded Aluminum/ CFRP-Joints by Electrical Resistance Measurements,” *Procedia Eng.*, vol. 10, pp. 433–438, Jan. 2011.

[60] H. Ascroft and D. Hughes, “WMG, University of Warwick Internal Report - Joining techniques for multi material forming,” 2013.

[61] L. Yan, N. Chouw, and K. Jayaraman, “Effect of triggering and polyurethane foam-filler on axial crushing of natural flax/epoxy composite tubes,” *Mater. Des.*, vol. 56, pp. 528–541, Apr. 2014.

[62] M. Guden, S. Yüksel, A. Taşdemirci, and M. Tanoğlu, “Effect of aluminum closed-cell foam filling on the quasi-static axial crush performance of glass fiber reinforced polyester composite and aluminum/composite hybrid tubes,” *Compos. Struct.*, vol. 81, no. 4, pp. 480–490, Dec. 2007.

[63] J. M. Rotter, “Elephant’s foot buckling in pressurised cylindrical shells,” *Stahlbau*, vol. 75, no. 9, pp. 742–747, Sep. 2006.

[64] J. G. Teng, T. Yu, and D. Fernando, “Strengthening of steel structures with fiber-reinforced polymer composites,” *J. Constr. Steel Res.*, vol. 78, pp. 131–143, Nov. 2012.

[65] M. R. Bambach, “Axial capacity and crushing of thin-walled metal, fibre–epoxy and composite metal–fibre tubes,” *Thin-Walled Struct.*, vol. 48, no. 6, pp. 440–452, Jun. 2010.

[66] M. R. Bambach, “Axial capacity and crushing behavior of metal–fiber square tubes – Steel, stainless steel and aluminum with CFRP,” *Compos. Part B Eng.*, vol. 41, no. 7, pp. 550–559, Oct. 2010.

[67] M. R. Bambach, “Fibre composite strengthening of thin-walled steel vehicle crush tubes for frontal collision energy absorption,” *Thin-Walled Struct.*, vol. 66, pp. 15–22, May 2013.

[68] H. C. Kim, D. K. Shin, J. J. Lee, and J. B. Kwon, “Crashworthiness of aluminum/CFRP square hollow section beam under axial impact loading for crash box application,” *Compos. Struct.*, vol. 112, pp. 1–10, Jun. 2014.

[69] J. Song, Y. Zhou, and F. Guo, “A relationship between progressive collapse and initial buckling for tubular structures under axial loading,” *Int. J. Mech. Sci.*, vol. 75, pp. 200–211, Oct. 2013.

[70] M. R. Bambach, *Rehabilitation of Metallic Civil Infrastructure Using Fiber Reinforced Polymer (FRP) Composites*. Elsevier, 2014.

[71] M. Elchalakani, “Plastic collapse analysis of CFRP strengthened and rehabilitated degraded steel welded RHS beams subjected to combined bending and bearing,” *Thin-Walled Struct.*, vol. 82, pp. 278–295, Sep. 2014.

[72] M. R. Bambach, H. H. Jama, and M. Elchalakani, “Axial capacity and design of thin-walled steel SHS strengthened with CFRP,” *Thin-Walled Struct.*, vol. 47, no. 10, pp. 1112–1121, Oct. 2009.

[73] M. R. Bambach and M. Elchalakani, “Plastic mechanism analysis of steel SHS strengthened with CFRP under large axial deformation,” *Thin-Walled Struct.*, vol. 45, no. 2, pp. 159–170, Feb. 2007.

[74] K. C. Shin, J. J. Lee, K. H. Kim, M. C. Song, and J. S. Huh, “Axial crush and bending collapse of an aluminum/GFRP hybrid square tube and its energy absorption capability,” *Compos. Struct.*, vol. 57, no. 1–4, pp. 279–287, 2002.

[75] M. R. Bambach, “Axial capacity and crushing of thin-walled metal, fibre–epoxy and composite metal–fibre tubes,” *Thin-Walled Struct.*, vol. 48, no. 6, pp. 440–452, Jun. 2010.

[76] M. R. Bambach, M. Elchalakani, and X. L. Zhao, “Composite steel–CFRP SHS tubes under axial impact,” *Compos. Struct.*, vol. 87, no. 3, pp. 282–292, Feb. 2009.

[77] H.-W. Song, Z.-M. Wan, Z.-M. Xie, and X.-W. Du, “Axial impact behavior and energy absorption efficiency of composite wrapped metal tubes,” *Int. J. Impact Eng.*, vol. 24, no. 4, pp. 385–401, 2000.

[78] J. K. Kim and P. F. Thomson, “Separation behaviour of sheet steel laminate during forming,” *J. Mater. Process. Technol.*, vol. 22, no. 2, pp. 147–161, 1990.

[79] J. K. Kim and P. F. Thomson, “Forming behaviour of sheet steel laminate,” *J. Mater. Process. Technol.*, vol. 22, no. 1, pp. 45–64, 1990.

[80] T. M. Link, “Formability and Performance of Steel-Plastic-Steel Laminated Sheet Materials,” *Soc. Automot. Eng. Tech. Pap.*, no. 2001–01–0079, Mar. 2001.

[81] M. Dunand and J.-N. Gacel, “USILIGHT: A Cost-Effective Solution to Lighten Cars,” *Soc. Automot. Eng. Tech. Pap.*, no. 2006–01–1216, Apr. 2006.

[82] I. Burchitz, R. Boesenkool, S. van der Zwaag, and M. Tassoul, “Highlights of designing with Hylite - a new material concept,” *Mater. Des.*, vol. 26, no. 4, pp. 271–279, 2005.

[83] N. Asnafi, G. Langstedt, C. H. Andersson, N. Östergren, and T. Håkansson, "A new lightweight metal-composite-metal panel for applications in the automotive and other industries," *Thin-Walled Struct.*, vol. 36, no. 4, pp. 289–310, 2000.

[84] K. P. Jackson, J. M. Allwood, and M. Landert, "Incremental forming of sandwich panels," *J. Mater. Process. Technol.*, vol. 204, no. 1–3, pp. 290–303, Aug. 2008.

[85] A. Carradò, J. Faerber, S. Niemeyer, G. Ziegmann, and H. Palkowski, "Metal/polymer/metal hybrid systems: Towards potential formability applications," *Compos. Struct.*, vol. 93, no. 2, pp. 715–721, Jan. 2011.

[86] J. Gresham, W. Cantwell, M. J. Cardew-Hall, P. Compston, and S. Kalyanasundaram, "Drawing behaviour of metal-composite sandwich structures," *Compos. Struct.*, vol. 75, no. 1–4, pp. 305–312, 2006.

[87] D. Mohr, "On the role of shear strength in sandwich sheet forming," *Int. J. Solids Struct.*, vol. 42, no. 5–6, pp. 1491–1512, 2005.

[88] K. J. Kim, D. Kim, S. H. Choi, K. Chung, K. S. Shin, F. Barlat, K. H. Oh, and J. R. Youn, "Formability of AA5182/polypropylene/AA5182 sandwich sheets," *J. Mater. Process. Technol.*, vol. 139, no. 1–3, pp. 1–7, 2003.

[89] M. Zrida, H. Laurent, V. Grolleau, G. Rio, M. Khlif, D. Guines, N. Masmoudi, and C. Bradai, "High-speed tensile tests on a polypropylene material," *Polym. Test.*, vol. 29, no. 6, pp. 685–692, Sep. 2010.

[90] D. Mohr and T. Wierzbicki, "Crushing of soft-core sandwich profiles: experiments and analysis," *Int. J. Mech. Sci.*, vol. 45, no. 2, pp. 253–271, 2003.

[91] D. Mohr and T. Wierzbicki, "On the Crashworthiness of Shear-Rigid Sandwich Structures," *J. Appl. Mech.*, vol. 73, no. 4, pp. 633–641, 2006.

[92] N. Fleck and I. Sridhar, "End compression of sandwich columns," *Compos. Part A Appl. Sci. Manuf.*, vol. 33, no. 3, pp. 353–359, Mar. 2002.

[93] Alu Matter, "Crash Box: Energy Absorption." [Online]. Available: http://aluminium.matter.org.uk/content/html/eng/default.asp?catid=7&pageid=2144416781.

[94] D. M. and T. Wierzbicki, "Crashworthiness of Thin Ultra-light Stainless Steel Sandwich Sheets: From the Design of Core Materials to Structural Applications," *Soc. Automot. Eng. Tech. Pap.*, no. 2004–01–0886, 2004.

[95] Lamera AB, "Lamera Hybrix." [Online]. Available: http://www.lamera.se/eng/.

[96] A. E. Markaki and T. W. Clyne, "Mechanics of thin ultra-light stainless steel sandwich sheet material: Part I. Stiffness," *Acta Mater.*, vol. 51, no. 5, pp. 1341–1350, 2003.

[97] 3A Composites, “3A Composites Home Page.” [Online]. Available: http://www.3acomposites.com/.

[98] W. T. M. Buters, T. Retter, and W. Stall, “Hem Flanging Hylite Sandwich Sheet for Mass Production,” *Soc. Automot. Eng. Tech. Pap.*, no. 982330, Sep. 1998.

[99] N. A. J. Langerak and S. P. Kragtwijk, “The Application of Steel and Aluminum in a New Lightweight Car Body Design,” *Soc. Automot. Eng. Tech. Pap.*, no. 982285, Sep. 1998.

[100] E. W. Veenstra, “Aluminum - Plastic - Aluminum Sandwich Sheet for Maximum Weight Reduction in Body Panels,” *Soc. Automot. Eng. Tech. Pap.*, no. 930706, Mar. 1993.

[101] C. G. Pickin, K. Young, and I. Tuersley, “Joining of lightweight sandwich sheets to aluminium using self-pierce riveting,” *Mater. Des.*, vol. 28, no. 8, pp. 2361–2365, 2007.

[102] ThyssenKrupp, “Stiffness-optimized sandwich material.” [Online]. Available: http://incar.thyssenkrupp.com/4_05_042_D02_Fuegen.html?lang=en.

3 Materials and methods

Chapter 3 details the sandwich materials tested; the production and characterisation of sandwich materials and production of crash structures.

The test equipment used and methods for processing the data obtained are described as well.

3.1 Materials

The sandwich materials used in this work were produced from three different grades of steel; Steelite, Electrolytically Chrome Coated Steel (ECCS) and DP600. When possible, three thicknesses of polypropylene core were also used, in combination with each grade of steel. The core increments were 0.7, 1.4 and 2.1 mm and are denoted single core, double core and triple core (SC, DC and TC respectively).

When specifying material thicknesses, the sandwich materials were designated in the following manner: Steel thickness/Polypropylene thickness/Steel thickness, e.g. 0.15/0.7/0.15 mm. However, the naming convention of a sandwich material is the name of the skin material followed by the abbreviation for the core thickness, e.g. Steelite SC or ECCS DC.

The constituent materials of the sandwich (steel and polypropylene) and the monolithic metals (steel and aluminium) were all tensile tested to the appropriate standard (discussed further in Section 3.4), representative flow curves in true stress *versus* true strain for each material are shown below.

3.1.1 Steelite (0.15 mm steel skin)

The first material produced was based on an existing layup originally manufactured by Hoogovens B.V. (now Tata Steel) in the 1990s. Steelite (trade name) is a polypropylene cored sandwich with a layup of 0.15/0.7/0.15 mm layers.

In this research Steelite sandwich material was produced in the three thicknesses (stated above) to thoroughly explore the effect of the core thickness on material performance. The Steelite skin material has a relatively low yield strength at 220 MPa, compared to over 400 MPa for the ECCS steel (Section 3.1.2). Additionally, the comparatively thin steel skin (0.15 mm) allows the properties of the core to dominate, highlighting the core's importance.

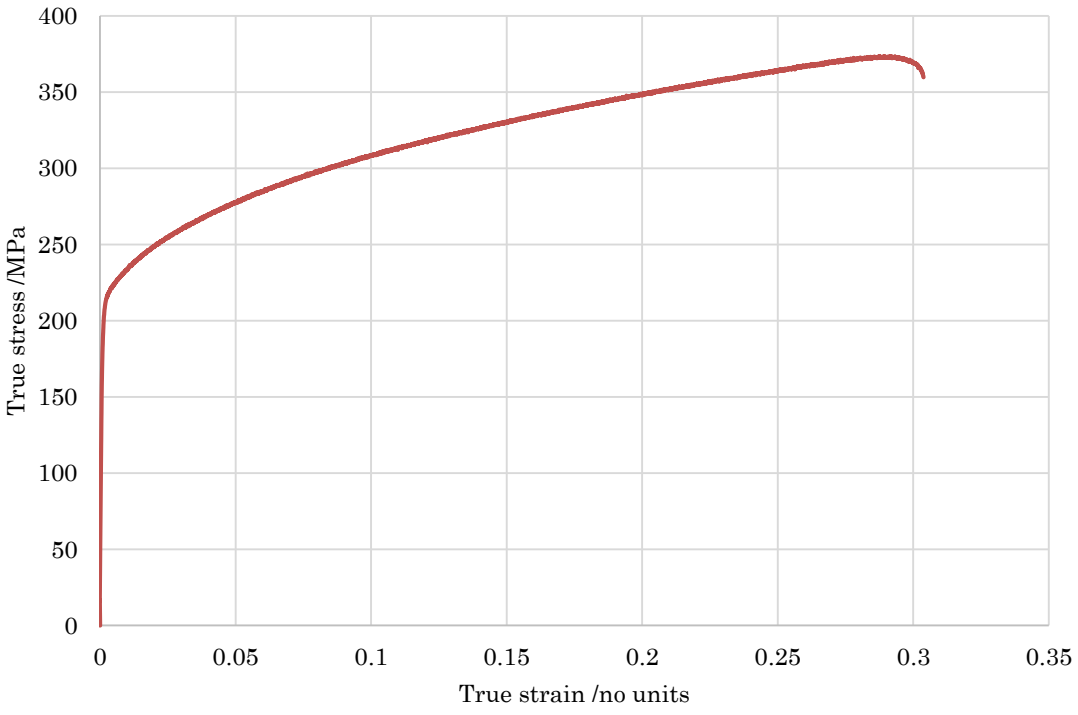

Figure 3.1 – True stress *vs.* true strain flow curve of 0.15 mm Steelite steel skin material.

3.1.2 Electrolytically Chrome Coated Steel (0.3 mm steel skin)

Sandwich materials produced with 0.3 mm ECCS steel skin were also assembled in the three core thicknesses previously described. The ECCS steel is of intermediate thickness (0.3 mm, compared to 0.15 mm for the thinnest steel skin and 0.5 mm for the thickest skin) and also of intermediate strength. Figure 3.2 shows the ECCS steel has a greater yield and ultimate strength than the Steelite skin (Figure 3.1), however a lower ultimate strength than the DP600 (Figure 3.3).

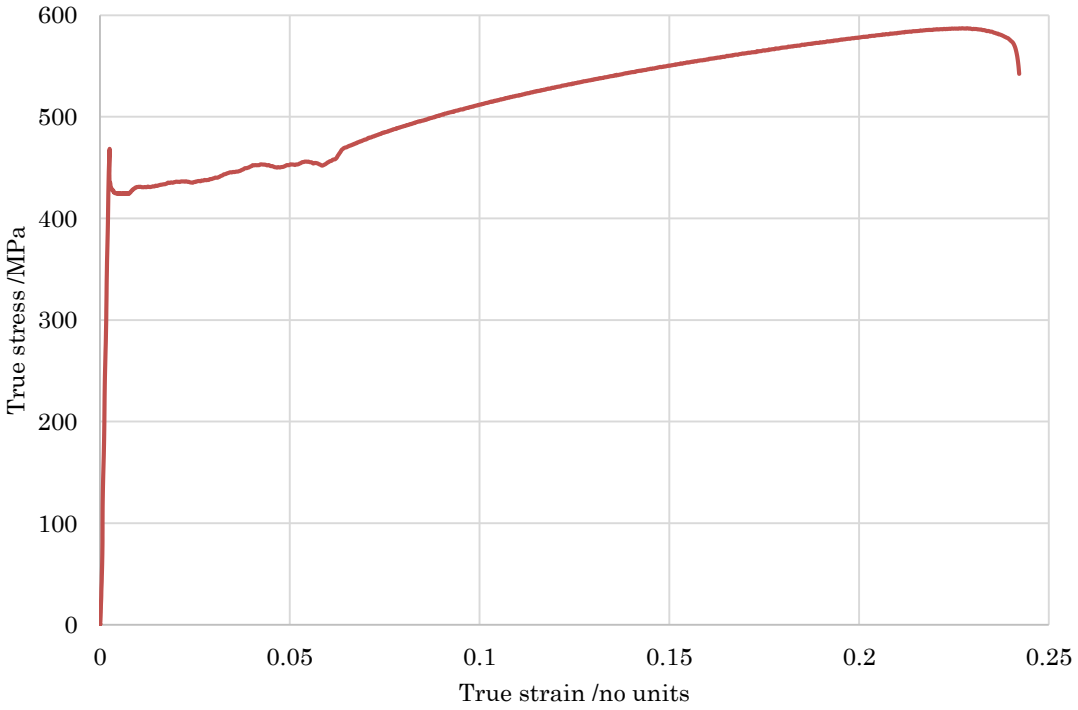

Figure 3.2 – True stress *vs.* true strain flow curve of 0.3 mm ECCS steel skin material.

3.1.3 DP600 steel (0.5 mm steel skin)

Finally, 0.5 mm DP600 steel (flow curve shown in Figure 3.3) was used in an attempt to produce a high strength steel sandwich material, comparable in strength to state of the art crash structure materials already found in the automotive sector. The DP600 steel used was the greatest thickness as well as the highest ultimate strength (750 MPa compared to 590 MPa). Moreover, the steel was galvanised (10 μm nominal thickness, 10 – 12 μm measured using light microscopy), as this is currently the preferred method for steel corrosion protection in the automotive industry. Galvanised coatings invariably lead to lower adhesion strengths due to the lower surface energy of the zinc surface due to its hydrophobic nature [1]; some methods to remedy this were attempted and will be described in Chapter 4.

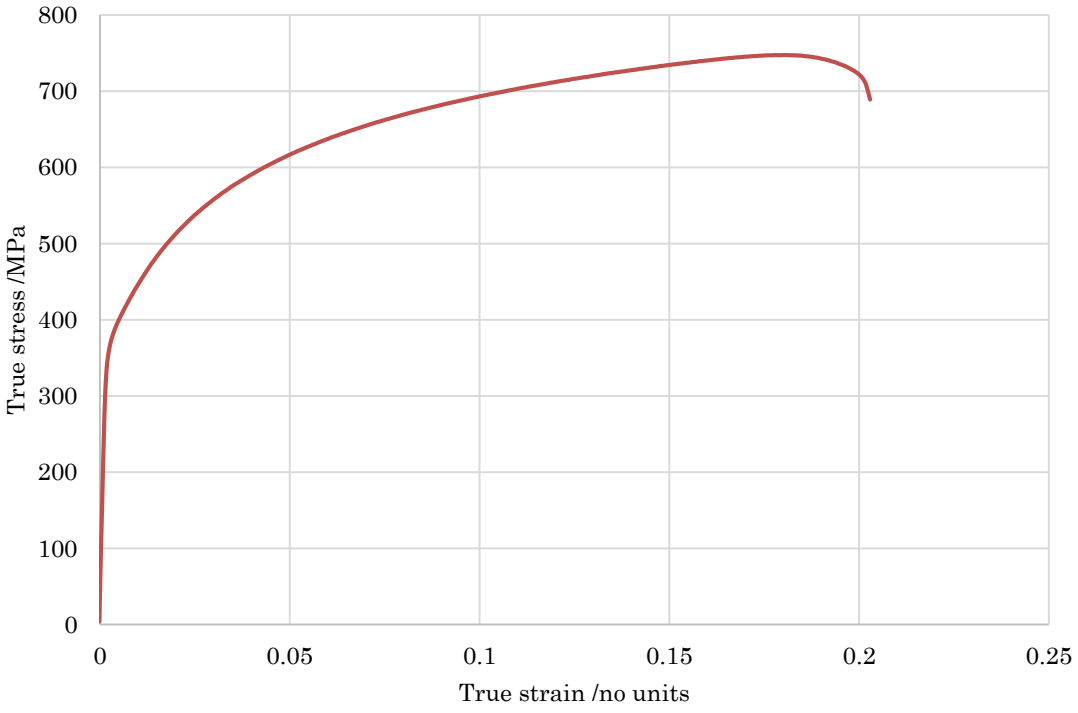

Figure 3.3 – True stress *vs.* true strain flow curve of 0.5 mm DP600 steel skin material.

3.1.4 Polypropylene core material

Polypropylene (PP) supplied by Tata Steel in 0.7 mm thick sheet form was used as the core material. In order to increase core thickness, multiple sheets of polymer were used. Therefore, the increments in core thickness were limited to nominally 0.7 mm. The naming convention for sandwich materials identify the thickness of the core by the number of sheets of polymer stacked to produce the core. Where one sheet of PP core is labelled single core, two sheets is denoted double core and three sheets is triple core.

The PP showed the characteristic stress–strain curve of a tough polymer, reaching tensile strength without a yield point [2], as well as a decrease in strength after ultimate strength without failure (Figure 3.4).

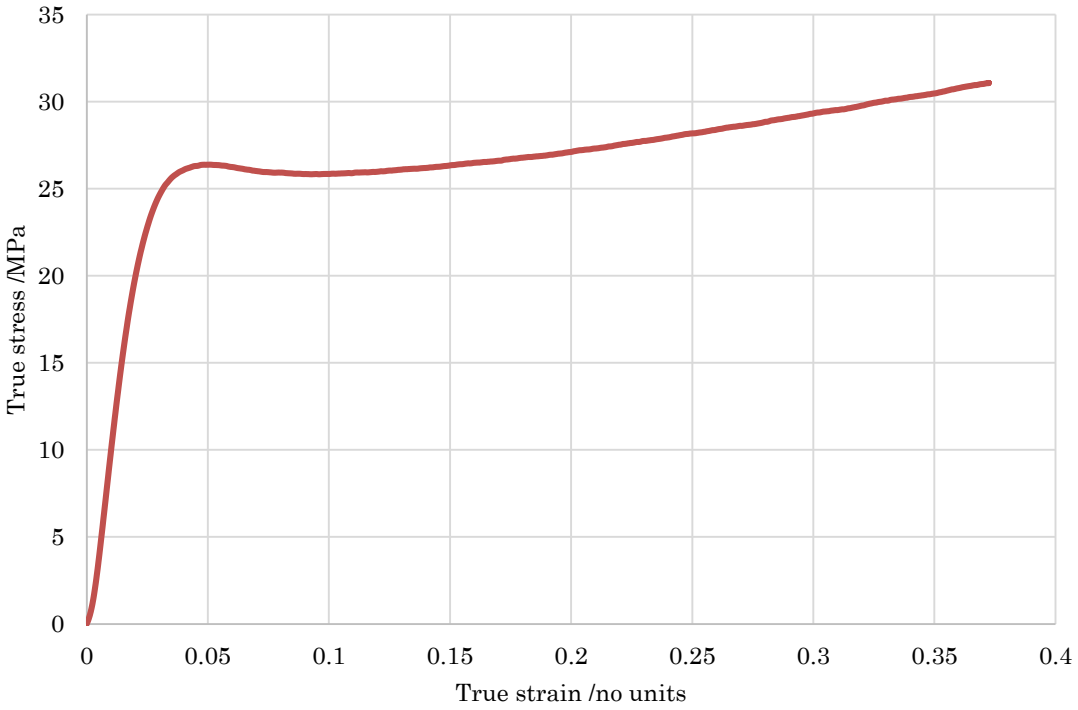

Figure 3.4 – True stress *vs.* true strain flow curve of 0.7 mm Polypropylene material.

3.1.5 Monolithic materials for comparison

The sandwich materials produced were compared to state of the art materials already used in the automotive industry; 1.6 mm DP600 supplied by Tata Steel, and two lightweight aluminium options, both supplied by Novelis (2.5 mm AA5754 and 2.5 mm AC300–T61).

The monolithic metals are of an appropriate grade, thickness and strength, and are currently used in the automotive sector for front–end impact structures. Therefore, they provide a suitable mean crush force target for the sandwich materials to attain.

3.1.5.1 1.6 mm DP600

The stress–strain curve for the 1.6 mm DP600 steel, Figure 3.5, shows the difference in strength of the thicker DP600 sheet to the 0.5 mm variant used as a skin material, Figure 3.3. The 1.6 mm steel has a greater yield strength (430 MPa compared to 380 MPa) and ultimate strength (775 MPa compared to 750 MPa) than the 0.5 mm DP600. This is due to batch variability and the different processing conditions required to produce the 0.5 mm gauge DP600, hence a different starting material is used, this is typical in steel manufacture. However, both materials meet the requirements to be classed as DP600 grade steel.

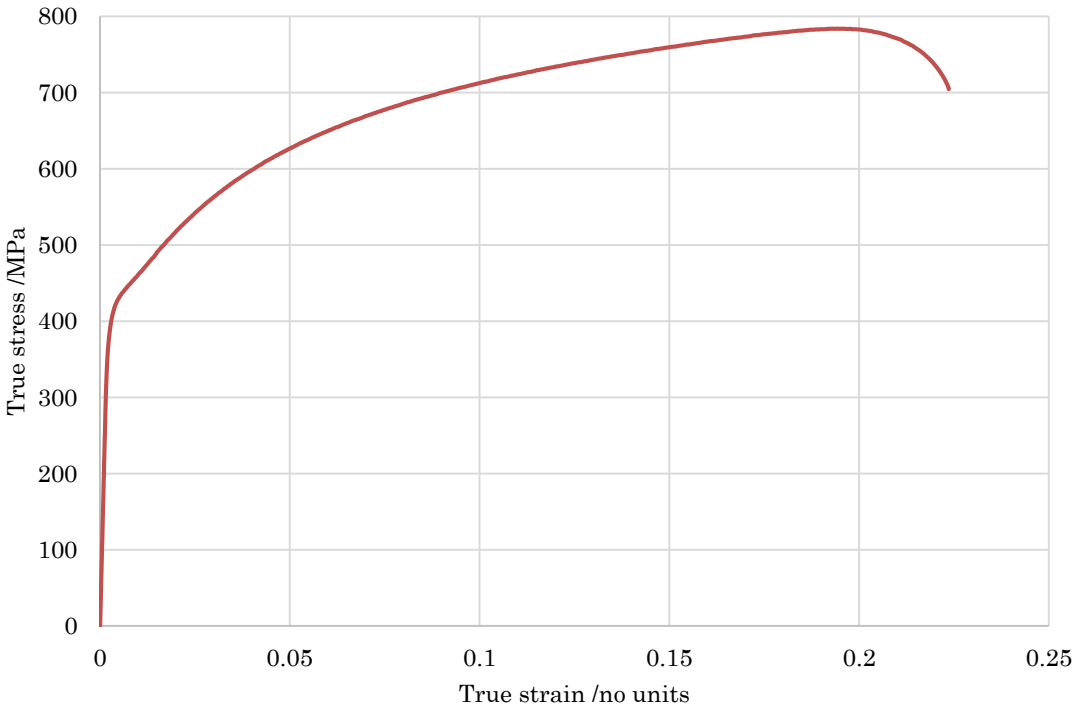

Figure 3.5 – True stress *vs.* true strain flow curve of 1.6 mm DP600 steel.

3.1.5.2 2.5 mm AA5754

AA5754 aluminium is currently used in high–end automotive crash structures, the stress–strain curve (Figure 3.6) shows the alloy has a 110 MPa yield strength and a 290 MPa ultimate strength, as well as the serrated plastic flow typical of 5xxx series aluminium alloys [3].

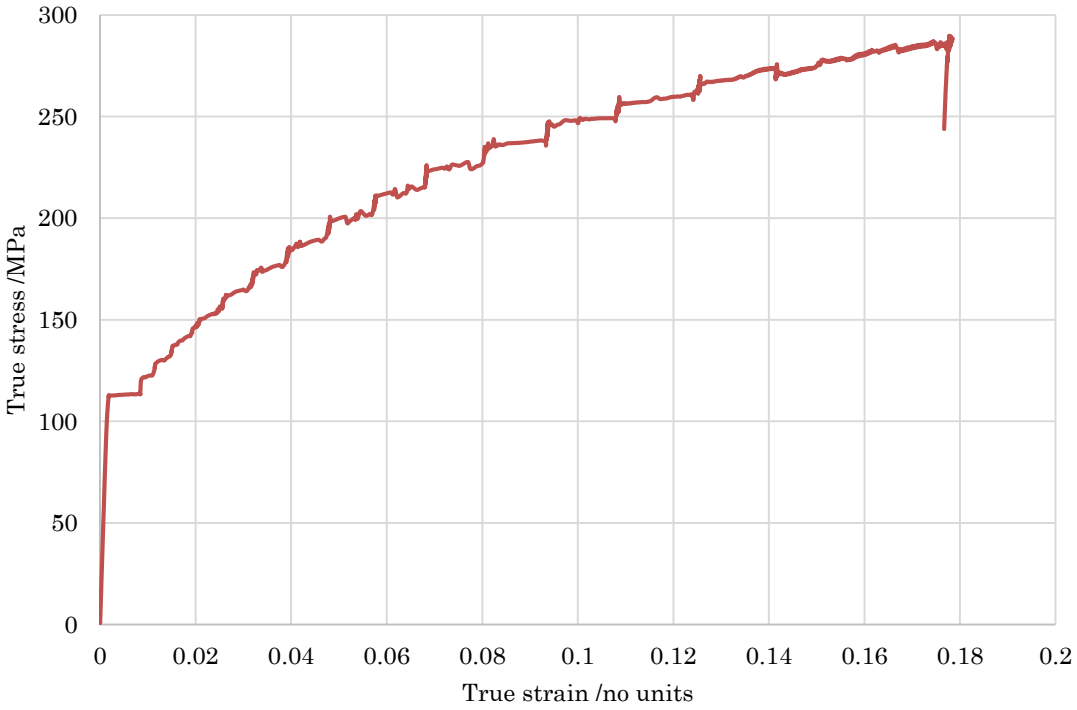

Figure 3.6 – True stress *vs.* true strain flow curve of 2.5 mm AA5754 aluminium alloy.

3.1.5.3 2.5 mm AC300–T61

2.5 mm AC300–T61 is a high strength 6xxx series alloy becoming available in the latest premium automotive applications. The ultimate tensile strength is similar to AA5754 at 290 MPa, however the yield strength is over 170 MPa, in comparison to 110 MPa for AA5754.

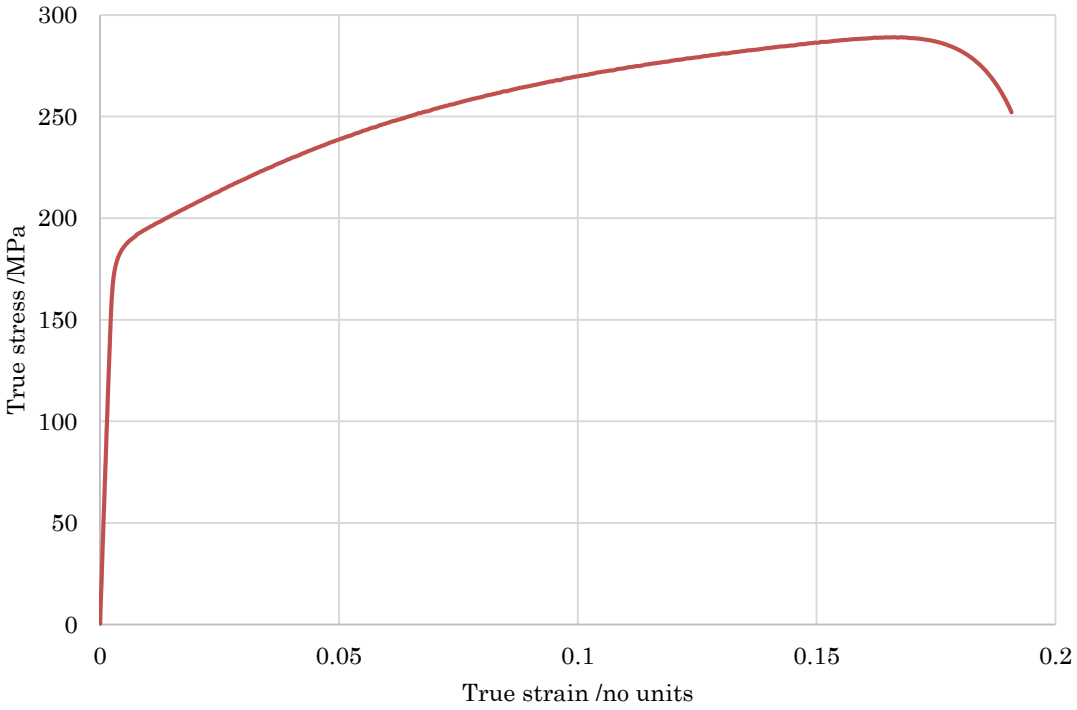

Figure 3.7 – True stress *vs.* true strain flow curve of 2.5 mm AC300–T61 aluminium alloy.

3.1.6 Summary of materials tested

Crash structures were produced and tested from the materials detailed in Table 3.1. The Steelite and ECCS sandwich materials were produced in three thicknesses, whilst the DP600 sandwich (DPSW) was produced in single core only. The comparison monolithic metals are also listed.

Table 3.1 – Monolithic and sandwich materials quasi–statically and dynamically tested.

Sandwich	Skin thickness /mm	Core thickness /mm	Total thickness /mm
Steelite single core	0.15	0.7	1
Steelite double core	0.15	1.4	1.7
Steelite triple core	0.15	2.1	2.4
ECCS single core	0.3	0.7	1.3
ECCS double core	0.3	1.4	2
ECCS triple core	0.3	2.1	2.7
DP600 single core	0.5	0.7	1.7
Monolithic materials			
DP600	N/A	N/A	1.6
AA5754	N/A	N/A	2.5
AC300-T61	N/A	N/A	2.5

3.2 Sandwich material production method

The overall process for production of sandwich materials is shown in Figure 3.8. The laboratory scale process involved coating the desired steel with an adhesive and curing the adhesive in an oven. Two sheets of adhesive coated steel were assembled with a polymer core in the middle. This assembly was then heated and pressed, the heating reactivated the adhesive (described in Section 3.2.1), the pressure of lamination and cooling then joined the steel to the core (described in Section 3.2.2). The optimisation of the processing parameters such as curing temperatures and times to produce the sandwich materials are discussed in Chapter 4.

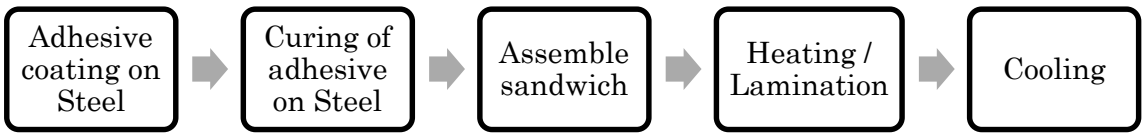

Figure 3.8 – Process for producing top hats from steel skin material and polymer core.

3.2.1 Adhesive coating and curing on steel

The process of adhesive coating is shown in Figure 3.9. The adhesive used was MO–RAD M801, a one–part straw coloured low viscosity epoxy containing polypropylene (PP) beads [4]. The epoxy bound to the steel upon curing and the PP beads bound to the PP core upon melting onto its surface.

The adhesive layer reduced in thickness to approximately 1/3 of the applied wet film thickness (WFT) when cured (Figure 3.9 – c). This reduction exposed the PP beads (of 10 µm diameter) above the surface of the adhesive and thus became available to bond with the PP core. PP is a thermoplastic polymer and may therefore be melted and re–melted without degradation or hardening as opposed to thermoset polymers.

Since PP is an unreactive polymer it is not chemically attacked or altered by the epoxy adhesive it is contained within. When the epoxy adhesive cures, it partly engulfs the PP beads "mechanically fastening" them into the surface of the adhesive. Therefore, upon re–heating the melted PP core and engulfed PP beads amalgamate.

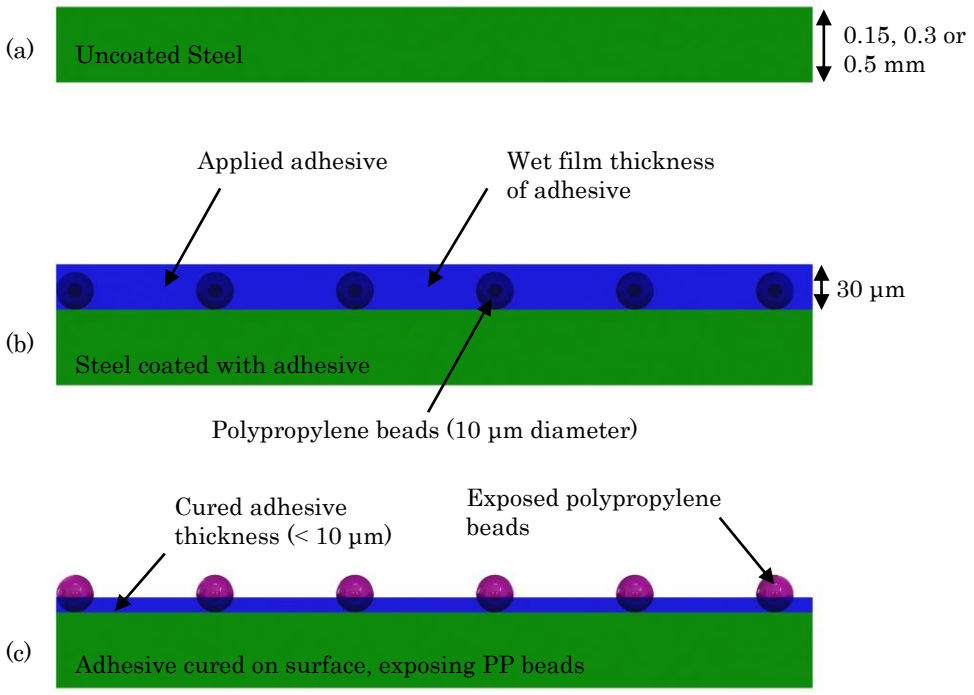

Figure 3.9 – Schematic of bonding process using MO–RAD adhesive (not to scale).

The technical data sheet for the adhesive suggests a possible 25 $N.mm^{-1}$ bond strength with an expected cohesive failure in the PP core [4]. Cohesive failure is considered the ideal bond, since it shows that the bond strength of the adhesive to the substrates is greater than the substrates own mechanical strength. Therefore, a greater bond strength cannot usually be achieved.

The wet film thickness applied was 30 microns, the amount recommended by the adhesive supplier (Rohm and Haas). The adhesive was applied using a Mayer bar, a steel bar wound with steel wire, Figure 3.10. The gaps between the windings on

the bar providing the required coating thickness as the bar is drawn down the steel sheet. This process was performed manually.

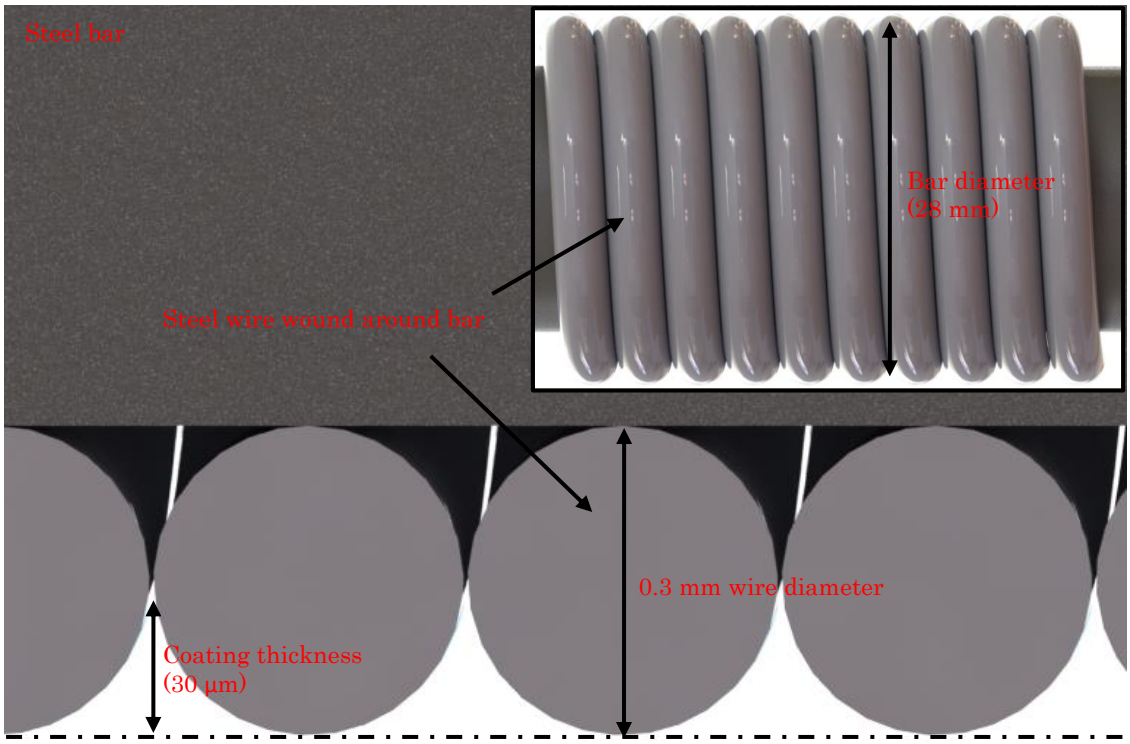

Figure 3.10 – Cut section through wire wound bar, showing how the coating weight is applied, inset shows a complete Mayer bar. Image is not to scale.

The adhesive coated steel sheet was then cured at elevated temperature (specific temperatures detailed in Chapter 4). The temperature reached by the steel was used an indicator for successful curing, this is known as the peak metal temperature (PMT). Measurement of the PMT is the method of curing optimisation suggested by the adhesive manufacturer. Upon reaching the required PMT, the steel was quenched in a bucket of cold water to prevent further heating of the adhesive. A PMT range, ensuring proper curing of the adhesive was given by the manufacturer TDS, which for M801 is between 200 and 240 °C. Therefore, this range was tested using T–peel tests (detailed in Section 3.2.3) to ascertain the optimum PMT, the results of these tests are described in Chapter 4.

The oven was set to a temperature of 260 °C, allowing the steel to reach the PMT in around 60 seconds, this was determined through trial and error. The PMT was measured using a temperature indicator strip (TMC Hallcrest Thermax strip), shown in Figure 3.11. When the strip attains a given temperature, it turns from yellow to black. Therefore, the temperature indicator strip can indicate a minimum peak metal temperature the steel has reached with an error of ±1% [5].

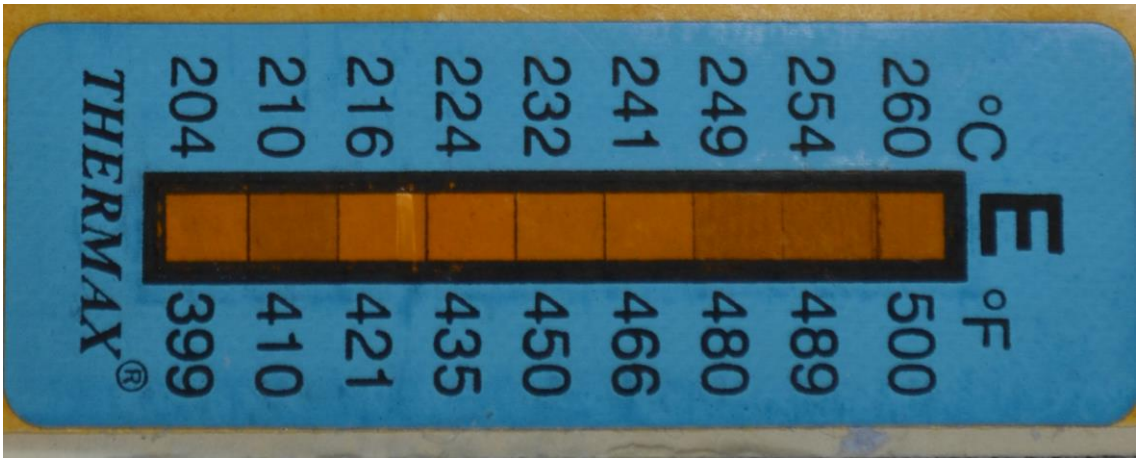

Figure 3.11 – 8 level irreversible temperature indicator strip.

3.2.2 Assembly, lamination and cooling process of the sandwich material

The adhesive coated skin panels were assembled with the PP core and taped with high temperature tape in the corners to ensure that the steel skins were as parallel as possible during lamination. The rolling direction was aligned for both skins. Lamination was performed using two different methods; the ECCS sandwich and the DP600 sandwich (DPSW) were produced using heated lamination while the Steelite sandwich materials were laminated using vacuum bagging, due to available equipment at the time of production.

3.2.2.1 Vacuum bagging

A schematic of the vacuum bagging lamination process is shown in Figure 3.12. The vacuum bagging process involves the complete evacuation of air from a bag,

which exerts consolidation pressure on its contents. The evacuated bag was placed in the oven and a vacuum pump maintained the vacuum within the bag.

The pressure difference in the bag compressed the material and the heat (210°C oven temperature) melted the adhesive allowing it to bind to the polypropylene core. The bond was maintained when the material cooled under the vacuum pressure. Once cooled to ambient temperature, the vacuum was removed and the flat sheet of sandwich material was assembled.

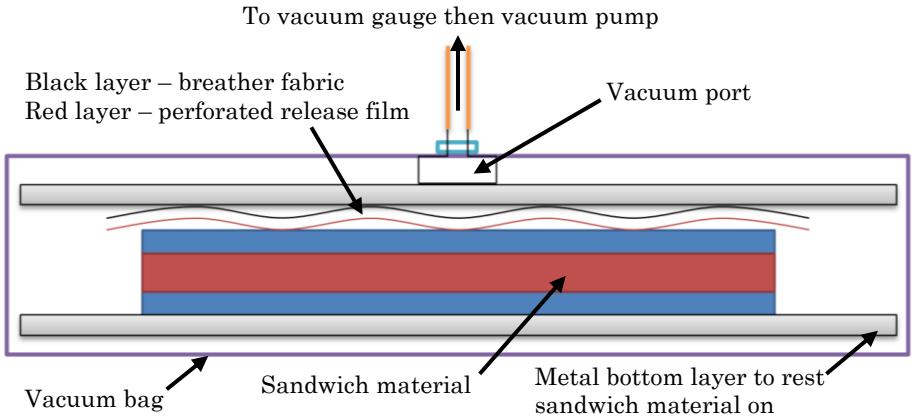

Figure 3.12 – Vacuum bagging process and the ancillaries used to produce the vacuum bag.

3.2.2.2 Heated lamination

Heated lamination was performed using a Schott & Meissner double belt press at Tata Steel Shotton works; a schematic is shown in Figure 3.13. The components of the panel were assembled and subsequently taped in the corners to ensure no slippage during lamination. Figure 3.13 shows the double belt press used, the assembled sandwich was fed in from the left hand side (in Figure 3.13) where two belts pressed and traversed the material. The material was heated to 200 °C (processing temperatures are discussed further in Chapter 4) in the hot zone (red) whilst simultaneously being pressed by the belts. The material was then cooled under pressure in the cold zone (blue), finally coming out of the right hand side (in Figure 3.13).

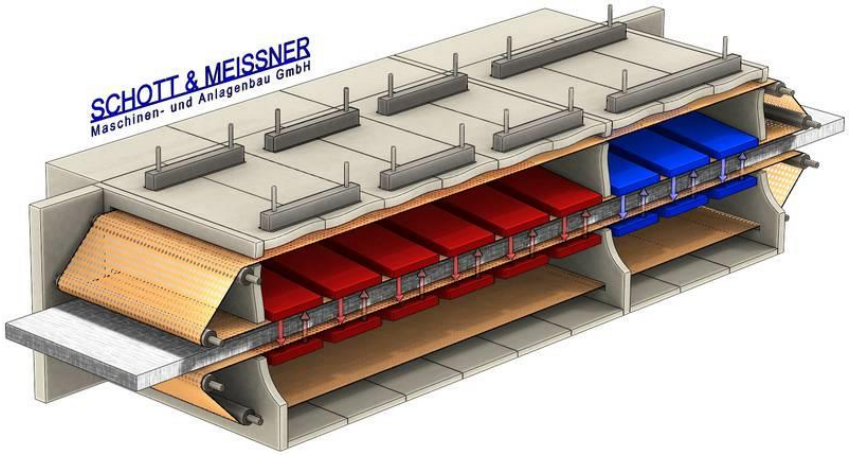

Figure 3.13 – Schott & Meissner double belt press for laminating sandwich panels. [6]

3.2.3 Optimising adhesive bond strength and T–peel testing

The production of sandwich material involves multiple stages which are summarised in Figure 3.8. There are two steps where changing the processing temperatures is possible. These are curing of the adhesive layer on to the steel skin and the lamination T–peel testing in accordance with ISO 11339:2010 [7] was performed to determine the peel strength of the sandwich material and to assess

processing parameters. The results of the t–peel tests were used to optimise the adhesive strength.

T–peel specimens were produced from the laminated sheet material, where a sheet of 250 mm × 300 mm was produced and cut into strips of 25 mm width. During lamination, a 50 mm (in width) piece of polyamide film was placed between the steel and polymer at one end of the sandwich. Since the melting temperature for the polyamide is higher than for the PP, this prevented bonding at this end allowing the T–peel specimen to be gripped in a testing frame. The 25 mm strips of sandwich materials were peeled using an Instron Universal 9800R universal testing machine. The T–peel specimen is shown in Figure 3.14.

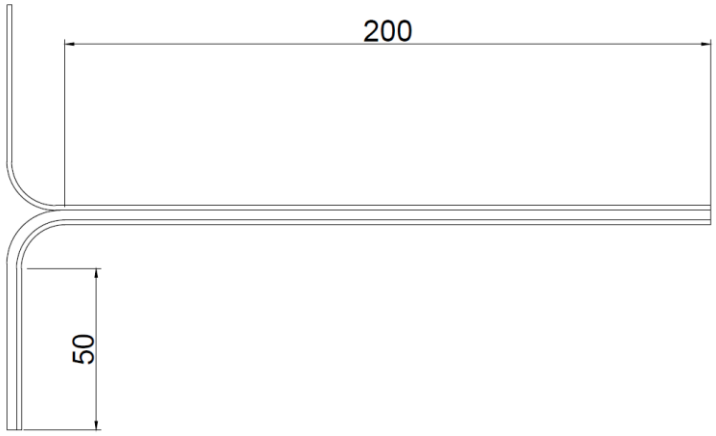

Figure 3.14 – T Peel specimen geometry. Specimen width is 25 mm. All dimensions are in millimetres.

In order to optimise the bond strength parameters including; peak metal temperature (PMT) seen by the adhesive, lamination temperature of the sandwich and lamination time were investigated, this is discussed further in Chapter 4.

3.3 Crash structure production method

The overall method for the production of crash structures from flat sheets of sandwich material or monolithic metal is described in Figure 3.15. Flat sheets were bent into a top hat shape. Top hats were then joined to either another top hat or a flat backplate using either blind rivets, self–pierced rivets or resistance spot welds.

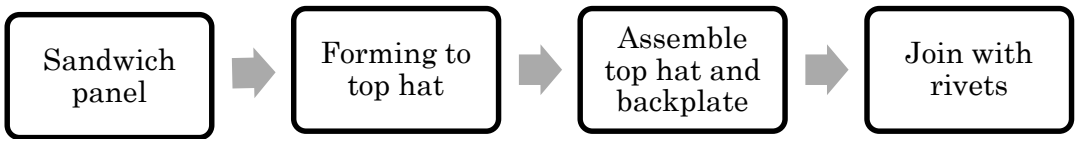

Figure 3.15 – Process for producing crash structures from sandwich panels.

In order for the crash tests to be as comparable as possible, a fixed geometry was chosen for the ECCS and DPSW sandwich materials, as well as the monolithic materials. The ECCS and DPSW crash structures were produced as a single hat structure, which is most representative of the current state of the art automotive longitudinal member. The chosen geometry required approximately 10 kJ of energy to fully deform the monolithic aluminium crash structures. The top hats were formed using press brake bending. An addendum to this is, due to the difficulty in producing a satisfactory bond between adhesive and steel in the DPSW material (discussed in Chapter 4), adhesive failure was observed in the top hat when press brake bending due to the low bond strength. Therefore, another method of top hat production was sought; the chosen method was heated press forming. The heated and pressed crash structure is of a different geometry to the press brake bent hats.

For the Steelite sandwich material, the energy absorbed was low in comparison to the energies provided by the drop tower (discussed in Section 3.7) therefore, a

larger double hat geometry was produced using press brake bending in order to operate in a higher energy range of the drop tower.

3.3.1 Top hat formation – Press brake bending

Press brake bending was used to produce top hats (sandwich and monolithic). The press brake method allowed the production of square–sided components, which can be clamped into a fixture more readily for testing; the method is shown in Figure 3.16. Press brake bending also provided the freedom to produce a geometry without having to remanufacture tooling. This allowed the inner surface of the crash structure to be the same geometry independent of material thickness, reducing the amount of tooling required for mounting crash structures for testing.

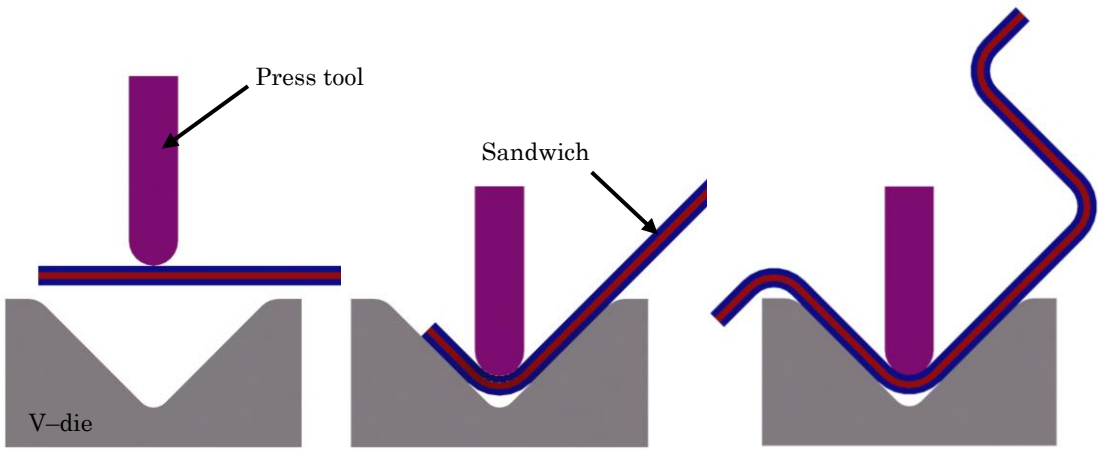

Figure 3.16 – Press brake bending of sandwich materials into top hat structures.

The geometries produced using press brake bending are shown in Sections 3.3.1.1 and 3.3.1.2.

Due to the method of manufacture, there is an inherent variability in the finished top hat structure. The positioning of the sheet for bending is computer numerically controlled (CNC) which allows repeatable positioning of the sheet material for bending. However, the setup of the machine for each bend is performed manually, as is the standard procedure. Additionally, manual inspection using a square edge is performed to judge whether a corner had been pressed to 90°, this also increases the variability in the folded top hat part. This led to a dimensional tolerance on the crash structures of ±10 % in both monolithic and sandwich materials.

3.3.1.1 Single hat geometry

A single hat geometry of 77 mm × 58.5 mm was used for the ECCS sandwich, DP600 sandwich (DPSW) and the monolithic materials, Figure 3.17.

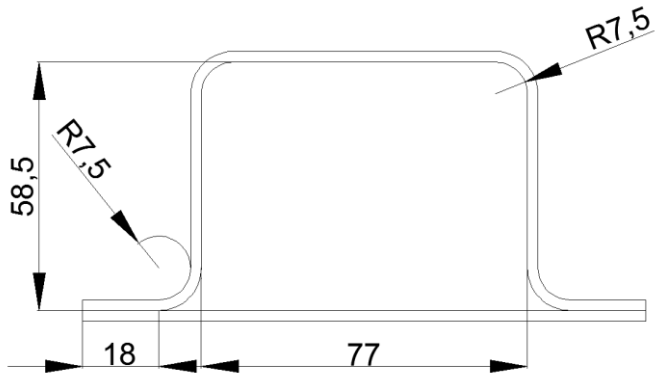

Figure 3.17 – Single hat crash structure geometry. Dimensions are in millimetres, angles are 90°.

3.3.1.2 Double hat geometry

The double hat geometry used for the Steelite materials (in all thicknesses) was 80 mm × 80 mm, Figure 3.18.

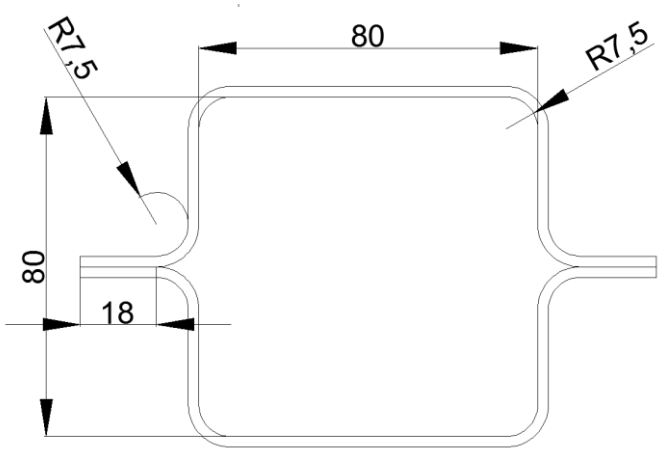

Figure 3.18 – Double hat crash structure geometry. Dimensions are in millimetres, angles are 90°.

3.3.2 Top hat formation – Heated stamp forming

Due to the difficulties in press brake bending the DPSW material a press–formed version was also produced. This was accomplished by reheating the DPSW material to at least 200 °C to soften the polypropylene core for stamp forming in an existing matched tool on an Enefco 500 tonne extrusion press. The softened core allows shear through the core without any strain imparted on the adhesive other than the forming strain on the steel. This method produced top hats without adhesive failure. However, the top hats are of a different geometry to that originally intended.

The press–formed top hat geometry, Figure 3.19, is smaller than the press brake bent single hat, Figure 3.17. A single top hat structure was still produced instead of a double top hat due to the strength of the sandwich material, as a double top hat would have required more energy to absorb than the drop tower is able to provide.

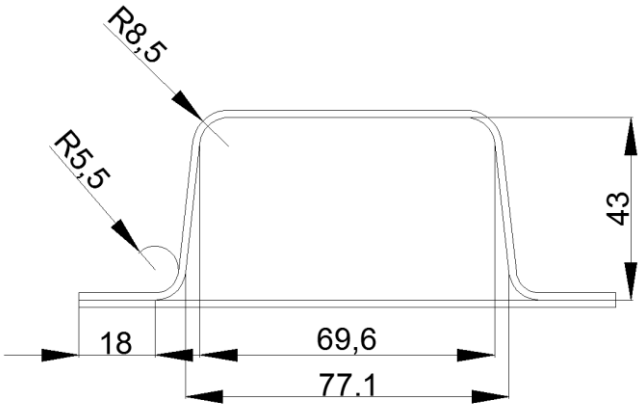

Figure 3.19 – Press–formed DPSW single top hat. Dimensions are in millimetres.

3.3.3 Crash structure assembly – Joining

Three types of joints were used to assemble the crash structures, the conventional blind rivet used to join all sandwich materials, self–pierced rivets (SPR) used to join sandwich materials and aluminium alloys, and finally resistance spot welds (RSW), which were only used to join the 1.6 mm DP600 material.

The monolithic metals were both joined using the conventional process used in the automotive body–in–white to join the respective materials [8], [9]. The use of RSW was not possible with sandwich materials due to the insulative properties of the polymer core. The use of SPRs was not possible with the Steelite and ECCS sandwich materials due to the thickness of the individual steel skins. There is a criterion for the minimum amount of material below the rivet after interlocking of the rivet with the bottom sheet [10]; the Steelite and ECCS sandwich materials do not meet this. Therefore, the joint used was one, which would perform as well as an automotive joint, the blind rivet. The DPSW was successfully joined using SPRs since the skin steel was thick enough to allow the rivet to interlock both sheets of the sandwich.

The sole function of the joining method was to spot–joint the material together. Therefore, the joining method, which was suitable for the purpose and most appropriate for the material was used. Allowing material behaviour to be studied as opposed to joint behaviour, since the intention was to have joints that did not fail and were all in the same position.

3.3.3.1 Joint placement – Single hat crash structures

All of the single hat structures were produced with the same spot–joint placement, Figure 3.20. This is not always ideal for all the crash structures as material thickness affects the folding wavelength. However, since the focus of this work was

material performance and not joint performance it was only important to have a joint, which did not fail hence maintained contact until the fold was produced.

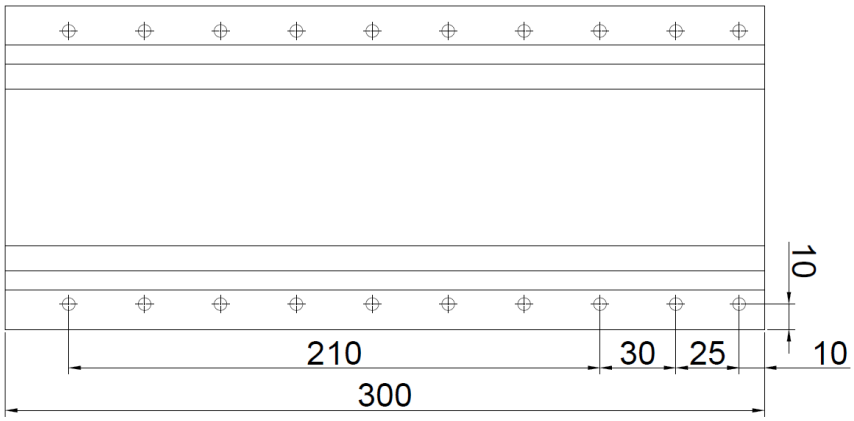

Figure 3.20 – Joint placement on flanges of the single hat crash structure. The impacted end is on the right.

3.3.3.2 Joint placement – Double hat crash structures

The Steelite double hat crash structures were joined using blind rivets. The placement of the rivets into the Steelite material was the same as in the single hat crash structures (Section 3.3.3.1). Figure 3.21 is included for clarity of rivet positioning in the double hat crash structure.

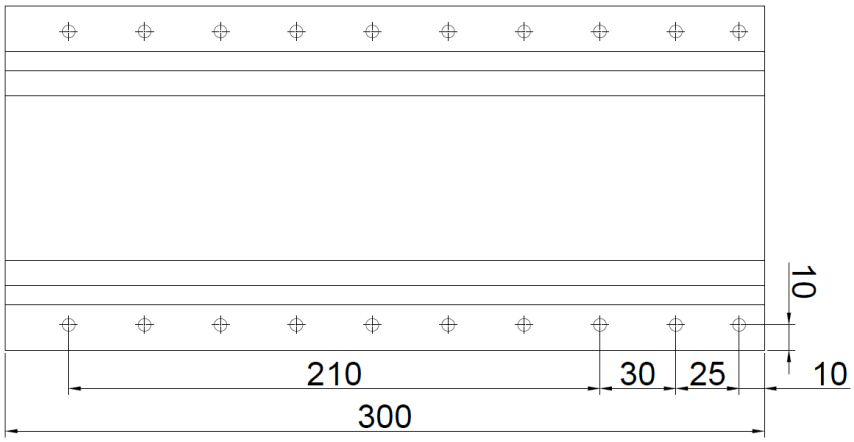

Figure 3.21 – Double hat crash structure showing joint placement in the flanges. All dimensions are in millimetres.

3.3.3.3 Backplate manufacture and manual blind rivet joining

The backplates for all single hat crash structures were machined using a 3–axis CNC milling machine (Datron M7HP). When required, holes for the blind rivets were machined into the backplate (not required for SPR joining). A machined backplate for blind riveting is shown in Figure 3.22.

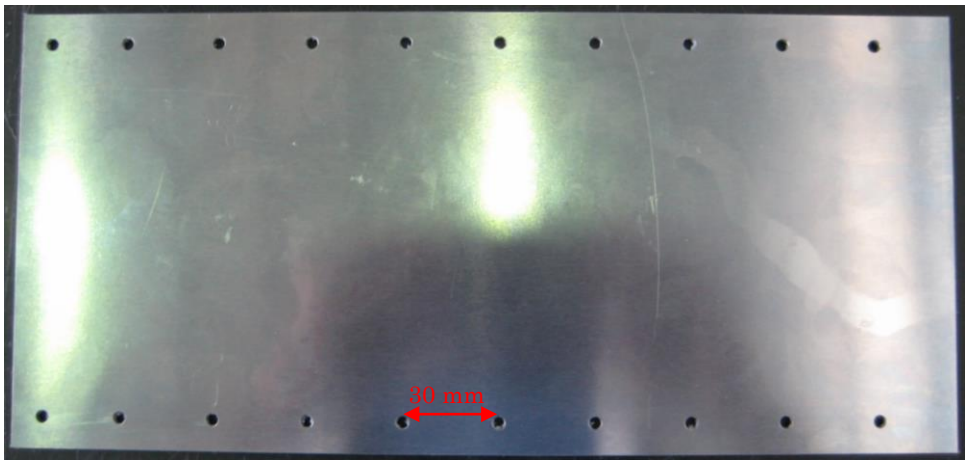

Figure 3.22 – Backplate machined using Datron M7HP CNC milling machine, holes for blind rivets CNC machined.

For blind riveting, the backplate (with pre–drilled holes) was clamped in place on a top hat, with the holes in the backplate used as a template to drill the rivet holes into the top hat, Figure 3.23. This was performed manually using a Hitachi DV180 pistol drill.

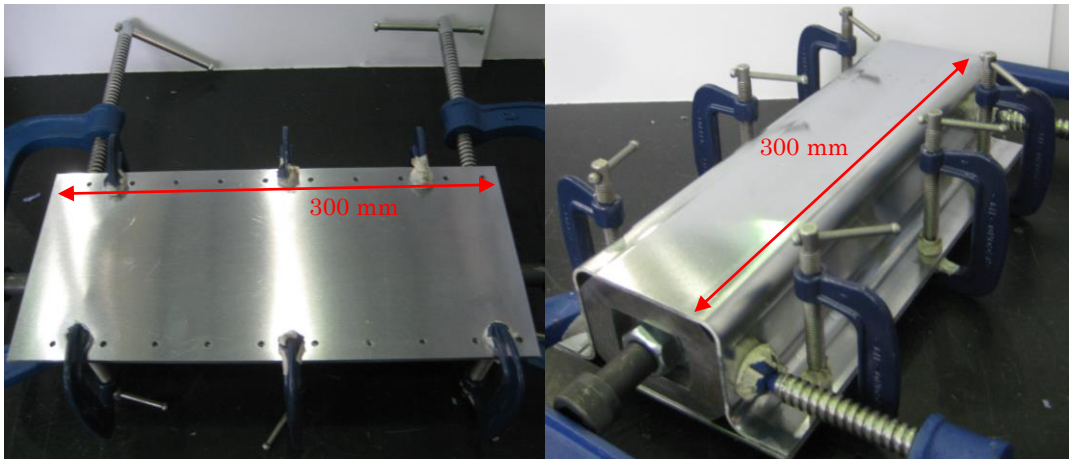

Figure 3.23 – Single top hat clamped to machined backplate, left shows the view from which the top hat was drilled. Right shows the top hat side, the clamps and centre plug at the fixed end.

The clamps were kept in place until the top hat and backplate were riveted together using an Avdel Genesis nG2 rivet tool and Avdel Avinox BE61 stainless steel rivets [11]. Figure 3.24 shows riveted ECCS sandwich crash structures, all three thicknesses are shown.

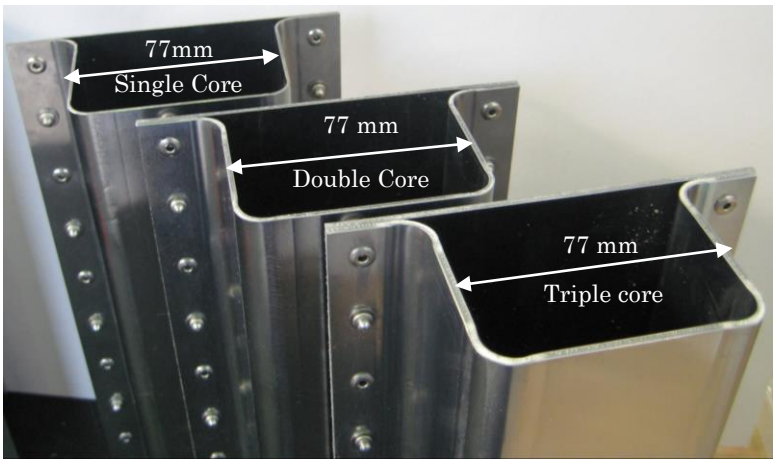

Figure 3.24 – Finished crash structures in ECCS sandwich, Single, double and triple core sandwiches (back to front). Internal geometry of crash structures is the same size, 77 mm × 58.5 mm.

For the Steelite sandwich double hat structure, a steel template and scribe was used to mark the hole positions on one of the top hats, the holes were again manually drilled. The drilled top hat was clamped to a top hat without holes and the holes drilled through. Due to the low strength nature of the Steelite materials, it was not necessary to use high strength rivets, therefore 3.2 mm diameter POP® aluminium rivets (model number – TAPD46BS) were used instead of stainless steel rivets.

3.3.3.4 Self–pierced riveting (SPR) joining

SPR joining was used to assemble the aluminium alloy single hat crash structures, the joint positions are shown in Figure 3.20. SPR joining is currently the conventional method used in the automotive body–in–white. SPR joining was performed using a Tucker SPR gun and Tucker 5.3 mm diameter × 7.0 mm long SPRs (Figure 3.25 – image 1) for the aluminium alloys.

Due to the thickness of the steel used in the DPSW sandwich material, SPR joining was also used to assess the applicability of the SPR for MPM sandwich crash structures. The result for the DPSW material was the use of 5.3 mm diameter × 6 mm long rivets, instead to prevent the rivet puncturing both sheets of sandwich material. Additionally, a die with a dimpled surface was found to better flare the rivet into the sandwich material, allowing for a better interlock, Figure 3.25 – image 2.

Parameters for an optimal joint were found by method of comparative visual inspection of the joint, once parameters were found which could be suitable, lap shear and T–peel tests were performed to find the strongest joint. This process was performed for the AA5754, AC300–T61 and the DPSW.

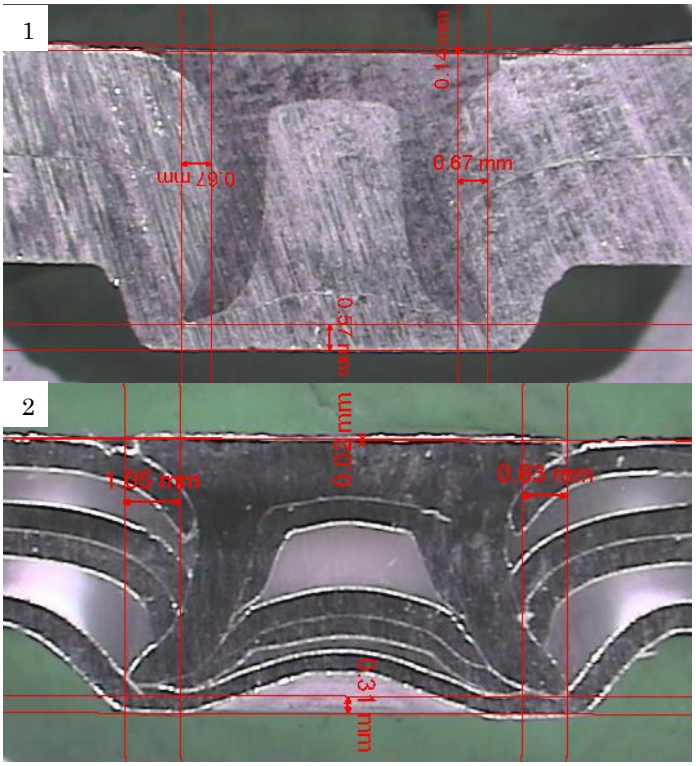

Figure 3.25 – Image 1 – Cut section of self–pierced rivet joining two sheets of AA5754 aluminium alloy. Image 2 – Cut section of self–pierced rivet joining two sheets of DP600 sandwich material.

Figure 3.25 – image 2 shows the riveted DPSW material, where the lower sandwich sheet interlocked with the rivet. With the thinner steel skins (Steelite and ECCS), there is not enough remaining thickness in the sandwich once the rivet is set.

3.3.3.5 Resistance spot weld (RSW) joining

The monolithic DP600 steel crash structures were assembled using RSW, the joint positions are shown in Figure 3.20. This is the conventional method of joining steel in the automotive body–in–white. It is possible to join steels with SPR joints; however, due to the hardness of the DP600 steel used it was not possible. The RSW joint was produced by a manually operated resistance spot welder, a nylon jig was used to position the welds. The joint was found to be successful since chisel peel tests of the joint showed the weld to be stronger than the parent material, a method widely used to ensure successful welding production [12].

3.3.3.6 Influence of joining techniques

As described previously, different joining techniques were used to join top hats to back plates for different materials. Monolithic steel was joined using resistance spot welds, aluminium alloys were joined using self–pierced rivets and sandwich materials were joined using blind rivets predominantly, however, one set of tests were performed using self–pierced rivets.

The function of the joining method chosen was to provide a spot–joint to assemble the crash structure, and the joints did not fail in a manner, which would alter the loading of the crash structure. Therefore, the results will show the differences in material performance and not joining technology.

3.4 Summary of tests

The finalised crash structure geometries and the forming and joining methods used are summarised in Table 3.2.

Table 3.2 – Geometry, forming methods and joining method used for the production of crash structures.

Sandwich	Geometry	Forming method	Spot– joint
Steelite single core	80 × 80 mm	Press brake bending	Blind rivet
Steelite double core	80 × 80 mm	Press brake bending	Blind rivet
Steelite triple core	80 × 80 mm	Press brake bending	Blind rivet
ECCS single core	77 × 58.5 mm	Press brake bending	Blind rivet
ECCS double core	77 × 58.5 mm	Press brake bending	Blind rivet
ECCS triple core	77 × 58.5 mm	Press brake bending	Blind rivet
DP600 single core	77 × 58.5 mm	Press brake bending	SPR
DP600 single core	N/A	Heated press forming	Blind rivet
Monolithic materials			
DP600	77 × 58.5 mm	Press brake bending	Spot weld
AA5754	77 × 58.5 mm	Press brake bending	SPR
AC300-T61	77 × 58.5 mm	Press brake bending	SPR

3.5 Tensile testing

Tensile testing was performed on all materials in order that accurate material data be used for finite element modelling. This was carried out on an Instron 5800R Universal Testing Machine, a screw driven 100 kN testing frame.

The test method used for testing metals and the assembled MPM sandwich materials was ISO6892–1. The geometry of the test specimen is shown in Figure 3.26. A 50 mm clip on extensometer was used for strain measurement.

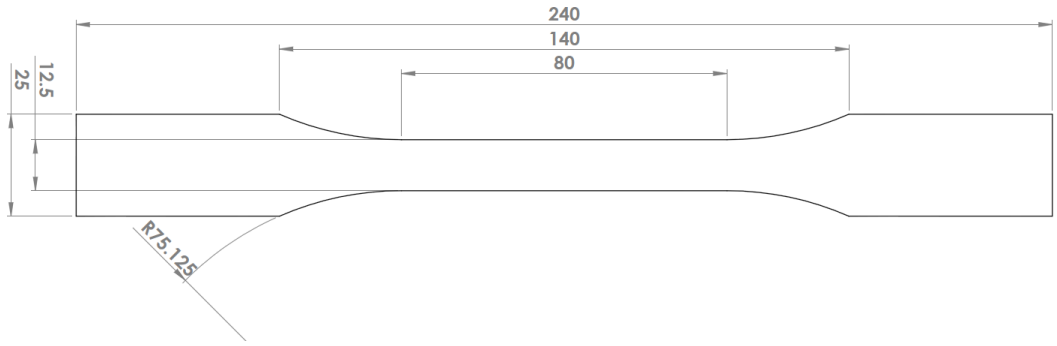

Figure 3.26 – Metallic dogbone tensile test geometry to ISO6892–1 standard.

In order to determine the elastic modulus, tests were conducted in the elastic region at 0.7 mm.min^{-1}. To produce a smooth singular plastic flow curve for finite element analysis input, tests at 32.16 mm.min^{-1} were performed.

The testing method used to ascertain the material properties of the polypropylene core was ISO527–3. The geometry chosen was for polymers which undergo large strains to failure (Figure 3.27). The testing speed was 1 mm.min^{-1} throughout. The strain was measured using a 25 mm virtual extensometer with digital image correlation software.

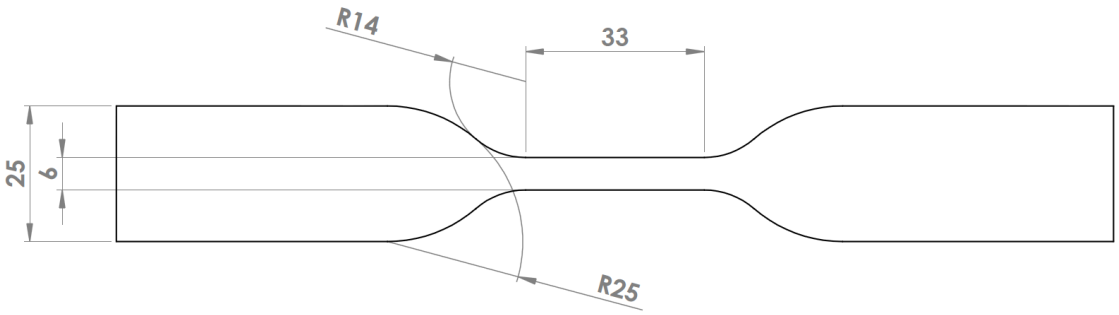

Figure 3.27 – ISO527–3 specimen geometry for polymers that undergo large strain to failure.

3.6 Quasi–static crush testing

Quasi–static end–wise crush testing experiments were performed on the crash structures using two testing frames. The Steelite sandwich materials crash structures were tested on the Instron 5800R universal testing frame, the same used for tensile testing, with its 100 kN load limit. The ECCS and DPSW sandwich materials as well as the monolithic steel and aluminium alloys were tested on a 250 kN Dartec testing frame, as the 100 kN load limit was not sufficient to accommodate the peak force experienced by the crash structures. As the Dartec frame has a 100 mm stroke limit, the crash structures were crushed twice to achieve a 200 mm displacement.

3.7 Dynamic testing

Dynamic (impact) tests were performed on a 11.5 kJ Instron drop tower, Figure 3.28. The drop tower has a 500 kN load cell fixed to a 75 mm thick steel plate. The drop tower is spring assisted, the free drop height of the carriage is approximately 0.7 metres above the impact surface of the load cell and above this height, spring–assistance is used to attain the remainder of the energy.

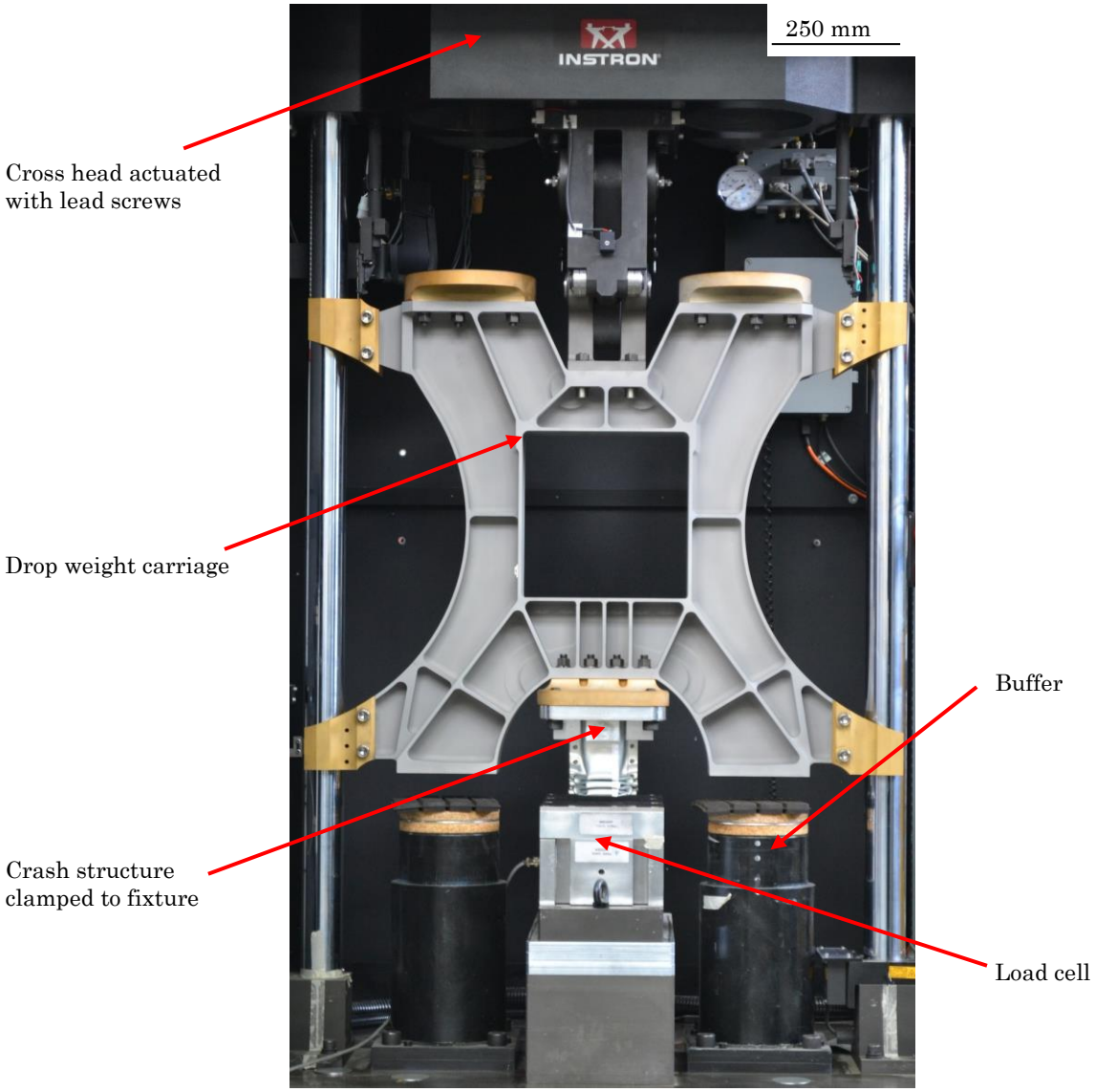

Figure 3.28 – 10.5 kJ Instron drop tower.

The drop weight carriage has a mass of 70.77 kg, when a fixture and crash structure are included this increases to approximately 80 kg in all cases.

The crash structure was rigidly clamped to the carriage. The crosshead hooks the carriage and loads it into the springs. The cross head was actuated using two motor driven lead screws. If the energy imparted is greater than the specimen can absorb, the buffers absorb the extra energy.

The drop tower is able to perform impact tests up to 17 $m.s^{-1}$ or (approximately 40 miles per hour), this is the speed at which vehicles are tested by the New Car Assessment Programme (NCAP) to assess a car's crash safety performance (previously discussed in Chapter 1).

3.8 Crash structure fixture

In order to clamp the crash structures in the same manner when testing on different machines (i.e. Instron frame, Dartec frame and Instron drop tower) self–designed fixtures were made.

The double top hat crash fixture, used for the Steelite (single, double and triple core) crash structures, was made with an 80 mm × 80 mm internal geometry, Figure 3.29. The clamping blocks incorporate a slot for the flanges to reside.

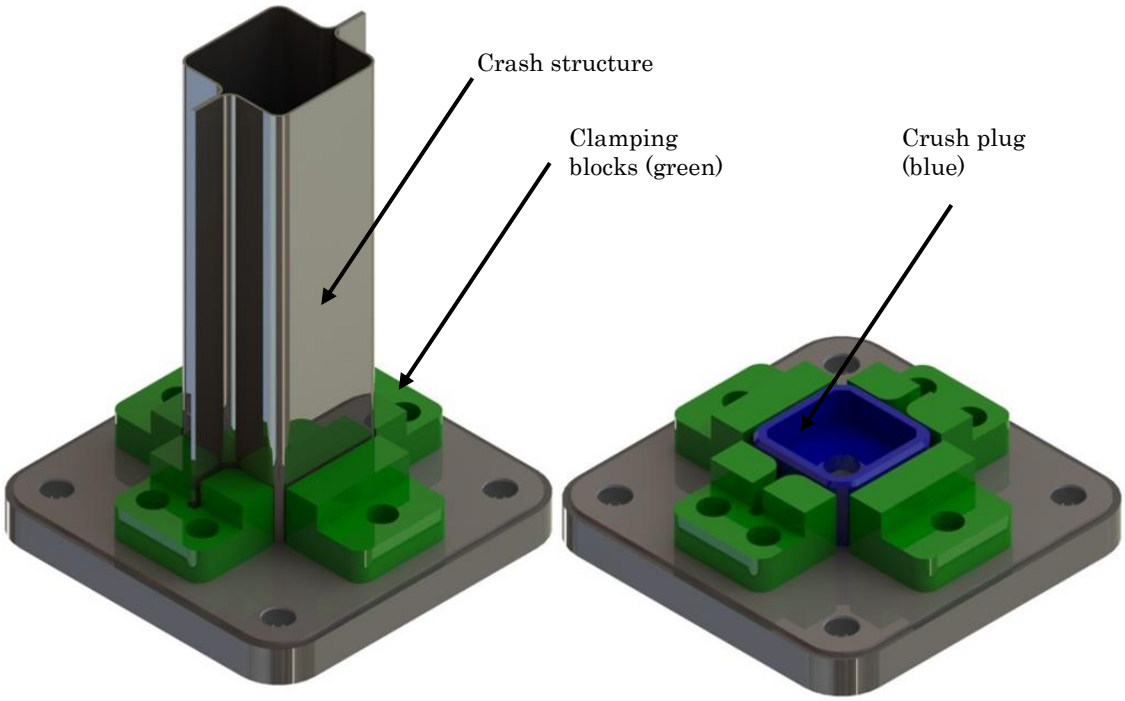

Figure 3.29 – Fixture for clamping the double top hat Steelite crash structures. Crush plug is 80 mm × 80 mm in size.

The single hat crash fixture was used for the 58.5 mm × 77 mm single top hat crash structures, Figure 3.30. The materials tested in this geometry were the DPSW (single core), ECCS (single, double and triple core), DP600, AC300–T61 and AA5754 materials.

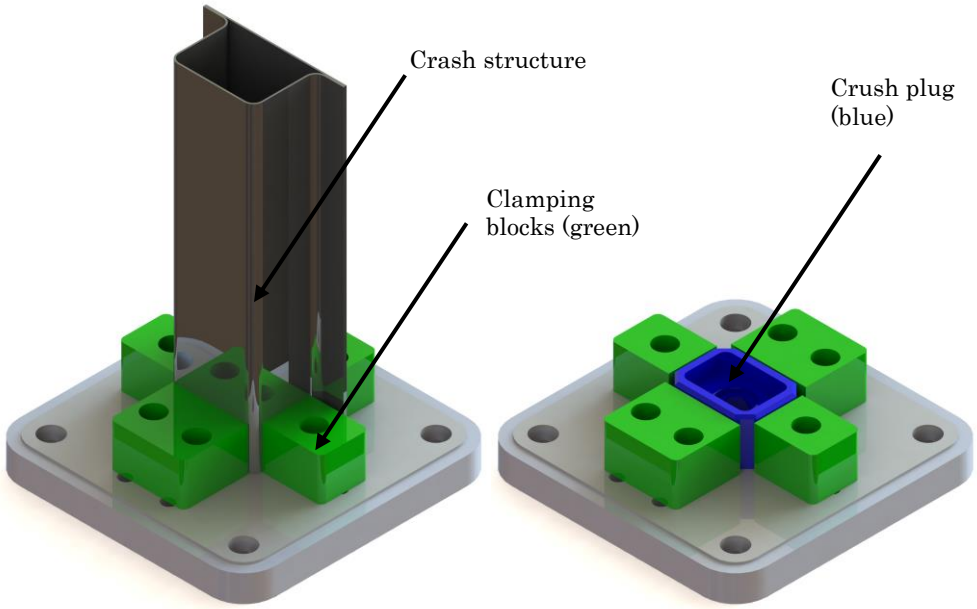

Figure 3.30 – Fixture for clamping press brake bent single top hat crash structures. Crush plug is 77 mm × 58.5 mm in size.

The pressed and heated single top hat crash fixture (not shown) is the same as the press brake bent single top hat structure (Figure 3.30). The smaller side clamping blocks were omitted and a centre plug matching the internal geometry of the crash box was instead used.

3.9 Mathematical description of drop testing

On the Instron 10.5 kJ drop tower, for very low energies, a drop test can be performed using gravity alone. This gives around 0.5 kJ of impact energy, according the gravitational potential energy (Equation 3.1).

$$PE = m \cdot g \cdot h \qquad \text{Equation 3.1}$$

Where, PE = Potential energy (J)

m = Drop weight mass (kg)

g = Gravitational acceleration ($m.s^{-2}$)

h = Drop height (m)

Above the free drop potential energy (PE), the additional energy is provided by the springs (Equation 3.2).

$$SE = \frac{1}{2} k \cdot x^2 \qquad \text{Equation 3.2}$$

Where, SE = Spring energy (J)

k = Spring constant ($N.m^{-1}$)

x = Spring displacement (m)

It is noteworthy that spring compression also has a small addition of height (equal to the spring displacement), which increases the gravitational potential energy (PE) and is accounted for in the energy calculation (see Equation 3.3 and Equation 3.4). Equation 3.4 is used to set the height to which the drop carriage was moved to for testing.

$$Impact\ energy = PE + SE \qquad \text{Equation 3.3}$$

Therefore, $$Impact\ energy = m \cdot g \cdot (h + x) + \frac{1}{2} k \cdot x^2 \qquad \text{Equation 3.4}$$

However, the actual energy (kinetic energy, KE) at impact was calculated from the light gate velocity at impact using Equation 3.5. This was due to the variability in the release of the drop weight, causing inconsistent release velocity.

$$KE = \frac{1}{2} m \cdot V^2 \qquad \text{Equation 3.5}$$

Where, KE = Kinetic energy (J)

m = Drop weight mass (kg)

V = Impact velocity ($m.s^{-1}$)

3.9.1 Drop testing uncertainties

The inconsistent impact velocity, although an inconvenience was accountable. Since the impact velocity could be confirmed by means of a light gate. However, from the calculated energy at impact (according to Equation 3.5), it could be seen that the energy absorbed in terms of the force–displacement data from the test was in all cases lower than the input energy. The amount varied from test to test; however, it was no more than 6% under the intended value.

The difference between the imparted energy at impact (according to the impact velocity) and the absorbed energy by the crash structure (according to the force–displacement data) is accounted for by losses in the system. These include noise and vibration production when the crash structure contacts the load cell. Additionally, heat is produced from the sliding of the crash structure on the load cell surface. These methods of energy absorption would not be accounted for in the load data.

3.10 References

[1] T. H. Muster, A. K. Neufeld, and I. S. Cole, "The protective nature of passivation films on zinc: wetting and surface energy," *Corros. Sci.*, vol. 46, no. 9, pp. 2337–2354, Sep. 2004.

[2] British Standards Institute, "BS EN ISO 527-1 2012 Plastics -- Determination of tensile properties -- Part 1: General Principles," 2012.

[3] D. Wowk and K. Pilkey, "Effect of prestrain with a path change on the strain rate sensitivity of AA5754 sheet," *Mater. Sci. Eng. A*, vol. 520, no. 1–2, pp. 174–178, Sep. 2009.

[4] Rohm and Haas, "MO-RAD M801 Technical Data Sheet (TDS)."

[5] TMC Hallcrest, "Thermax 10 Level Strips," 2006. [Online]. Available: http://www.tmchallcrest.com/industrial.php?medical_product=68&sublvl_id=5&subcat_id=6#. [Accessed: 14-Mar-2013].

[6] Schott & Meissner Maschinen- und Anlagenbau GmbH, "Thermofix double belt press laminator." [Online]. Available: http://www.schott-meissner.de/Thermofix-Double-Belt-Press.33+M52087573ab0.0.html.

[7] British Standards Institute, "BS EN ISO 11339:2010 - Adhesives. T-peel test for flexible-to-flexible bonded assemblies," British Standards Institute, 2010.

[8] T. Barnes and I. Pashby, "Joining techniques for aluminium spaceframes used in automobiles," *J. Mater. Process. Technol.*, vol. 99, no. 1–3, pp. 62–71, Mar. 2000.

[9] T. Barnes and I. Pashby, "Joining techniques for aluminium spaceframes used in automobiles," *J. Mater. Process. Technol.*, vol. 99, no. 1–3, pp. 72–79, Mar. 2000.

[10] L. Han, M. Thornton, D. Li, and M. Shergold, "Effect of Setting Velocity on Self-Piercing Riveting Process and Joint Behaviour for Automotive Applications," Apr. 2010.

[11] Stanley Engineering Fastenings, "Avdel Avinox BE61 rivets." [Online]. Available: http://www.avdel-global.com/en/products/breakstem-fasteners/avinoxr.html.

[12] L. Han, M. Thornton, D. Boomer, and M. Shergold, "A correlation study of mechanical strength of resistance spot welding of AA5754 aluminium alloy," *J. Mater. Process. Technol.*, vol. 211, no. 3, pp. 513–521, Mar. 2011.

4 Material production results

This chapter details the results of the sandwich material production optimisation described in Chapter 3 – Materials and methods. The method of sandwich material production involves coating two sheets of steel skin material with an adhesive layer on one side. This adhesive is then cured in an oven at elevated temperature (260 °C oven temperature). The two sheets of sandwich material are then assembled with the polymer core and reheated to around 200 °C to bond the polymer core with the adhesive layer (described in greater detail in Chapter 3). This process allowed for a degree of process variability, therefore these variables had to be controlled and optimised. The variables to be optimised were the temperature to which the adhesive was cured (peak metal temperature), and the lamination temperature and time when assembling the sandwich. The optimised process is therefore discussed in this chapter.

4.1 Optimisation of Steelite sandwich material production

Steelite steel skin material was supplied by Tata Steel pre–coated with MO–RAD M801 adhesive primer. Therefore, only assembly and lamination was required to produce the sandwich material. Lamination of Steelite sandwich materials was performed using vacuum bagging, the vacuum bagging process is described in Chapter 3.

4.1.1 Optimisation of process

In order to determine a suitable lamination temperature, temperatures between 190 to 210 °C were examined at 10 °C increments. In order to determine the temperature within the sandwich a thermocouple was placed inside a separate smaller piece of sandwich material (100 mm × 100 mm) within the vacuum bag, which was used as the internal standard. The same method was used for all materials made. Three repeats panels were produced at each temperature, and five tests performed on each panel.

The results for the peel tests to ascertain the best lamination temperature are shown in Table 4.1. The force, range and standard deviation of the peel force at 210 °C were the best suggesting greater repeatability and bond strength in the material produced at this temperature.

Table 4.1 – Peel force results for the Steelite sandwich materials laminated at different temperatures. The results shown are the average force across the length of the peel (mean force), the standard deviation of the peel forces (S.D.) and the range of the results from the maximum result to the minimum result.

Temperature / °C	Mean force /N	S.D. /N	Range /N	Force per unit width /N.mm^{-1}
190	102.3	11.8	37.2	4.1
200	92.2	18.9	53.3	3.7
210	112.7	5.3	12.8	4.5

The bond failure seen in the Steelite at all lamination temperatures was the same, an interfacial failure. The adhesive peeled from one of the steel skins showing superior bonding to the polymer core compared to the steel, Figure 4.1.

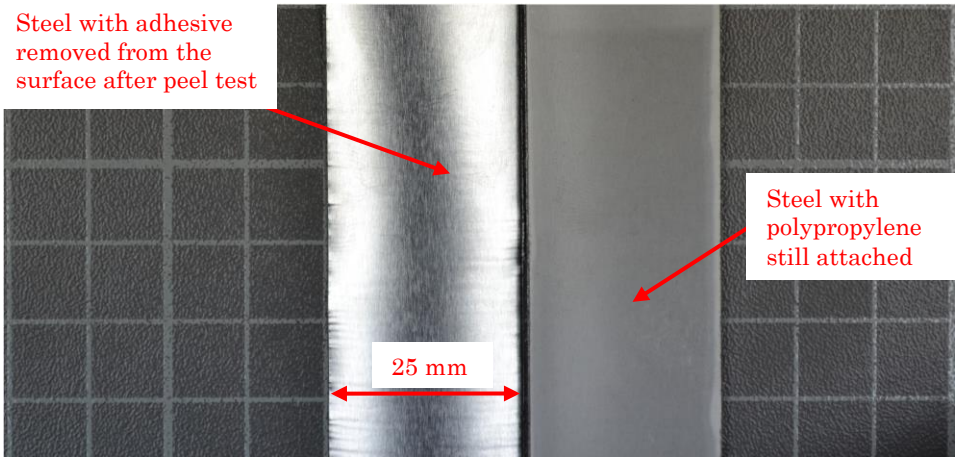

Figure 4.1 – T–peel specimen of the Steelite sandwich, showing the adhesive failure of the sandwich material.

In order to assess the suitability of the bond strength achieved, laminated Steelite sandwich material was formed around a 15 mm diameter bar using press brake bending equipment, the press braking process is explained in Chapter 3. This test ensured whether a crash structure was producible from the material. The sandwich materials did not exhibit any failure in the adhesive bond; therefore, an increase in bond strength was not pursued.

4.2 Optimisation of ECCS sandwich material production

The ECCS steel was received without the adhesive pre–applied and subsequently coated with MO–RAD M801 adhesive with a wet film thickness of 30 μm, using the process described in Chapter 3. The steel was first degreased using methyl ethyl ketone (MEK) removing any contaminants from the chrome coated surface, as recommended by the manufacturer TDS [1]. The failure type achieved when peel tested was a cohesive failure with a bond strength of 25 $N.mm^{-1}$, the maximum suggested by the adhesive manufacturer [1]. Cohesive failure was observed, which

meant that the bond of the adhesive to both the steel and core was strong enough to cause the polypropylene core to fail. Figure 4.2 shows cohesive failure in the ECCS sandwich when peel tested.

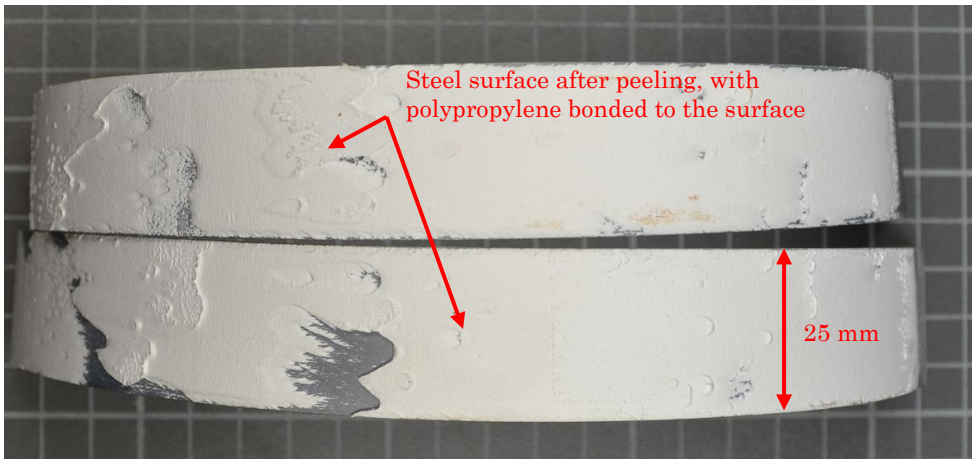

Figure 4.2 – Cohesive failure of the ECCS steel sandwich. Failure can be seen through the polypropylene core rather than at the steel–adhesive interface.

The chosen method of production for the ECCS sandwich was heated lamination, described in Chapter 3.

In order to determine optimal conditions for the heated lamination of ECCS sandwich material, the peak metal temperature (PMT) and lamination time were investigated. The lamination temperature used was 210 °C as per the Steelite lamination temperature, previously found in Section 4.1.1. The lamination time was first set to 60 seconds while changing only the PMT. The highest peel force and most consistent results (i.e. lowest standard deviation) was observed at a PMT of 241 °C, Figure 4.3, according to the temperature indicator strip measurement method described in Chapter 3.

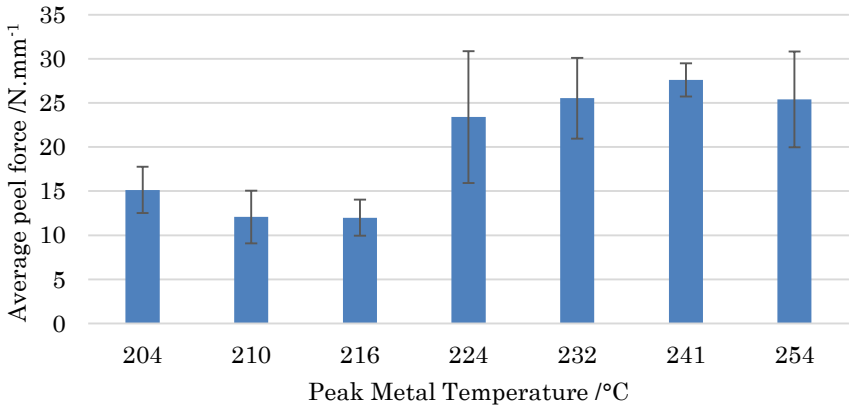

Figure 4.3 – Change in peel force with increasing Peak Metal Temperature (PMT).

Subsequently, while the PMT for the adhesive curing process was maintained at 241 °C, according to the temperature indicator strip, the lamination time for the sandwich assembly was modified. Interestingly, no significant difference in peel force was observed at lamination times between 30 and 120 seconds, Figure 4.4. This suggested that once the polypropylene core was heated to 210 °C, the bond between the core and the adhesive was produced. Thus, 90 seconds lamination time was used as it exhibited the lowest standard deviation. Further, the strength of the bond was consistent with a cohesive failure mode in all cases, Figure 4.2.

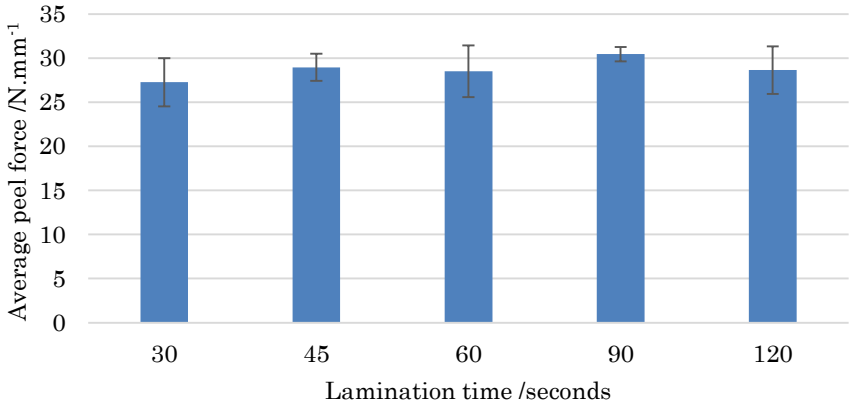

Figure 4.4 – Changing the lamination time for the ECCS sandwich with a fixed PMT of 241 °C.

Thus, by varying the PMT and lamination time for the heated lamination process of ECCS steel, appropriate curing conditions were determined to be a 241 °C peak metal temperature. The adhesive cure time was set to 60 seconds. For lamination

of the sandwich, the oven temperature was fixed to 210 °C as per the Steelite sandwich lamination, and a 90 second lamination time chosen to produce the assembled sandwich.

4.3 Optimisation of DP600 sandwich material production

The DP600 sandwich (DPSW) was also produced using heating lamination, the process is described in Chapter 3.

Initially, to ascertain whether the bond strength of MO–RAD M801 adhesive to the galvanised DP600 steel was sufficient, panels were made and press brake bent (process is described in Chapter 3) to determine if the material was able to form a crash structure. The steel was first prepared by degreasing with acetone and MEK. The level of mill scale on the steel was significant, and MEK alone was not able to remove it. The steel was found to peel away from the adhesive during pressing and thus a greater bond strength was sought. Therefore, methods to improve the adhesive bond are considered in the following section.

4.3.1 Surface preparation

In order to determine the influence of the steel's (DP600) zinc surface on the adhesive bond strength, the surface of the steel was prepared using a range of methods, shown in Table 4.2. The PMT was fixed to 241 °C as it produced the highest bond strength in the ECCS sandwich.

In the first two methods, the surface was first etched using sulphuric acid to remove the zinc coating of the steel and then cleaned with either xylene or acetone and propan–2–ol (IPA). In methods 3–5, the surface was abraded and cleaned to remove the zinc oxide layer and then degreased. In methods 6–9, the steel surface was treated with an iron phosphate solution; this is known as conversion coating or passivation. The phosphate solution reacts with the zinc to produce zinc

phosphate, to increase the adhesive bond strength. Method 6 has a passivated zinc surface, in method 7 the passivation was performed after the surface was abraded. After passivation, a polymer coating was applied to the top surface in method 8. In method 9, the passivated surface was degreased using xylene (the main solvent in the adhesive).

Table 4.2 – Methods attempted to improve the adhesive bond strength.

Method	Description of action taken
1	Etch using sulphuric acid to remove zinc, abrade surface with 180 grit sand paper, clean and degrease with xylene
2	Etch using sulphuric acid to remove zinc, abrade surface with 180 grit sand paper, clean and degrease with acetone and IPA
3	Abrade zinc surface with 180 grit sand paper, clean and degrease using Xylene
4	Clean and degrease zinc surface with acetone and IPA
5	Abrade zinc surface with 180 grit sand paper, clean and degrease with acetone and IPA
6	Phosphate conversion of surface using iron phosphate solution
7	Abrade zinc surface and then apply phosphate conversion of surface using iron phosphate solution
8	Phosphate conversion of zinc surface using iron phosphate solution and then addition of polymeric coating
9	Phosphate conversion of zinc surface using iron phosphate solution, addition of polymeric coating, clean and degrease with xylene

Even after surface treatment, the peel force was low compared to the ECCS and Steelite sandwich materials (over 25 $N.mm^{-1}$ and around 5 $N.mm^{-1}$ respectively), see Figure 4.5. The removal of zinc from the surface (method 1 and 2) had a beneficial effect on adhesive bonding compared to merely cleaning or abrading the steel (methods 3, 4 and 5). The phosphate conversion combined with the addition of a polymeric coat on the steel surface showed the highest peel force (method 8). Degreasing of the passivated surface is not recommended (method 9). It is noteworthy that the peel force is still low at 3.57 $N.mm^{-1}$.

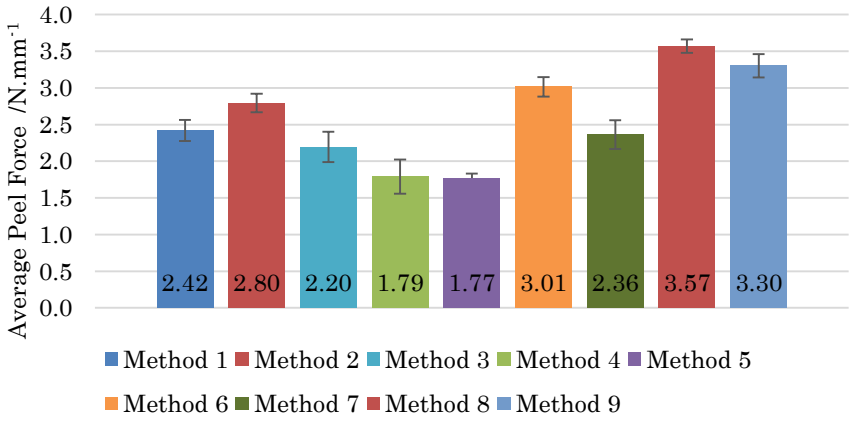

Figure 4.5 – Average peel force for differing methods of steel preparation, errors are the standard deviation of the result.

4.3.2 Optimisation of adhesive curing and sandwich lamination processes

After identifying the best method for surface preparation, the PMT and lamination time were then optimised. No significant pattern with respect to PMT was observed, Figure 4.6. Thus 232 °C was chosen as the optimal PMT, since a high bend strength and lowest variability was obtained. Additionally, the low value at 224 °C would also be avoided.

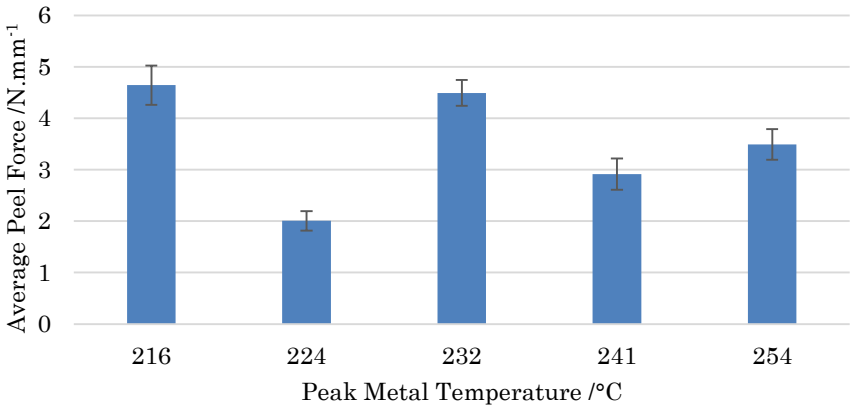

Figure 4.6 – Peel strength of the DPSW material when changing the adhesive curing PMT.

Next, the lamination time was altered to further improve the bond strength. The lamination time was found to have a significant effect on the bond strength, as demonstrated by the resulting peel force, Figure 4.7. The dashed line in Figure 4.7

shows a guide to the eye of the trend in the results. 90 seconds again showed the highest average peel force, but also the greatest variability. It was decided that between 60–180 seconds, the greatest bond strength was achieved.

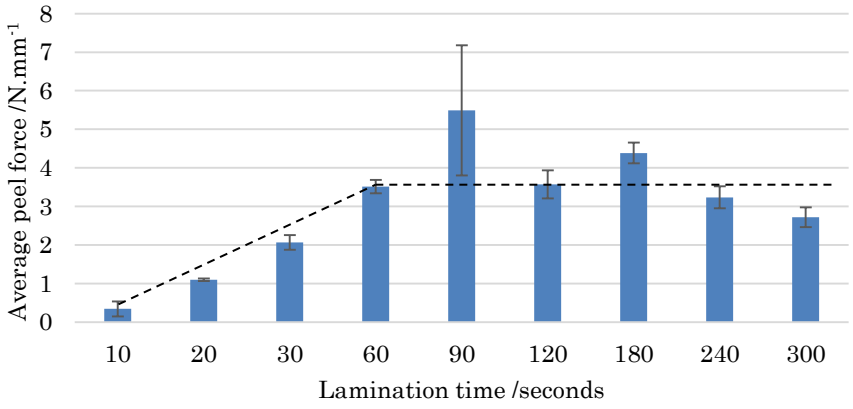

Figure 4.7 – Lamination time vs. peel strength for the DPSW material. The dashed line shows the suggested pattern in the results.

In conclusion, by carrying out a range of experiments, it was determined that the greatest adhesive bonding strength was achieved by first treating the zinc coated DP600 with a phosphate conversion coating and then applying a polymeric layer on top. Adhesive curing at a PMT of 232 °C then followed. Lamination of an assembled sandwich was performed at 210 °C. This temperature showed the most consistency in the case of Steelite sandwich and was therefore used for the DP600 sandwich. The optimal lamination time was determined to be 90 seconds, resulting in an increase in bond strength from 1.8 $N.mm^{-1}$ to 5.5 $N.mm^{-1}$.

4.4 A final note on adhesion

Any further improvement in the adhesion of the DP600 steel was out of scope for the project, which would involve producing a grade of steel with the correct surface treatment. This work has shown a galvanised surface is not recommended for adhesive bonding. A chrome passivation would undoubtedly increase the bond strength as shown by the ECCS steel. However, due to the toxic nature of

chromates it was not possible to find a company in the UK willing to perform chromate conversion coating of a small batch of material.

4.5 Discussion on differences in sandwich production processes

In this work, sandwich materials were assembled using two processes; heated lamination and vacuum bagging. The function of the lamination process is to join adhesive coated steel to a polypropylene core under pressure, at a temperature of 210 °C. Therefore, both the vacuum bagging process and the heated lamination process meet this criteria. There are however differences between these processes which may effect their performance; the lamination pressure applied is different between both processes, whilst the pressure is measurable using a vacuum gauge for the vacuum bagging process it was not measurable for the heated lamination process. Second, the cooling rate applied to the sandwich material to enable amalgamation of the PP core to the PP beads in the adhesive was different in both processes. In the vacuum bagging process, the oven is turned off and it cools naturally to ambient temperature, taking around 30 minutes to reach ambient temperature. Where as in the heated lamination process, active cooling is used to bring the material to ambient temperature in approximately one minute.

These differences had the potential to effect the bond strength of the adhesive, and whilst bond strength differences were seen, this could not be accounted for by the method of lamination alone as there are other differences between the sandwich materials, such as grade, gauge, surface coating and surface treatment of the steel.

4.6 Observations in manufacture

4.6.1 Steelite sandwich

A key learning outcome of the pressing of Steelite sandwich materials was regarding the fracture strain limit of the steel skin and the behaviour of the material at this point. Producing single core (0.7 mm) and double core (1.4 mm) materials proved to be successful. However, due to the thickness of the triple core (2.1 mm), the strain on the outer surface of the bend caused by the larger radius proved to be too great for the steel to withstand. Therefore, in most cases the skin of the triple core material failed on the outer surface of the bend, the failure of the steel did not cause failure of the polymer core. It was decided to impact test the triple core crash structures in order to see what effect this failed outer skin has. The failure of the outer skin after pressing is shown in Figure 4.8.

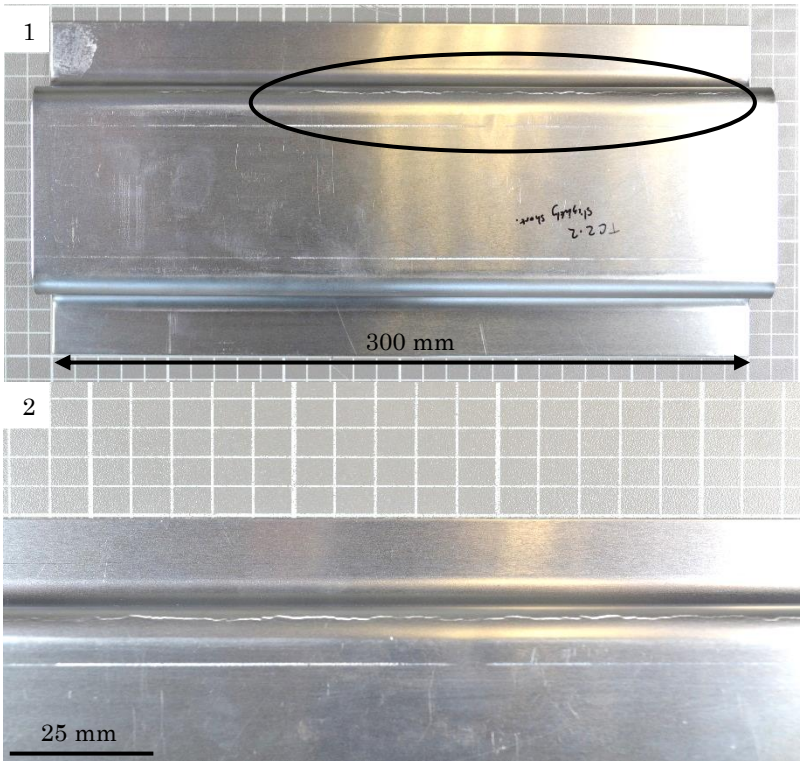

Figure 4.8 – Image 1 – Triple core Steelite material crash structure showing the failure in the outer skin of the steel highlighted with a black circle. Image 2 – Failed skin magnified.

4.6.2 Electrolytically Chrome Coated Steel (ECCS) sandwich

The high adhesive bonding strength seen in the ECCS sandwich material allowed a straightforward production process, where adhesive failure during forming of crash structures was not seen. As a result of the thicker grade of steel, in comparison to the Steelite skin, the ECCS skin could withstand greater elongation before failure. Thus, the skin failure seen when bending the triple core Steelite sandwich did not occur in the triple core ECCS sandwich.

The most noticeable defect in the ECCS sandwich materials when press brake bending was the core crushing along the length of the bent corners, shown in Figure 4.9. In the single core material, Figure 4.9 – image 1, the sandwich was observed to be 30 µm thinner in the bent corner than in the unbent material. For the double and triple core sandwich, Figure 4.9 – image 2 and Figure 4.9 – image 3 respectively, the thickness difference was between 180 and 250 µm. Crushing of the core was most likely due to the increased thickness and strength of the ECCS skin, which required higher pressing forces, and over–bending to produce the 90° corner (after spring back).

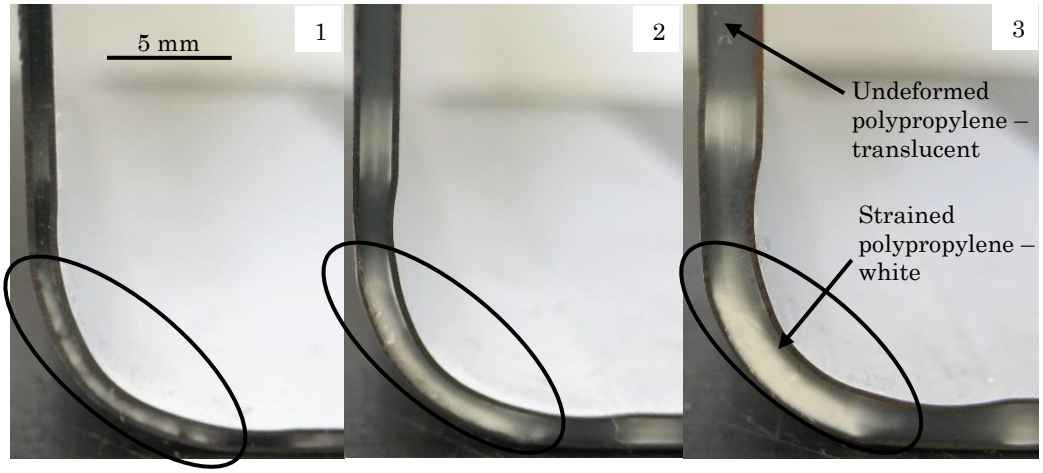

Figure 4.9 – Core crushing in ECCS top hats. Image 1 – Single Core. Image 2 – Double core. Image 3 – Triple core. The increase in core crush with increasing thickness when bent can be seen. Circles indicate the crazing in the polypropylene. The 5 mm scale bar is applicable to all images.

Figure 4.9 also shows strain imparted on the polymer core from the press brake bending process, this is visibly indicated by the crazing in the polypropylene, Figure 4.9 – images 1, 2 & 3 – circles. Crazing being an alignment of a polymer chain after undergoing plastic strain [2], this led to the whitening of the polymer.

4.6.3 DP600 sandwich (DPSW)

4.6.3.1 Press brake bent

The low adhesive bond strength in the DP600 sandwich material led to difficulty in producing top hats. This was further aggravated by the increased thickness and strength of the steel, which led to increased forming forces.

Production of top hats using press brake bending produced only a few successful parts. Without the optimised surface preparation (discussed in Section 4.3.2), the bent sandwich material tended to peel apart, this is shown in Figure 4.10. The peeling is due to the low bond strength (1.8 $N.mm^{-1}$) of the MO–RAD M801 epoxy to the steel, hence showing interfacial failure.

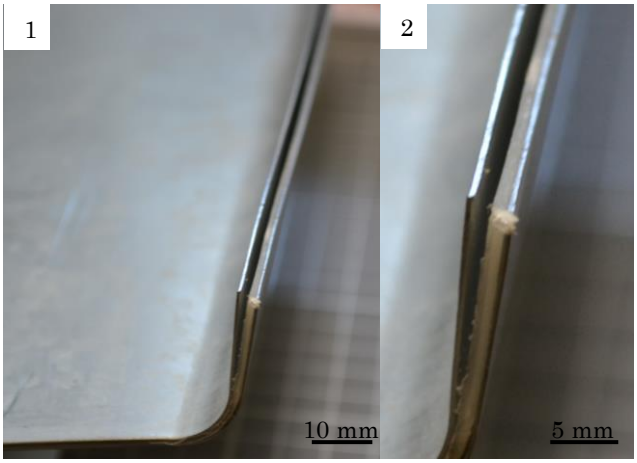

Figure 4.10 – Image 1 – Peeled material when bent using press brake. Image 2 – Close up of failure.

The increased bond strength of the phosphated steel (5.5 $N.mm^{-1}$) was in general enough to prevent the sandwich peeling. However, it led to a change in the method of failure, showing a reverse folding, Figure 4.11. This has been previously

reported in forming research on sandwich materials by Nakagawa [3]. Nakagawa's solution in this case was a further increase in the bond strength. Nevertheless, due the reverse folding, press brake bending of DPSW was found to be unsuitable. Any further improvement was out of scope for the project since this would have required remanufacture of the steel grade without the zinc coating.

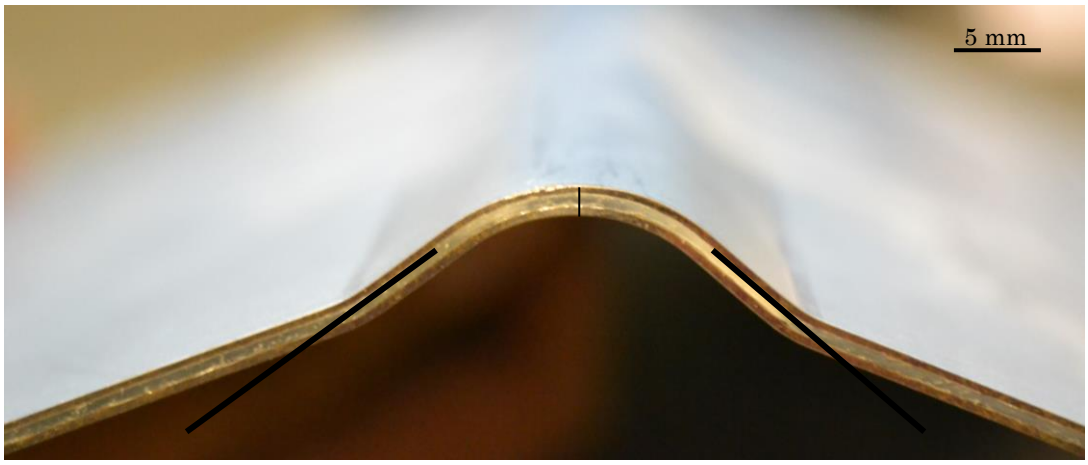

Figure 4.11 – Collapsed material when bent using press brake. Black lines show how the material should have formed.

The DPSW press brake bent top hats also suffered similar problems as the Steelite and ECCS top hats, localised core crushing and incorrect geometry were both observed.

4.6.3.2 Heated stamp forming

The defects observed in the press brake bent top hats were not observed for the stamped hats. However, the stamp formed hats did exhibit significant spring back, shown in Figure 4.12.

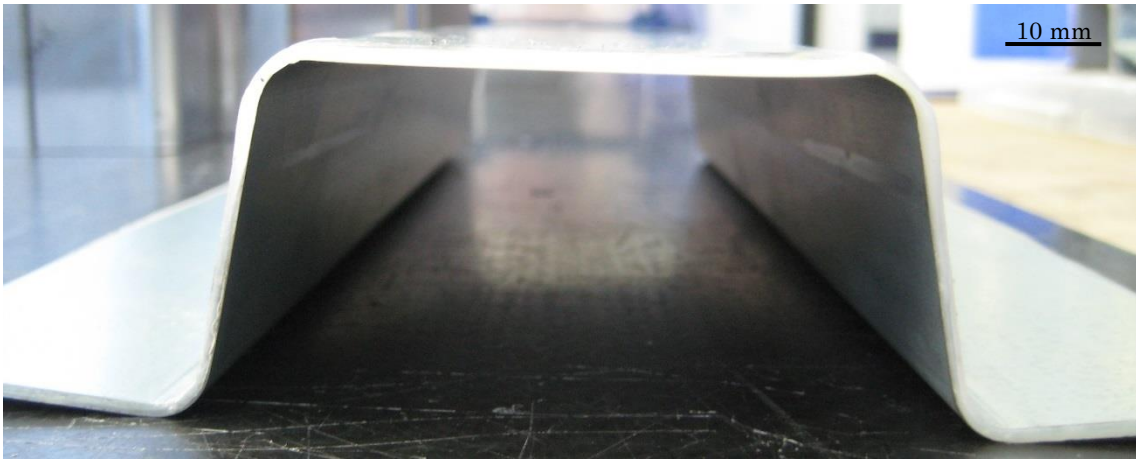

Figure 4.12 – Spring back seen in press–formed DPSW top hat.

Figure 4.13 – a shows the pressed shape before the flanges were trimmed to the correct size. Polymer run out occurred due its low viscosity during heating and the use of 1×10^6 Newton of force to form the shape. This also caused the top and bottom steel skins to press independently, resulting in the different edge lengths seen in Figure 4.13 – b.

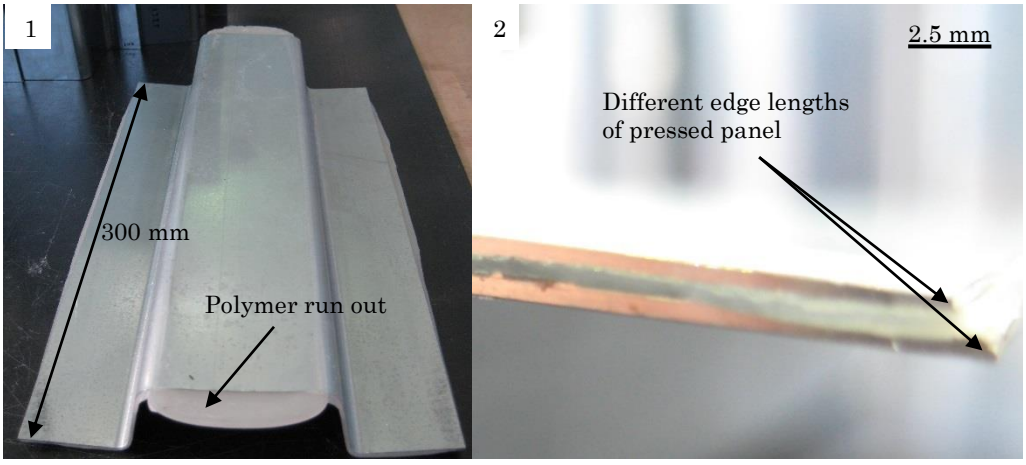

Figure 4.13 – Image 1 – Heated and press–formed top hat showing spring back and polymer run out at over 200 °C. Image 2 – Differing edge lengths of the steel in the heated sandwich.

4.6.4 Differences between crash structure geometry to the intended shape

Press brake bending has an inherent variability to the process. Therefore, in order to assemble the crash structures, the top hat and backplate required clamping together to fix them to the correct shape (shown in Chapter 3). Additionally, there was a variation in the thickness of the sandwich materials an order of magnitude greater than observed in monolithic metals (10 – 100 µm in sandwich materials, compared to 1 – 10 µm in monolithic sheet metals). This increased the variability in the press brake bending process, since the pressed corner position is defined by the thickness of the material. Additionally, the manually produced initiators lead to localised thinning of the material.

4.6.5 Monolithic materials

All monolithic metals were press brake bent and no difficulties observed in their pressing. The geometry was the same as that of the ECCS sandwich, though each top hat is not identical due to the nature of the press braking process.

An SPR joined aluminium alloy crash structure, Figure 4.14 were held in a fixture to position them correctly for riveting.

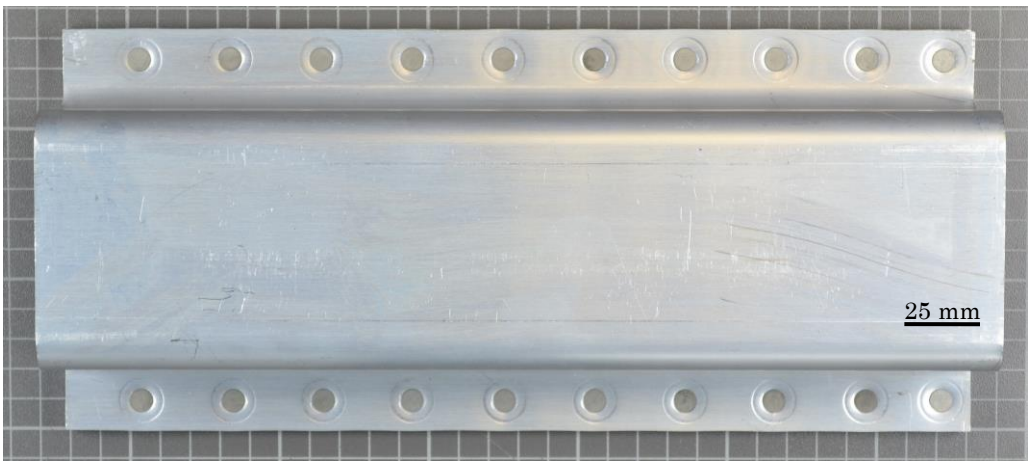

Figure 4.14 – Self–pierced rivet (SPR) joined aluminium alloy crash structure.

The DP600 steel crash structures were manually spot–welded, the top hats were held on a fixture to aid alignment of the welds in the crash structure over the welding electrodes, to allow for a more repeatable positioning, Figure 4.15.

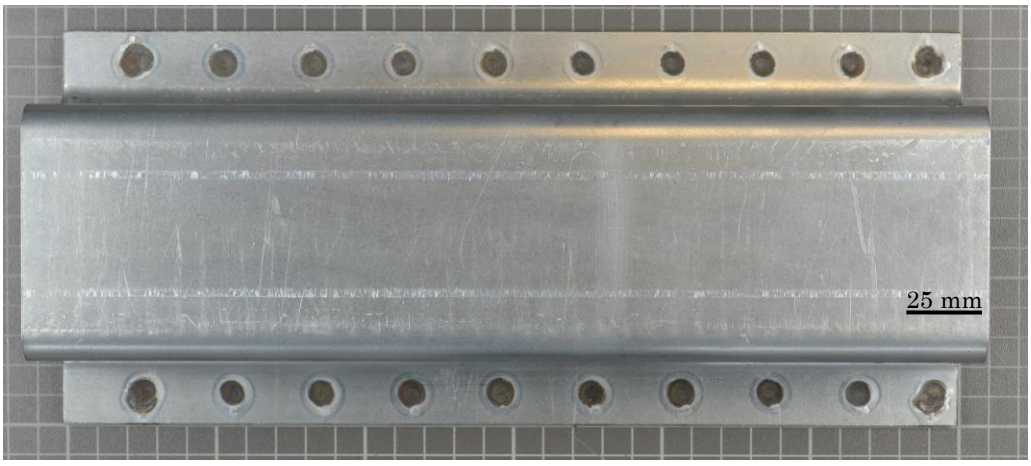

Figure 4.15 – Manually spot–welded DP600 steel crash structure.

4.7 References

[1] Rohm and Haas, "MO-RAD M801 Technical Data Sheet (TDS)."

[2] A. I. Zubkov, S. D. Khizhnyak, and P. M. Pakhomov, *Deformation and Fracture Behaviour of Polymers*. Springer, 2001.

[3] T. Nakagawa, "Recent Developments in Auto Body Panel Forming Technology," *CIRP Ann. - Manuf. Technol.*, vol. 42, no. 2, pp. 717–722, Jan. 1993.

5 Quasi–static and dynamic test results

This chapter details the results of the quasi–static crush and dynamic (impact) testing performed on the metal–polymer–metal sandwich material crash structures, as well as benchmarking against monolithic metals.

The sandwich materials tested are detailed below;

1. The Steelite sandwich is the lowest strength and thinnest material, having 0.15 mm steel skins and 0.7, 1.4 or 2.1 mm of polypropylene core. Due to the low strength of the Steelite materials, they were tested in an 80 mm × 80 mm double hat structure (Chapter 3 – Materials and methods).
2. The electrolytically chrome coated steel (ECCS) sandwich materials are of intermediate strength and thickness. Having 0.3 mm steel skins and produced with 0.7, 1.4 and 2.1 mm of polypropylene core. The ECCS materials were produced in a 77 mm × 58.5 mm single hat structure (Chapter 3).
3. The DP600 steel sandwich materials (referred to as DPSW) was constructed of 0.5 mm thick, high strength steel skins with only a 0.7 mm polypropylene core. DPSW was produced in both the 77 mm × 58.5 mm single hat geometry and a smaller press formed single hat geometry (Chapter 3).

This chapter highlights the difference in performance quasi–statically and dynamically of the sandwich materials listed above, as well as considering the following monolithic metals; 1.6 mm DP600 steel, 2.5 mm AA5754 and AC300 aluminium alloys. All monolithic metals were produced in the 77 mm × 58.5 mm single hat geometry. Testing carried out on the monolithic metal is detailed first to highlight the performance of the current state of the art materials used for the conventional automotive body–in–white, as well as acting as a control; showing the difference between static quasi–crush and dynamic impact testing.

The intention of this chapter was to compare the energy absorption performance of monolithic metals to steel sandwich materials directly, not via literature comparison. Literature comparison being limited in its use due to different testing methods and crash structure geometries.

In order to compare the performance of materials directly, all other variables (crash structure geometry, joining method, test setup, testing methodology) must be kept the same. Since only two of the three sandwich material variants produced (ECCS and DP600) were tested in the same geometry as the monolithic metals, this made comparison difficult in this chapter. Additionally, the change in steel skin thickness also had a change in steel strength, therefore changing two variables at once. However, where possible, comparisons are made between materials.

Hence, direct performance comparison is not provided in this section; instead, it is made by finite element analysis (FEA) in the following chapters. The FEA having been validated using the test results from this chapter.

Force–displacement plots are shown for a representative test from each variant of sandwich and monolithic material tested. Repeats are not shown for clarity, since the overlaid results makes interpretation difficult. To show repeatability of the results, the mean crush force, peak impact force and specific energy absorption for each test is shown in the summary at the end of each section.

Energy–displacement plots for all repeats tests are shown for the dynamic (impact) tests but not for the quasi–static tests. Quasi–static tests being for comparison to the dynamic tests and not entirely concerned with energy absorption.

An image series is presented for each sandwich variant to show the deformation of the material throughout the impact or crush event. Where further analysis is required, magnified images are shown to aid in explanation.

5.1 Testing regime

Sandwich materials with three grades of steel skin material were tested. The two thinnest skins were produced with three thicknesses of polypropylene core. The thickest grade of steel tested was only produced with the smallest core thickness (0.7 mm) due to the manufacturing difficulties described in Chapter 4 – Material production results. The ratio of steel to polymer and an approximation of the material density for each sandwich configuration are detailed in Table 5.1.

Table 5.1 – Sandwich and monolithic materials tested, as well as their constituent material thicknesses and approximate densities. *Densities are calculated using the standard densities [1] of the component materials and their volume fractions.

Steel Grade	**Thickness /mm**			**Volume percentage /%**		**Approx. density* /kg.m^{-3}**
	Skin	Core	Total	Skin	Core	
Steelite skin	0.15	0.7	1.0	30.0	70.0	3000
Steelite skin	0.15	1.4	1.7	17.6	82.4	2100
Steelite skin	0.15	2.1	2.4	12.5	87.5	1800
ECCS	0.3	0.7	1.3	46.2	53.8	4100
ECCS	0.3	1.4	2.0	30.0	70.0	3000
ECCS	0.3	2.1	2.7	22.2	77.8	2400
DP600	0.5	0.7	1.7	58.8	41.2	5000
Monolithic materials						
DP600	N/A	N/A	1.6	100	0	7850
AA5754	N/A	N/A	2.5	100	0	2600
AC300–T61	N/A	N/A	2.5	100	0	2600

The static crush tests were repeated three times for each sandwich material layup.

Multiple drop tests were performed on each layup to ascertain the maximum amount of energy absorbable, and three repeats performed at the finalised energy. This method was used in order to find the maximum energy the crash structure could absorb before "bottoming out" (defined in Chapter 1).

Due to the use of spring assistance to provide impact energy (as described in Chapter 3), the impact energies varied from the intended value, usually being 10% over. Therefore, the impact energy was defined for each test by the measured velocity at impact and the known mass. Additionally, the energy absorbed was less than the calculated impact energy due to losses in the form of noise, vibration and frictional heat production (as previously discussed in Chapter 3).

Photogrammetry was performed on all tests both quasi–statically and dynamically. Each variant of sandwich was captured in three different orientations for a single hat structure (anterior, posterior and laterally) and two orientations for the double hat due to symmetry (anterior and posterior). High–speed imagery was used to capture the deformation of the material during impact tests for visual assessment.

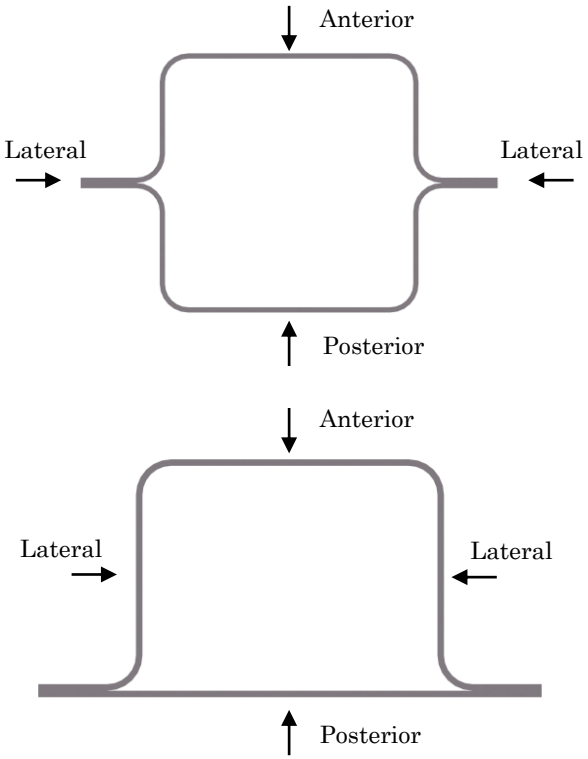

Figure 5.1 – Naming convention for images of deformed crash structures, for both single and double hats.

5.2 Monolithic material testing

5.2.1 Quasi–static crushing

A conventional response of the monolithic metals to axial impact (discussed in Chapter 1 – Introduction) was observed. With a characteristic peak force followed by a lower secondary force and then finally a progressive crushing response (Figure 5.2). The horizontal dashed line shows the mean crush force of the material over the three tests performed. DP600 (Figure 5.2 – red) showed the highest mean crush force followed by AC300 (Figure 5.2 – green) and lastly AA5754 alloy (Figure 5.2 – blue). A single test from each material is shown as the tests for the monolithic materials were very repeatable. The mean crush force variation being within 2% for the AC300 material and 0.6% for the DP600 and AA5754.

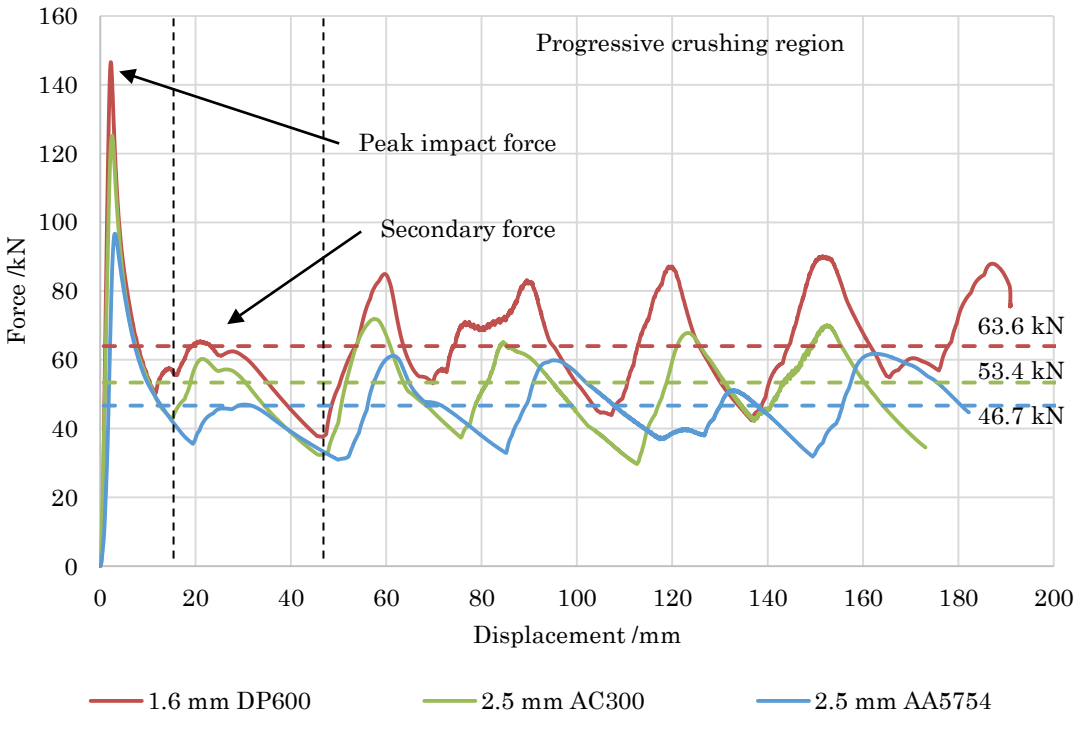

Figure 5.2 – Monolithic metals quasi–static crush force–displacement results. A representative result for each material is shown. The horizontal dashed lines indicate the mean crush force for the three repeats. Vertical dashed lines show the peak force region, transition region and the progressive crushing region.

The monolithic metals were crushed until bottoming out, which was determined to have taken place when the force began to rise markedly. These data values were omitted from Figure 5.2, hence the final data point in the curve indicating where progressive crushing was deemed to have ended and the crash structure begins to bottom out". The two thicker aluminium alloys were found to bottom out before the thinner steel, as is expected since the thicker material produces larger radius folds, hence cannot compress as far (discussed in Section 5.2.3). The AA5754 produced the same number of folds as the higher strength AC300 alloy, but over a greater displacement; hence the AA5754 bottomed out at a lower displacement and lower energy, despite identical thickness.

5.2.2 Monolithic material drop testing

The dynamic force–displacement data (Figure 5.3 – solid) showed similarities to the quasi–static crush results. However, the response curve did not show the defined progressive crushing as clearly as the quasi–static tests did, with the peaks and troughs of the fold production being less evident. The integrated energy–displacement data (Figure 5.3 – dotted) shows a linearity to the energy absorption over the length of the crash box. The steeper line indicates a higher mean crush force as is confirmed by the horizontal dashed lines. The variability in the results was within 1.5% in all tests, hence only a representative result is shown for each material (Figure 5.3).

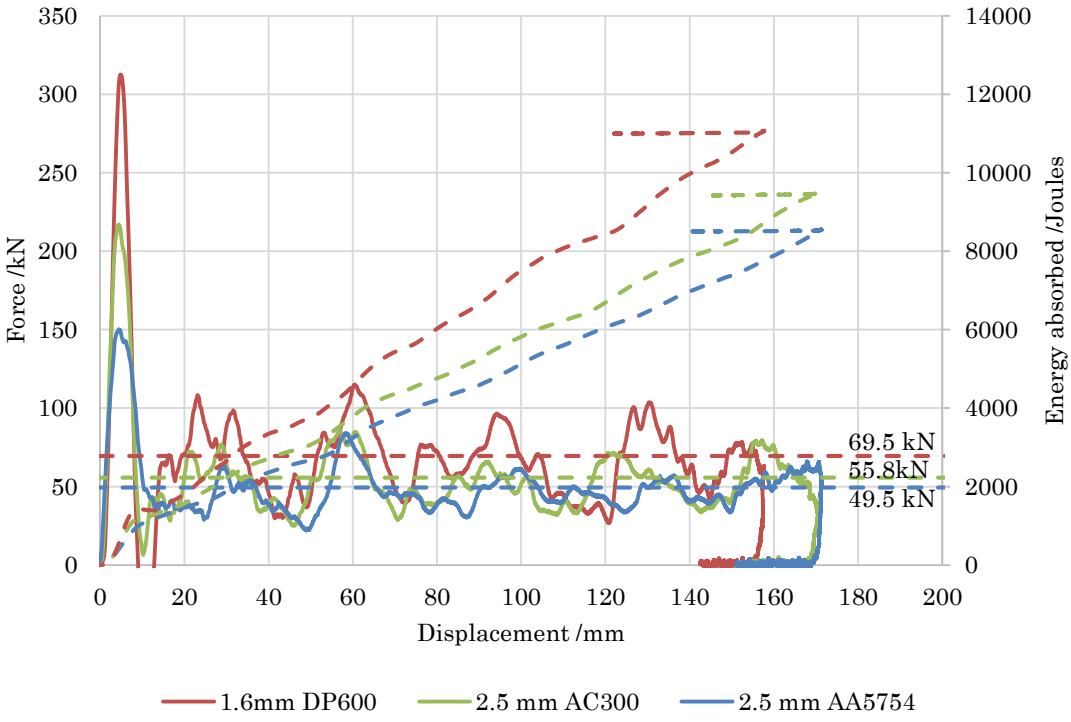

Figure 5.3 – Monolithic metals dynamic (impact) results. The force–displacement and energy–displacement is shown for each material. A representative result for each core thickness is shown. The horizontal dashed lines shows the mean crush force for the three repeats.

The AA5754 absorbed 8.5 kJ, the AC300–T61 absorbed 9.5 kJ; the DP600 was limited by the maximum energy output of the drop tower, of 11.0 kJ.

5.2.3 Deformation of the monolithic metals

The monolithic crash structures exhibited asymmetric folding, and were visually similar both quasi–statically and dynamically, therefore, only the quasi–static images are shown (Figure 5.4, Figure 5.5 and Figure 5.6).

The 1.6 mm DP600 (Figure 5.4 – images 1 & 2) fold wavelength was approximately 80 mm, as determined by the ruler on the surface. Three complete folds were produced on the front face in the 190 mm of quasi–static displacement. It is apparent than an additional half fold was possible; nevertheless, this would not have increased the mean crush force.

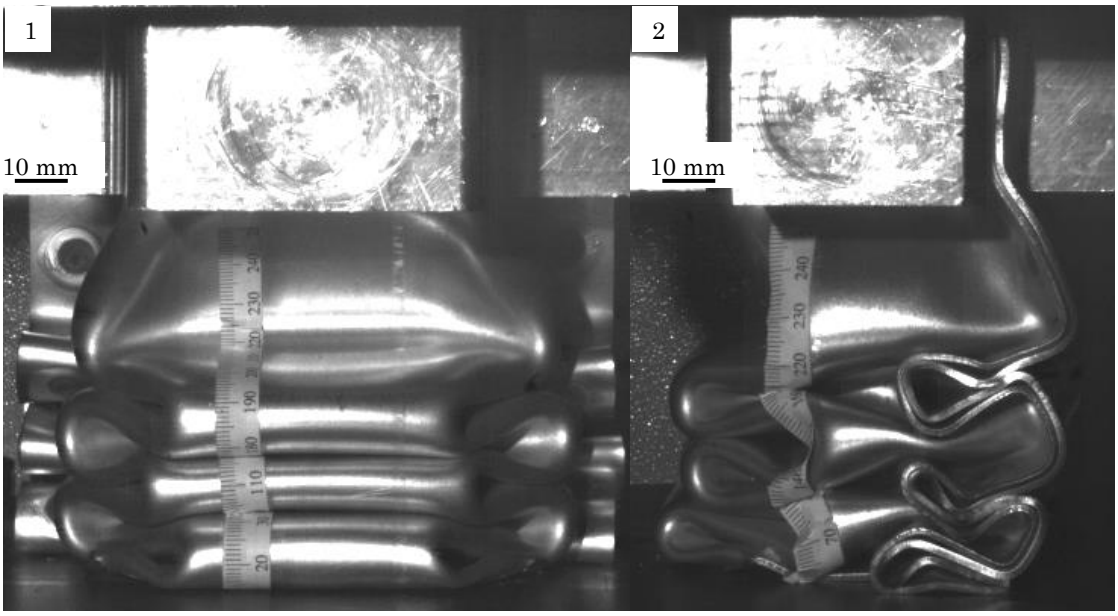

Figure 5.4 – Quasi–static crush deformation of the DP600 steel crash structures. 1 – Anterior view. 2 – Lateral view. Crash structure has been deformed approximately 190 mm in both images.

A greater fold radius was observed for the thicker AA5754 alloy (Figure 5.5 – images 1 & 2), being on average a 12 mm radius per fold in the aluminium, compared to 8 mm in the steel. The fold wavelength was approximately 100 mm, and due to the large amount of material involved in the fold, the number of completed folds reduced to two. Additionally, the final fold showed a much tighter radius due to the limiting length of the crash structure.

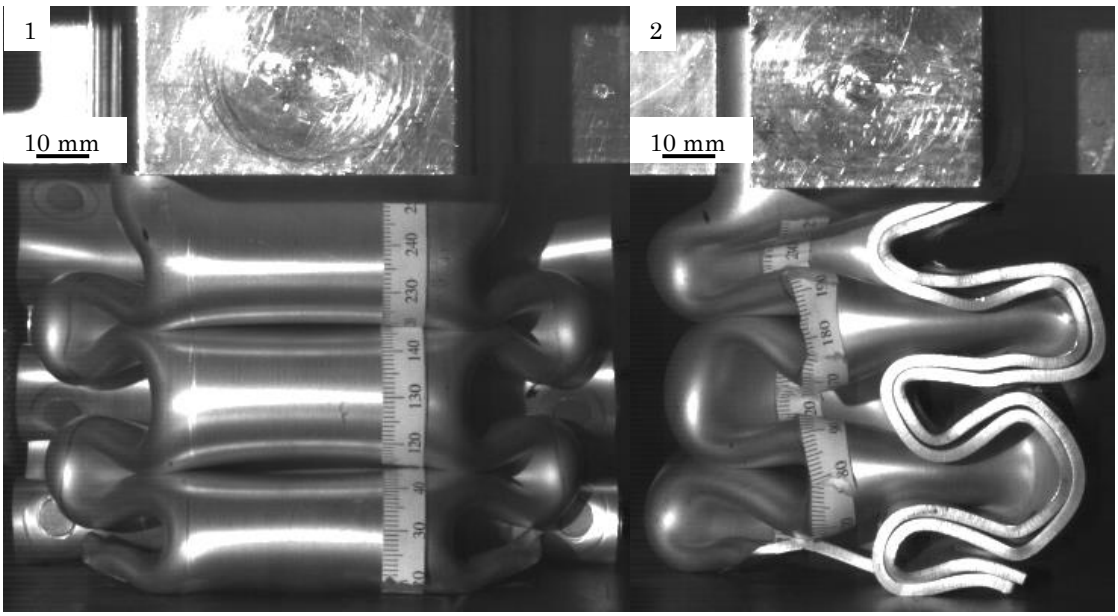

Figure 5.5 – Quasi–static crush deformation of the AA5754 alloy crash structures. 1 – Anterior view. 2 – Lateral view. Crash structure has been deformed approximately 190 mm in both images.

AC300 alloy crash structures again exhibited the same deformation as AA5754 (Figure 5.6 – images 1 & 2), but with a smaller fold radius at 10 mm per fold. This was unexpected since both alloys have the same thickness. The surface ruler shows the fold wavelength was approximately 90 mm, 10 mm less than the AA5754 alloy.

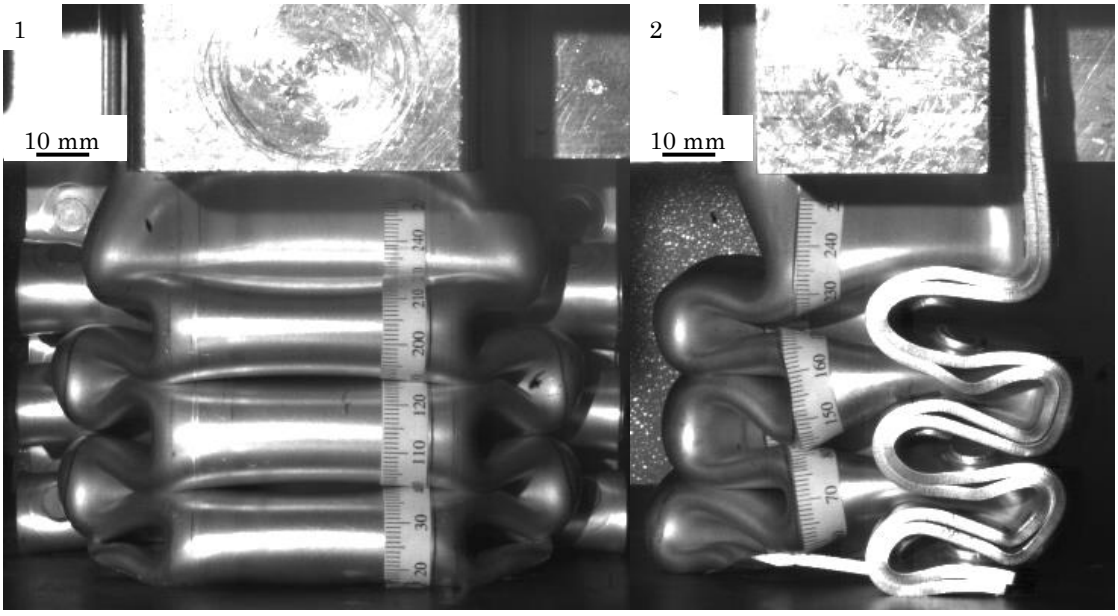

Figure 5.6 – Quasi–static crush deformation of the AC300–T61 alloy crash structures. 1 – Anterior view. 2 – Lateral view. Crash structure has been deformed approximately 190 mm in both images.

5.2.4 Summary of monolithic material quasi–static and dynamic test results

The monolithic metals displayed a repeatable deformation performance, the mean crush force and specific energy absorption of the crash structures is summarised in Figure 5.7. The DP600 steel showed the highest mean crush force both quasi–statically and dynamically (63.6 kN and 69.5 kN respectively) but the lowest specific energy absorption (SEA) at 15.3 J.g^{-1} dynamically. A mean crush force of 55.8 kN was observed for the high strength AC300–T61 dynamically, with an SEA of 22.3 J.g^{-1}.

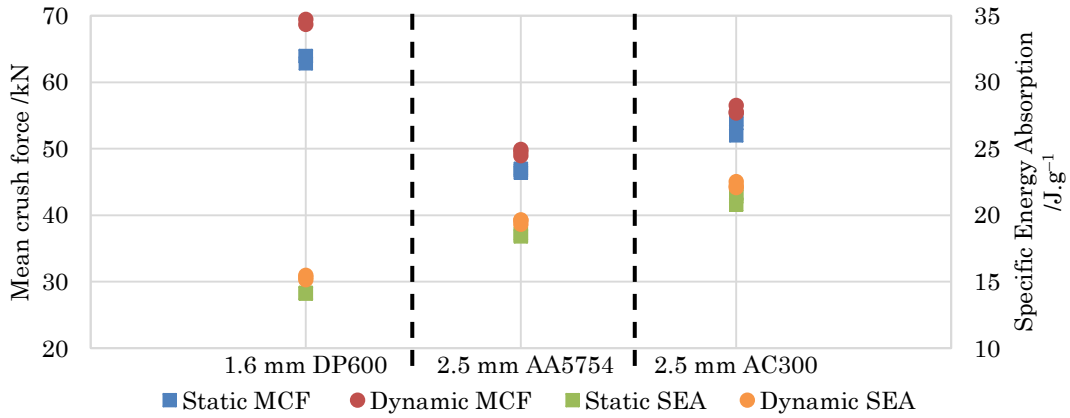

Figure 5.7 – Summarised results for the monolithic metals tested. The mean crush force and specific energy absorption of the monolithic materials are shown quasi–statically and dynamically for each test. Noteworthy, is the repeatability of the tests, since the individual results are indistinguishable from one another.

The SEA achieved for the steel (Figure 5.7) was higher than expected, with values of around 12 J.g^{-1} being reported in the literature [2]. Lower SEA values than expected were achieved for aluminium alloys (Figure 5.7) with literature reporting values in the region of 25 J.g^{-1} [3]. The AA5754 was well below this target, its mean crush force being 49.5 kN dynamically, with an SEA of 19.5 J.g^{-1}.

The higher than expected SEA achieved by the high strength steel is in part due to the greater thickness of the DP600 than required to absorb an 11 kJ impact. The thickness of steel used was due to material availability at the time of testing. As

was discussed in Chapter 2 – Literature review, the specific energy absorption is intrinsically linked to the mean crush force. For a given grade of material, increasing the thickness of the material and fixing all other variables, the mean crush force of the crash structure will increase and the SEA will increase with it. This is due to the mean crush force increasing to the square of the thickness, whereas the mass of the crash structure increases linearly with thickness.

All monolithic materials showed a slight strengthening at high strain rates. This was expected for AA5754 [4], whereas the strengthening of the AC300 alloy has not been previously reported. However, the increased crush force in the AC300 was due to inertia [5], [6]. This is a commonly seen phenomenon in impact and high–speed testing, where materials that have no strain rate sensitivity, have an increased strength dynamically due to the inertial effects of a mass travelling at high speed when impacted.

The lack of strain rate sensitivity of the DP600 in comparison to conventional mild steels is characteristic of high strength steels. Mild steels exhibit significant strengthening at high strain rates and are expected to absorb up to 50% more energy when dynamically impacted compared to when quasi–statically tested [7]. Whereas the DP600 absorbed only 9.3% more energy dynamically over the quasi–static case. The static to dynamic ratio of the monolithic metals for the mean crush force and SEA shows there was little difference in these materials quasi–statically and dynamically (Figure 5.7). Therefore, the quasi–static result can be assumed the dynamic case, both in terms of performance figures and deformation. Since no strain rate dependent failure was observed, which is the case in some steel and aluminium alloys [8].

5.3 0.15 mm Steelite sandwich quasi–static crush testing

Quasi–static crushing of the Steelite showed a force–displacement response similar to the monolithic materials at all thicknesses (Figure 5.8). All variants of Steelite responded similarly for the first 100 mm, with the peak impact force broadening in displacement with increasing polymer core thickness. An increase of 10 kN per increase in core thickness was seen in the peak impact force. The increasing core thickness resulted in an increase in the mean crush force (Figure 5.8 – dashed horizontal lines). After the initial peak force, a secondary smaller peak was observed which was followed by the progressive crushing region.

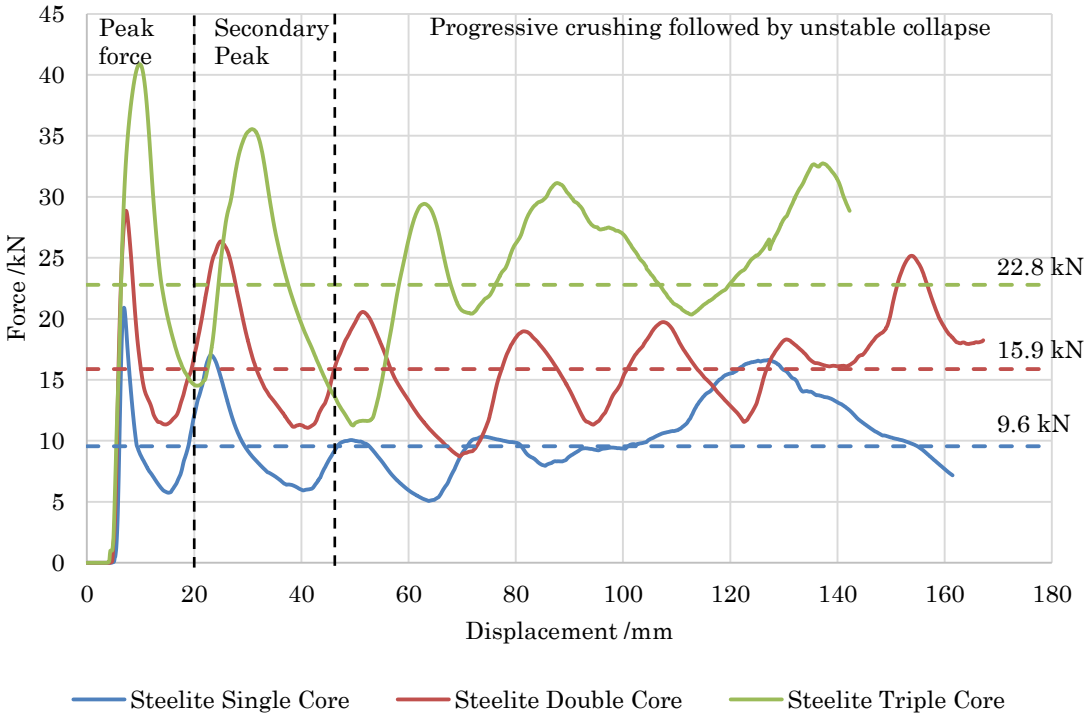

Figure 5.8 – Steelite quasi–static crush force–displacement results. A representative result for each core thickness is shown. The horizontal dashed lines show the mean crush force for the three repeats. There is a 6.3 kN increase in mean crush force from single core to double core and a 6.9 kN mean crush force increase from double core to triple core.

With increasing material thickness, broadening of the peaks and troughs in the progressive crushing was observed, suggesting the folds increased in radius with material thickness. The progressive crushing did not continue for the entire length

of the test, the crash structure showed a transition to an unstable collapse mode in all instances, and is further discussed in Section 5.3.2.

5.3.1 Image series

The folding behaviour in the Steelite sandwich materials resembles monolithic metals in both the peak force and progressive crushing region (Figure 5.9, Figure 5.10 and Figure 5.11). The folds are regular in nature, but the radius of the folds was smaller than observed for the monolithic steel and aluminium alloys. The fold radius was in the range of 8–12 mm, assuming the folds are circular. However, the fold radius in the Steelite sandwich materials was in the range of 1.5–4 mm. The smaller radius can be accounted for by the reduced thickness of the sandwich rather than being a property of the MPM sandwich materials.

The biggest difference was the folds appeared to flatten into one another during crushing (Figure 5.9, images 2–4, red circles), a feature not witnessed in monolithic metals. This flattening of the folds was also emulated in the double and triple core materials (Figure 5.10, images 3–5 and Figure 5.11).

It is hypothesised and supported by Chapter 6 – Results comparison, that this compacting/flattening of the fold is the cause of the double peak in the initial stages of crushing, as well as the lack of stiffness of the MPM sandwich material once bent through 180° in the first fold. The low strength nature of the MPM sandwich in the transverse direction, due to the compliance (relative compressibility and low modulus) of the polymer results in the second fold fully crushing into the first fold, stiffening the material; hence, increasing the force in the second peak.

An important aspect to consider when increasing the thickness of the core is the increased likelihood of failure of the steel skin. No failure of the steel skin was witnessed in the single core Steelite (Figure 5.9), whereas, small fractures

appeared after gross deformation in the double core (Figure 5.10 – image 5). More notably, failure of the skin occurred early on and propagated through the material in the triple core (Figure 5.11 – images 3–5). The most common point for the skin to fail in all instances was in the corner folds, and within the triple core Steelite across the plastic hinge line of the anterior face of the crash structure.

Failure occurred in these locations since they are the areas, which undergo the largest strain, particularly the corners. This was confirmed using Finite Element Analysis, however, is also well documented in the literature [9]. The plastic hinge line failure occurred due to the plane strain loading across the face of the crash structure. Plane strain loading having the lowest strain to failure [8], [10].

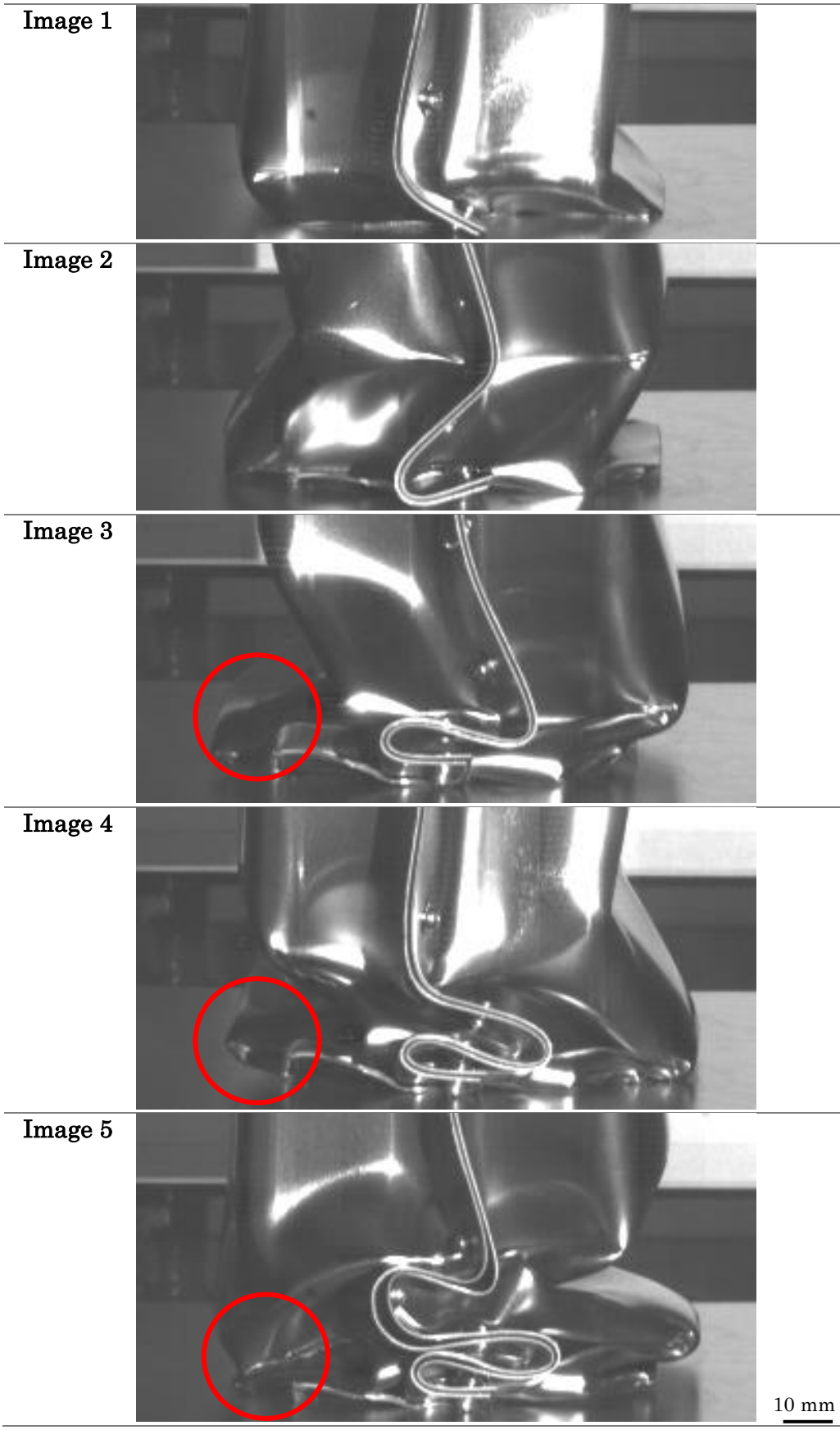

Figure 5.9 – Progressive crushing seen in the single core Steelite quasi–statically crushed. Red circles indicate new fold formed compacting into previous. 1 to 5 – Lateral views. Scale bar applies to all images.

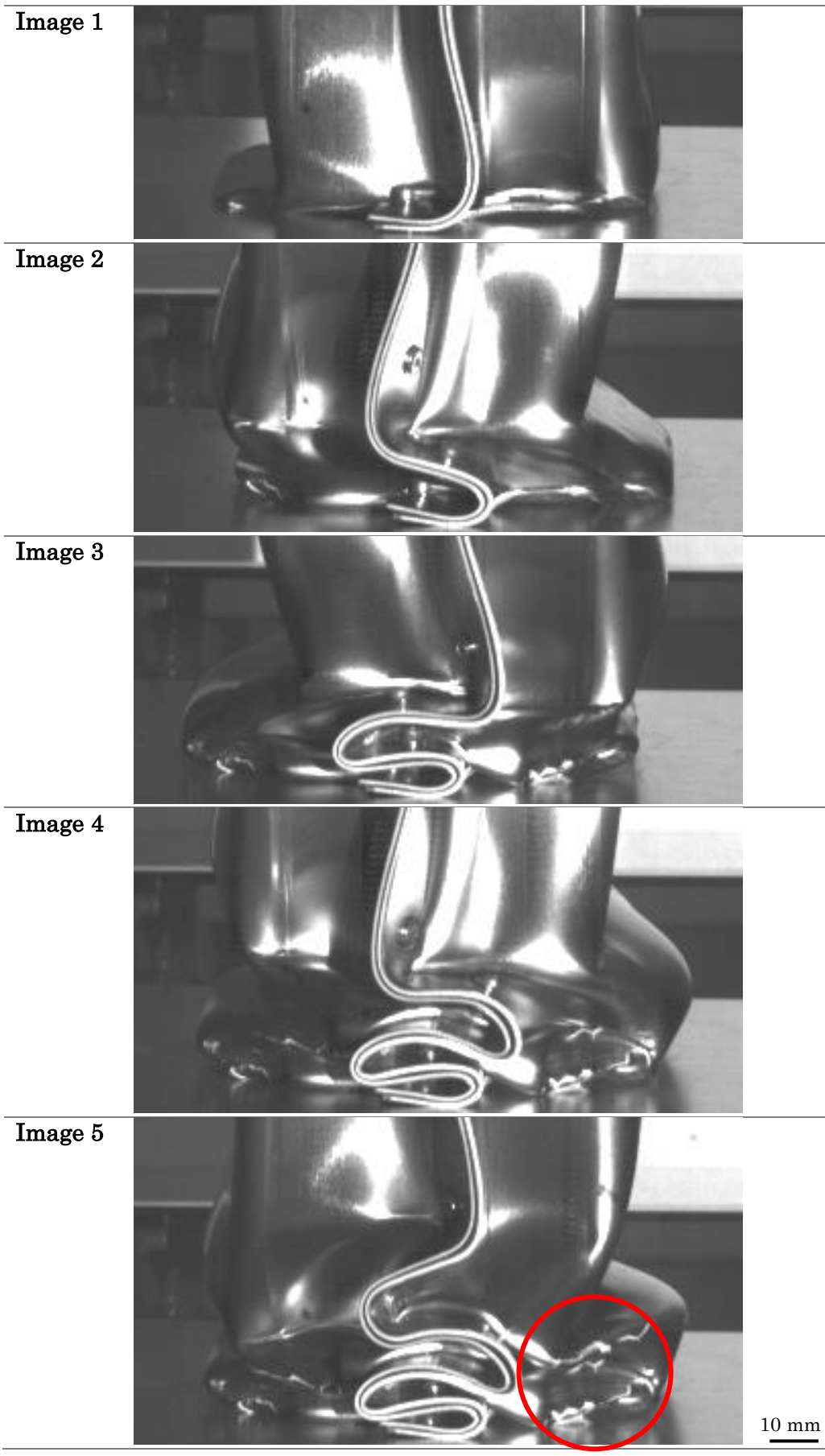

Figure 5.10 – Progressive crushing seen in the double core Steelite quasi–statically crushed. Red circle indicates onset of skin failure. Images 1 to 5 – Lateral views. Scale bar applies to all images.

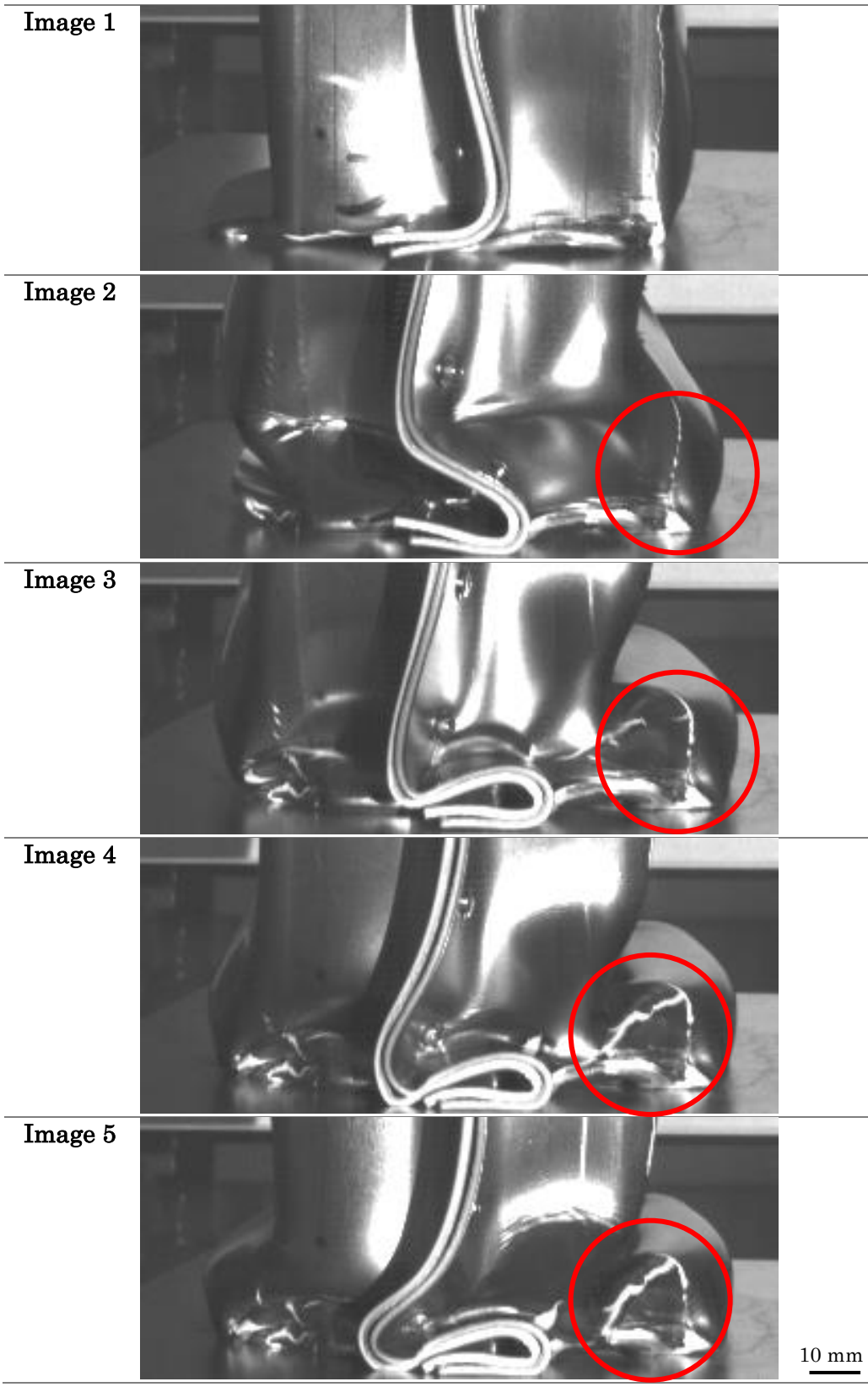

Figure 5.11 – Progressive crushing seen in the triple core Steelite quasi–statically crushed. Red circles highlight the progression of a fracture through the steel skin as the structure collapses. Images 1 to 5 – Lateral views. Scale bar applies to all images.

5.3.2 Unstable collapse

A feature of the Steelite material quasi–static crush tests was a change from progressive crush to unstable collapse. For the single core sandwich material, this occurred after approximately 100 mm, and approximately 180 mm displacement for the double and triple core. The transition from stable to unstable collapse was not repeatable from specimen to specimen.

A mix of global bending and extensional collapse was observed in the single core Steelite material (Figure 5.12). Whereas, double core (not shown) and triple core Steelite sandwich materials (Figure 5.12 – image 3) also experienced some extensional behaviour. Progressive crushing was more dominant in these structures, particularly the double core Steelite (Figure 5.12 – image 4).

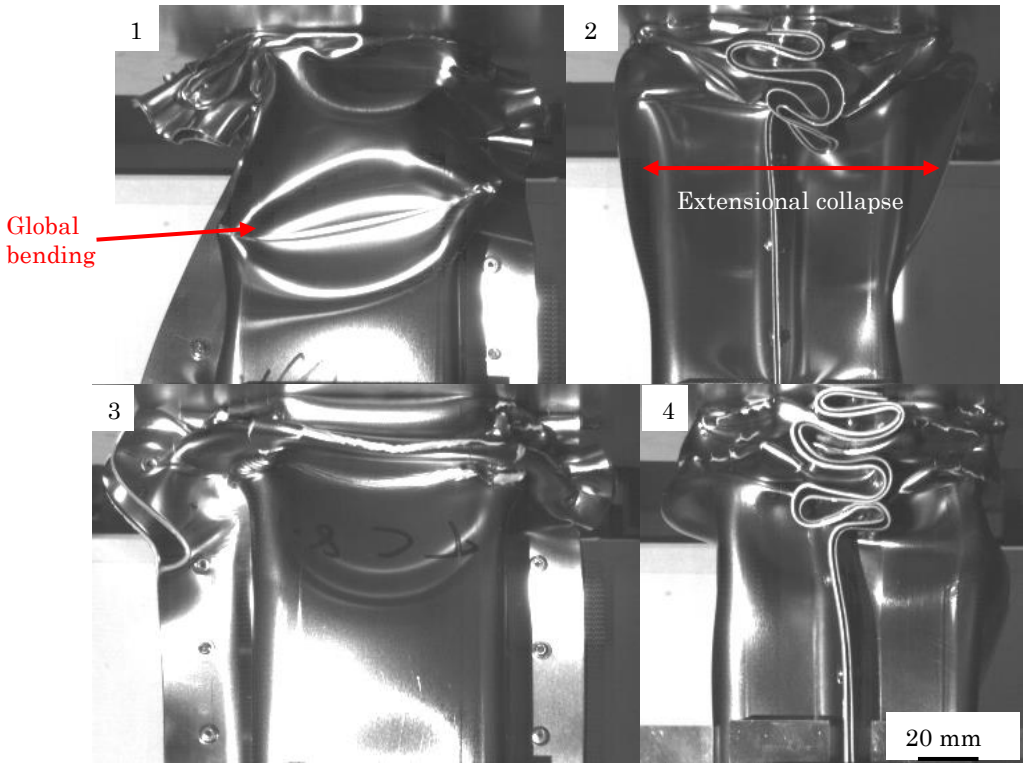

Figure 5.12 – Collapse modes witnessed in single, double and triple core Steelite sandwich materials. 1 – Global bending. 2 – Extensional collapse. 3 – Extensional collapse in the triple core Steelite. 4 – Progressive crushing in double core Steelite. Scale bar applies to all images.

5.3.3 Summary of Steelite quasi–static test results

A summary of the salient facts of the Steelite quasi–static testing are shown in Figure 5.13; the mean crush force (green), peak impact force (red) and the SEA (blue) for each of the tests is plotted. A linear relationship was observed in the increasing mean crush force and peak impact force with respect to increasing core thickness. The peak impact force was found to increase at a greater rate than the mean crush force.

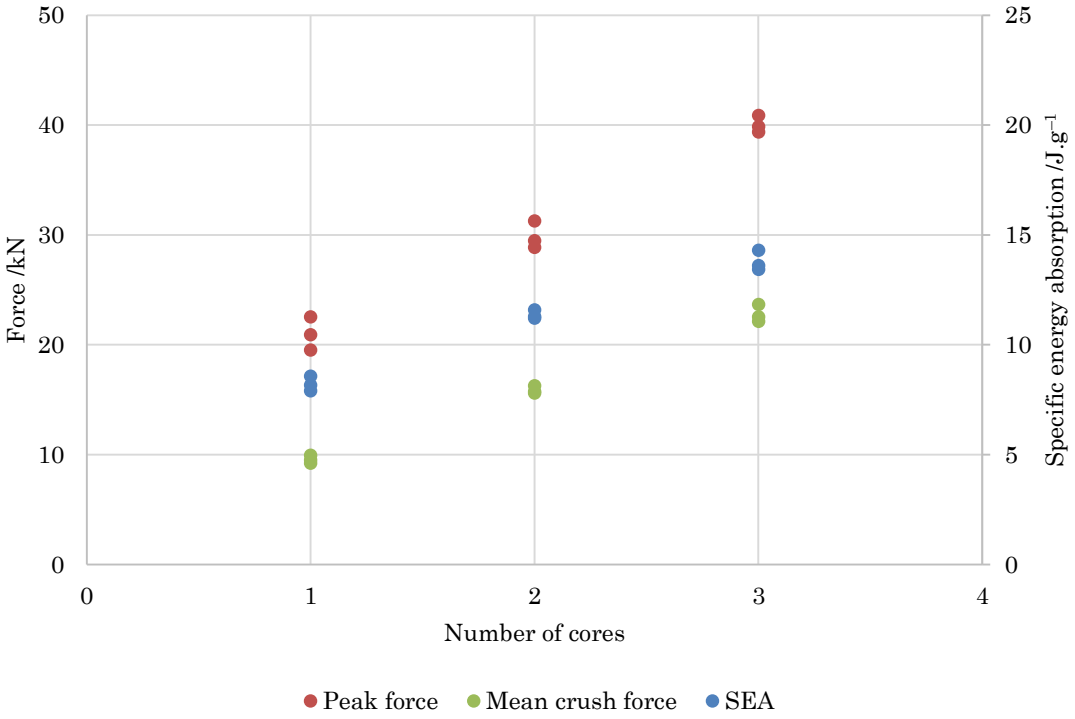

Figure 5.13 – Summarised results for the single, double and triple core variants of Steelite sandwich materials. The mean crush force, peak impact force and specific energy absorption for the three repeat quasi–static crush tests are shown.

Since the quasi–static crush specimens were not displaced to the predicted 190 mm in all instances due to unstable folding, a theoretical prediction for their complete crushing energy was calculated based on the mean crush force achieved at the end of the crush test.

The specific energy absorption had a diminishing return with increased core thickness; the triple core material was not as effective as it should be. Increasing the thickness should increase the energy absorption with the square of the thickness. This effect was attributed to failure of the steel skins when folding and non–ideal folding modes towards the end of the test.

The SEA values achieved by the Steelite sandwich materials ranged from 8.2 – 13.8 $J.g^{-1}$, these values were lower than those of the monolithic crash structures tested. However, this is due to the strength and thickness of the sandwich components and the low energy nature of the tests. The significance in this case being the level of improvement with increased core thickness, not the raw values.

5.4 0.15 mm Steelite sandwich drop testing

Three repeats tests at finalised energy performed on Steelite sandwich materials are shown in Table 5.2. The impact energies are within 5 %, the variation was due to the spring–assisted mechanism, which provides the impact energy (previously discussed in Chapter 3).

Table 5.2 – Drop test energies for repeat tests on Steelite sandwich materials.

Test name	Layup – skin/core/skin /mm	Mass /grams	Impact speed /m.s^{-1}	Impact energy /kJ
SC1	0.15 / 0.7 / 0.15	344	8.5	2.9
SC2	0.15 / 0.7 / 0.15	349	8.3	2.8
SC3	0.15 / 0.7 / 0.15	350	8.5	2.9
DC1	0.15 / 1.4 / 0.15	426	11.1	4.9
DC2	0.15 / 1.4 / 0.15	429	11.0	4.9
DC3	0.15 / 1.4 / 0.15	427	11.1	4.9
TC1	0.15 / 2.1 / 0.15	502	13.1	6.9
TC2	0.15 / 2.1 / 0.15	499	13.1	6.9
TC3	0.15 / 2.1 / 0.15	499	13.2	7.0

The force–displacement plots for a representative test for each thickness of Steelite MPM sandwich highlights the crushing response of these sandwich materials (Figure 5.14). The horizontal dashed line indicates the mean crush force for each sandwich layup. The thinnest variant had a particularly flat response, and increasing thickness of the sandwich showed an increase in the oscillatory amplitudes in the progressive crushing region. The oscillations are difficult to interpret in comparison to the quasi–static crush results due to the high frequency noise in the data. This is owing to the nature of high–speed impact testing where high order frequencies such as noise and vibration were also transmitted to the load cell. Attributes seen quasi–statically were also observed in the impact tests,

such as the secondary peak and increasing fold radius with increasing core thickness.

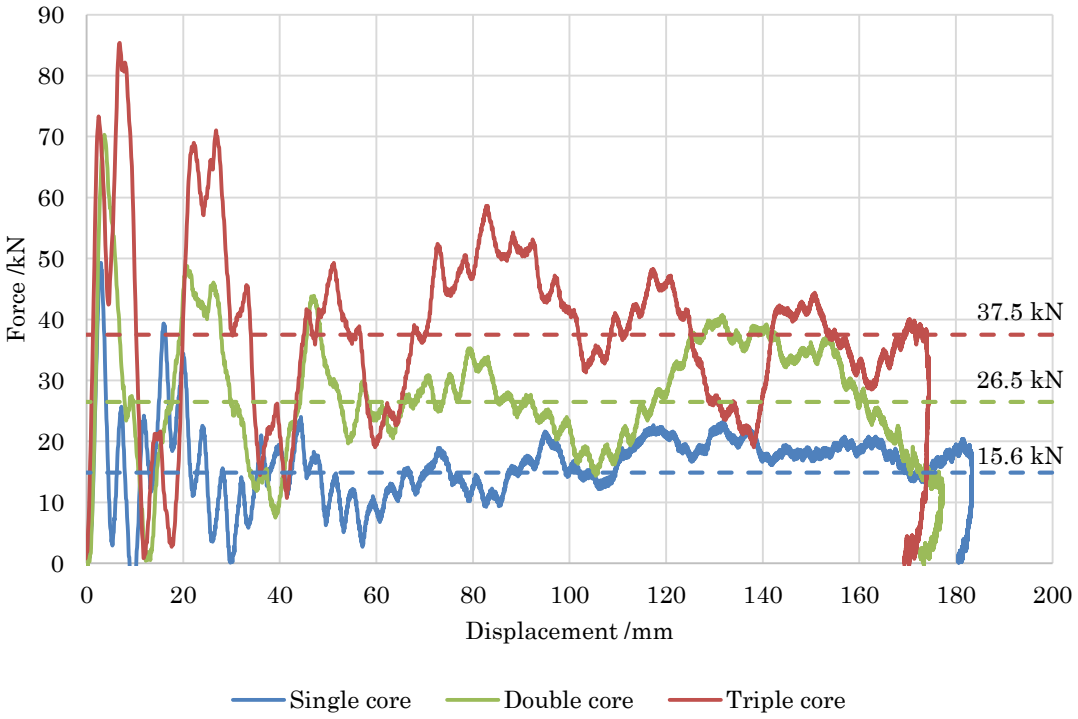

Figure 5.14 – Steelite dynamic (impact) force–displacement results. A representative result for each core thickness is shown. The horizontal dashed lines shows the mean crush force for the three repeats.

5.4.1 Rate of energy absorption

The repeatability of the tests is best seen by plotting the rate of energy absorption with respect to displacement (Figure 5.15), where the mean crush force is the gradient of the line.

Interestingly, the non–ideal folding observed did not seem to affect the linearity of the results. The only minor discrepancy being the steeper gradient at the beginning of the test due to the peak impact force. The difference in the energy absorption rate between sandwich materials can also be seen, the steepest gradient being the triple core material (Figure 5.15 – dashed line), and the shallowest gradient that of the single core (Figure 5.15 – solid line).

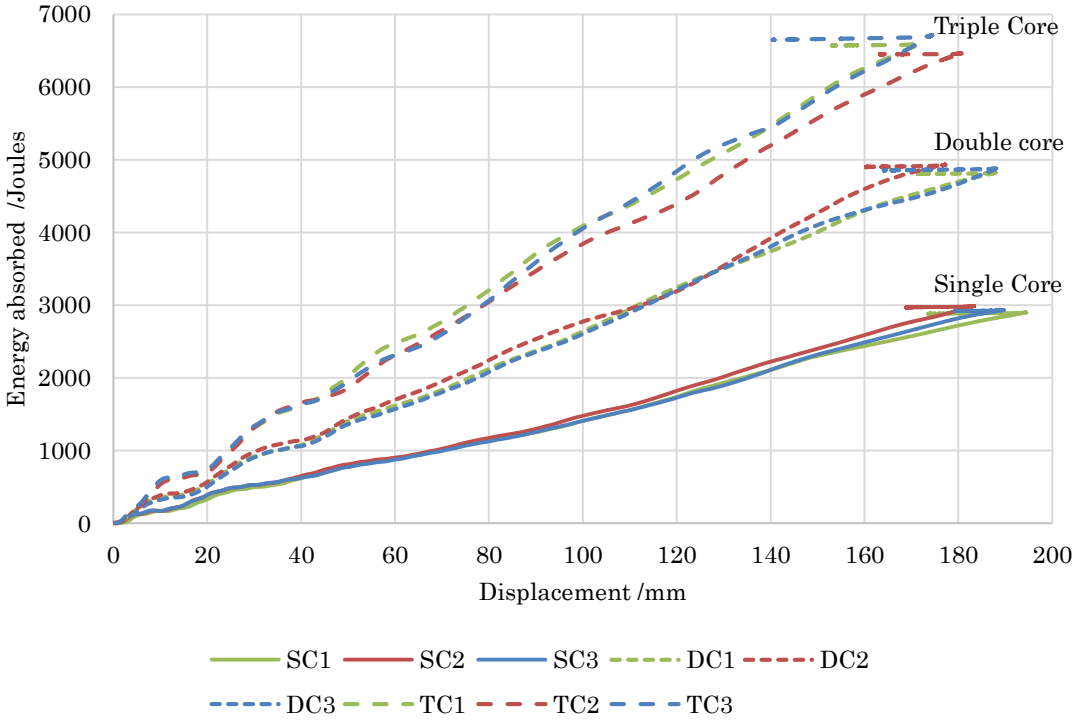

Figure 5.15 – Cumulative energy–displacement results for Steelite sandwich material dynamic (impact) tests. All three repeats for each core thickness (single, double and triple core) are shown.

5.4.2 Image series

Figure 5.16, Figure 5.17, Figure 5.18 show the image series for impact tests on single, double and triple core Steelite sandwich materials respectively. A paper ruler was attached to the surface of the crash structure to readily determine the fold wavelengths. Figure 5.16, Figure 5.17, Figure 5.18 highlight the conventional asymmetric folding modes in the MPM sandwich materials analogous to monolithic materials. Folding became somewhat extensional and less stable towards the end of the test (Figure 5.16 – image 5 and Figure 5.17 – image 5. This change in deformation mode was also observed in the quasi–static crush tests of same materials (see Section 5.1), and is also seen in monolithic structures in a double hat form [11]. As a result of the instability in the crash structures towards the end of the impact, the maximum displacement before "bottoming out" was not achieved for these materials.

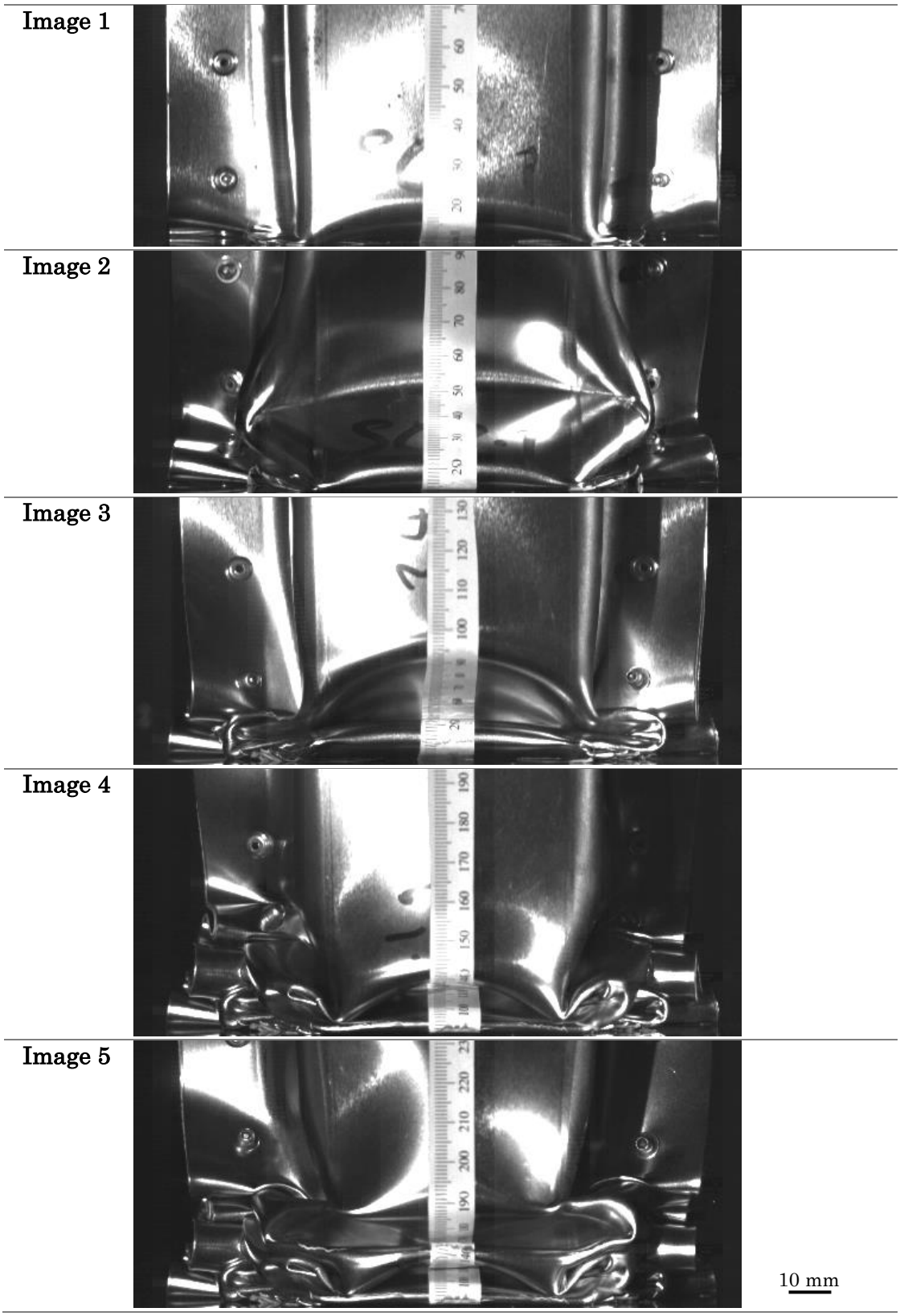

Figure 5.16 – Progressive crushing seen in the single core Steelite for a 2.9 kJ impact at 8.5 $m.s^{-1}$.

Images 1 to 5 – Anterior views. Scale bar applies to all images.

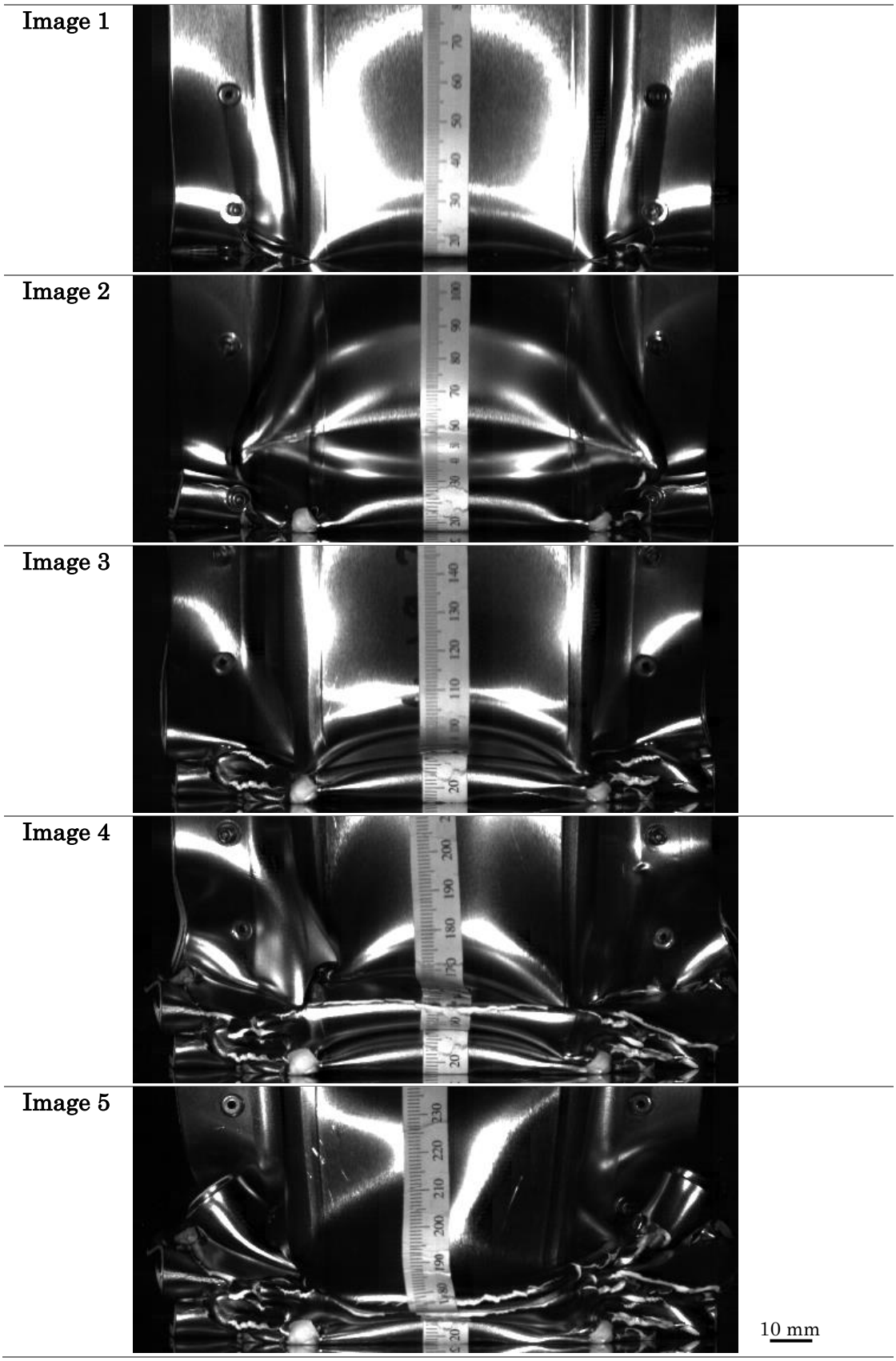

Figure 5.17 – Progressive crushing seen in the double core Steelite for a 4.5 kJ impact at 11.0 $m.s^{-1}$.

Images 1 to 5 – Anterior views. Scale bar applies to all images.

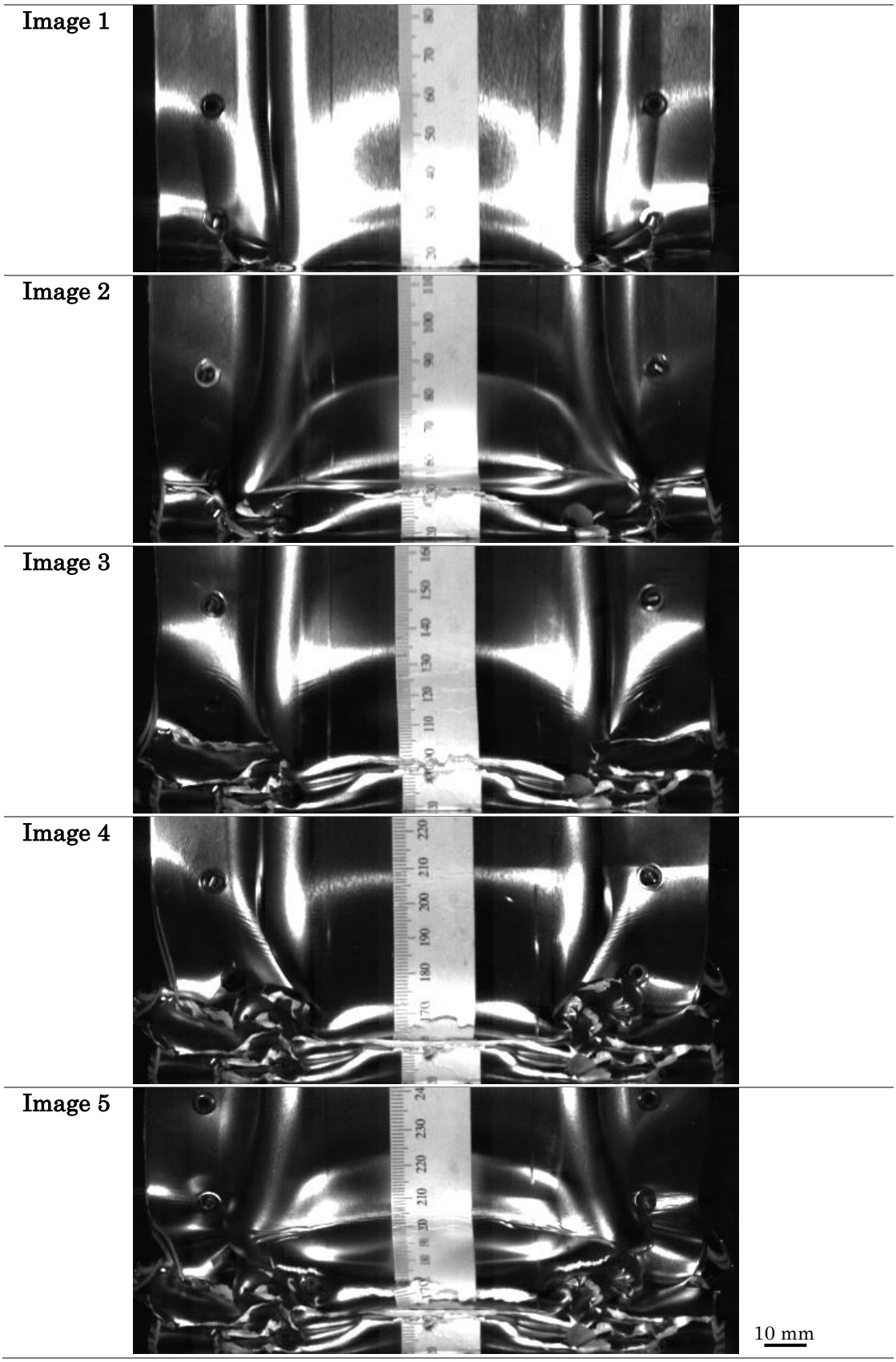

Figure 5.18 – Progressive crushing seen in the triple core Steelite for a 6.25 kJ impact at 13.1 $m.s^{-1}$.

Images 1 to 5 – Anterior views. Scale bar applies to all images.

5.4.3 Deformation and failure

A discrepancy in the fracture of the steel skin was observed between the quasi–static and dynamic testing, fracture was found to be far more prevalent in the dynamic tests. The double and triple core material exhibited skin steel fracture in both quasi–static and dynamic testing. With regards to the triple core materials, this was an expected result before testing, due to the forming strains causing failure of the steel skin in production of the crash structure (discussed in Chapter 3). Nevertheless, all variants exhibited steel skin failure dynamically, which was not witnessed quasi–statically. This is most likely due to a reduction in fracture strain of the steel at higher strain rate, a well–known phenomenon in steels [8].

Failure of the steel skin led to a change in the deformation of the sandwich material under axial impact. For example, the double core Steelite primarily deformed in the conventional asymmetric collapse mode (see Chapter 1). Failure of the steel skin was observed in the second fold (Figure 5.19 – image 1, red circle), this failure propagated into a continued tearing of the face of the crash structure (Figure 5.19 – images 2 & 3), changing the mode of collapse.

As expected the steel failure was more apparent in triple core Steelite where the impact caused failure on the front face of the sandwich, the steel skin peeled away from the core completely and towards the camera (Figure 5.20 – image 1, red circle). Subsequently, the tear progressed along the length of the crash box corner, failure of the polymer core (Figure 5.20 – image 2) as well as delamination of the steel from the polymer (Figure 5.20 – image 3) was also observed.

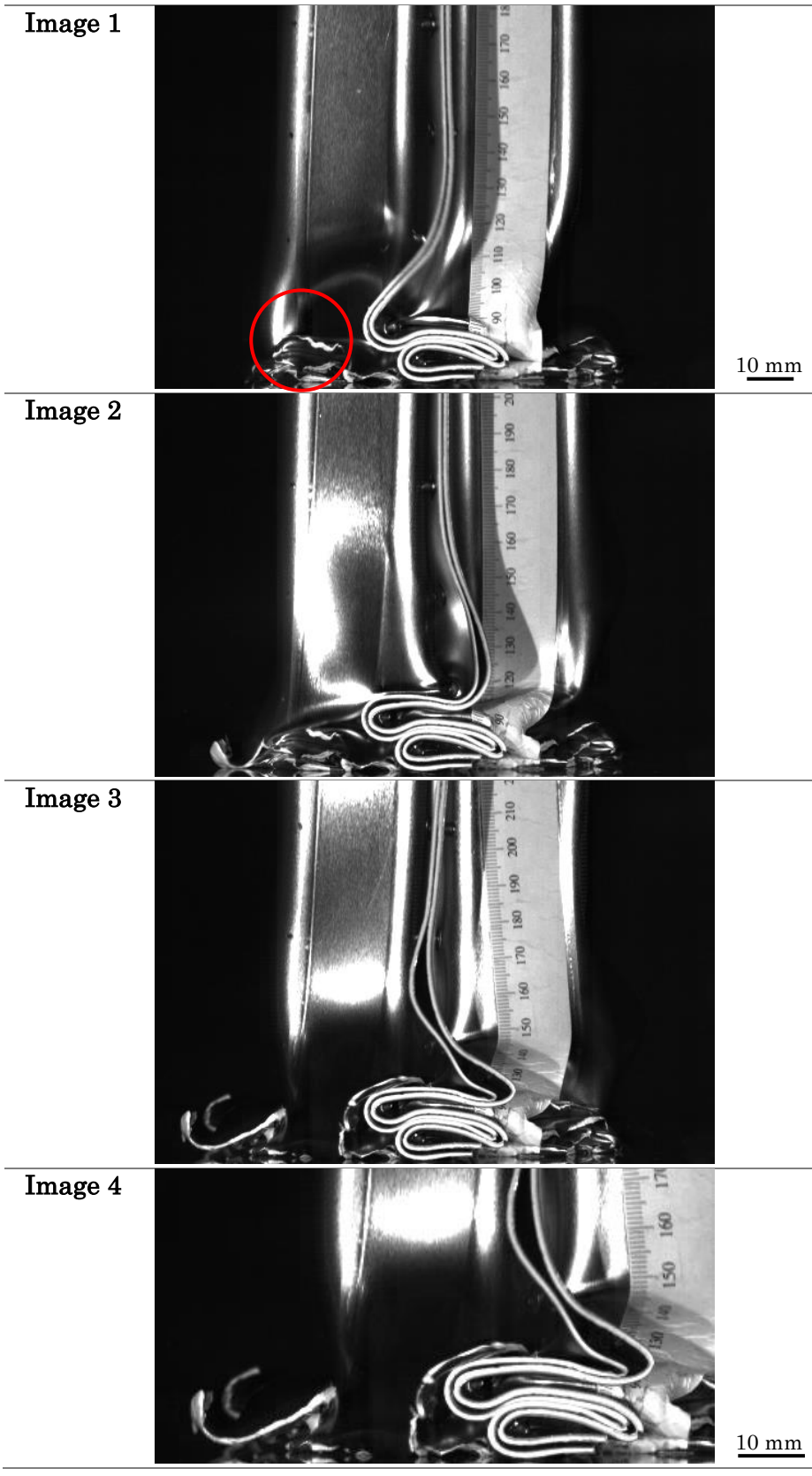

Figure 5.19 – Progression of failure seen in the double core Steelite. Images 1 to 4 – Lateral views. Image 4 – magnification of image 3.

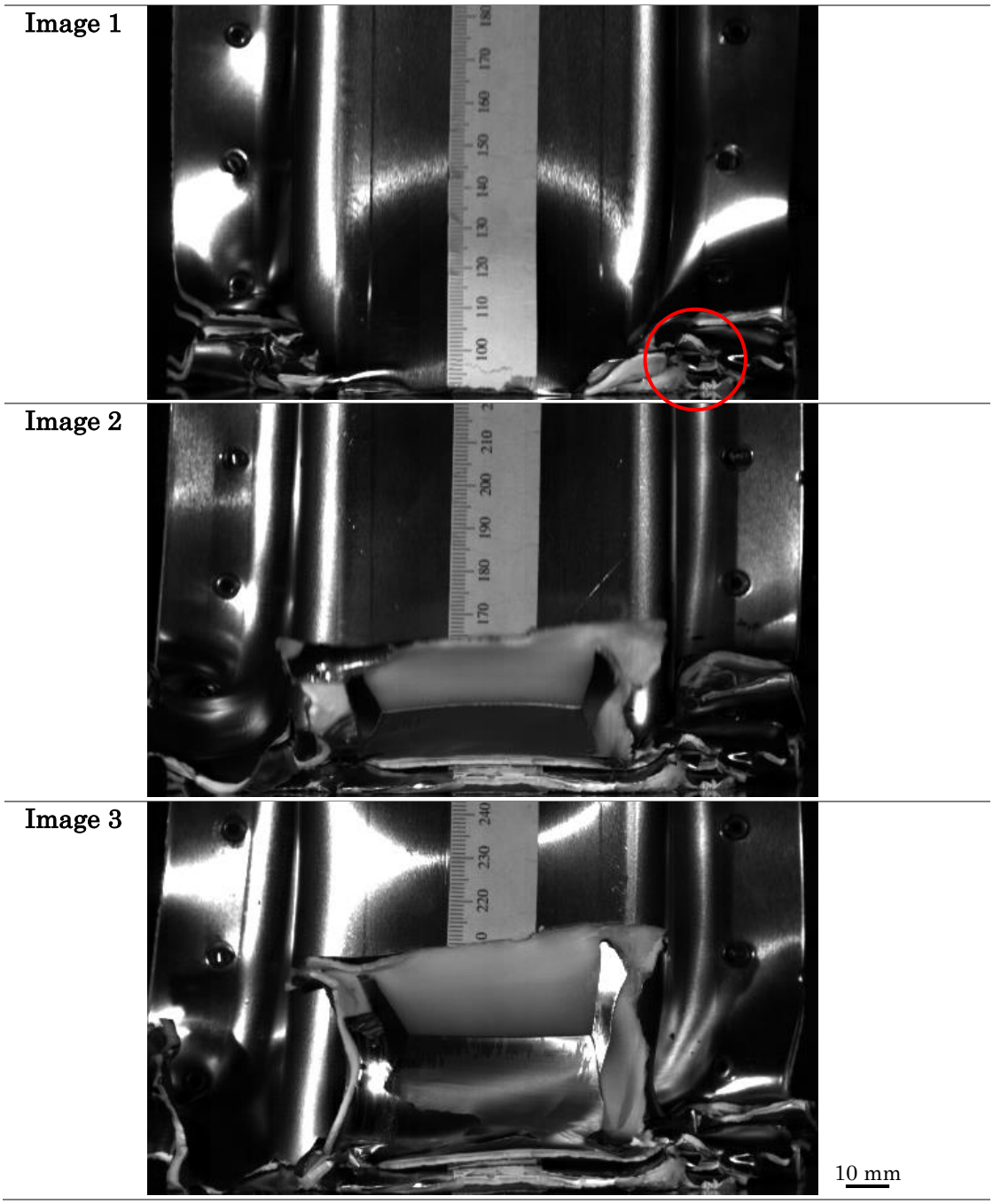

Figure 5.20 – Progression of failure seen in the triple core Steelite. Images 1 to 3 – Anterior views. Scale bar applies to all images.

Unstable collapse modes were more commonly observed in the single core material than in the double and triple core variants (Figure 5.21), this was due to the collapse modes being heavily geometry dependent [12], [13]. The crash structure began by collapsing asymmetrically (Figure 5.21 – image 1), which was most likely due to the initiators in the crash structure. Initiators forcing the crash structure to collapse in the asymmetric mode (described in Chapter 3). The onset of instability

occurred on the left hand side of the crash structure (Figure 5.21 – image 2), with full progression of unstable collapse following (Figure 5.21 – image 3). The left hand face of the crash structure instead of folding traversed over the previous fold, until the next fold began. This was attributed to the poor width to thickness ratio of the single core crash structures and the double hat geometry, increasing the likelihood of non–ideal collapse modes [12], [13]. However, the geometry choice was limited due to the available test energies.

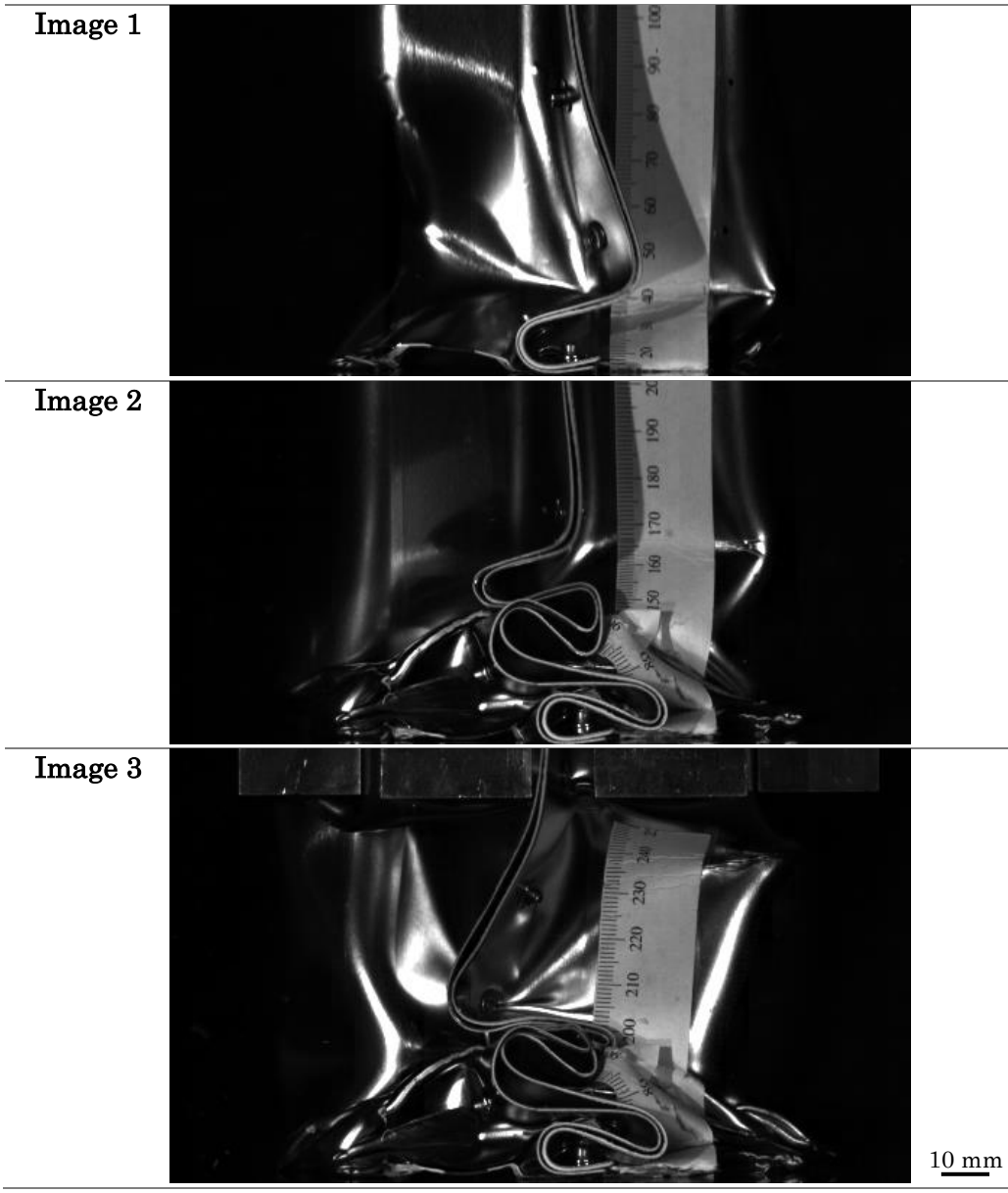

Figure 5.21 – Transition from progressive crushing (images 1 & 2) to unstable collapse (image 3) in single core Steelite sandwich material. Scale bar applies to all images.

5.4.4 Summary of Steelite impact test results

A linear relationship between the increase in core thickness and mean crush force has been determined for the Steelite sandwich (Figure 5.22 – green). The mean crush force increasing from 15.6 to 26.5 kN from single to double core and to 37.5 kN for the triple core variant. The peak impact force was found to increase with increasing sandwich thickness. However, it was difficult to evaluate since the crash structure initiators were produced manually (Figure 5.22 – red). The specific energy absorption (SEA) had a fairly linear trend also (Figure 5.22 – blue). Single core being 13.4 $J.g^{-1}$, double increasing to 18.6 $J.g^{-1}$ and triple up to 22.5 $J.g^{-1}$. With only three points of reference, any further analysis was performed using finite element analysis (see Chapter 7 – Performance prediction).

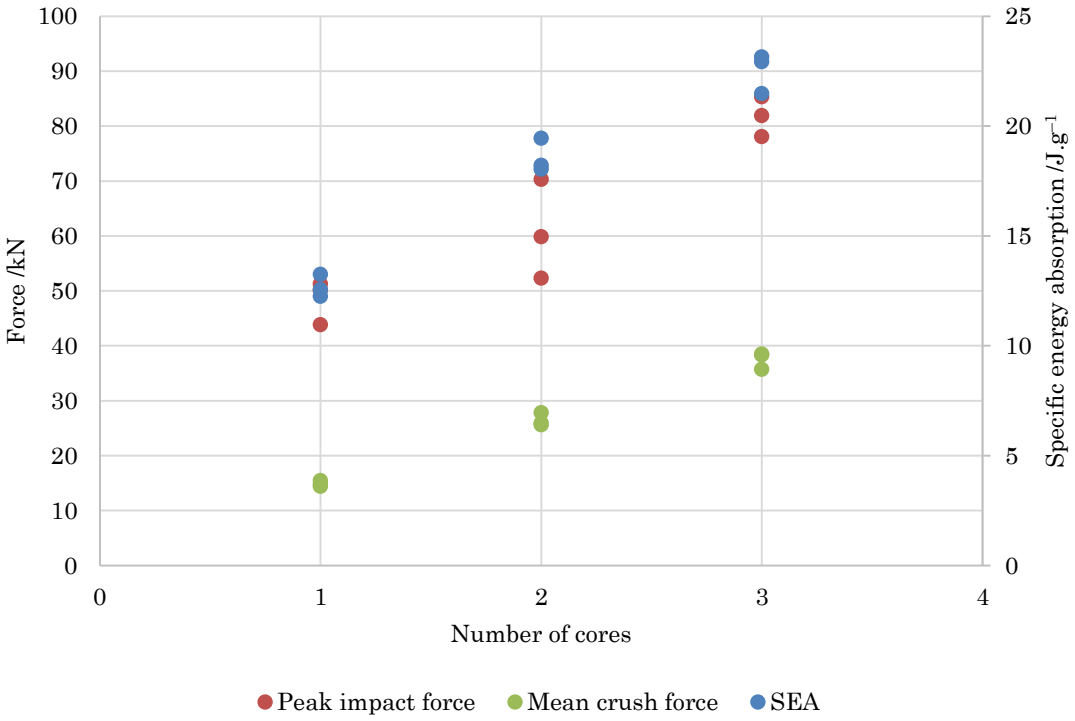

Figure 5.22 – Summarised results for the single, double and triple core variants of Steelite sandwich materials. The mean crush force (green), peak impact force (red) and specific energy absorption (blue) for the three repeat dynamic (impact) tests are shown.

5.5 0.3 mm ECCS sandwich quasi–static crush testing

A very flat response was seen in all ECCS sandwich materials (Figure 5.23) when quasi–statically crushed. This was different to the Steelite material, which exhibited more distinct oscillations. The peak force for the single core was 39.5 kN on average and an increase of approximately 20 kN was observed for each 0.7 mm increase in thickness of the polymer core. This is an increase on the Steelite, which saw a 10 kN increase in peak force per thickness increase and can be accounted for in the doubling in the thickness of the steel and in the increase in material strength.

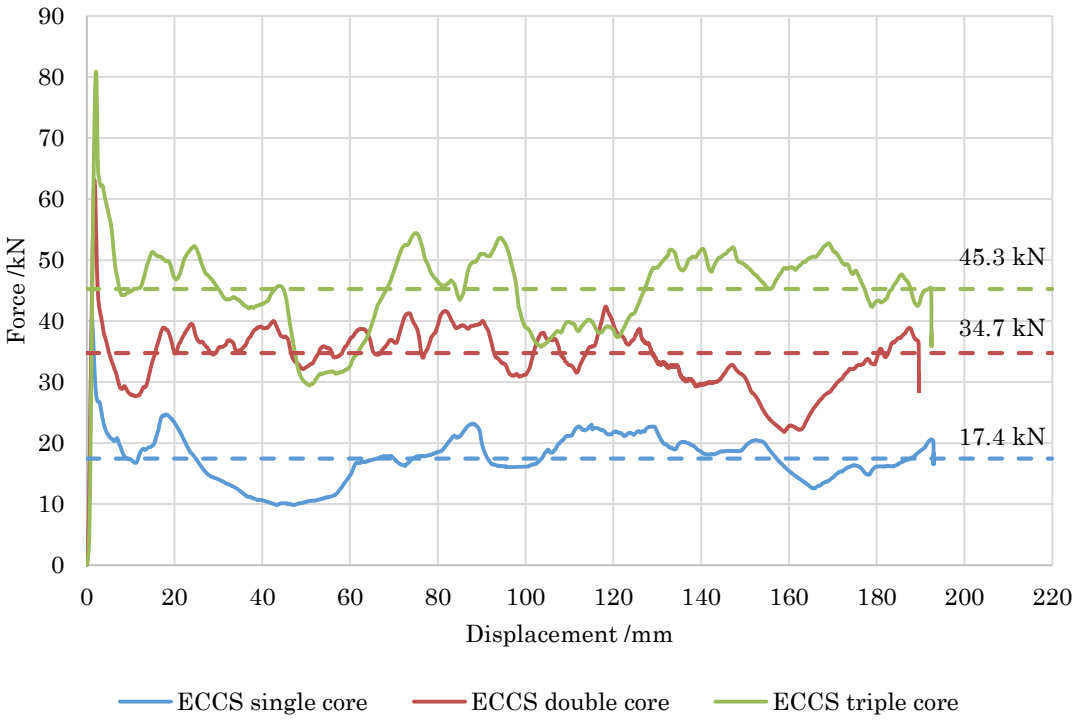

Figure 5.23 – ECCS quasi–static crush force–displacement results. A representative result for each core thickness is shown. The horizontal dashed lines show the mean crush force for the three repeats.

5.5.1 Image series

The deformation of the ECCS sandwich materials was in general reminiscent of metallic structures at all thicknesses, asymmetric collapse being the dominant mode of deformation. The single core variant showed the most inconsistent folding (Figure 5.24), this was most likely due to low thickness of the sandwich (1.3 mm) hence the crash structure having a small thickness to width ratio. The double (Figure 5.25) and triple core (Figure 5.26) materials having more consistent folding with larger fold radii.

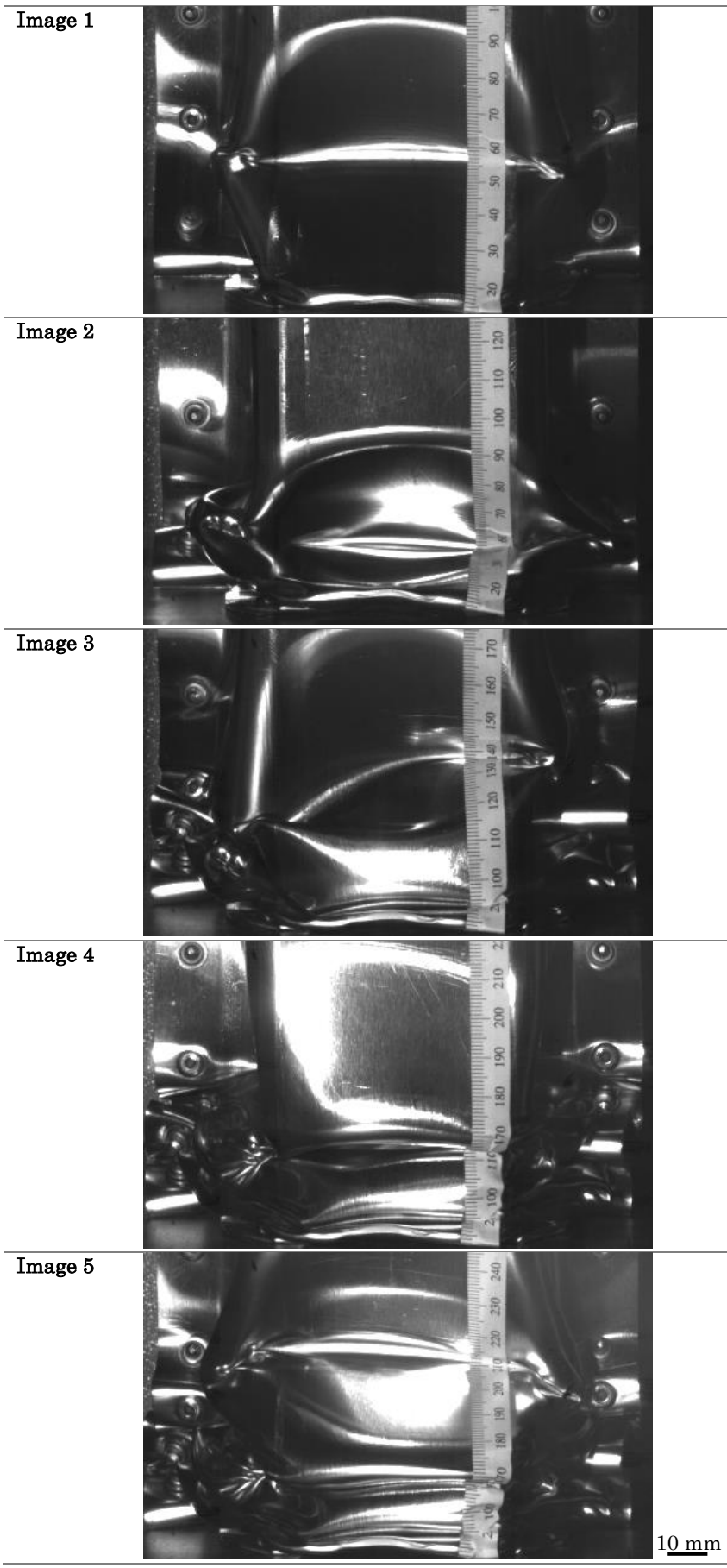

Figure 5.24 – Progressive crushing seen in the single core ECCS quasi–statically crushed. Scale bar applies to all images.

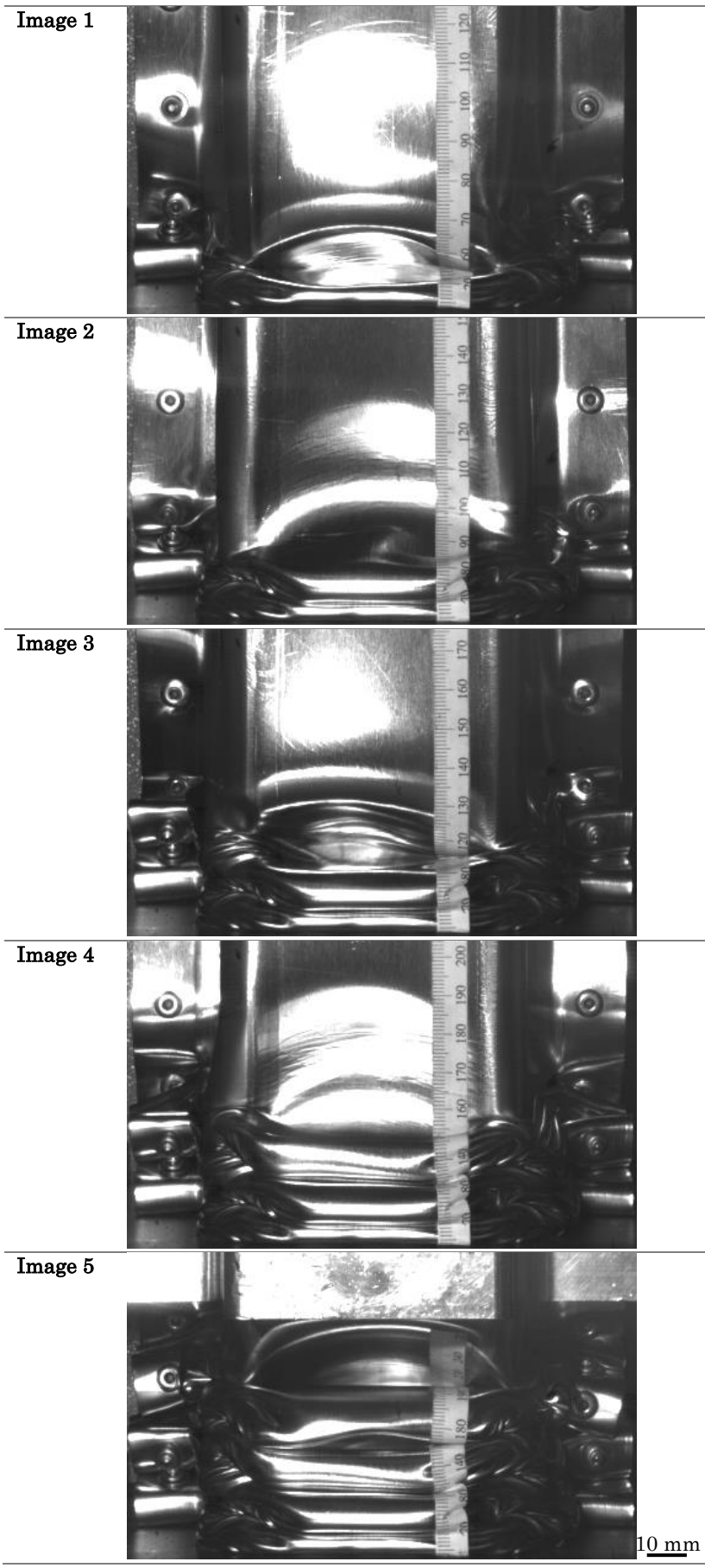

Figure 5.25 – Progressive crushing seen in the double core ECCS quasi–statically crushed. Scale bar applies to all images.

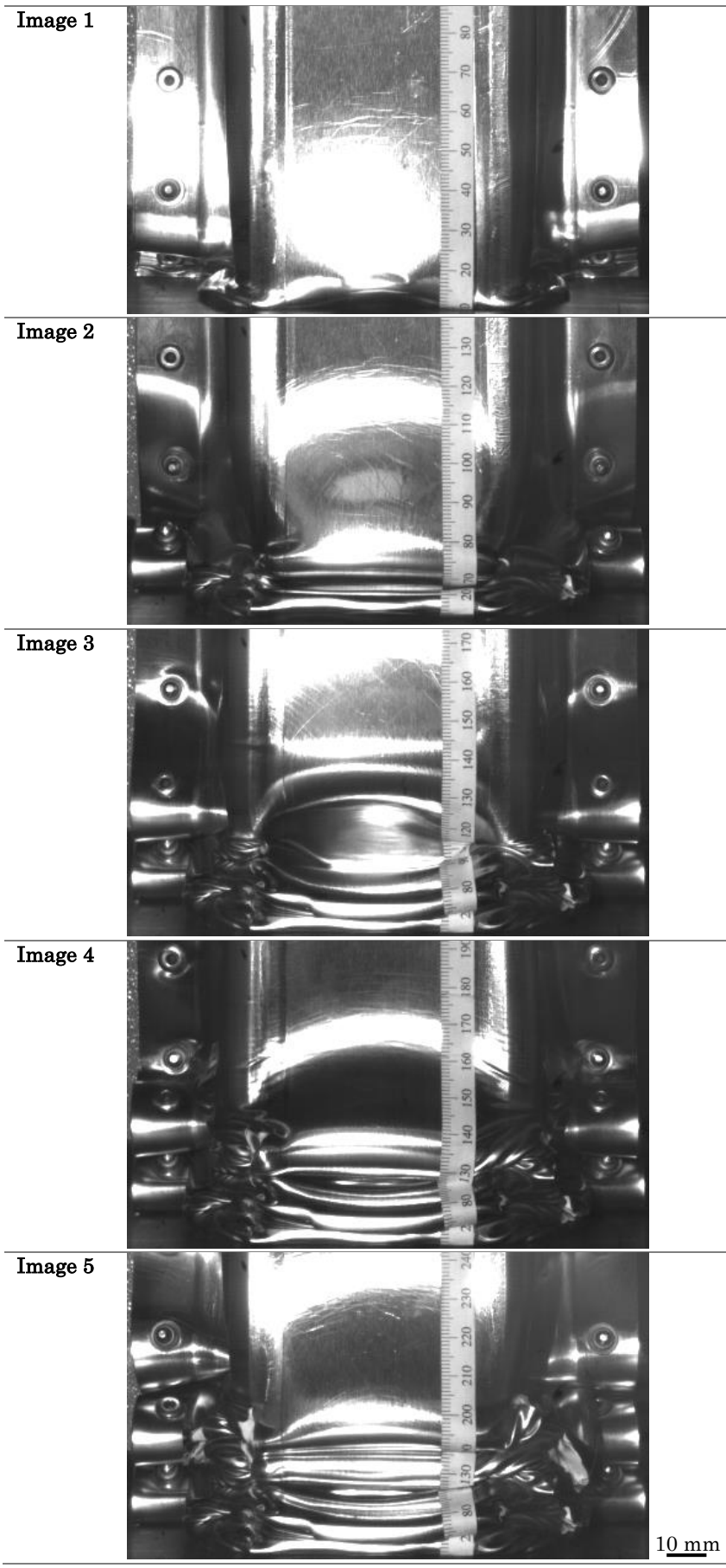

Figure 5.26 – Progressive crushing seen in the triple core ECCS quasi–statically crushed. Scale bar applies to all images.

The fold lengths in the single core variant were longer than expected, at 85 mm (Figure 5.27), and approximately the same as the monolithic 2.5 mm AC300 at 90 mm. Quasi–static crush of the material was highly repeatable with two crush tests shown (Figure 5.27– images 1 & 2) producing a near identical response in terms of wavelength and visual similarity.

Figure 5.27 also shows the plastic hinging seen in the monolithic metals (Section 5.2.3), however, a difference being crimping/wrinkling of the sandwich in the edges of the fold (Figure 5.27 – image 1 – red dashed circles).

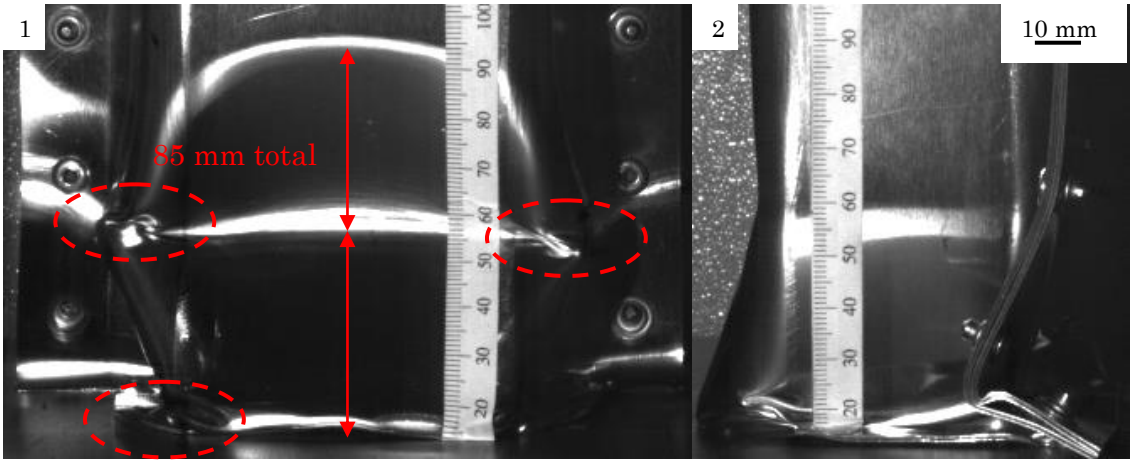

Figure 5.27 – Folding behaviour in single core ECCS material when quasi–statically crushed. Image 1 – Anterior view. Image 2 – Lateral view. Scale bar applies to both images.

With regards to the double and triple core, the corners of the structure showed considerable wrinkling (Figure 5.28 – red circles), far more than seen in the single core ECCS (Figure 5.27 – red dashed circles) where only a small amount of crimping/wrinkling was observed. The triple core also exhibited steel skin failure (Figure 5.28 – red dashed circle).

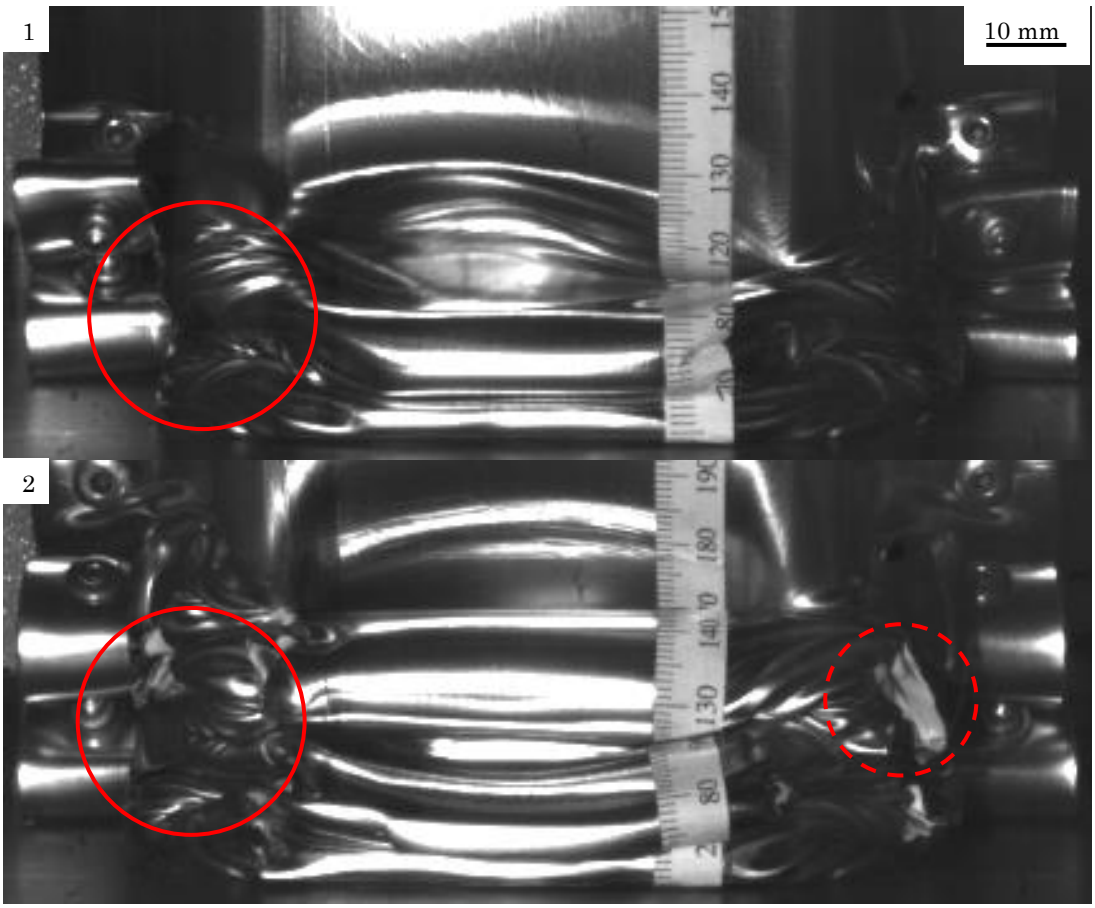

Figure 5.28 – Wrinkling behaviour in double (image 1) and triple (image 2) core ECCS crash structure corners shown by red circles. Red dashed circle shows failure of the metal skin. Scale bar applies to both images.

5.5.2 Summary of ECCS quasi–static testing results

The 0.3 mm ECCS sandwich materials showed an increasing trend with respect to core thickness, for peak force, mean crush force and SEA. Excellent repeatability was observed, especially for the mean crush force (Figure 5.29 – green) as the three repeats were within 6% of each other. There is a variation (range of 7 kN) in the peak force (Figure 5.29 – red) due to the manual method of initiator production. The SEA for the ECCS materials was between 8.6–17.9 $J.g^{-1}$. Since the ECCS crash structures were of the same geometry as the monolithic crash structures, a comparison is appropriate. The single and double core crash structures were in a low mean crush force range, however, the triple core was in a similar range to the AA5754 aluminium. The MCF and SEA of the aluminium alloy being 46.7 kN and 18.5 $J.g^{-1}$ respectively, in comparison to the ECCS triple sandwich which achieved 45.3 kN mean crush force and a SEA of 17.9 $J.g^{-1}$.

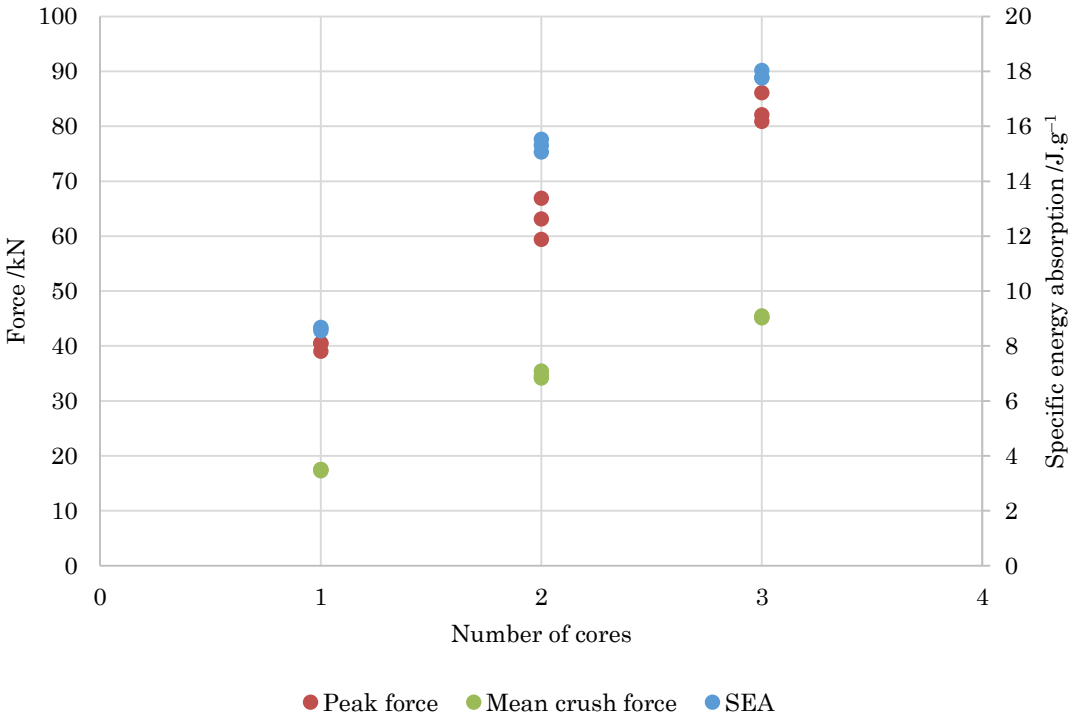

Figure 5.29 – Summarised results for the single, double and triple core variants of ECCS sandwich materials. The mean crush force, peak impact force and specific energy absorption for the three repeat quasi–static tests are shown.

5.6 0.3 mm ECCS sandwich drop testing

The drop tests for the ECCS sandwich materials are shown in Table 5.3, detailing the specimen mass, test impact speed and calculated impact energy.

Table 5.3 – Drop test energies for three repeat tests on ECCS sandwich materials.

Test name	Layup – skin/core/skin /mm	Mass /grams	Impact speed /m.s^{-1}	Impact energy /Joules
SC1	0.3 / 0.7 / 0.3	612	11.2	5.1
SC2	0.3 / 0.7 / 0.3	608	11.1	4.9
SC3	0.3 / 0.7 / 0.3	606	11.1	4.9
DC1	0.3 / 1.4 / 0.3	678	14.6	8.5
DC2	0.3 / 1.4 / 0.3	682	14.5	8.5
DC3	0.3 / 1.4 / 0.3	676	14.4	8.3
TC1	0.3 / 2.1 / 0.3	763	16.6	11.1
TC2	0.3 / 2.1 / 0.3	764	16.7	11.2
TC3	0.3 / 2.1 / 0.3	759	16.6	11.0

The response of all the ECCS sandwich materials was dominated by small irregular oscillations and the individual folds in the material are not distinguishable in the force–displacement plot (Figure 5.30).

As expected, the double core and triple core materials had an increased mean crush force over the single core material. The horizontal dashed lines (Figure 5.30) show the mean crush force values for each of the materials averaged over the three repeats. The double peak seen in the Steelite materials was not observed in the ECCS materials. Instead, the force reduced after the peak, consistent with the monolithic metals. The peak force itself increases from 90 to 120 and 180 kN (single, double and triple respectively) compared to 40, 60 and 80 kN (single, double and triple respectively) for the quasi–static tests, essentially doubling from

static to dynamic. The increase in peak impact force dynamically over quasi–statically was consistent with the monolithic metal crash structures of the same geometry. The monolithic metals dynamic peak force increase ranged between 50 % to 215 %. Whereas, the ECCS sandwich materials showed an increase between 100 and 125 % increase in peak force dynamically over quasi–statically.

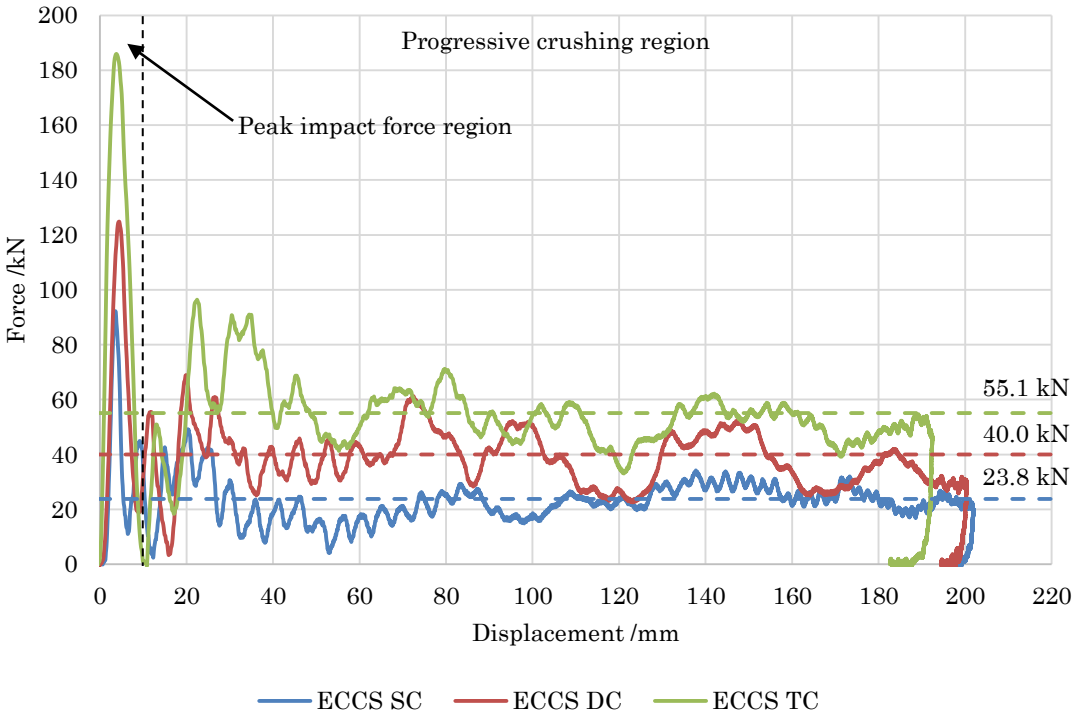

Figure 5.30 – ECCS sandwich material force–displacement response when drop tested. The horizontal dashed lines show the mean crush force for the three repeats.

5.6.1 Rate of energy absorption

Figure 5.31 shows the integrated energy–displacement plots for all three thicknesses of ECCS sandwich. The single core sandwich absorbed on average 4.8 kJ, double core sandwich averaged 7.95 kJ and triple core absorbed 10.7 kJ. The repeatability of the tests can be seen in the energy–displacement. The energy absorption was approximately linear over the entirety of the length of the crush as was seen in the monolithic metals and the Steelite sandwich materials. The gradient difference between double and triple core was less than that between

single and double core suggesting a diminishing return when increasing the core thickness, however, this cannot be definitively stated from three points of reference. Factors seen in the Steelite sandwich materials such as crash structure instability were not seen in the ECCS sandwich materials due to the single hat geometry and thicker material. However, the results in Figure 5.31 would suggest the instability seen in the Steelite sandwich materials had little effect on the mean crush force result.

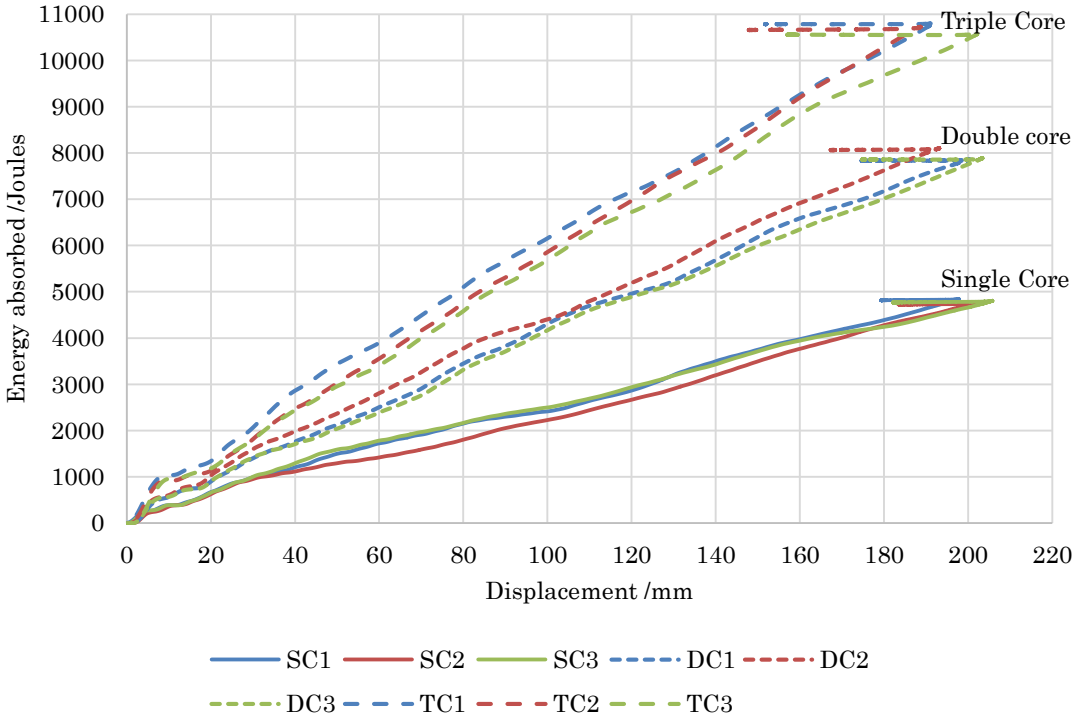

Figure 5.31 – Cumulative energy–displacement results for ECCS sandwich material dynamic (impact) tests. All three repeats for each core thickness (single, double and triple core) are shown.

5.6.2 Image series

The characteristics of the ECCS single core sandwich are similar to the Steelite sandwich material with respect to the folding; conventional folding modes occurred, however, the folds exhibited small radii (Figure 5.32 – image 1 and 2). The range of the fold radius being between 2 mm and 4.5 mm, Figure 5.33 – image 2 shows the small radius aptly.

Failure was less commonly observed in the steel skin of the ECCS SC material (Figure 5.32 – image 1) in comparison to the Steelite sandwich materials, this is attributed to the increased steel thickness. Increased steel thickness reduces the overall stress through thickness hence, reducing the likelihood of failure.

A stiffer response was seen in the double core ECCS sandwich material. The side profile shows the folding formation is regular, although untidy in comparison to monolithic metals (Figure 5.35). Individual folds flattened into one another as was previously observed with the Steelite materials when impacted (see Section 5.3).

Closer inspection of the deformation showed the more symmetric folding response of the double core ECCS sandwich (Figure 5.32 – image 2) over the single core sandwich (Figure 5.32 – image 1). The symmetric folding is advantageous due to its predictability and repeatability. The combination of thicker steel (0.3 mm) with the double core (1.4 mm) of polypropylene produced a visually more conventional fold. Although, the folds had a smaller radius than the monolithic steels and aluminium alloys (see Section 5.2.3 for monolithic crash structure deformation). Smaller radii folds allowed for a greater number of folds per length of crash box hence, increasing the amount of material undergoing significant strain, increasing the energy absorption of the crash structure. The double core sandwich produced four folds (Figure 5.32 – image 2) whereas; the monolithic metals had two to three folds over the same length.

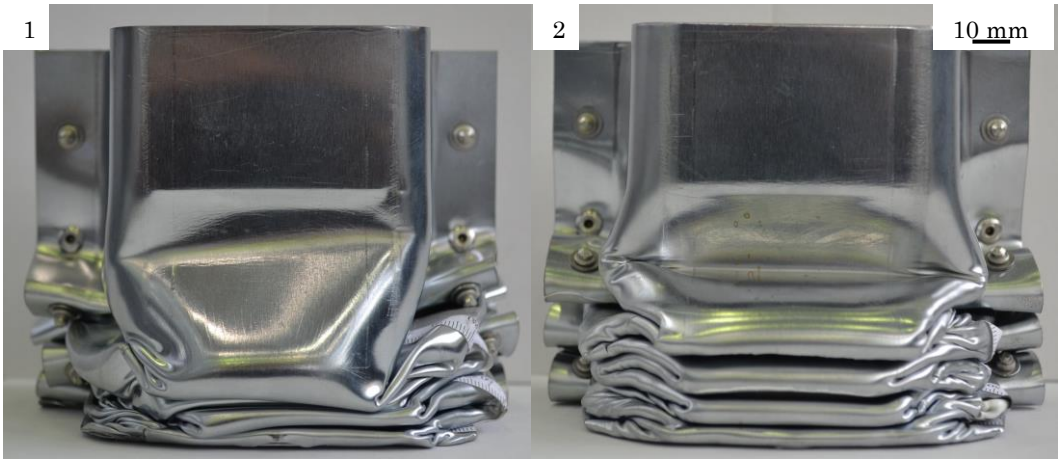

Figure 5.32 – ECCS crash structures impacted at 11 (image 1) and 14.5 $m.s^{-1}$ (image 2) respectively. Image 1 – ECCS SC and Image 2 – ECCS DC. Scale bar applies to both images.

The corners of the sandwich crash structures produced both long and short folds (Figure 5.33) as reported previously by Mohr & Wierzbicki [14] for axially crushing steel sandwich materials with fibre–reinforced cores. The short folds are particularly apparent in the double core crash structures (Figure 5.33 – image 2).

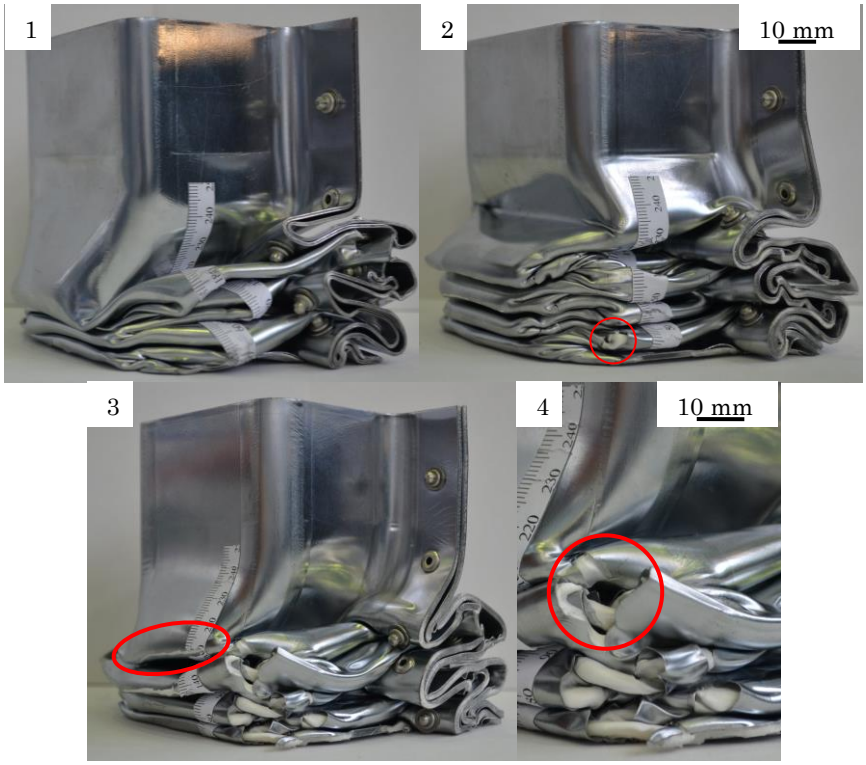

Figure 5.33 – Long and short fold transitions in single (image 1) and double (image 2) core ECCS sandwich materials, compared to material failure in the triple (image 3) core sandwich. Image 4 is image 3 magnified.

The triple core sandwich exhibited failure of the steel skin in the corners (Figure 5.33 – image 3 and – image 4). Increased bending strain in production and the large strains undergone by the corners increased the likelihood of steel skin failure. Noticeably, when the skin of the triple core sandwich failed in the corners, the bond between the steel and the polypropylene core failed (Figure 5.33 – image 4). Whereas, when quasi–statically testing the bond (see Chapter 3) the polymer core itself failed through thickness, suggesting the bond strength may well be strain rate dependent.

In general, the polypropylene core did not fail when the steel skin failed (Figure 5.33 – image 3); the polypropylene remained intact and conformed to the shape of the corner fold. The reason for the polypropylene not failing was deemed to be its greater ductility than the steel.

The outer steel skin of a fold failed in tension therefore, the inner steel skin was in compression. Hence, the inner steel skin did not fracture and remained bonded to the polypropylene core. The straight sections of the crash structure also showed skin failure (Figure 5.33 – image 3, red ellipse); this was due to the plane–strain tensile loading along the plastic hinge.

There were instances of the entire sandwich failing through thickness (Figure 5.33 – image 4, red circle). From video analysis, the reason for the failure was determined to be the loading of the sandwich changing once one of the steel skins failed in tension. The compressed side of the sandwich then could not sustain the load applied and failed in compression.

The fold wavelength was seen to decrease in the ECCS with increasing skin thickness. The first fold after the peak impact was used as the reference for this fold wavelength, as it is the easiest to identify, therefore, the most repeatable value to measure. The fold wavelengths were approximately 80, 65, 65 mm for single,

double and triple core respectively, being consistently shorter in length than the monolithic metals of similar thickness and geometry (approximately 90 mm). However, these folds are much more compacted with flatter radii (discussed previously); hence, more folds were produced from the crash structure length (Figure 5.34, Figure 5.35 and Figure 5.36).

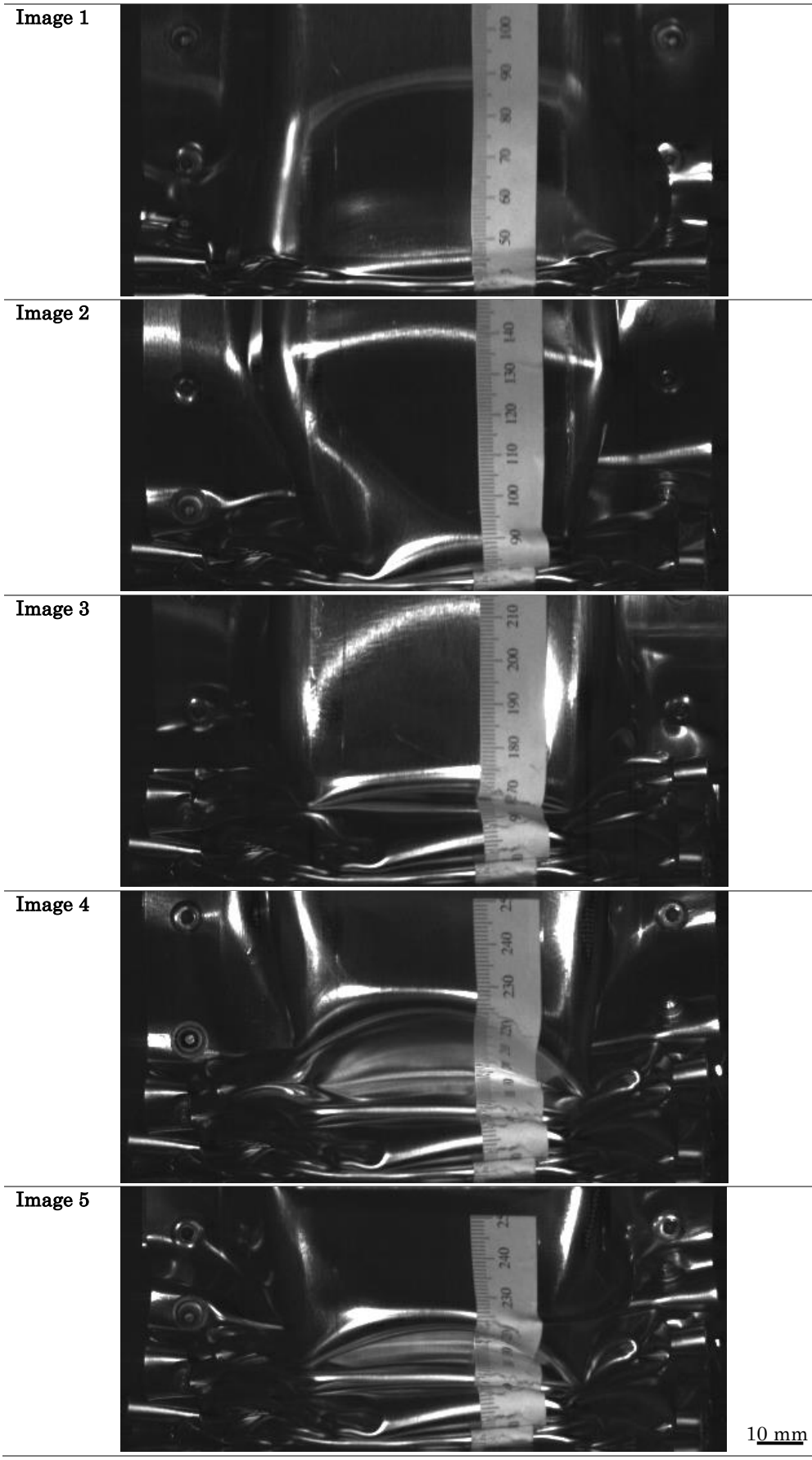

Figure 5.34 – Progressive crushing seen in the single core ECCS for a 4.9 kJ impact at 11.0 $m.s^{-1}$. Images 1 to 5 – Anterior views. Scale bar applies to all images.

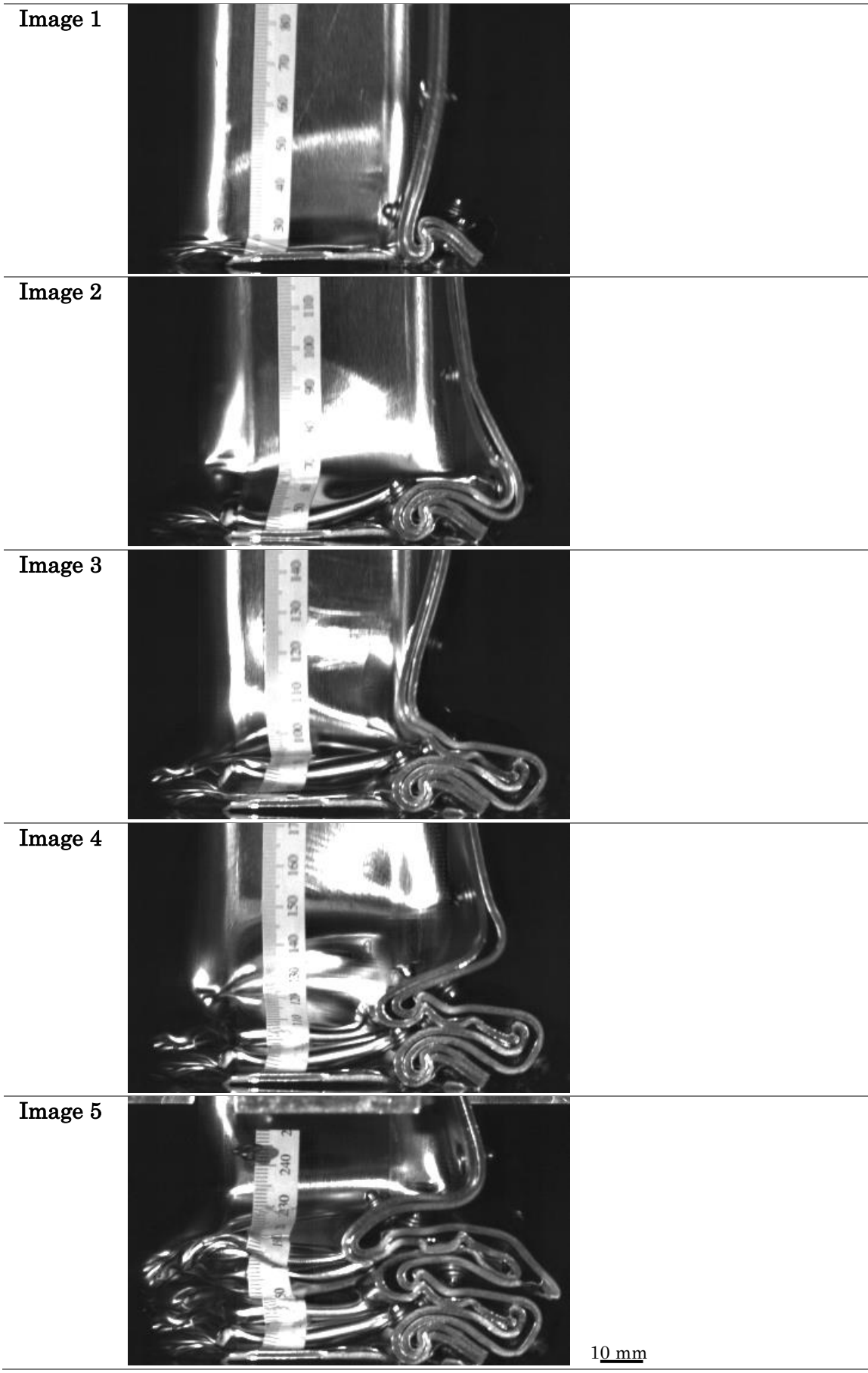

Figure 5.35 – Progressive crushing seen in the double core ECCS for an 8.4 kJ impact at 14.5 $m.s^{-1}$.

Images 1 to 5 – Lateral views. Scale bar applies to all images.

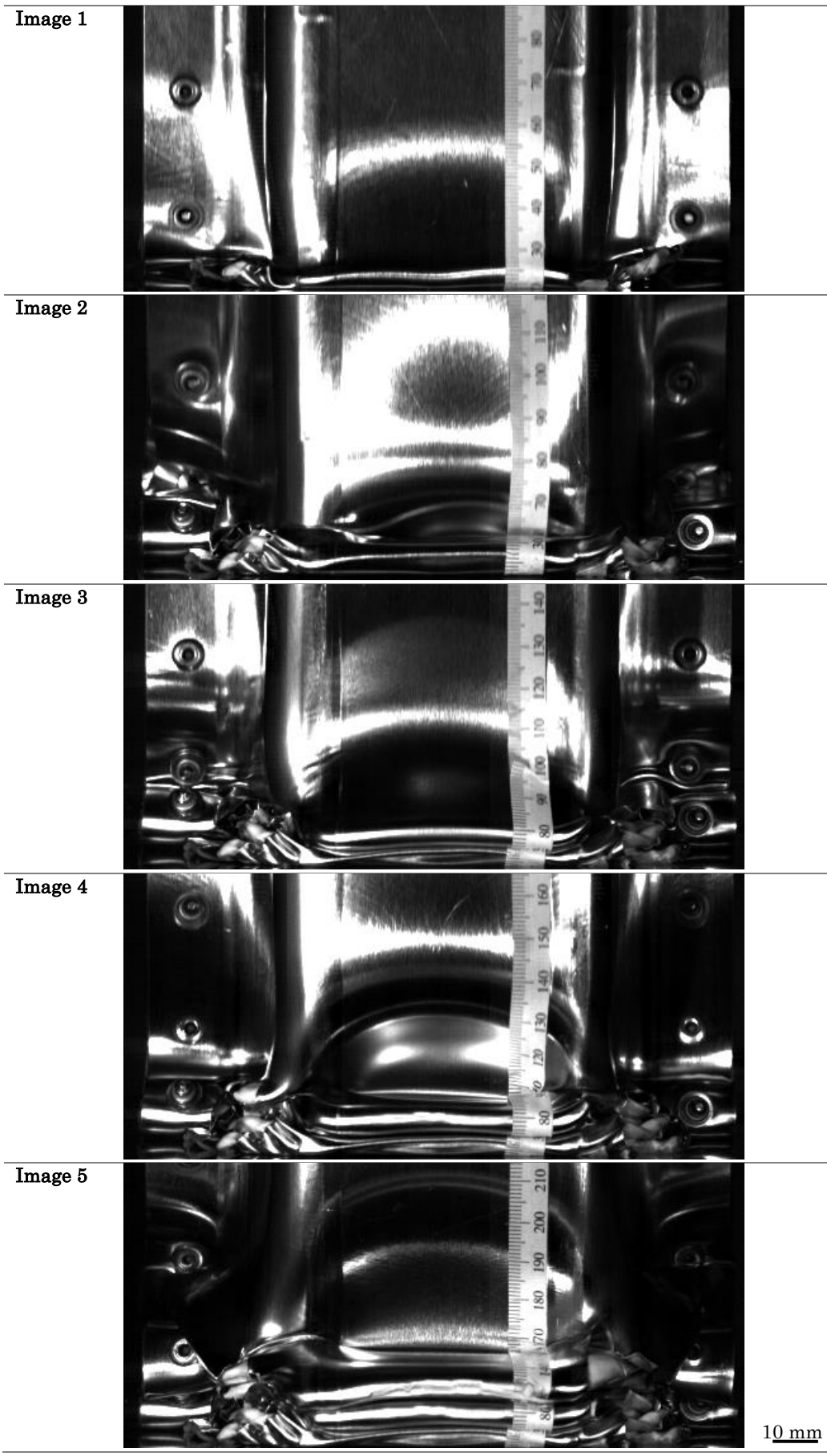

Figure 5.36 – Progressive crushing seen in the triple core ECCS for a 11.1 kJ impact at 16.6 m.s^{-1}. Images 1 to 5 – Anterior views. Scale bar applies to all images.

5.6.3 Summary of ECCS sandwich drop test results

Figure 5.37 shows the summarised outputs from the drop testing on the ECCS sandwich materials in all three forms (single, double and triple core). The linear increase in mean crush force witnessed in Steelite impact tests was also seen in the ECCS sandwich.

Under impact conditions the ECCS single core achieved 11.7 $J.g^{-1}$, double core achieved 17.7 $J.g^{-1}$ and the triple core attained 21.7 $J.g^{-1}$. The triple core reaching both the mean crush force (55.2 kN) and specific energy absorption (22.3 $J.g^{-1}$) of the AC300 aluminium alloy.

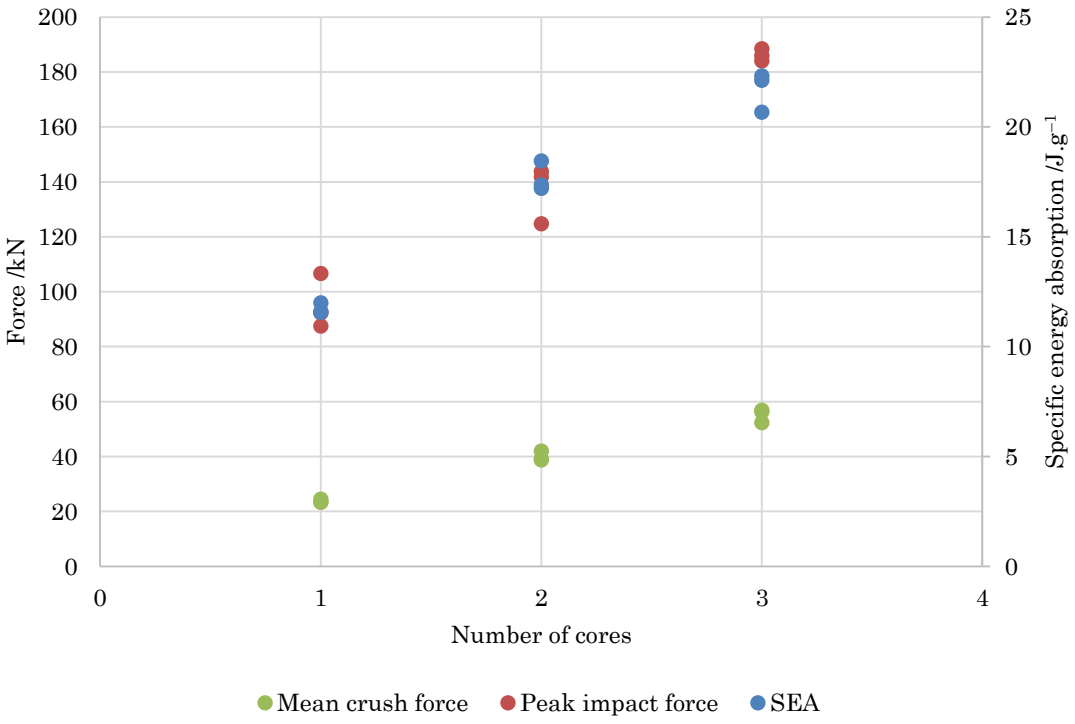

Figure 5.37 – Summarised results for the single, double and triple core variants of ECCS sandwich materials. The mean crush force, peak impact force and specific energy absorption for the three repeat dynamic (impact) tests are shown.

5.7 0.5 mm DP600 sandwich quasi–static crush testing

Quasi—static crush testing was only performed on the press–formed single hat DP600 sandwich (DPSW) crash structures. This was due to the low bond strength in this material preventing double and triple core variants being produced (discussed in Chapter 3). These press–formed DPSW crash structures produced a flat crushing force response (Figure 5.38), the magnitude of the oscillations in the progressive crushing region were small in comparison to the Steelite sandwich and the monolithic metals. Even so, the crushing force was repeatable even with the variable adhesive strength exhibited by the material (see Chapter 3).

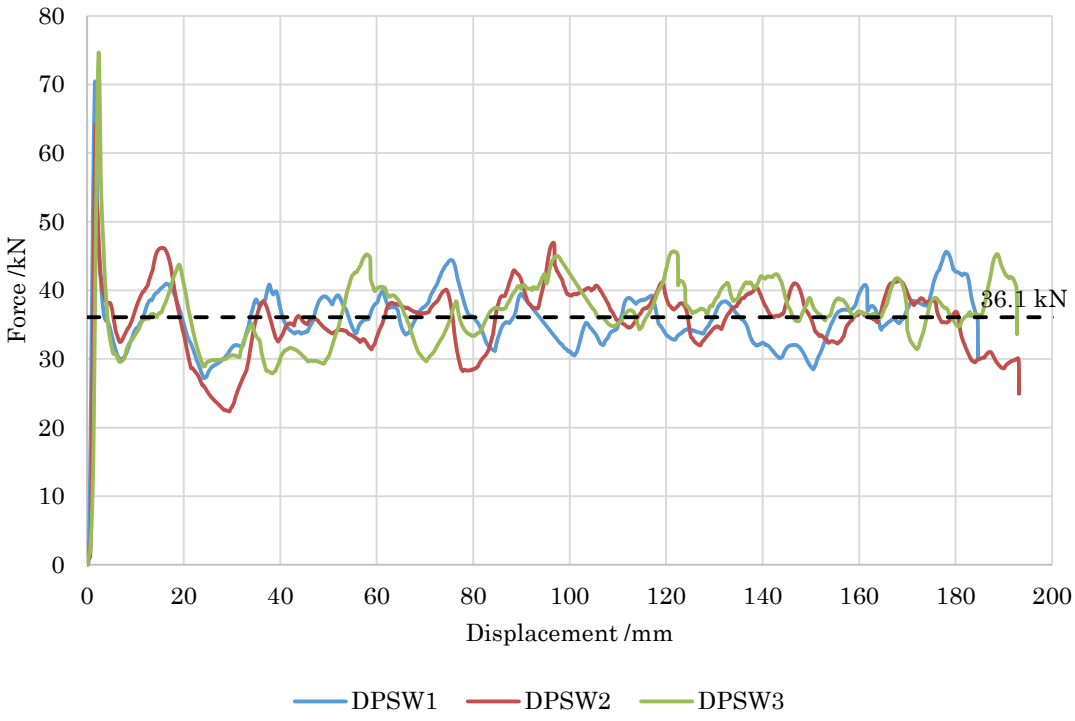

Figure 5.38 – Single core DP600 sandwich quasi–static crush force–displacement results. The horizontal dashed lines show the mean crush force for the three repeat tests plotted.

5.7.1 Images series

The DPSW sandwich exhibited a small fold radius (in the range of 40 mm) when quasi–statically crushed (Figure 5.39, images 1–5). The number of folds in comparison to the Steelite and ECCS sandwich materials was noteworthy; the expectation of the DPSW was to have larger radius folds due to the thickness of the steel in the sandwich (total 1.0 mm). However, the deformation concurs with the force–displacement result seen. The larger number of small folds manifesting a higher frequency of force oscillations.

The deformation mode observed was the conventional asymmetric folding much like the previous sandwich materials tested, and only stable collapse modes were witnessed (Figure 5.40). The deformation occurred along the entire free length of the crash structure without any sign of bottoming out in the force (Figure 5.38). If bottoming out occurred, a sharp rise in the force would have be observed at the end of the test. The lack of bottoming out was due to the small fold wavelength witnessed.

Failure of the blind rivets joining the backplate to the stamp formed top hat was common (Figure 5.40 – image 2 – red circles); however, it was felt this did not weaken the crash structure since the rivet was ejected towards the end of the fold. The ejected rivet showed no sign of failure or damage upon examination, instead the rivets had punctured the sandwich material. Therefore, failure of the joint was adjudged to be due to the small radius folds of the DPSW material causing removal of the rivet. Since the sandwich material occupied the space of the rivet. Additionally, due to the thickness and ductility of the 0.5 mm DP600 steel, no failure of the skin was observed, even with the tight radius of the folds.

Image 1

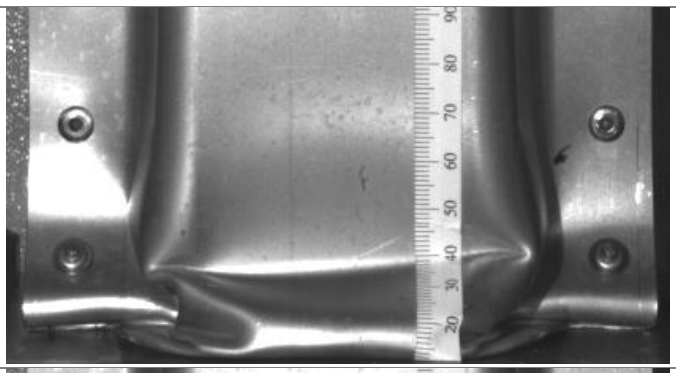

Image 2

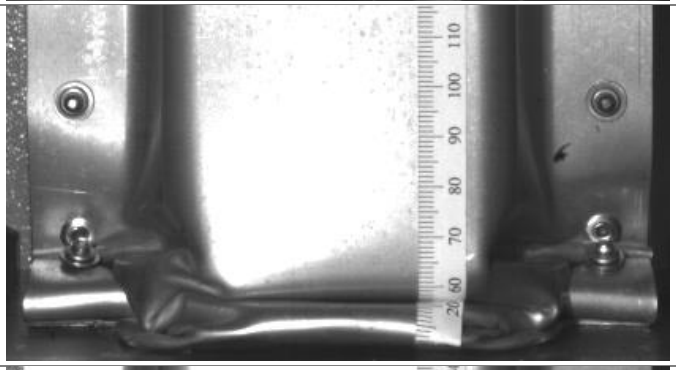

Image 3

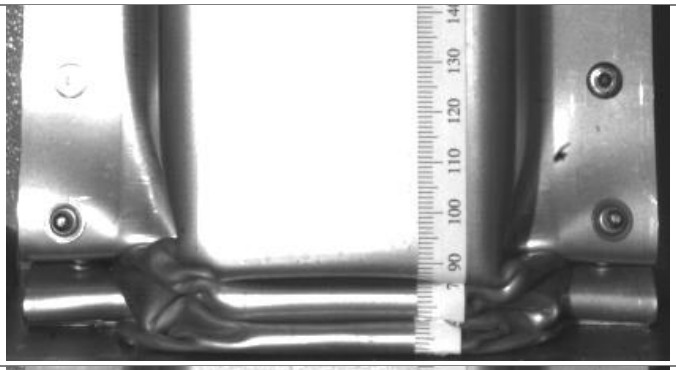

Image 4

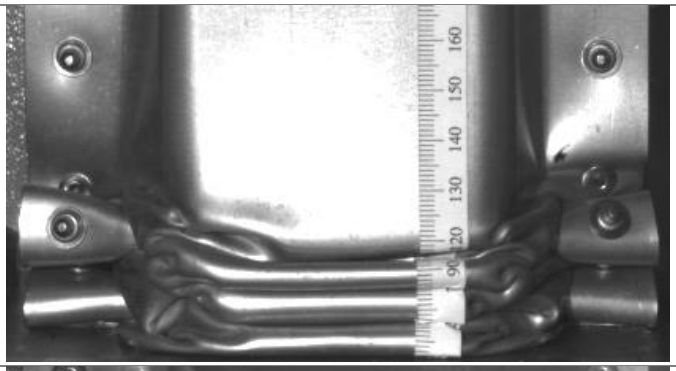

Image 5

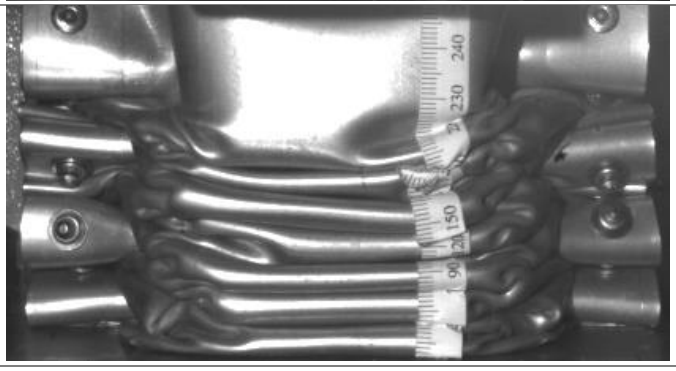

Figure 5.39 – Progressive crushing seen in the single core DP600 sandwich quasi–statically crushed. 1 to 5 – Lateral views.

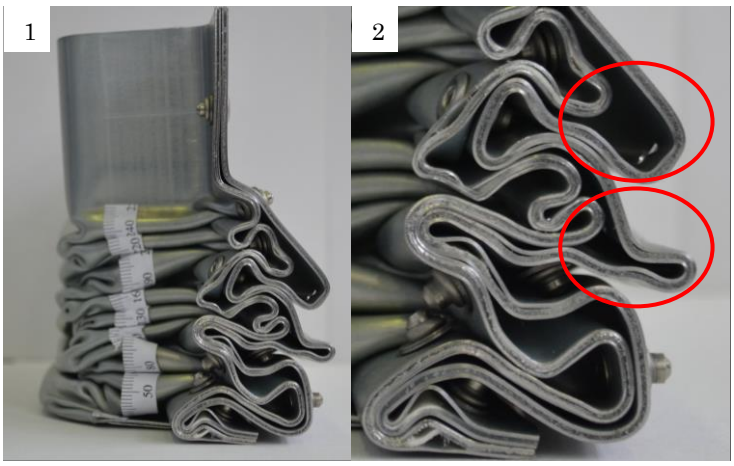

Figure 5.40 – Small fold radii seen in the single core DP600 sandwich material. Failure of blind rivet joints highlighted with red ellipses. Image 2 is a magnified version of image 1.

5.7.2 Summary

Figure 5.41 shows the mean crush force (green), peak impact force (red) and the SEA (blue) for the three repeat quasi–static tests on the DPSW. The mean crush force for the material and geometry combination is 36.1 kN, the SEA is 12.5 $J.g^{-1}$ compared to 1.6 mm DP600 at 64 kN producing 14 $J.g^{-1}$. The ratio of peak to mean crush force is similar to the 2.0 mm thick ECCS double core (ECCS DC) sandwich when quasi–statically crushed. However, the specific energy absorption is lower (ECCS DC attains an SEA around 15 $J.g^{-1}$). This was due to the polymer to steel ratio in the ECCS DC sandwich (1.4:0.6) being higher than the DPSW (0.7:1.0) and the greater total thickness of the ECCS double core.

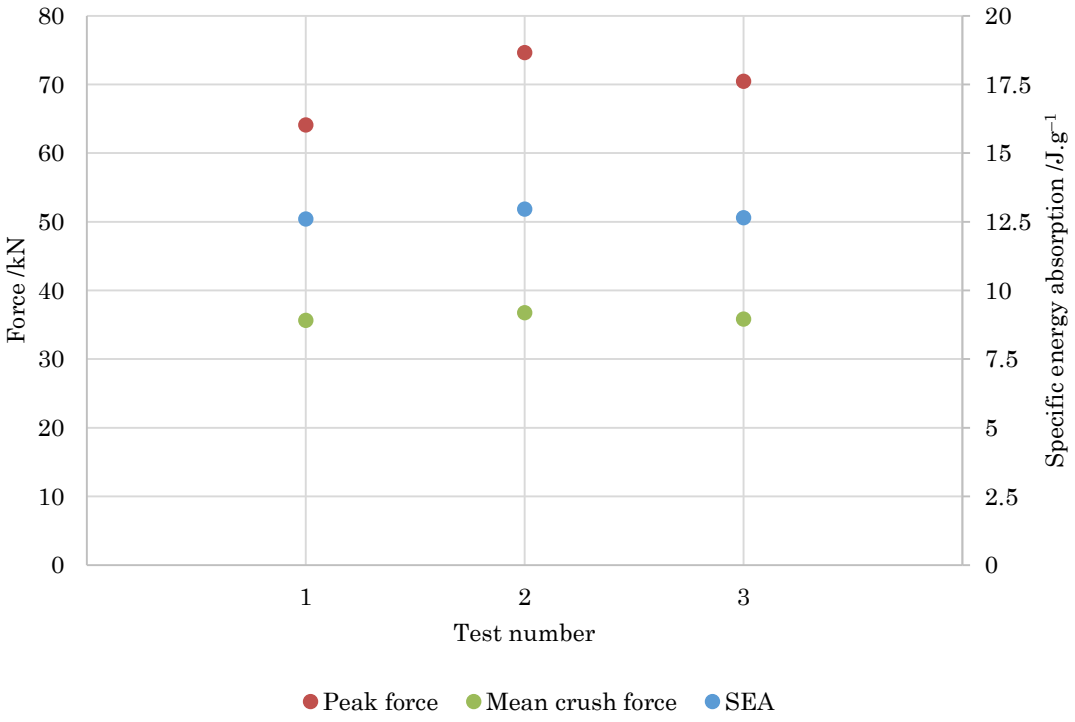

Figure 5.41 – Summarised results for the single core variant of DP600 sandwich material in the press–formed geometry. The mean crush force, peak impact force and specific energy absorption for the three repeat quasi–static crush tests are shown.

5.8 0.5 mm DP600 sandwich drop testing

Both the press–formed and press brake bent geometries of DP600 sandwich materials (DPSW) were crash tested. The first described is the press formed single hat to compare to the quasi–static testing (Section 5.7). The 77 × 58.5 mm press brake bent geometry is then detailed; this was the same geometry as the monolithic materials as well as the ECCS sandwich materials. Layup of the DPSW material tested in all instances was 0.5/0.7/0.5 mm (steel/PP/steel).

At the time of testing the press brake bent crash structures; the drop tower was operating at a reduced capacity of 4 kJ due to damage sustained by the test equipment. Therefore, the first of the three produced press brake bent crash structures was impacted three times, twice at 4 kJ and once at 2 kJ to completely deform the crash box (named 4–4–2 kJ test). The top hat and backplate were joined using self–pierced rivets (SPRs).

The second was joined using blind rivets and tested at 4 kJ, although the crushing performance was similar to the SPR joined sample, the joint eventually failed, causing the backplate to peel from the top hat. This crash structure was therefore, not impacted further.

The third crash structure was tested with 9.7 kJ at Tata Steel R&D Centre, IJmuiden, Netherlands (with their kind permission) whilst the department drop tower was out of order. The result was comparable; however, there were some differences in testing. First, the drop tower used free drop height to achieve impact speed. Second, the impact mass was 104 kg (24 kg higher than the university drop tower). Third, the crash structure was attached to the load cell, and impacted by the falling mass rather than being attached to the falling mass. Due to the higher mass, the impact velocity was lower to achieve the same impact

energy. The 30 kHz data collection rate was ample for both load and laser displacement.

Table 5.4 – Drop test energies for all tests on single core DP600 sandwich materials in the press–formed geometry.

Test name	Joining method	Mass /grams	Impact speed /m.s^{-1}	Impact energy /kJ
DPSW–1–1	Blind rivet	845	10.6	4.4
DPSW–1–2	Blind rivet	845	10.3	4.2
DPSW–2	Blind rivet	852	14.6	8.5
DPSW–3	Blind rivet	850	15.6	9.6
DPSW–4	Blind rivet	851	15.1	9.0
DPSW–5	Blind rivet	854	15.3	9.3

Table 5.5 – Drop test energies for all tests on DPSW sandwich materials in the press brake bent geometry.

Test name	Joining method	Mass /grams	Impact speed /m.s^{-1}	Impact energy /kJ
4–4–2 kJ	SPR	937	10.5–10.5–7.2	10.5
IJmuiden 9.7 kJ	SPR	932	15.1	11.8

5.8.1 Press–formed single hat crash structure

The force–displacement response of the DPSW material was much like the quasi–static response with small oscillations in the force (Figure 5.42). The first crash structure was tested twice at low energy to ensure the bond strength was adequate and to ascertain a full impact energy. The occurrence of failure of the sandwich led to a large variation in the results. The first two results outlined, DPSW–2 and DPSW–3 (Figure 5.42 – blue and Figure 5.42 – red), had a mean crush force of 45 kN (Figure 5.42 – black dashed). Both had a similar response even with the increase in impact energy between the two tests. However, in subsequent tests (DPSW–4 and DPSW–5), a reduction in the mean crush force was observed. The mean crush force results were 34.8 and 38.7 kN for tests DPSW–4 and DPSW–5 respectively.

The reduction in mean crush force was due to delamination of the sandwich. The adhesive failure led to a reduction in material stiffness and the inability for the core to transmit shear between layers, therefore, the material behaved as two individual sheets. This meant the energy input was not absorbed by the crash structure. Hence, the crash structure bottomed out between 200 and 225 mm displacement (Figure 5.42 – green). After this point, the buffers of the drop tower absorbed the remaining energy the crash structure was not able to absorb. The height of the buffers set to allow approximately 220 mm displacement before being activated. This remaining unabsorbed energy was also not recorded in the force–displacement history since at the point of contact with the buffers the load cell is no longer active in the test.

The failure of the adhesive was detrimental to the performance of the crash structure, leading to a mean crush force of 36.7 kN (Figure 5.42 – dotted) *versus* 45 kN (Figure 5.42 – dashed) for the successful impacts. The point at which failure

occurred is seen as a drop in force (Figure 5.42 – red dashed circle on green line). This is more conspicuous in the energy–displacement plot (Figure 5.43 – red circles).

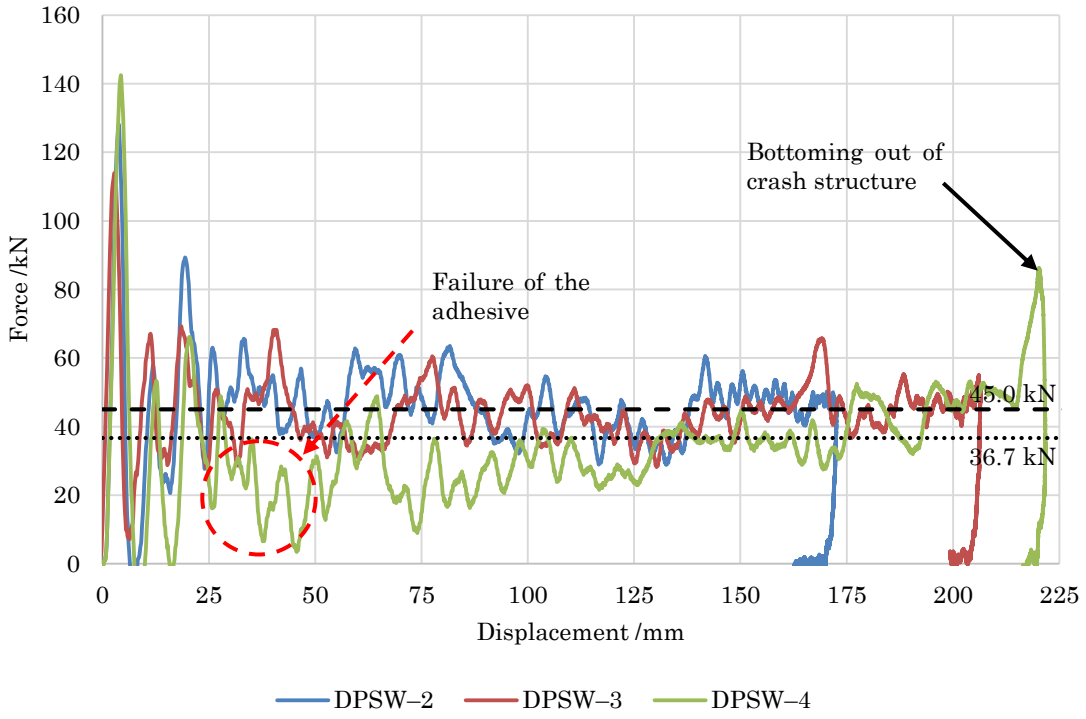

Figure 5.42 – Single core DP600 sandwich impact test results for the press–formed crash structures. The force–displacement data is shown for three impact tests. The horizontal dashed line shows the mean crush force for the successful tests. The horizontal dotted line shows the mean crush force for the tests where failure of the adhesive occurred. DPSW–5 is omitted for clarity.

5.8.1.1 Rate of energy absorption

The energy–displacement plots clearly show the difference in performance due to sandwich material delamination. The first two tests (Figure 5.43 – blue and Figure 5.43 – red) can be seen to have a linear energy absorption over the displacement range as seen in all previous tests on both monolithic and sandwich materials. Whereas, in the third and fourth tests (Figure 5.43 – green and Figure 5.43 – purple), the adhesive failure can be readily seen by the drop in energy absorption gradient (highlighted with red dashed circles). The circled points are suggested as the points where failure of the adhesive occurred.

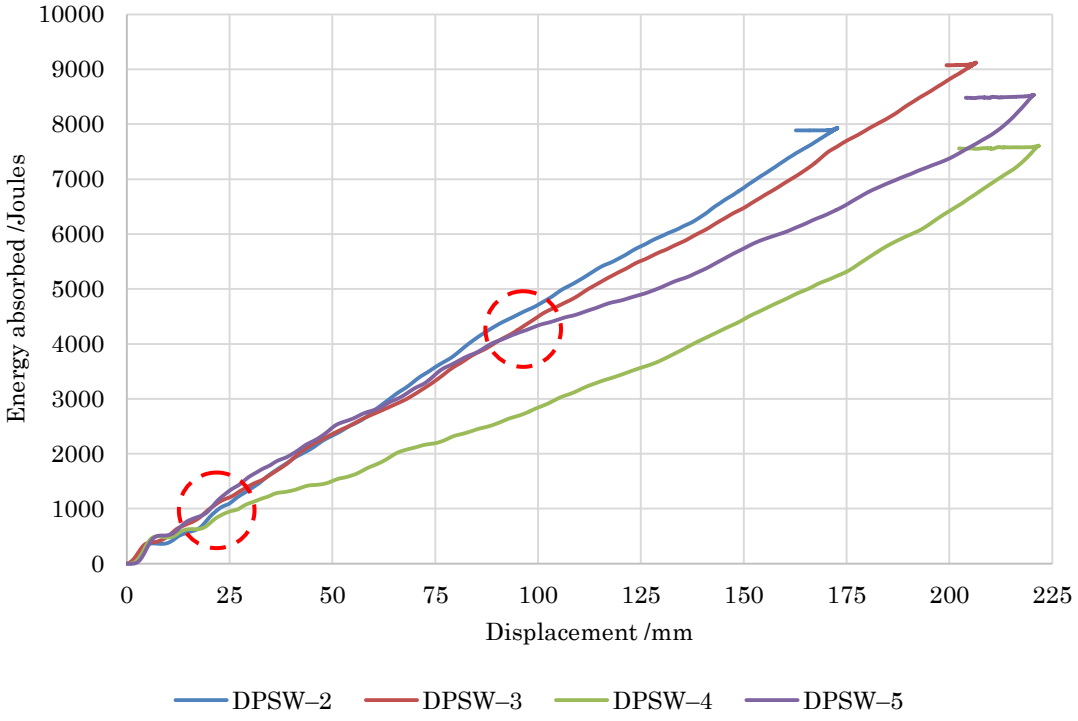

Figure 5.43 – Cumulative energy–displacement results for DPSW sandwich material dynamic (impact) tests. All tests are on single core DPSW with the press–formed geometry. Red dashed circles highlight initial adhesive failure.

5.8.1.2 Image series

The press–formed DPSW crash structures were observed to deform in the same manner as the quasi–static tests when successfully impacted. Figure 5.44 shows test DPSW–2 where delamination did not occur and hence the material absorbed the impact energy. The multiple small radius folds can be seen, however, the folding still conforms to the asymmetric crush seen in the monolithic metals. No significant failure was seen in the steel skin, however, there are small fractures due to the small radius folds and Figure 5.45 confirms this.

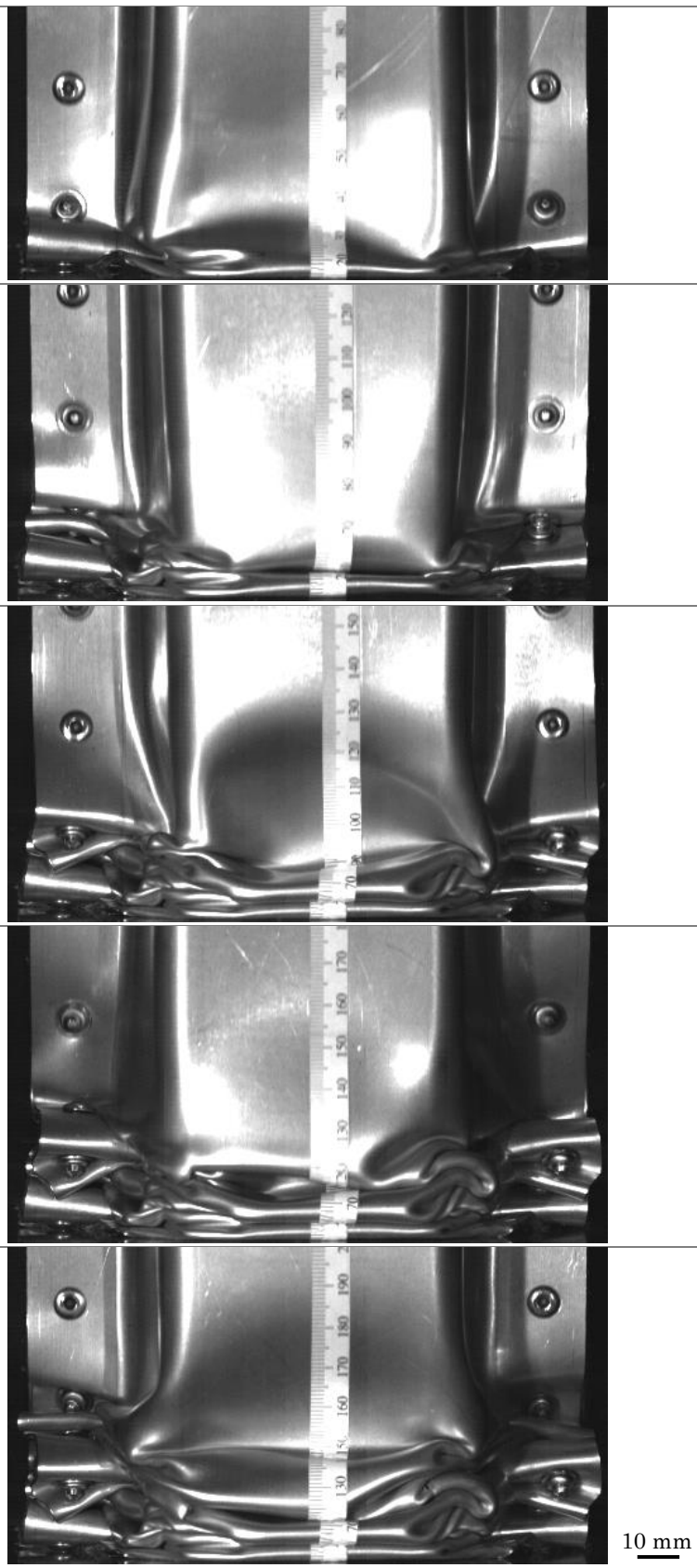

Figure 5.44 – Progressive crushing seen in the single core DPSW press–formed crash structures for an 8.5 kJ impact at 14.6 $m.s^{-1}$ (test DPSW–2). 1 to 5 – Anterior views. The image series highlights the small radius folds seen in the single core DP600 sandwich material. Scale bar applies to all images.

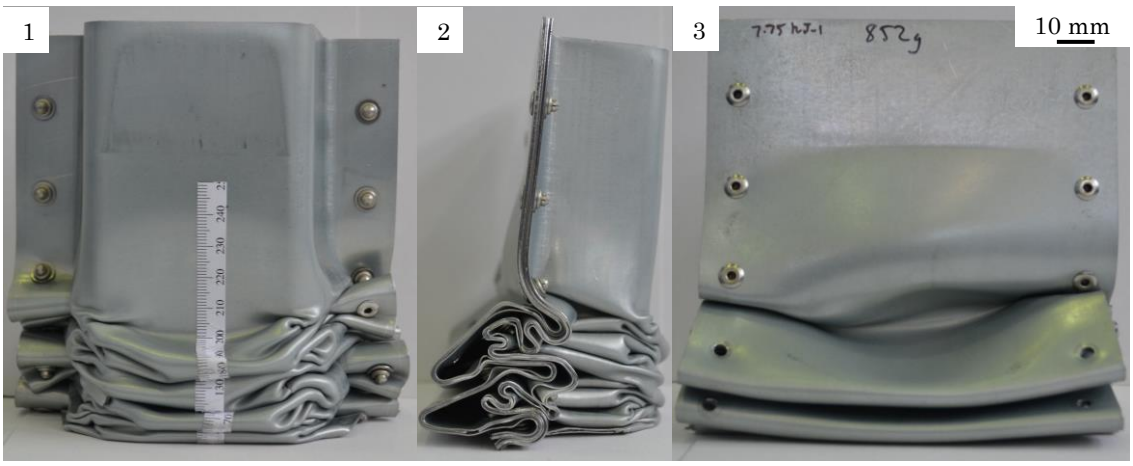

Figure 5.45 – DPSW deformed crash structure. Image 1 – Anterior view, image 2 – lateral view, image 3 – posterior view. Scale bar applies to all images.

The radius of the folds in the press–formed geometry were in the order of 4 mm. In comparison to monolithic metals impacted in this geometry which were between 8–12 mm. A press–formed AA5754 crash structure result is shown in Figure 5.46, this shows the monolithic metals had the same folding behaviour in both the press brake bent geometry (Figure 5.5) and the press–formed geometry.

Figure 5.46 – AA5754 aluminium impacted in the press–formed geometry.

5.8.2 Press brake bent single hat crash structure

Testing of the press brake bent crash structures is detailed in this section. The press brake bent geometry is the same as that of the monolithic crash structures and the ECCS sandwich material crash structures. This allows a certain amount of comparison between the materials to assess performance, particularly in terms of deformation and failure. Performance in terms of energy absorption will be dealt with in Chapter 7. Image series are not available for these tests; therefore, only images of the two fully deformed crash structures is shown.

Figure 5.47 shows the energy and force–displacement plots for the two fully impacted crash structures. The 4–4–2 kJ impact test and the 9.7 kJ impact test (performed at IJmuiden).

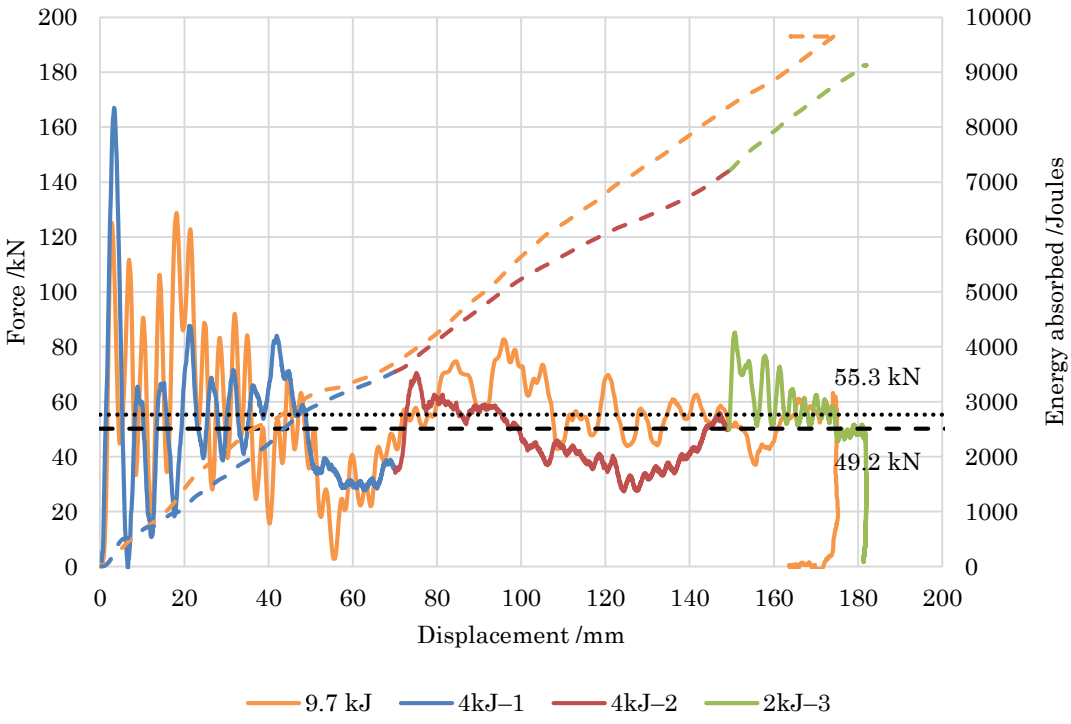

Figure 5.47 – Impact tests performed on DPSW 58.5 mm × 77 mm press brake bent crash structures. The dashed line shows the mean crush force for the 4–4–2 test, the dotted line shows the mean crush force for the 9.7 kJ test performed at IJmuiden.

A distinct peak impact force was not seen in the 9.7 kJ test (Figure 5.47 – orange), this was unexpected since it did not occur in the monolithic tests on the same load cell.

5.8.2.1 Deformation images

The deformation of the DPSW material (Figure 5.48) resembles that of the thicker ECCS sandwich materials (double and triple core); the transition of the long folds into shorter folds is visible in the corners. The front face hinged as per monolithic metal crash structures (discussed in Chapter 1). However, the folds flattened into one another as per the sandwich materials previously tested. The lateral view (Figure 5.48 – images 2 & 3) shows the failure of the SPR joints, failure of the bond between the polymer and the steel was also observed (Figure 5.48 – image 3, circle).

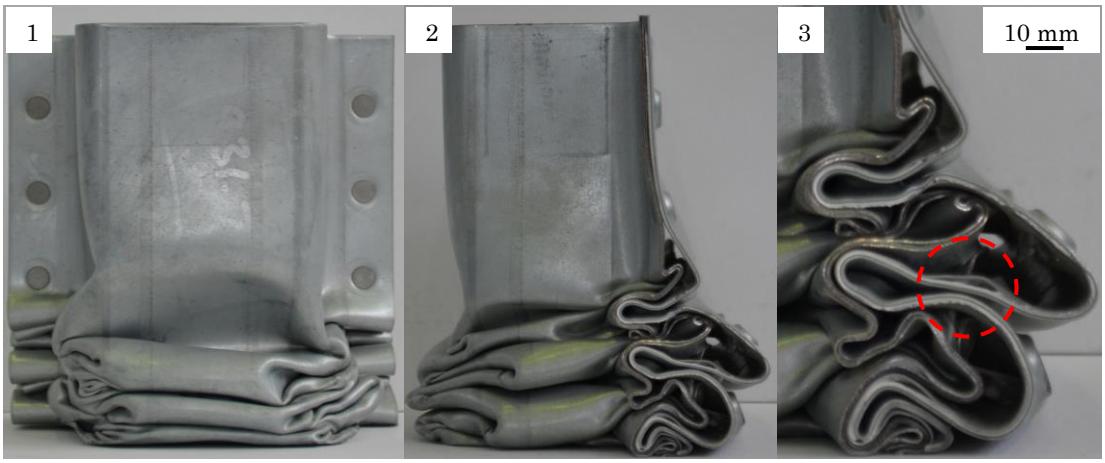

Figure 5.48 – DPSW press brake bent crash structure. Image 1 – Anterior view, image 2 – lateral view. Image 3 is image 2 magnified. Scale bar applies to all images.

The increased proportion of steel in the DPSW crash structure over the Steelite and ECCS sandwich materials produced folds of a greater radius. The folds being in the region of 5 mm in radius, compared to 1.5 mm and 2 mm for the single core Steelite and ECCS sandwich materials respectively.

5.8.3 Summary

The DPSW materials were crashed successfully, even with the difficulty in material production (discussed in Chapter 3). Disregarding the tests where the adhesive failed and delamination occurred, the results are summarised in Figure 5.49.

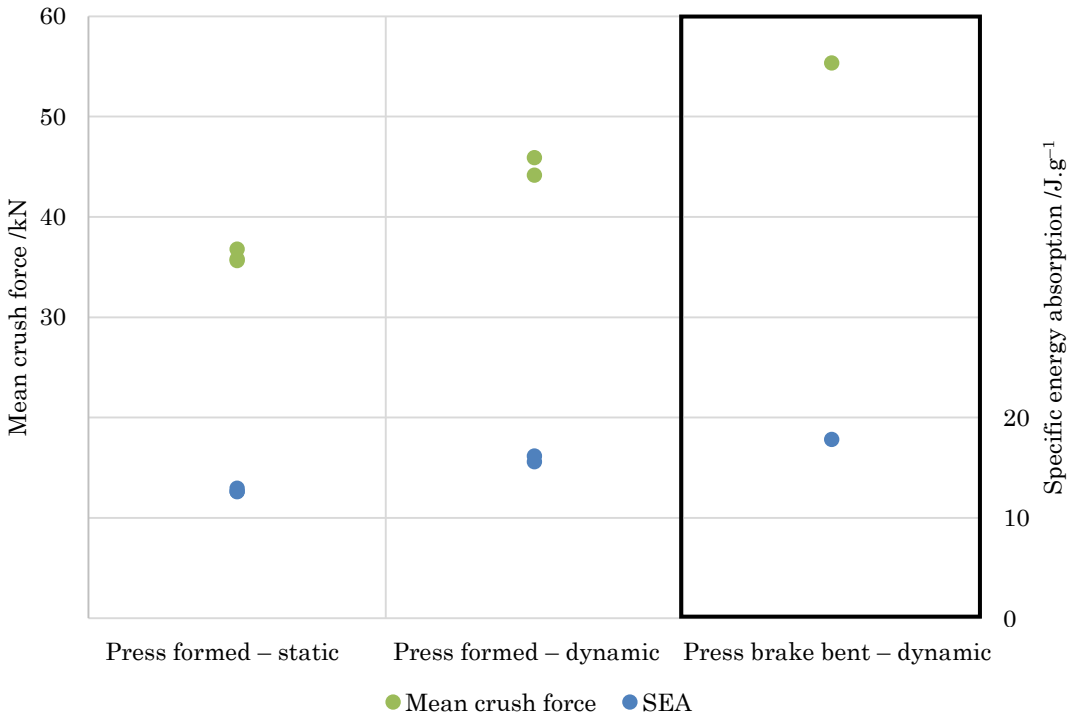

Figure 5.49 – Summarised results for the single core variant of the DP600 sandwich material. The mean crush force and specific energy absorption (SEA) are shown for each test. The tests included are the repeats on the press–formed geometry, quasi–statically and dynamically, and the dynamic result for the press–brake bent geometry.

The press–formed crash structure was tested both quasi–statically and dynamically, showing a 25% increase in the mean crush force (36.0 to 45.0 kN respectively). This is a more significant increase in energy absorption than was seen in monolithic DP600. The monolithic DP600 showing a 9.3% increase in mean crush force dynamically over quasi–statically. Increased strain rate sensitivity of metal–polymer–meal sandwich materials over the monolithic metal itself has been previously reported in the literature [15].

Dynamically, the DP600 sandwich material in the press brake bent geometry (same geometry as monolithic crash structure) achieved 17.8 $J.g^{-1}$ for a 55.3 kN mean crush force. In comparison, the 1.6 mm DP600 only achieved 15.3 $J.g^{-1}$ for a 69.3 kN mean crush force. However, the 2.5 mm AC300 dynamically had a mean crush force of 55.8 kN but had a specific energy absorption of 22.3 $J.g^{-1}$. The DPSW crash structure is therefore, 25% heavier than the high strength AC300 aluminium alloy for the same energy absorption. The triple core ECCS sandwich was able to compete with the AC300–T61, however, the DP600 sandwich with thicker steel skins (0.5 mm compared to 0.3 mm) and thinner core was not as effective.

The force response of the press brake bent crash structures was flat, similar to the press–formed crash structures (Section 5.8); the folds could not be seen in the force data. The nominal force value was greater than the press formed crash structures due to the larger geometry. The folding mode was the same asymmetric collapse; however, fewer folds were produced. Since the material is the same as the press–formed geometry, it can be confirmed the geometry was the cause of the small fold radius in the press–formed geometry. The corners showed significant wrinkling as per the single and double core ECCS sandwich materials.

5.9 Static to dynamic comparison

5.9.1 Crushing behaviour

The monolithic metal crash structures folding behaviour was similar both quasi–statically and dynamically (Figure 5.50), and there was an increase in mean crush force in all instances. The increase in mean crush force dynamically was expected in all cases due to the inertial response of the metals when impacted. The inertial response is due to the impact mass and crash structure travelling at high velocity and contacting a stationary object (load cell), this phenomenon is well documented in the literature [5], [6], [16]. The increase in mean crush force for the AC300–T61 alloy was determined to be due to inertia alone (confirmed by finite element analysis in Chapter 6). For the AA5754 alloy and the DP600 steel, a combination of both inertial and strain rate sensitivity were the case of the increased strength, both experiencing inertial strengthening and both having strain rate hardening effects [4], [17].

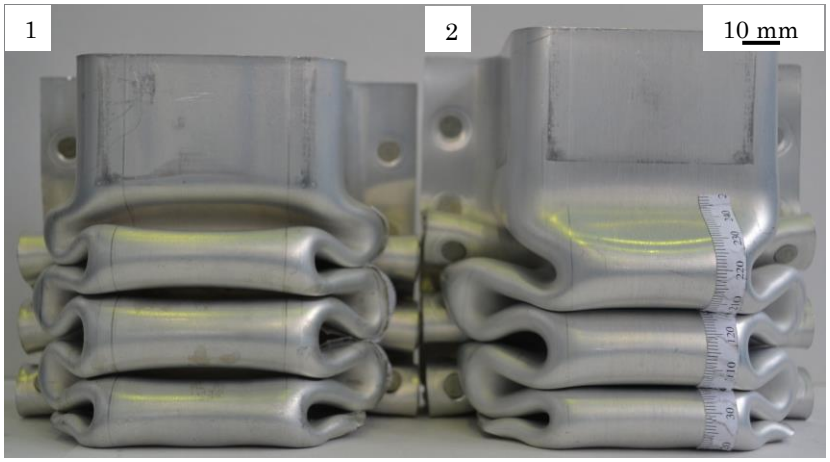

Figure 5.50 – Image 1 – AC300 aluminium quasi–statically tested, image 2 – AC300 aluminium dynamically tested. Images show similarity in deformation. Scale bar applies to both images.

The single core Steelite sandwich materials exhibited unstable collapse modes due to the double hat geometry and the thinness of the steel both quasi–statically and dynamically, particularly in the single core variant. The double core Steelite

showed progressive collapse, in most cases as is the intention, however, dynamically the Steelite double core exhibited steel skin failure. The triple core Steelite crash structures exhibited significant failure of the steel skin both quasi–statically and dynamically. This failure altered the collapse mode to show progressive failure (Figure 5.51 – image 2) much like fibre–reinforced composite materials (discussed in Chapter 2). Furthermore, failure through the entire thickness of the sandwich was also observed dynamically for the triple core Steelite sandwich materials. The Steelite testing showing the potential for failure dynamically when it is not seen quasi–statically (Figure 5.51). This is contrary to the monolithic metals tested, which had similar behaviour both quasi–statically and dynamically. Although, through thickness fracture of monolithic metals when axially impacted has been reported previously [9].

Figure 5.51 – Failure dynamically (image 2) not seen quasi–statically (image 1) in Steelite triple core. Scale bar applies to both images.

Steel skin failure was less common in the ECCS sandwich materials compared to the Steelite materials, since the ECCS sandwich materials had double the thickness of steel. Quasi–statically and dynamically, only the triple core material showed significant failure of the steel skin and this did not alter the overall progressive crushing mode of the crash structure (Figure 5.52). However, the quasi–static tests did exhibit more pronounced wrinkling in the corners than the dynamic tests, a property which was not expected.

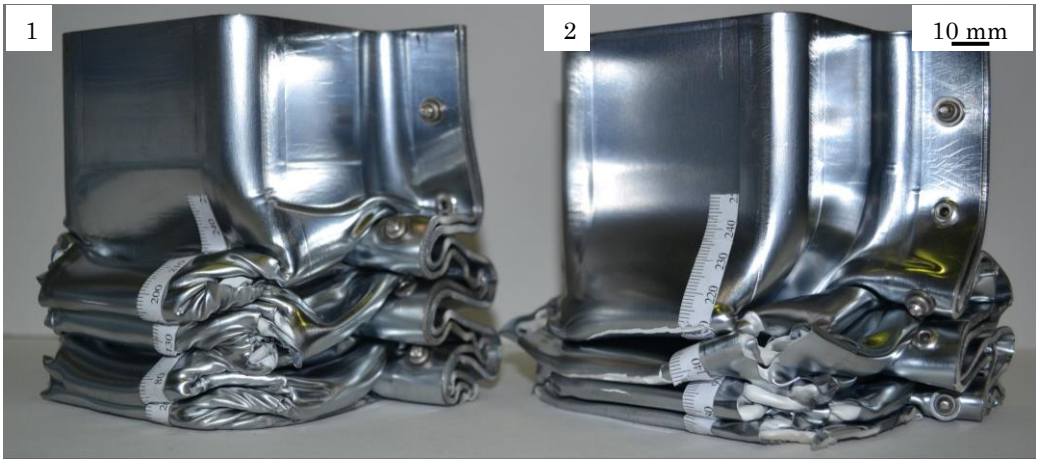

Figure 5.52 – ECCS TC quasi–static (1) *vs.* dynamic (2) test. Failure seen dynamically not seen quasi–statically. Scale bar applies to both images.

The DP600 sandwich (DPSW) material was only tested in the single core variant, and no significant differences were seen quasi–statically and dynamically. The DPSW with the thickest steel skins (0.5 mm) of all sandwich materials tested, showed small fractures (less than 5 mm in length) in highly strained corners of the crash structure. However, these fractures did not have an adverse effect on the folding behaviour.

Potentially, the geometry of the crash has a significant effect on the folding of sandwich materials. This was not categorically defined, however, when comparing the two geometries tested, the folding in the press–formed crash structures showed smaller radius folds, the folds being in the order of 25 mm in length, in comparison to 40 mm for the press brake bent geometry. When testing monolithic materials in

the press–formed geometry, the folding radius did not alter significantly from the press brake bent crash structures.

5.9.2 Energy absorption

The metal–polymer–metal sandwich materials showed considerable strain rate hardening, this is shown by a ratio of their quasi–static to dynamic mean crush force, see Figure 5.53.

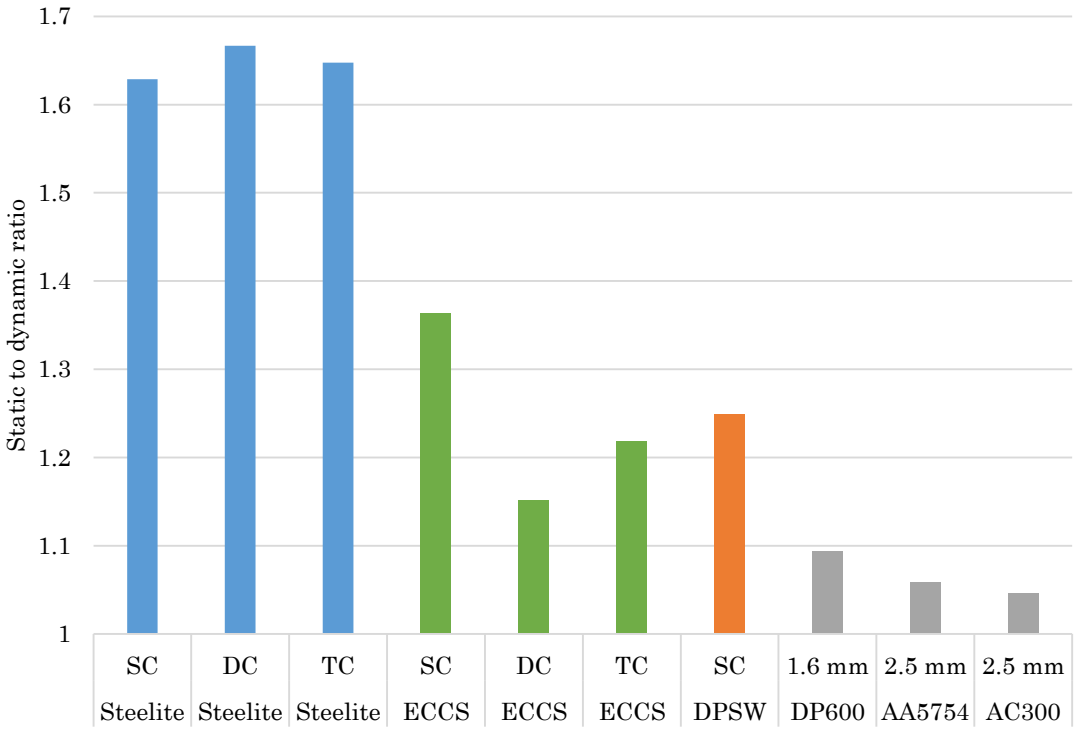

Figure 5.53 – Static to dynamic ratio for all crash structures.

The Steelite sandwich materials all absorbed over 60% more energy dynamically (Figure 5.53 – blue). There was no significant difference in the percentage increase in the energy absorbed between the different thicknesses. The 60% increase dynamically over quasi–statically is unprecedented; the most commonly reported maximum value is a 50% increase in energy absorption for mild steels [7]. For higher strength steels, the difference in energy absorption has been shown to be around 10% [18], this is confirmed by the testing (Figure 5.53 – grey). Therefore, this much of a difference must be due to the properties of the sandwich layup; the

polymer cores' strain rate hardening and the effect of placing the steel further away from the neutral axis. Placing the steel away from the neutral axis increasing the average strain experienced. The use of the sandwich allowing thinner steels to be used further increases the stress seen in the steels, since the load experienced must be withstood by a smaller amount of steel compared to a monolithic metal.

The ECCS sandwich materials (Figure 5.53 – green) showed the single core variant to have the greatest difference dynamically. The 15% to 37% increase is lower than that observed in the Steelite sandwich materials. This is most likely due to the greater strength of the ECCS steel skin over the Steelite skin (material data shown in Chapter 3), which invariably means the ECCS steel has a lower strain rate hardenability than the Steelite steel skin.

The DPSW materials (Figure 5.53 – orange) absorbed 25% more energy in crash over quasi–static crush, whereas monolithic DP600 (Figure 5.53 – grey) only absorbed 9% more dynamically, showing the sandwich to be more effective than the monolithic materials.

5.10 Summary

The physical testing both quasi–static and dynamic confirmed the folding modes seen in monolithic metals are also seen in the sandwich materials, this is important in understanding the behaviour of the materials. The ability to predict the folding behaviour shall become more feasible, as the asymmetric collapse folding mechanisms are well understood for monolithic materials.

The Steelite sandwich materials tested provided a valuable insight into the behaviour of metal–polymer–metal sandwich materials. The properties of the core were more dominant due to the thin steel skins (0.15 mm) and relatively thicker cores (0.7, 1.4 and 2.1 mm). The Steelite sandwich materials exhibited progressive crushing in all thicknesses. However, the single core variant exhibited unstable collapse modes due to the thickness to width ratio of the crash structures. Failure of the steel skin was observed in the double and triple core variants, both quasi–statically and dynamically. In extreme cases, failure of the steel would lead to either delamination of the sandwich, or progressive failure modes akin to fibre–reinforced composite materials (discussed in Chapter 2). The crushing forces were lower than the range suitable for automotive crash structures, but the insight into the performance of sandwich material with a 7:1 polymer core to steel ratio was invaluable. Additionally, the testing showed the potential of MPM sandwich materials to achieve specific energy absorption values comparable to monolithic aluminium alloys.

The ECCS sandwich materials had a thicker (0.3 mm) and higher strength steel skin. The increased skin thickness meant failure was less common in the skin; the thicker skin was also able to sustain higher stress before failure due to its higher strength. However, the ECCS sandwich materials exhibited differences quasi–statically and dynamically not seen in the Steelite materials. Namely wrinkling of

the steel skin, which impeded the conventional asymmetric collapse modes. Dynamically, the crash structures behaved more conventionally, showing only progressive crushing. The ECCS sandwich materials showed no progressive failure modes owing to the thicker steel skin. The double and triple core ECCS sandwich materials outperformed monolithic steels in terms of specific energy absorption values, although not to the extent of the Steelite triple core sandwich.

The DP600 sandwich materials had the thickest steel (0.5 mm) along with the highest strength of steel. The crash structures again displayed progressive crushing in an asymmetric collapse mode as per monolithic metals, albeit with smaller radius folds. The method of collapse did not change quasi–statically to dynamically for the DPSW materials., though adhesive failure was observed in some of the dynamic tests due to the poor adhesive strength in the sandwich. However, little failure was seen in the steel skins, in any case, it had no perceptible effect on the performance of the sandwich when axially impacted.

The DP600 sandwich material testing showed there is a potential for a stronger bond requirement when using thicker or higher strength steels as the skin materials. The Steelite sandwich having a similar bond strength but did not exhibit delamination in the single core variant and has enough bond strength to be readily press brake bent.

Of further interest, the DPSW tests showed there maybe an effect of geometry on the folding behaviour. The press–formed crash structures exhibited small radius folds; however, the press brake bent crash structures had larger radius folds (50% greater fold length) comparable to the ECCS and Steelite sandwich materials. Therefore, fold wavelength in sandwich materials maybe more geometry dependent than in monolithic metals.

Conceptually, to achieve the greatest light–weighting, the thickness of the steel must be reduced as much as possible. However, to maintain a progressive folding/crushing mechanism as opposed to the progressive failure type, the skin must be thick enough not to fail considerably. By this, it is meant some small fractures of the steel skin would be acceptable, but not a significant amount which would change the mode of energy absorption or indeed cause catastrophic failure.

When considering the materials tested, it could be said the double and triple core Steelite sandwich materials tested would not be appropriate, nor would the triple core ECCS sandwich. The double core ECCS and the single core Steelite would be acceptable. From this, a thickness ratio of 70%:30% (polymer to steel) is suggested as a limit to the amount of polymer acceptable before failure of the sandwich is likely to occur. This ratio being that of the single core Steelite and double core ECCS sandwich materials.

The sandwich materials also exhibited an increased strain rate sensitivity over monolithic metals. This was due to the polymer core's strain rate sensitivity and the positioning of the steel in the sandwich away from the neutral axis increasing the steels' strain levels in the folds.

5.11 References

[1] M. F. Ashby, *Materials: Engineering, Science, Processing and Design*. .

[2] N. Reynolds, *Advanced Composite Materials for Automotive Applications: Structural Integrity and Crashworthiness*. Wiley, 2013.

[3] Alu Matter, "Crash Box: Energy Absorption." [Online]. Available: http://aluminium.matter.org.uk/content/html/eng/default.asp?catid=7&pageid=2144416781.

[4] D. Wowk and K. Pilkey, "Effect of prestrain with a path change on the strain rate sensitivity of AA5754 sheet," *Mater. Sci. Eng. A*, vol. 520, no. 1–2, pp. 174–178, Sep. 2009.

[5] V. Tarigopula, M. Langseth, O. S. Hopperstad, and A. H. Clausen, "Axial crushing of thin-walled high-strength steel sections," *Int. J. Impact Eng.*, vol. 32, no. 5, pp. 847–882, May 2006.

[6] X. Y. Su, T. X. Yu, and S. R. Reid, "Inertia-sensitive impact energy-absorbing structures part I: Effects of inertia and elasticity," *Int. J. Impact Eng.*, vol. 16, no. 4, pp. 651–672, Aug. 1995.

[7] W. Abramowicz and N. Jones, "Dynamic axial crushing of square tubes," *Int. J. Impact Eng.*, vol. 2, no. 2, pp. 179–208, 1984.

[8] R. A. Beaumont, "Determining the effect of strain rate on the fracture of sheet steel," PhD Thesis, WMG, University of Warwick, 2012.

[9] Ø. Fyllingen, O. S. Hopperstad, and M. Langseth, "Robustness study on the behaviour of top-hat thin-walled high-strength steel sections subjected to axial crushing," *Int. J. Impact Eng.*, vol. 36, no. 1, pp. 12–24, Jan. 2009.

[10] T. Wierzbicki, Y. Bao, Y.-W. Lee, and Y. Bai, "Calibration and evaluation of seven fracture models," *Int. J. Mech. Sci.*, vol. 47, no. 4–5, pp. 719–743, Apr. 2005.

[11] M. D. White, N. Jones, and W. Abramowicz, "A theoretical analysis for the quasi-static axial crushing of top-hat and double-hat thin-walled sections," *Int. J. Mech. Sci.*, vol. 41, no. 2, pp. 209–233, 1999.

[12] N. Jones, "Energy-absorbing effectiveness factor," *Int. J. Impact Eng.*, vol. 37, no. 6, pp. 754–765, 2010.

[13] M. D. White and N. Jones, "Experimental quasi-static axial crushing of top-hat and double-hat thin-walled sections," *Int. J. Mech. Sci.*, vol. 41, no. 2, pp. 179–208, 1999.

[14] D. Mohr and T. Wierzbicki, “Crushing of soft-core sandwich profiles: experiments and analysis,” *Int. J. Mech. Sci.*, vol. 45, no. 2, pp. 253–271, 2003.

[15] K. J. Kim, D. Kim, S. H. Choi, K. Chung, K. S. Shin, F. Barlat, K. H. Oh, and J. R. Youn, “Formability of AA5182/polypropylene/AA5182 sandwich sheets,” *J. Mater. Process. Technol.*, vol. 139, no. 1–3, pp. 1–7, 2003.

[16] C. R. Calladine and R. W. English, “Strain-rate and inertia effects in the collapse of two types of energy-absorbing structure,” *Int. J. Mech. Sci.*, vol. 26, no. 11–12, pp. 689–701, Jan. 1984.

[17] L. Durrenberger, X. Lemoine, and A. Molinari, “Effects of pre-strain and bake-hardening on the crash properties of a top-hat section,” *J. Mater. Process. Technol.*, vol. 211, no. 12, pp. 1937–1947, 2011.

[18] N. Abedrabbo, R. Mayer, A. Thompson, C. Salisbury, M. Worswick, and I. van Riemsdijk, “Crash response of advanced high-strength steel tubes: Experiment and model,” *Int. J. Impact Eng.*, vol. 36, no. 8, pp. 1044–1057, 2009.

6 Modelling methodology

Finite Element Analysis (FEA) is the conventional method used to predict the performance of a structure with known material properties, or perform sensitivity analyses to see the effect of changes in properties. FEA allows the study of the sandwich material and the crash structure geometry; hence, the effect of each accounted for. Additionally, the use of FEA is imperative to be able to simulate the performance of MPM sandwich materials in crash structures, in order for MPM sandwich materials to be adopted by the automotive sector.

FEA of the crash structures was carried out using LS–DYNA, a commercially available FEA package. The process of modelling, Figure 6.1, is as follows: The geometry of the model was drawn in SolidWorks, where an .IGES was produced for meshing. The mesh was created in LS–PrePost, where it was outputted as a .key file. The .key file was then imported into Arup OASYS Primer where pre–processing was carried out, which included assigning of material properties, element properties, boundary conditions and solving techniques. The completed .key file was then run in LS–DYNA and the resulting outputs analysed with OASYS D3PLOT and OASYS T/HIS.

Figure 6.1 is a process model of the workflow, showing the stages of modelling.

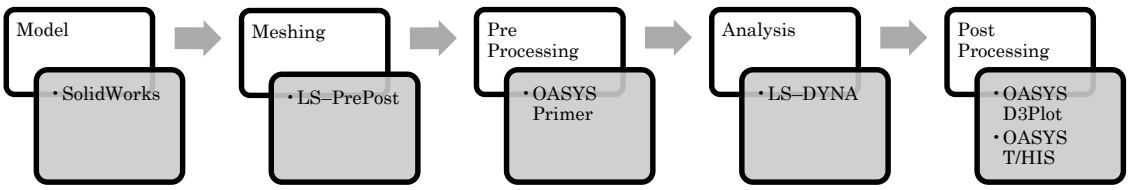

Figure 6.1 – The modelling process.

The outputs of interest were produced in the post–processing step, the data required for comparison are the force, energy and displacement; the calculation of these was discussed in Chapter 1 – Introduction. Additionally, the performance

was judged visually ensuring the crash structures behaved as per the physical tests. However, importance is placed on the mean crush force result over the matching the folding behaviour.

In this chapter, the current literature is explored to ascertain the latest methods of modelling sandwich materials. Additionally, the literature is related to attempts made to model sandwich materials in crash structures. The literature review is summarised as a methodology for finite element modelling of sandwich materials in axial impact, as well as the important information for modelling monolithic materials.

6.1 Model Setup

The FEA model was setup in the same manner as an axial impact test, as shown in Figure 6.2. The crash structure (purple) is rigidly attached to a drop weight (blue) and impacted into a rigid impact plate (yellow) on a load cell (spring). The ground plate (red) is fully constrained hence unable to move, while the impact plate is able to move in the z direction. The spring is compressed when the impact plate moves in relation to the fixed ground plate; the spring force was outputted as the load.

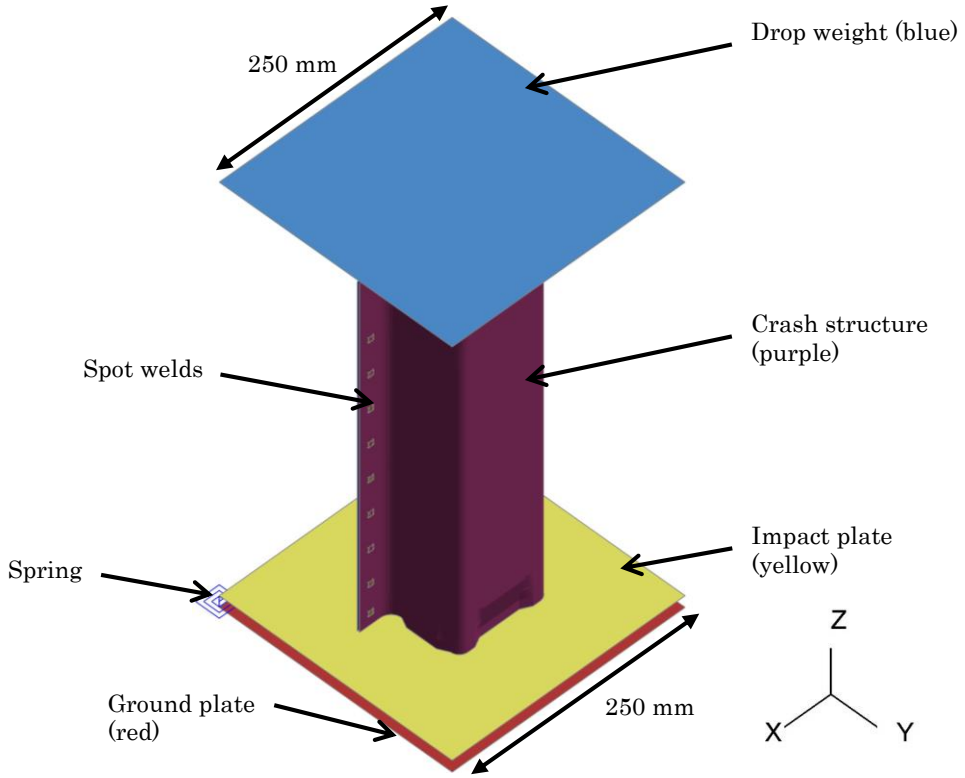

Figure 6.2 – Model setup for impact testing, mimicking the quasi–static and dynamic test.

To model the end of the crash structure that is rigidly clamped to the drop weight, the LS–DYNA function *CONSTRAINED_EXTRA_NODES was employed. This attaches the drop weight to the crash structure and rigidifies the end of the structure, hence mimicking the clamping used on the fixture (see Chapter 3 – Materials and methods). A contact model (*CONTACT_AUTOMATIC_GENERAL) was used to model the contact between the crash structure and the impact plate.

6.2 Monolithic materials

This section details the modelling behaviour of monolithic metals, the element type, element size and number of integration points were considered to produce an optimised model, whilst also considering simulation times.

6.2.1 Model consideration 1 – Element type

When considering conventional monolithic metals such as aluminium alloys or steels, shells and solids are both used to great effect for modelling axial impact scenarios [1], [2].

The thickness of the material to be modelled is of fundamental importance when choosing between solids and shells. Fyllingen *et al.* [3] modelled impacts of 5 mm thick aluminium crash structures, the results showed an 18.4% disparity in crushing force between solids and shells in LS–DYNA, with the solids producing the stiffer result. In comparison, Tarigopula *et al.* [4] modelled 1.2 mm DP800 steels successfully using under–integrated shell (Type 2) elements, producing a result within ±5% of the physical test outcome. This crush force disparity between shells and solids seen by Fyllingen *et al.* [3] can be explained by the thickness of the material modelled. Shell elements have a plane stress assumption, which is only valid for sufficiently thin materials [5], [6]. Therefore, thicker materials should be modelled using solid elements. However, for thinner materials, the deformation result in general was shown to be in good agreement regardless of whether shells or solids were used. The most significant hindrance to the use of solid elements is the simulation time. Fyllingen *et al.* [3] showed solids took 450 times longer to run than shells. Bai *et al.* [2], when modelling the crushing of 1.2 mm thick aluminium crash structures under axial impact using ABAQUS, compared solids to shells. Shell elements with nine integration points through

thickness gave a similar response to using five solids through thickness; however, the solid model took 25 days to produce a result.

The decision was made to use shell elements rather than solids to model the monolithic metal crash structures. Since the monolithic metal crash structures could be considered a thin walled structure, with the plane stress assumption of shell elements being adequate to model them. The decision was supported by good agreement with the experimental work.

6.2.2 Model consideration 2 – Element formulation

The second consideration is the shell element formulation, the two most commonly use in LS–DYNA are the under–integrated Type 2 shell element and fully–integrated Type 16 shell element. The difference between them being the number of integration points in the plane of the element. Type 2 elements have one in–plane integration point, allowing the element to deform without energy input; this is disadvantageous, since it is incorrect and sometimes problematic to control. Type 16 elements have four in–plane integration points preventing zero energy modes of deformation (hourglassing); however, more integration points increases the computation time.

Due to the lack of definitive guidance from the literature for the use of under–integrated shells (Type 2) over fully–integrated shells (Type 16), both formulations were simulated in order to see the effect of such. Type 2 elements are preferred for impact modelling due to solving speed [7].

A model with fixed impact mass and impact speed (hence energy) and three integration points through thickness (the minimum recommended for shell elements in bending [6]) was used for the comparison. The material was set to a

generic DP600 material model (provided by Tata Steel) with a 1.6 mm thick section.

The results showed that there was indeed a low stiffness response from Type 2 elements as seen by Xiao *et al.* [8]. The Type 2 elements were on average 6.5% lower in mean crush force than Type 16 elements across the range of element sizes compared (8, 4, 2, 1 and 0.5 mm elements). The amount of hourglassing seen in the Type 2 elements was low (less than 5%), hence acceptable. Even so, the Type 16 elements were chosen since the Type 2 elements under–predicted the test result by 10% compared to the Type 16 elements which were within 4% (results are shown in Chapter 7 – FEA Comparison).

6.2.3 Model consideration 3 – Element size

The element size is an important consideration; an overly large element will not capture the local strain gradient, while an excessively fine mesh will increase the simulation time for no increase in accuracy. Therefore, a mesh refinement study was performed to find the optimal mesh density, to produce a more accurate result and reduce the simulation time. This was performed for both the monolithic and sandwich materials separately, the monolithic results are shown here, the sandwich results are shown in Section 6.3.2.2.

The force–displacement and energy–displacement results, Figure 6.3, along with the visual deformation, Figure 6.5, were used to assess the performance of the differing mesh densities. A converged solution was found with 1 mm elements with the 0.5 mm elements producing essentially the same result, Figure 6.3.

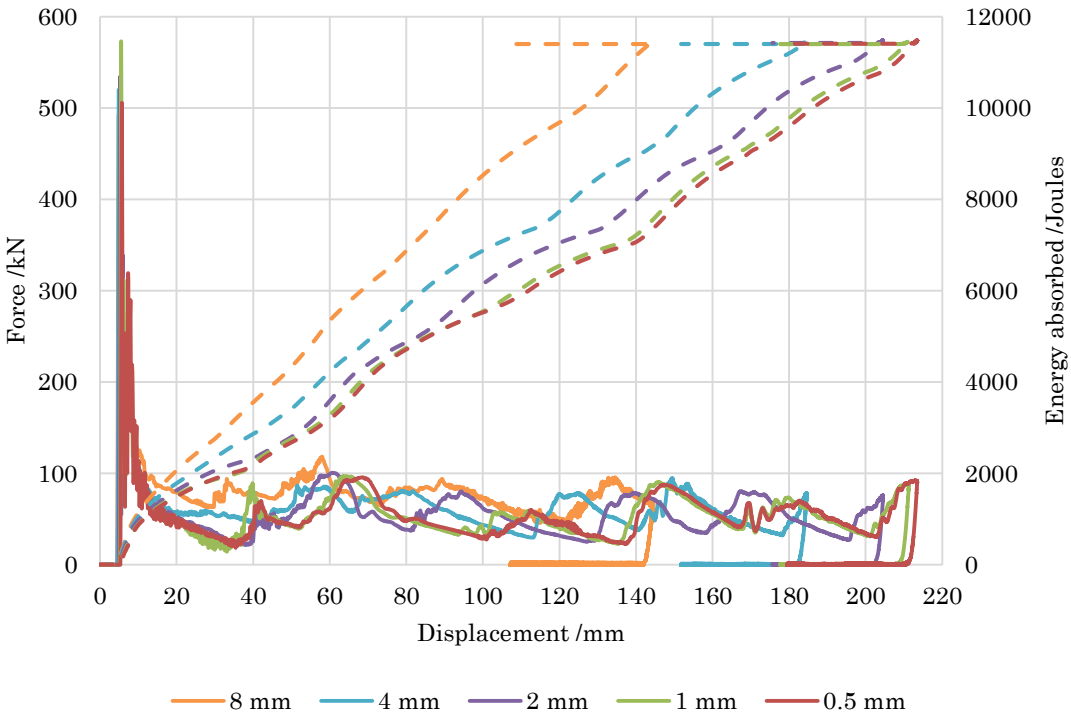

Figure 6.3 – Force (solid) and energy absorbed (dashed) *versus* the displacement of the crash structure for each element size.

Figure 6.4 shows a magnified version of Figure 6.3 with the 8 and 4 mm element results omitted since they are markedly different. The force is clipped at 120 kN to emphasise the progressive crushing response over the peak force. The near identical response of the 1 and 0.5 mm elements can be seen clearly, the 2 mm element model was also relatively similar. The force–displacement plot, Figure 6.4, shows the smaller fold wavelength of the increasingly refined meshes, however, the energy–displacement plots, Figure 6.3 – dashed shows the change in fold wavelength was of little significance to the global performance of the structure. The mean crush force for the 1 mm elements being 1% greater than the 0.5 mm elements and the 2 mm elements being 4% greater.

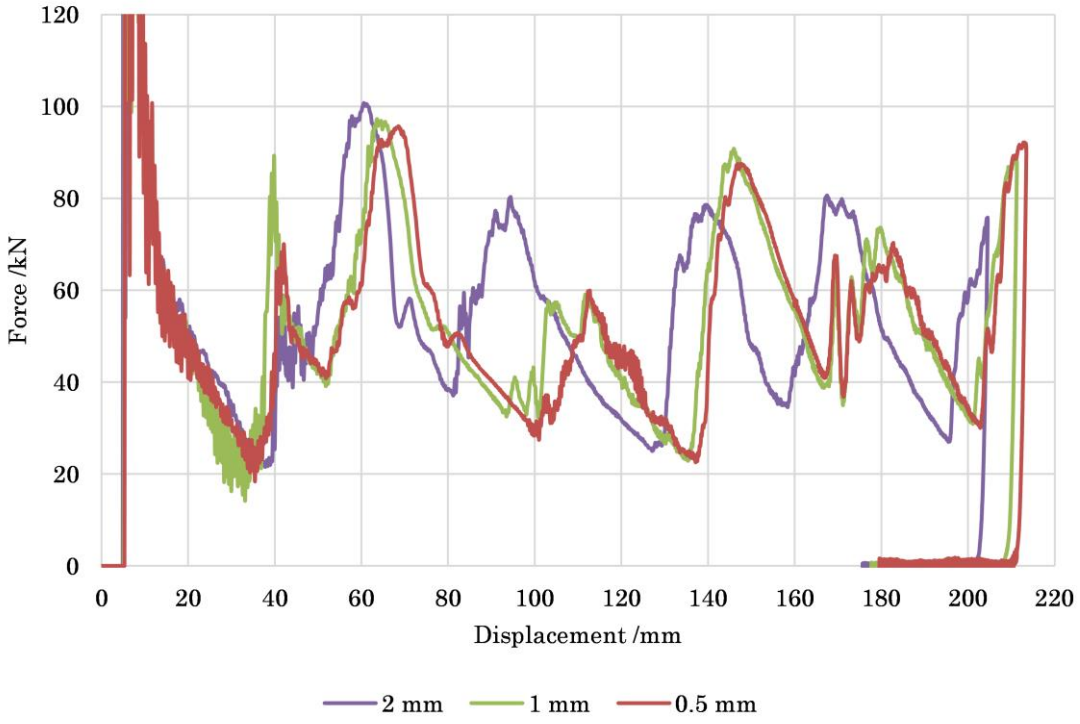

Figure 6.4 – Force–displacement plot cropped at 120 kN to emphasize the progressive crushing data.

The comparative deformation of the monolithic crash structure with differing mesh densities are shown in Figure 6.5. The deformed geometry and a Von Mises strain plot are presented.

The images in Figure 6.5 confirmed that the 8 and 4 mm element meshes were too coarse preventing the material from folding adequately. This led to the over–stiff response seen in the force–displacement plots, Figure 6.3 – solid. There was little difference in the kinematic response of the elements in the 2, 1 and 0.5 mm models, the 1 mm model is considered to have converged, however, visually the 2 mm model is similar. The 0.5 mm element model is omitted from the results since they are visually identical to the 1 mm model.

The most significant difference seen between the mesh refinement models is the Von Mises strain plot. The increased detail of the finer element size became apparent, allowing localisation of strains, but the increased level of detail did not change the result significantly.

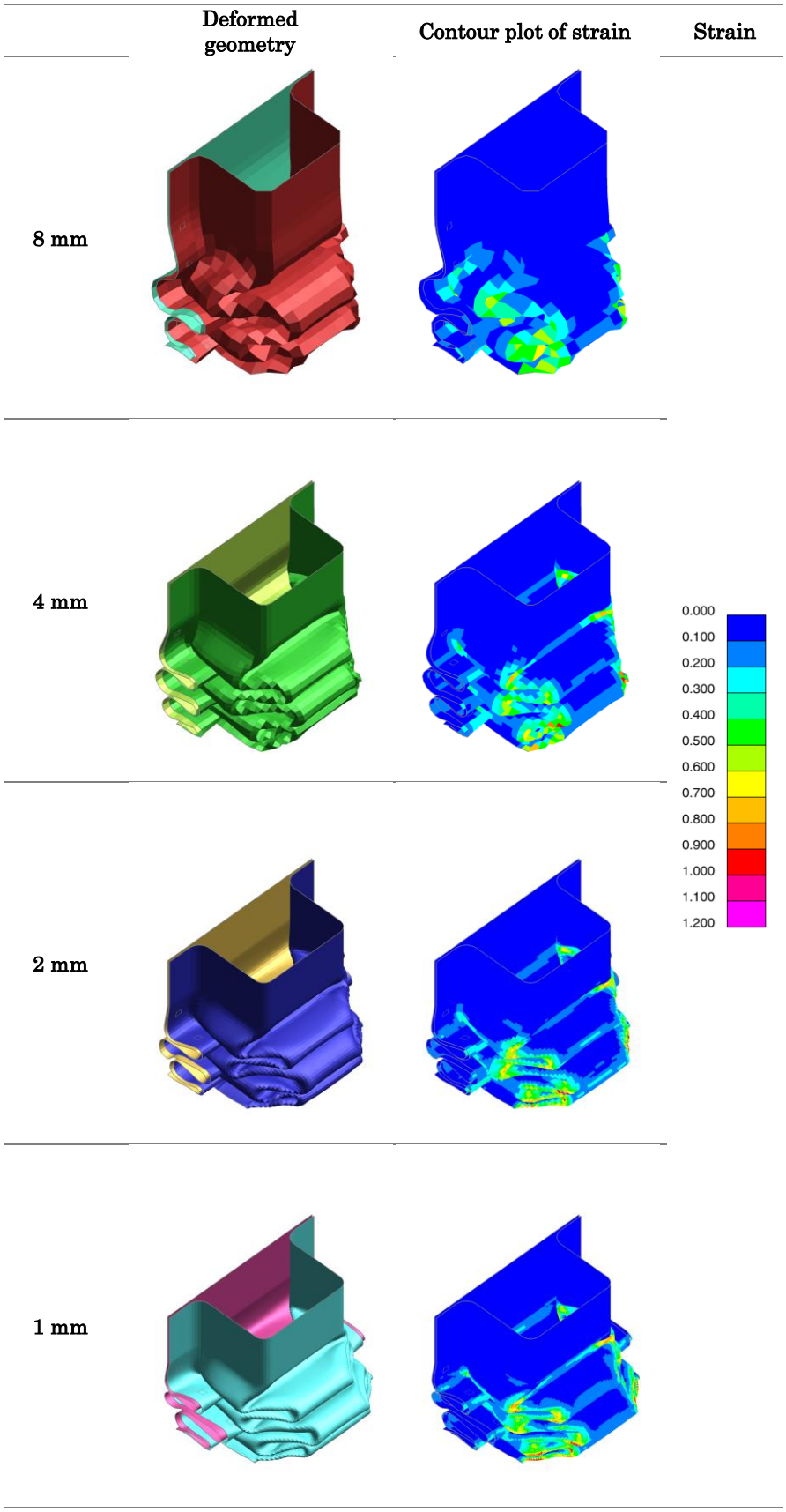

Figure 6.5 – Deformation images from mesh refinement simulations, showing the geometry of crash structure, the mesh deformation and the strain in the elements, the 0.5 mm element model is omitted due to similarity to the 1 mm element model.

6.2.4 Model consideration 4 – Number of integration points

The number of integration points was also considered, two, three, four, five, seven and nine integration points were compared. Two is the default for LS–DYNA, the use of three integration points is recommended so the mid–plane is modelled. From the literature, between five and nine were commonly used [4], [9]–[13]. The integration point analysis showed that five or more integration points yielded the same result. Since integration point position is defined using Gaussian quadrature, using five or more integration points, the outer point is placed within 10% of the edge of the material. Therefore, little difference was observed in strain for integration points placed closer to the material surface.

6.2.5 Model consideration 5 – Simulation time

The final factor considered was the simulation time; the models of particular interest were the 2, 1 and 0.5 mm elements. The 1 and 0.5 mm element models took 7.4 and 57.7 times longer to run respectively than the 2 mm element model. All models produced a mean crush force result with less than 5% variability, and visually the kinematic deformation of all models was acceptable.

6.2.6 Monolithic material model decision

Considering all factors, the 2 mm fully–integrated elements with five integration points through thickness were chosen, as this was the best compromise of mean crush force result and computational expense. The visual result was similar in the 2 mm elements to the finer meshes, and the force–displacement result was 3.3% stiffer than 1 mm elements, hence felt to be an acceptable result.

6.3 Sandwich materials

Sandwich material modelling is considered in this section. The methods used in the literature and other methods attempted in order to model MPM sandwich materials are discussed.

6.3.1 Modelling sandwich material behaviour

The common methods suggested for modelling layered materials in LS–DYNA are shown in Figure 6.6. They are; (a) – One Shell Element, (b) – Layers of Solid Elements, (c) – Layers of Shell Elements [14].

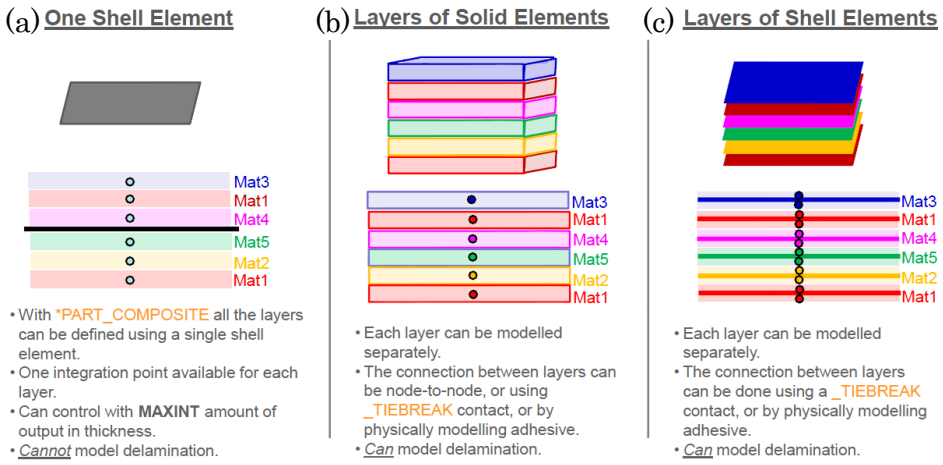

Figure 6.6 – Methods of modelling composite layered materials using LS–DYNA [14]. (a) – One shell element, (b) – Layers of solid elements and (c) – Layers of shell elements.

There are other possible methods of modelling layered materials in LS–DYNA, which include the use of combinations of solid and shell elements and the use of thick shell elements. These methods are discussed in Section 6.3.1.4.

6.3.1.1 One Shell Element (a)

This method uses a single shell layer to model the entire MPM sandwich material, this is performed by the *PART_COMPOSITE function in LS–DYNA. Integration points through the thickness of the shell are designated with material properties and a thickness. The disadvantage of the model is the use of a single shell to model

all materials; therefore, delamination cannot be modelled since the model assumes a perfect bond between the layers. The importance of this depends on the amount of failure seen in physical testing and the strength of the bond between the layers.

Failure of individual components of the sandwich can be modelled, as this is defined in the material card, hence individually for each material. Therefore, integration point failure defines failure of the shell, and the number of integration points that fail before the element is deemed to have failed can be defined.

The conventional shell element model assumes constant shear stress through the thickness of the shell element (plane stress assumption); this is known as Kirchoff–Love plate theory [15]. This is overcome by the use of a shear correction factor (SCF) [6]. The SCF is calculated in Mindlin plate theory, an improvement on Kirchoff–Love plate theory. Mindlin theory considers through thickness shear (as opposed to assuming it to be zero) in a cantilever beam bending of an isotropic material (materials with the same properties in all directions) being bent. The SCF was shown by Timoshenko to be approximately 5/6 regardless of Poisson's ratio of the material [6]. Therefore, for isotropic materials such as metals and bulk polymers this proves acceptable.

MPM sandwich materials are not isotropic, due to the lower modulus and strength of the core in comparison to the metallic skins. When considering the bending of a sandwich material beam, one can see the steel on the top surface in tension would impart a shear stress onto the core's outer surface. Assuming elasticity only for simplicity, the large disparity in elastic modulus (two orders of magnitude) would mean that the bending stress in the steel would be larger than the core could sustain. If indeed, it did so, the sandwich would perform as well in bending as a monolithic metal of the same thickness, with a significantly reduced mass. *PART_COMPOSITE in its default formulation uses the Mindlin plate theory for

bending and through thickness shear prediction. This however does not account for the disparity in shear stress through thickness. Therefore, the bending displacement is calculated, but the shear displacement of the low modulus core ignored, hence producing an *over–stiff* result.

Hallquist *et al.* [6] presented a solution to the potential over–stiff behaviour of the *PART_COMPOSITE model by using a formulation known as Laminated Shell Theory (LST). LST assumes the shear strain (and not the shear stress) is continuous at the interface between layers. Therefore, strains are transferred from the metal skin to the polymer core (i.e. a perfect bond). The shear stress of the layer is then calculated using the modulus of the material. An increased shear displacement in the core during bending compared to the SCF assumption is seen, "softening" the response of the material. This reduces the over–stiff behaviour of the single shell approach, and is suggested by Hallquist *et al.* [6] to be a requirement for sandwich material modelling.

Contrary to Hallquist *et al.* [6], Dunand & Gacel [16] modelled a steel–polypropylene–steel sandwich (SPS) material using a single shell layer, whilst using the 5/6 shear correction factor as per an isotropic material. The modelling of an axial impact of the SPS materials was within 10% of the physical test result. The author felt this was due to the relatively high modulus (1 GPa) of the polypropylene core being sufficiently stiff enough to resist significant shear.

Therefore, the literature does not provide enough evidence to determine whether LST is required for simulation of the behaviour of MPM sandwich materials. For small deformations such as three point bends, LST may not be strictly necessary. However, in gross deformation situations such as the deformation of a crash structure it may be required, hence was explored (discussed further in Section 6.3.2.1).

There is potential in the use of the single shell element to model MPM sandwich materials. It is possible with LST to model layered materials using a single shell whilst accounting for the low shear strength of the core. The use of a shell model is applicable due to the suitability of shells to model thin wall structures, which includes all the sandwich material thicknesses considered in this research. Furthermore, shell elements are the preferred choice for industrial simulations due to their speed. Therefore, if useable, would be advantageous, even with the inability to model failure of the adhesive.

6.3.1.2 Layers of Solid Elements (b)

The use of multiple solids has many possible permutations. Three solids may be used for the entire MPM sandwich (one per layer) or multiple used per layer. The solids may be joined through thickness in the conventional manner with coincident nodes. This does not readily allow adhesive failure to be modelled but does allow failure of the individual materials. When modelling the separate layers of the sandwich with an adhesive, a contact maybe used to model the adhesive, allowing failure of the adhesive layer to be modelled.

The disadvantage of the use of solids to model sandwich materials is the requirement for smaller elements than for monolithic materials, since the element size is defined by material thickness. The use of cubic solids results in a fine mesh, assuming the edge length is the same as the skin thickness. For example, a sandwich in solids could have 0.1 mm × 0.1 mm × 0.1 mm cubic elements (for a 0.1 mm thick skin), whereas this may be simulated in shells elements using millimetre range elements. Therefore, the use of solids in an explicit crash simulation are prohibitively expensive to compute and therefore were not considered further.

6.3.1.3 Layers of Shell Elements (c)

The final method considered was the use of a single layer of shell elements per layer of material. This method allowed each layer of material to be modelled separately, hence allowing failure of each layer to be simulated. The shell layers must then be joined together using a contact or connection, which may then be given failure criteria in order to model adhesive failure.

Layers of shell elements appeared to be a promising method, since it is able to predict all the required properties of MPM sandwich materials; deformation, failure of bulk materials and failure of the adhesive. Additionally, the sole use of shell elements reduces the computation time in comparison to solid elements.

However, there are triple the number of elements in the model compared to a single shell layer. Each layer in the sandwich would require a contact to its adjacent layer to act as an adhesive bond. These contacts add significant processing time to a simulation and are disadvantageous for a full–scale vehicle crash model.

El Hage *et al.* [9] modelled aluminium–GFRP composite hybrid crash structures using two shell layers, one layer for the aluminium, one layer for the GFRP. The adhesive connection was made using a *CONTACT_TIEBREAK. The aluminium was modelled using *MAT_24 and the composite layer employed *INTEGRATION_SHELL (an archaic version *PART_COMPOSITE) [17]. The composite had four through thickness integration points, one per lamina in the composite. They showed good agreement with physical testing in terms of energy absorbed and the deformation modes. However, it is unknown whether this method would model structures where the composite layers did not conform to the shape of the progressive crushing observed in the monolithic crash structure, as was discussed in Chapter 2 – Literature review.

Although various authors have found this method to be successful, in practice in this work it was found to be difficult to find a stable solution using a layer of shells per layer of the MPM sandwich. Element penetration was common suggesting the contact modelling was not sufficiently robust, which led to gross instability and errors. This was due to the different elastic stiffness of the materials in the sandwich. For this reason, the use of layers of shell elements was not explored further.

6.3.1.4 Other methods attempted

There are various other ways in which an MPM sandwich material may be modelled. These were attempted and reported briefly below.

Firstly, the skins were modelled using shells and the core modelled using solids. However, the use of contacts to join the shell and solid layers produced unstable simulations, due to the multiple numbers of elements in contact with varying material stiffness.

An improved solution was to produce a solid element with a thickness of the separation of the shell elements mid–plane. The solid core was then coated with shell elements, the shells being used to model the steel skins. The core was therefore modelled with a greater thickness than the actual polymer core. The advantage of this model was that this was a more stable simulation due to reduction in the number of simultaneous contacts. The simulation times were 5.5 times longer using the hybrid model than using a shell element model. The element size being the same in both the hybrid model and the shell element model. The mean crush force result for the hybrid model was 22% lower than the physical test result.

Another option was the use of *MAT_ARUP_ADHESIVE (*MAT_169) [17] to model the adhesive. Three layers of shells were used to model the layers of the sandwich, the shell layers were then joined at their mid–planes using solids. Therefore, the solids modelling the adhesive were two orders of magnitude larger than the adhesive layer they model. The solids were defined using *MAT_169, where the actual adhesive thickness and properties were applied. This model would have provided the complete definition of the MPM sandwich, but the solid elements when defined as *MAT_169 compressed under impact without conserving volume; therefore, this model was discarded as this phenomenon was irreparable.

Hufenbach *et al.* [18] compared physical testing to FE modelling of a three–point bend test on aluminium–polypropylene–aluminium sandwich materials using ANSYS. Multiple solids through thickness, layered solids, shells, thick shells and a shell–solid hybrid were all used to simulate the bend test. All models predicted elastic stiffness well; however, all over–predicted the plastic stiffness of the MPM sandwich. Assuming the solid model is the most correct, the single shell element model was 5% stiffer than multiple solids through thickness due to the shell model over–estimating the through thickness shear behaviour of the core. Overall, there was little difference in response between all the methods used. The deflections in the three–point bend were not severe as seen in crash structures; therefore, the applicability of this work was uncertain.

6.3.1.5 Conclusion

A study of the possible methods of simulating MPM sandwich materials has been made. Preliminary models were developed to assess their applicability. The choice of modelling method was not clear from the literature, although the use of solids is the most accurate in terms of deformation [15]. Shells have been shown in

monolithic materials to perform as well as solids provided a suitably refined mesh is used, and the material is appropriately thin [1], [6].

Layers of shell elements may be a good solution, which would invariably be faster computationally than solids. The disadvantage to the layers of shell elements model is the increased number of elements, but more importantly the requirement for more computationally expensive contacts [6], [17]. However, the most significant drawback was the lack of stability in the crash model.

The hybrid models which employed shells for the metal skins and solids for the polypropylene core showed reasonable deformation similarity to the test results. However, the crash performance was lower than the tested value by 22%. Additionally, the run times were unacceptable, being over five times longer than a refined shell element model.

The single shell approach with the use of *PART_COMPOSITE was thus considered the best method. The sandwich materials tested were of thin gauge in comparison to the size of the structure, therefore, could be modelled as a shell. Without core shear correction the model could be potentially over–stiff, but this was not evident from the literature, however laminated shell theory may be invoked to correct the shear stiffness. Additionally, the ability to use a shell element model over solids has the advantage that it can model multiple sandwich constrictions using a single mesh. Whereas, using solids, the crash structure requires re–drawing and re–meshing.

6.3.2 Optimisation of MPM sandwich model

Based on the discussion in Section 6.3.1, the modelling method chosen was the One Shell Element method, Figure 6.6 – a. With the element type chosen as shell elements, the use of under–integrated (Type 2) and fully–integrated shells (Type 16) was compared. From the monolithic modelling (see Section 6.2.2) it could be seen that the Type 2 elements were under–stiff. Additionally, a mesh refinement study was performed to define the optimal element size; this was carried out for both the under–integrated and fully–integrated elements.

In order to optimise the model, one sandwich material combination was considered; this is the 1.7 mm DP600 sandwich (0.5 / 0.7 / 0.5 mm). This material had the thickest steel skins, hence, the model with the least optimal conditions for shell element modelling; thick material in comparison to the crash structure geometry.

The use of laminated shell theory (LST) was also considered (discussed in Section 6.3.1), therefore, two material models were used in the *PART_COMPOSITE model. The first was the standard metals material model (*MAT_24) and the laminated shell theory version of it (*MAT_114). Both models used Von Mises yield criterion with an associated flow rule, which allows the tensile test data for the material to be used for the plastic flow.

6.3.2.1 Model consideration 1 – Comparison of conventional (*MAT_24) and laminated (*MAT_114) shell theory

To assess the deformation of the material using conventional shell theory and laminated shell theory, a 2 mm element model was run using each formulation. Both models used the *PART_COMPOSITE function to define the sandwich material a single shell.

A comparison of these is shown for a 2 mm mesh element model, Figure 6.7. The *MAT_24 model, Figure 6.7 – 1, which uses conventional shell theory incorrectly portrays the deformation of the DPSW material when physically crash tested, Figure 6.7 – 2. The model, which used laminated shell theory, Figure 6.7 – 3, was seen to deform much like the tested crash structure, Figure 6.7 – 2. Additionally, as can be seen by the remaining un–deformed length of *MAT_24 model, Figure 6.7 – 1, is greater than for *MAT_114 model, Figure 6.7 – 3 for the same energy absorption. The *MAT_114 model predicted the remaining length of the crash structure within one millimetre of the test value (124 mm compared to 125 mm). This is due to the over–stiff behaviour of *MAT_24 not predicting correctly the through thickness shear in the polypropylene core. This is visually indicated by the rounded folds, Figure 6.7 – 1, compared to the flattened folds, Figure 6.7 – 3, portraying the test specimen, Figure 6.7 – 2.

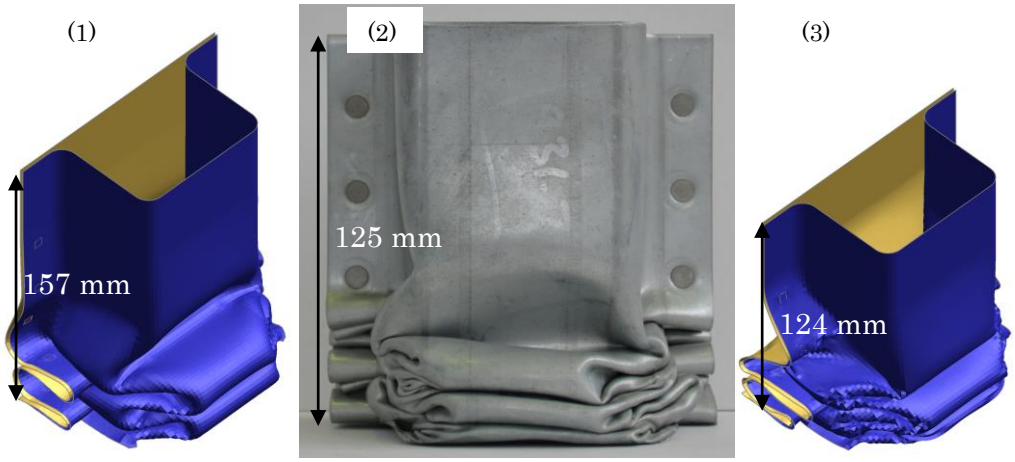

Figure 6.7 – A comparison of the deformation of (1) – *MAT_24 and (3) – *MAT_114 models. (2) – A physical test result performed at the same impact energy.

Hence, from this point forward only the *MAT_114 material model with laminated shell theory will be used with the *PART_COMPOSITE function.

6.3.2.2 Model consideration 2 – Element size and formulation

An investigation was performed into the effect of element size, the element sizes considered were 8, 4, 2, 1 and 0.5 mm. The 0.5 mm element model was discarded at an early stage due to length of time required for simulations. The deformation results are shown in Figure 6.8; the outcome was similar to the monolithic metals. The 8 mm and 4 mm element models have too large an element size to correctly depict the deformation, hence produced over–stiff results. The 2 and 1 mm elements were visually similar; however, the 1 mm elements produced an instability where the elements adjacent to the fixed end of the crash structure began to collapse.

The force–displacement and energy–displacement plots for the mesh refinement study, Figure 6.9, showed a reduce in mean crush force with decreasing mesh size due to the correct portrayal of the folding behaviour. However, there was a 6.3% discrepancy in the mean crush force result between the 1 and 2 mm models. The 2 mm model showed the greater mean crush force. The reason for the discrepancy between the 1 mm and 2 mm element models was the instability in the 1 mm elements adjacent to the fixed end of the crash structure. This occurred between 140 and 160 mm displacement, Figure 6.9 – green. If the instability in the 1 mm element model had no occurred, both mesh sizes would have produced a more similar result.

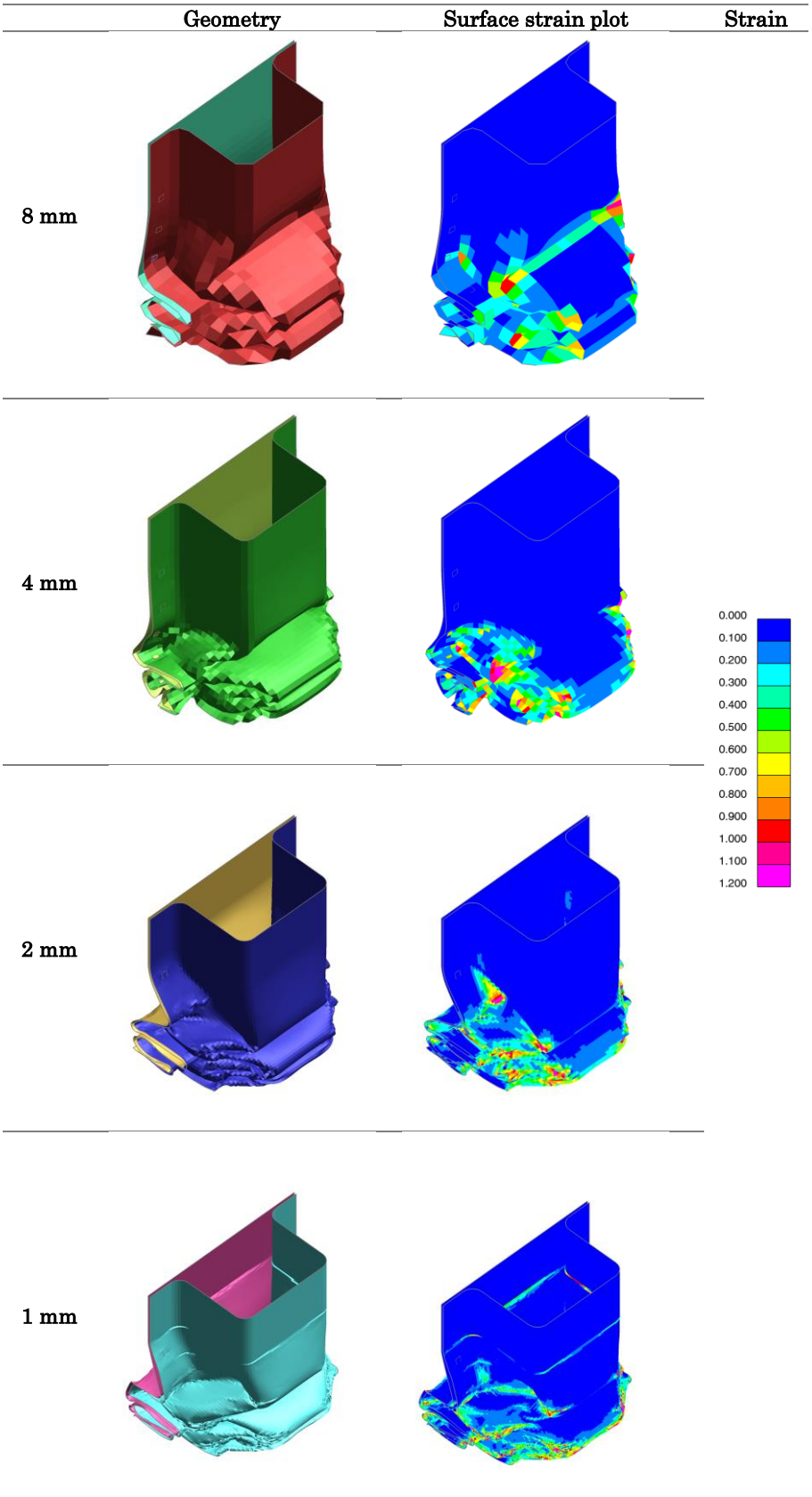

Figure 6.8 – Mesh refinement study of MPM sandwich material with *MAT_114.

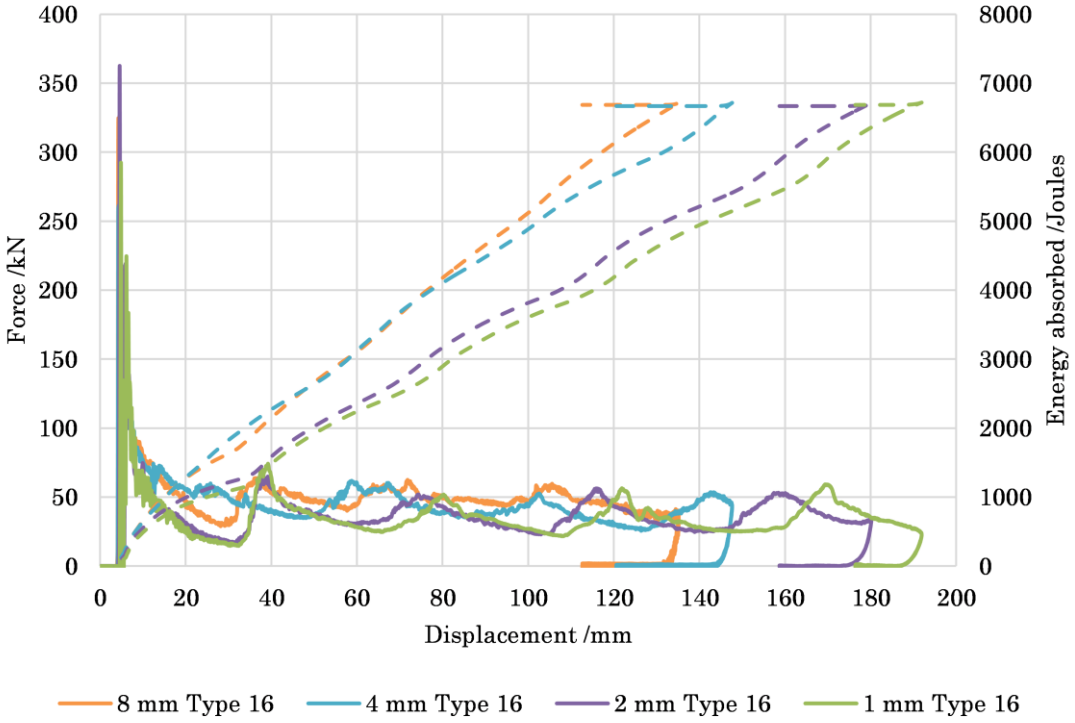

Figure 6.9 – Force–displacement and energy–displacement plots for DPSW material at different element sizes.

The run times for the models were similar to the monolithic models due to the use of shell elements. However, the *PART_COMPOSITE models took approximately 20% longer to run for the 2 mm element model than the comparative monolithic model.

6.3.2.3 Model consideration 3 – Number of integration points

An integration point analysis was performed to ascertain the minimum number of integration points required through the thickness of the sandwich to model the material. Unlike isotropic materials where more points are placed through thickness according to Gaussian quadrature, using *PART_COMPOSITE the points could be biased to the steel skin or the polymer core. Therefore, a full factorial test was run with the use of one, two, three, and five integration points through each layer of steel and polymer, and an additional experiment with an integration point every 0.1 mm was also performed. The results showed no

significance in the use of more integration points, all the results being within ±2% of the use of one integration point per layer. Therefore, one integration per layer of the MPM sandwich was used.

6.3.2.4 Sandwich material model decision

From the mesh refinement and element formulation modelling described in the previous sections, the decision was made to use *PART_COMPOSITE with *MAT_114 (using LST) material model, 2 mm elements, fully–integrated (Type 16) elements and one integration point per layer.

The reasons for such are:

- The combination of *PART_COMPOSITE with *MAT_114 was shown to model the deformation of the sandwich material correctly.
- The 2 mm elements modelled the deformation better than larger element sizes.
- The smaller elements had no significant difference kinematically and the run times increased an order of magnitude with each refinement.

Therefore, a compromise of performance and simulation expense was reached.

6.4 Strain rate modelling

Strain rate modelling is required to account for the increase in strength seen in metals and polymers when loaded at increasing speed. It is well known that steel's strength is strain rate dependent at higher strain rates (above 1 s^{-1}); also more recently it has been shown to be a significant effect in polymers [19], [20].

The conventional method of modelling strain rate dependency of materials in LS–DYNA is *via* the use of the Cowper–Symonds model [6], see Equation 6.1 [21]. This model uses a power law to increase the flow stress of a metal experiencing a specified strain rate.

$$\frac{\sigma_d}{\sigma_s} = 1 + \left(\frac{\dot{\varepsilon}}{C}\right)^{\frac{1}{q}} \qquad \text{Equation 6.1}$$

Where, σ_d = Flow stress at increased strain rate (Pa)

σ_s = Static flow stress (Pa)

$\dot{\varepsilon}$ = Strain rate (s^{-1})

C = Cowper–Symonds coefficient (s^{-1})

q = Cowper–Symonds exponent

6.4.1 DP600 steel

Tata Steel provided the strain rate sensitivity data for the DP600 material, and this data was used to produce a Cowper–Symonds model of the material. This allowed the use of tensile test data with the correct strain rate sensitivity as opposed to generic material data. This was important since the DP600 steel was seen to bake harden upon production of the sandwich in the curing of the adhesive and the laminating of the sandwich panel. Therefore, the standard model provided

was not useable, hence post–baking tensile test data was used with Cowper–Symonds model to provide the strain rate hardening.

6.4.2 Steelite and ECCS steels

The Steelite and ECCS skins strain rate sensitivity was unknown; therefore, the finite element models were calibrated with dynamic and quasi–static crush data from Chapter 5 – Quasi–static and dynamic testing. The sandwich material models were simulated quasi–statically and dynamically, and the Cowper–Symonds model used to produce the additional energy absorbed dynamically. The dynamic test was setup in the same manner as the drop test in order to ensure the inertia in the impact was accounted for [4] and this mass removed for the quasi–static simulations to remove the inertial response.

6.4.3 Polypropylene

The strain rate sensitivity of the polypropylene material was also unknown and high speed testing of polymers are notoriously difficult due to the low material stiffness. Ebert *et al.* [19] successfully tensile tested a polypropylene co–polymer at strain rates between 0.001 and 100 s^{-1}. A parameter fitted model for the elastic–plastic flow and the strain rate dependency was produced from this work, Figure 6.10 – solid. The model was used to approximate the Cowper–Symonds strain rate dependency of the polypropylene co–polymer Figure 6.10 – dashed. Although this was not the same as the polypropylene grade used in this study, it provided a good basis for the strength increase in the material at higher speeds. Therefore, the strain rate sensitivity was assumed the same, but tensile test data of the correct grade was used to produce the base material flow curve.

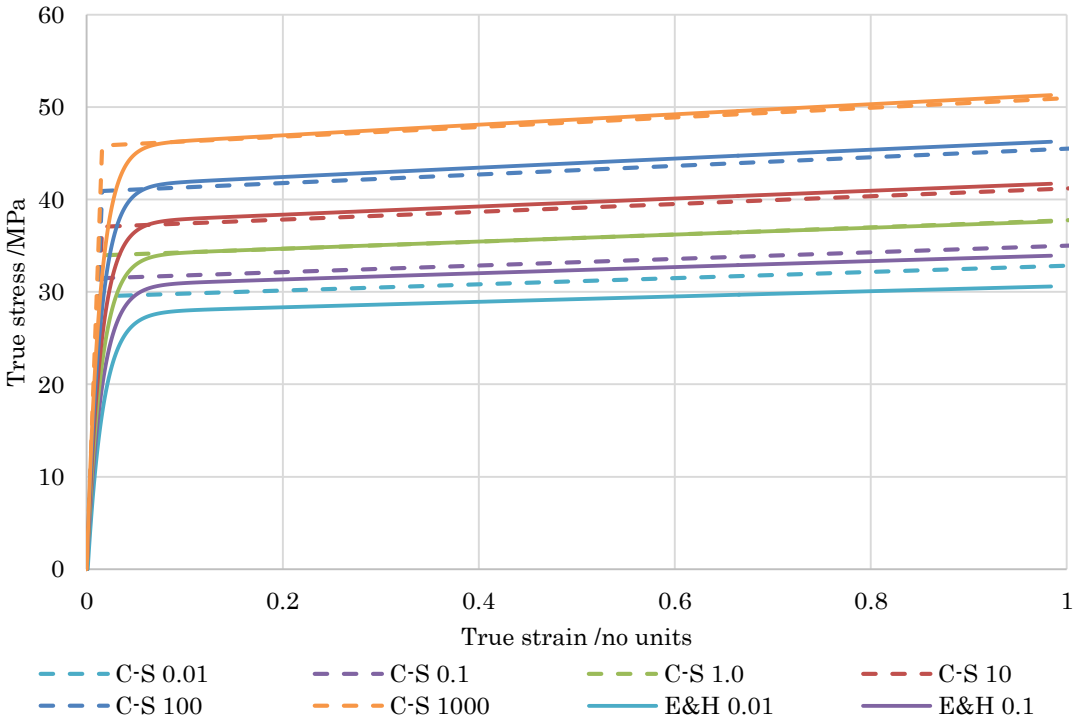

Figure 6.10 – Cowper–Symonds (C–S) model fitted to Ebert & Hufenbach (E&H) model for polypropylene hardening at increasing strain rate.

6.4.4 AA5754 and AC300–T61

Wowk [22] showed AA5754 does increase in strength with increasing strain rate. However, the work also showed a strength reduction at low strain rates (0.001 to 0.1 s^{-1}) and a strength increase at higher strain rates (0.1 to 1500 s^{-1}). However, at automotive crash strain rates (~100 s^{-1}) McGregor *et al.* [23] showed that although the yield strength of the alloy may increase up to 25%, the ultimate strength is not effected, hence there is little effect of on the energy absorption of the AA5754 alloy's strain rate sensitivity.

AC300–T61 is the highest strength aluminium tested and no information could be found regarding its strain rate dependency. In general, 6xxx series alloys have little strain rate sensitivity when fully aged (such as the T61 condition), which was consistent with physical test results in Chapter 5.

6.4.5 Summary

6.4.5.1 Polypropylene

A least squares regression fit was used to approximate the Cowper–Symonds values for the polypropylene material, the parameter fitted model from Ebert & Hufenbach [19] was therefore re–fitted. This gave values of C = 450 s^{-1} and q = 10.

6.4.5.2 Steelite 0.15 mm steel skin

The Steelite skin Cowper–Symonds values were found using trial and improvement using the single and double core drop test results only. Triple core results exhibited too much material failure and were ignored for the fitting. The Cowper–Symonds values were calculated at C = 1000 s^{-1} and q = 10.

6.4.5.3 ECCS 0.3 mm steel skin

The same method as used above for the Steelite skin was used for the 0.3 mm ECCS skin steel. The Cowper–Symonds values were C = 5000 s^{-1} and q = 5.

6.4.5.4 DP600 0.5 mm steel skin and 1.6 mm monolithic metal

The Cowper–Symonds values for the DP600 steel were found using the same least squares regression process used for the polypropylene core material in Section 6.4.5.1. However, the data Cowper–Symonds model was fitted to the Tata Steel material data. The Cowper–Symonds values were C = 1.8×10^6 s^{-1} and q = 5.

6.4.5.5 AA5754 and AC300–T61 monolithic aluminium alloys

The aluminium alloys were assumed strain rate insensitive.

6.5 Corner strain modelling

In production of top hats, the corners of the top hat were bent using press braking (process shown in Chapter 3). The V–bending process work hardens the corners of the crash structure. For simplicity, the stress increase was assumed to be only in the corners of the material. A prediction for the strain in the corner was based on calculating the average strain in a corner when the thickness of the material and the bend radius is known (Equation 6.2) [24].

$$\varepsilon_b = \ln\left(1 + \frac{y}{\rho}\right) \qquad \text{Equation 6.2}$$

Where, ε_b = bending strain

y = distance away from the neutral axis (mm)

ρ = radius of curvature (mm)

Although this model is crude, it showed the effect of the bending strain on the energy absorption of a formed crash structure, and accounted for some of the energy absorbed. The ideal solution using FEA is a forming simulation to show the local strain formation across the bent corner and the flat faces .

Figure 6.11 shows the effect of forming strains on the material strength in the corners using the ECCS steel skin as an example. The yield strength increases are shown over the original material. Since the strain to failure was not modelled the stress data was then extrapolated to a strain of 100%. The extrapolated values are not shown for clarity.

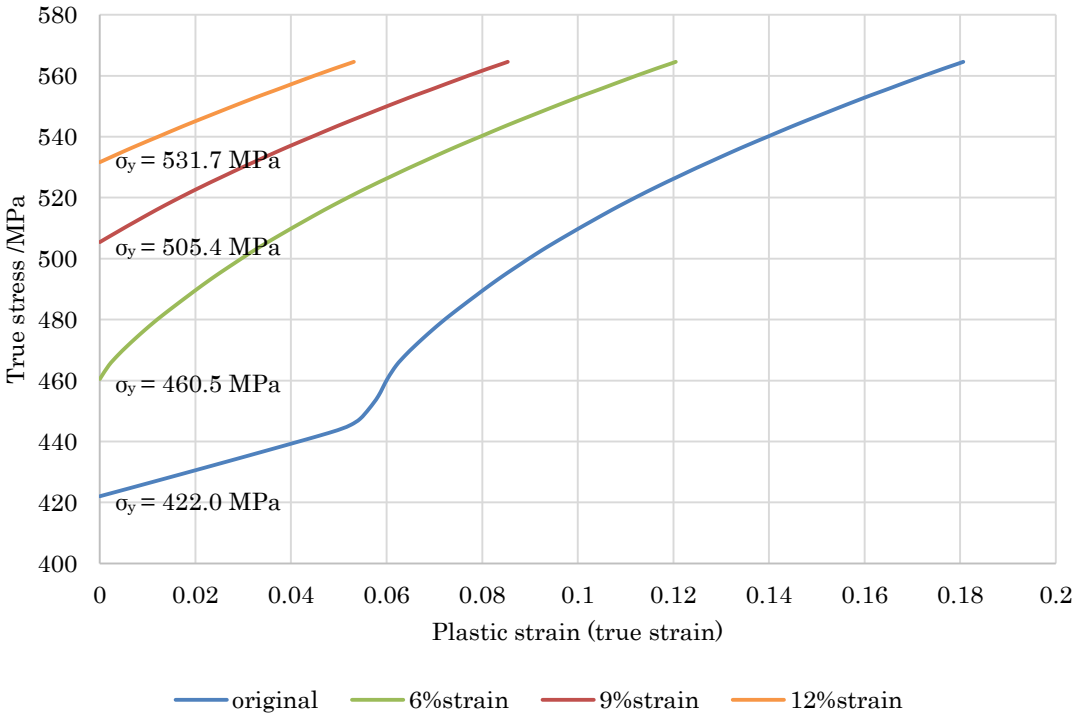

Figure 6.11 – True stress – true plastic strain plot, showing the plastic flow data for ECCS steel with no forming strains, then with increasing forming strains for each of the corner thickness increments.

The corner strains were inputted into the model using a separate part card and material card for the corners, based on the flow curves shown in Figure 6.11. This allowed the corners to have an increased strength over the rest of the material.

The strain rate sensitivity of a material was assumed not to change for a material which had been plastically deformed. The increased strength of the steel in the corners of the crash structure used the same C coefficient and p exponent as the unstrained material. Wowk [22] has shown plastic deformation before strain rate testing reduced the strain rate sensitivity of AA5754 aluminium.

The forming effect on the polypropylene core was ignored due to the small strength increase expected in the polymer. First due to its low strength in comparison to the steel skins. Second, due to the relatively flat plastic hardening curve of the polymer, making little difference to yield stress at onset of plasticity. Finally, since

the polypropylene is the core material its centreline is about the neutral axis of the material in bending, therefore it does not strain significantly.

6.5.1 Thickness reduction

Thickness reduction in the corners was also accounted for. This was calculated by ignoring the elastic strain and assuming volume conversation in the plastic region. Hence, the percentage thickness reduction of the material in the corners was half of the plastic strain percentage in forming (calculated using Equation 6.2).

6.6 Quasi–static and dynamic testing

Quasi–static and dynamic tests were both modelled using explicit finite element methods. In order to decrease the simulation times in the quasi–static tests, the simulations were performed at 1 $m.s^{-1}$ as opposed to the physical test speed of 1 $mm.s^{-1}$. The quasi–static tests were modelled without strain rate data and to ensure the validity of modelling quasi–static at higher speeds, the mass of the drop weight was reduced (to 1×10^{-2} kg). This ensured the kinetic energy input was less than 5% of the total internal energy in the simulation, as a well recognised method [4]. The kinetic energy input was less than 0.1% in all tests, hence inconsequential.

In the dynamic (impact) testing, an initial velocity was set instead of a constant velocity, and the drop weight mass set to 80 kg in order to mimic the weight of the drop tower mass. The velocity was set in order to achieve the required impact energy according to the kinetic energy equation (Equation 6.3).

$$KE = {}^{1}/_{2} \cdot m \cdot v^{2} \qquad \text{Equation 6.3}$$

Where, KE = Kinetic Energy (J)

m = mass (kg)

v = velocity ($m.s^{-1}$)

6.7 Simulation data filtering

For presentation of force–displacement curves and visual comparison of simulation data to physical test data, the simulation output was filtered. The filtering technique used was an exponential filter (described by Equation 6.4) [25].

$$s_t = \alpha \cdot x_{t-1} + (1-\alpha) \cdot s_{t-1} \qquad \text{Equation 6.4}$$

Where, s_t = Filtered observation

α = Smoothing factor, $\alpha = 0.9$

x_{t-1} = Previous observation

s_{t-1} = Previous filtered observation

In all instances, the filtering did not alter the results significantly; but reduced the local oscillations (noise) and reduced the peak force. An example of a filtered result is shown in Figure 6.12.

The peak force was however, over–predicted in simulations. This was due to the contact modelling; contacts in the finite element model require a large initial force on impact between the impact surface and the crash structure to prevent penetration of nodes, which caused a large peak force to be produced. Additionally, matching the peak force to the test was out of scope for this work, more importance was placed on mean crush force prediction.

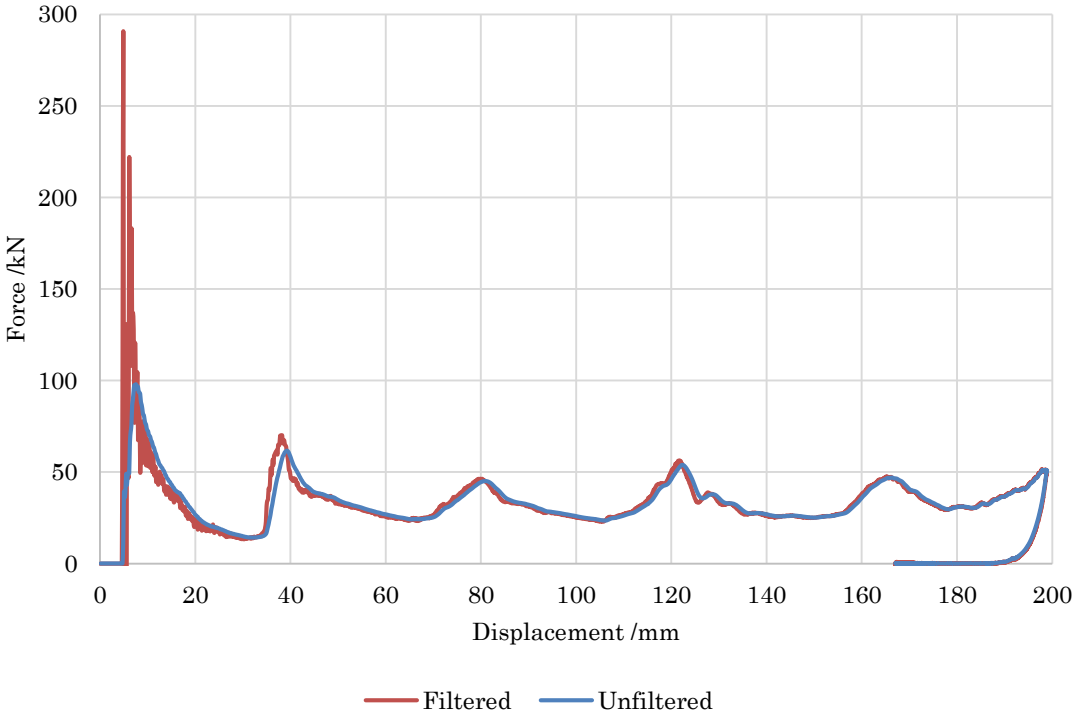

Figure 6.12 – Filtered data *vs.* unfiltered data, using exponential filtering technique.

6.8 References

[1] Ø. Fyllingen, O. S. Hopperstad, A. G. Hanssen, and M. Langseth, "Brick versus shell elements in simulations of aluminium extrusions subjected to axial crushing," in *7th European LS-DYNA Conference*, 2009.

[2] Y. Bai, Y. Bao, and T. Wierzbicki, "Fracture of prismatic aluminum tubes under reverse straining," *Int. J. Impact Eng.*, vol. 32, no. 5, pp. 671–701, May 2006.

[3] Ø. Fyllingen, O. S. Hopperstad, A. G. Hanssen, and M. Langseth, "Modelling of tubes subjected to axial crushing," *Thin-Walled Struct.*, vol. 48, no. 2, pp. 134–142, Feb. 2010.

[4] V. Tarigopula, M. Langseth, O. S. Hopperstad, and A. H. Clausen, "Axial crushing of thin-walled high-strength steel sections," *Int. J. Impact Eng.*, vol. 32, no. 5, pp. 847–882, May 2006.

[5] A. Stuehmeyer, "The thick shell element type 3: The thick shell element for metalforming and other applications," in *5th European LS-DYNA Conference*, 2005.

[6] J. O. Hallquist, *LS-DYNA Theory Manual*. Livermore Software Technology Corporation, 2006.

[7] T. Belytschko, J. I. Lin, and T. Chen-Shyh, "Explicit algorithms for the nonlinear dynamics of shells," *Comput. Methods Appl. Mech. Eng.*, vol. 42, no. 2, pp. 225–251, Feb. 1984.

[8] X. Xiao, C.-K. Hsiung, and Z. Zhao, "Analysis and modeling of flexural deformation of laminated steel," *Int. J. Mech. Sci.*, vol. 50, no. 1, pp. 69–82, 2008.

[9] H. El-Hage, P. K. Mallick, and N. Zamani, "A numerical study on the quasi-static axial crush characteristics of square aluminum–composite hybrid tubes," *Compos. Struct.*, vol. 73, no. 4, pp. 505–514, Jun. 2006.

[10] R. Gümrük and S. Karadeniz, "The influences of the residual forming data on the quasi-static axial crash response of a top-hat section," *Int. J. Mech. Sci.*, vol. 51, no. 5, pp. 350–362, May 2009.

[11] X. Zhang and H. Huh, "Crushing analysis of polygonal columns and angle elements," *Int. J. Impact Eng.*, vol. 37, no. 4, pp. 441–451, Apr. 2010.

[12] Ø. Fyllingen, O. S. Hopperstad, and M. Langseth, "Simulations of a top-hat section subjected to axial crushing taking into account material and geometry variations," *Int. J. Solids Struct.*, vol. 45, no. 24, pp. 6205–6219, Dec. 2008.

[13] M. Langseth, O. S. Hopperstad, and T. Berstad, "Crashworthiness of aluminium extrusions: validation of numerical simulation, effect of mass

ratio and impact velocity," *Int. J. Impact Eng.*, vol. 22, no. 9–10, pp. 829–854, Oct. 1999.

[14] Arup, *Introduction to LS-DYNA: Training Manual*. .

[15] A. Tabiei, "LS–DYNA Training Manual: Composite modelling in LS–DYNA."

[16] M. Dunand and J.-N. Gacel, "USILIGHT: A Cost-Effective Solution to Lighten Cars," *Soc. Automot. Eng. Tech. Pap.*, no. 2006–01–1216, Apr. 2006.

[17] J. O. Hallquist, *LS-DYNA Keyword User's Manual*, Version 97. Livermore Software Technology Corporation, 2007.

[18] W. Hufenbach, J. Jaschinski, T. Weber, and D. Weck, "Numerical and experimental investigations on HYLITE sandwich sheets as an alternative sheet metal," *Arch. Civ. Mech. Eng.*, vol. 8, no. 2, pp. 67–80, 2008.

[19] C. Ebert, W. Hufenbach, A. Langkamp, and M. Gude, "Modelling of strain rate dependent deformation behaviour of polypropylene," *Polym. Test.*, vol. 30, no. 2, pp. 183–187, Apr. 2011.

[20] M. Zrida, H. Laurent, V. Grolleau, G. Rio, M. Khlif, D. Guines, N. Masmoudi, and C. Bradai, "High-speed tensile tests on a polypropylene material," *Polym. Test.*, vol. 29, no. 6, pp. 685–692, Sep. 2010.

[21] G. Cowper and P. Symonds, "Technical report (Brown University. Division of Applied Mathematics), Strain-hardening and strain-rate effects in the impact loading of cantilever beams," 1957.

[22] D. Wowk and K. Pilkey, "Effect of prestrain with a path change on the strain rate sensitivity of AA5754 sheet," *Mater. Sci. Eng. A*, vol. 520, no. 1–2, pp. 174–178, Sep. 2009.

[23] I. McGregor, D. Meadows, C. Scott, and A. Seeds, "Impact Performance of Aluminium Structures," in *Structural Crashworthiness and Failure: Proceedings of the Third International Symposium on Structural Crashworthiness held at the University of Liverpool, England, 14-16 April 1993*, 1993, pp. 333–359.

[24] J. Hu, Z. Marciniak, and J. L. Duncan, *Mechanics of Sheet Metal Forming*, 2nd ed. 2002.

[25] M. Natrella, *NIST e-Handbook of Statistical Methods*. National Institute of Standards and Technology, 2010.

7 Results comparison

This chapter details the results achieved from Finite Element Analysis (FEA). The results are compared to the physical test in Chapter 5 – Quasi–static and drop testing. A comparison was made based on the mean crush force, energy absorbed and the displacement of each fold in the material as it collapsed, as well as the visual deformation of the material.

7.1 Monolithic materials

The monolithic results are included to show the difference in performance compared to the sandwich materials, Table 7.1. As expected, the deformation matched the physical tests well, Figure 7.1.

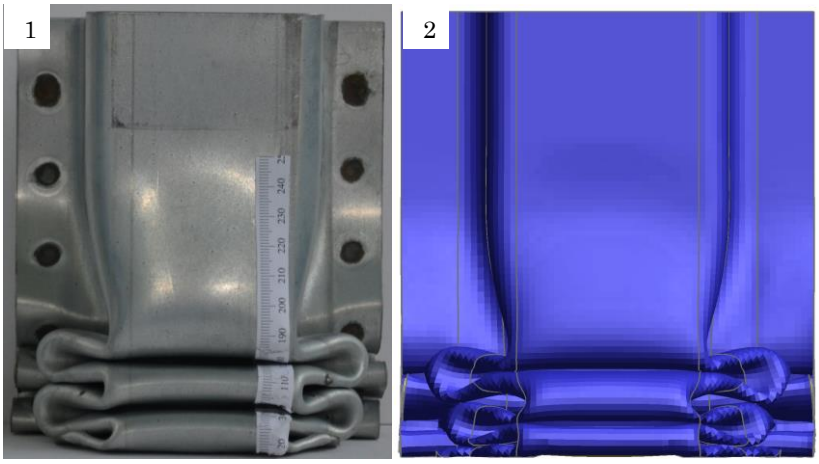

Figure 7.1 – 1.6 mm DP600 crash test result (1) and the simulated version (2).

The mean crush force results comparing the FEA to the physical tests are summarised in Table 7.1.

Table 7.1 – Comparison of FEA results to physical tests for the monolithic metals. Bracketed values are physical test results.

Material	Mean crush force /kN		Percentage difference	
	Quasi–static	Dynamic	Quasi–static	Dynamic
1.6 mm DP600	61.2 (63.5)	70.5 (69.5)	–3.6%	+1.4%
2.5 mm AA5754	45.4 (46.7)	46.9 (49.5)	–2.7%	–5.2%
2.5 mm AC300–T61	52.0 (53.4)	54.3 (55.5)	–2.6%	–2.1%

7.1.1 AC300–T61

The result for AC300–T61 differed from the test result by approximately the same amount both quasi–statically and dynamically (2.1 to 2.6%). Hence, confirming the strength increase in the material was due to the inertial response of the material and not its strain rate sensitivity.

7.1.2 AA5754

The AA5754 does have some strain rate sensitivity, which was not accounted for in the simulations. The dynamic result was 5% lower compared to the quasi–static results being only 3% lower.

7.1.3 DP600

The DP600 was under–predicted quasi–statically but over–predicted dynamically, this suggests that the strain rate model used for the DP600 steel over estimates the strength increase in the steel at higher strain rates. This was most likely due to the tensile strength of the DP600 being higher than expected, hence its strain rate sensitivity being lower.

7.1.4 Discussion

Overall, a single layer of shells with five integration points through thickness and fully–integrated elements modelled monolithic materials well. The deformation of the material was well predicted for all metals tested (all being within 5.2%). The DP600 steel performance was under–predicted statically and only 1% over dynamically, however this model used the strain rate sensitivity suggested by Tata Steel (steel manufacturer). Both aluminium alloys were under–predicted. The AA5754's larger discrepancy dynamically can be accounted for by strain rate hardening which would increase the mean crush force result. The AC300–T61 was around the 2% mark, both statically and dynamically, suggesting there is little strain rate hardening. In conclusion, the models worked well for monolithic materials.

7.2 0.15 mm Steelite sandwich

7.2.1 Quasi–static

The single core tests exhibited unstable collapse modes due to the thinness of the sandwich in comparison to the width of the crash structure (discussed in Chapter 2 – Literature review). As Figure 7.2 – image 1 shows, unstable collapse modes were predicted by the simulations; the simulations also suggested the folds in the sandwich would become more stable with increased thickness, Figure 7.2 – image 2 & 3. This was confirmed by the physical testing of the Steelite sandwich materials (Chapter 5).

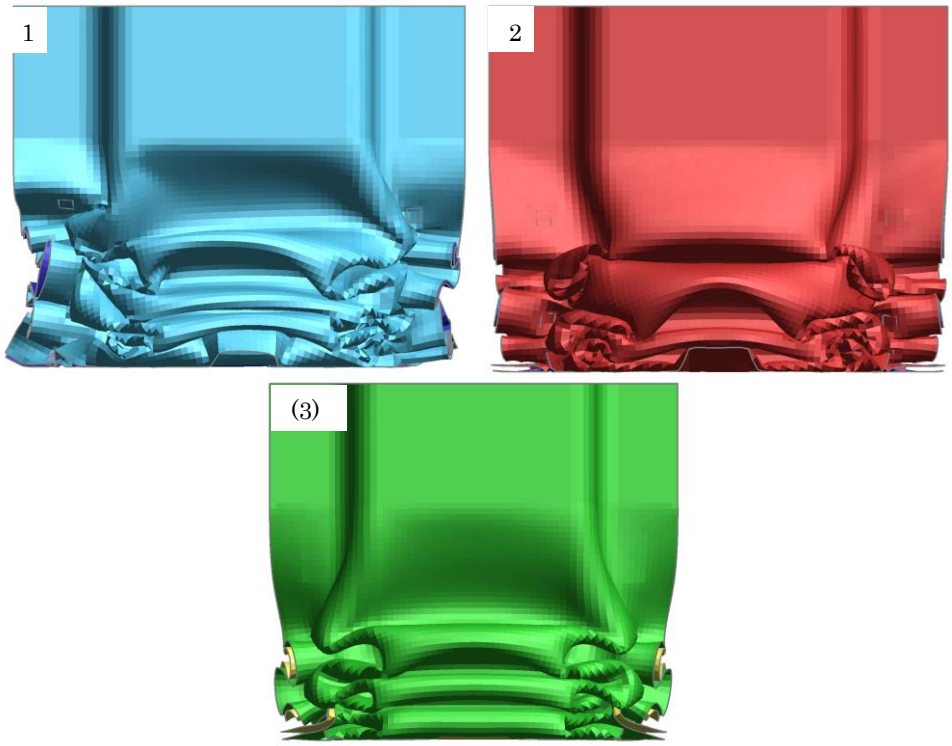

Figure 7.2 – Collapse modes in quasi–static tests modelled in LS–DYNA simulations. (1) – single core, (2) – double core and (3) – triple core Steelite sandwich materials.

Force–displacement curves for the Steelite quasi–static crush tests, Figure 7.3, show the displacements are laterally shifted in the simulations compared to the physical tests. This was due to the peak force in the simulation being over a greater displacement than in the tests, which is most likely due to the nature of the

initiator production in the physical tests. The initiators were manually set and therefore vary in geometry and are consequently not modelled perfectly.

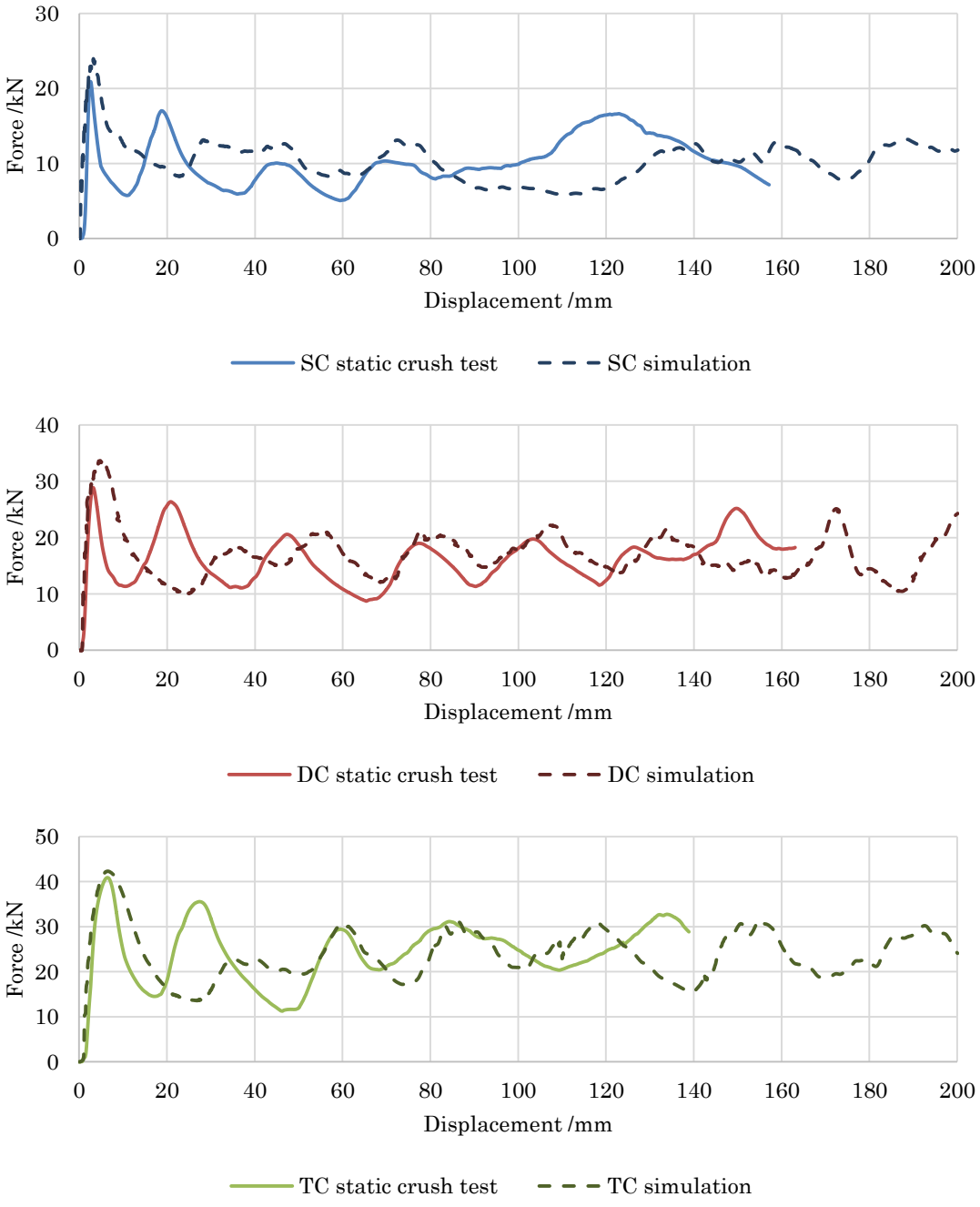

Figure 7.3 – Steelite quasi–static crush test simulations (dashed), from top to bottom single, double and triple core respectively, compared to physical tests (solid).

The unexpected secondary peak force was not simulated; this is likely to be due to the idealised crushing response in simulation not predicting the compacting of the secondary fold into the primary fold as it occurred in testing. The cause for this is

the definition of the contact model in LS–DYNA. The contact model prevents shell element intersection by searching for potential contacts before they occur and applying a contact force. This increases the effective thickness of the element to prevent intersection and reduce simulation instability. This potentially prevented the compaction of the second fold into the first being modelled correctly.

Of the quasi–static results, the double core, Figure 7.3 – red, was the closest match to the simulation. This was due to the thicker core over the single core producing more regular folding and a more stable crushing response, leading to less instability and hence closer to the idealised model. Since the single core exhibited instability, only approximately 100 mm of displacement showed progressive crushing when quasi–statically crushed. This led to a deviation in the force–displacement response in the simulation from the physical tests, since the simulations did not predict instability to the extent it was seen in the physical tests. The idealised geometry and thickness of the crash structure in the simulations could account for the lack of instability prediction. As described in Chapter 3 – Materials and methods, the geometry of the crash structure when press brake bent varied from that intended. Additionally, the thickness of the sandwich material was seen to vary an order of magnitude more than rolled sheet, again previously discussed (Chapter 3).

The triple core variant exhibited an increased likelihood of failure of the skin when the material deformed during crushing. Since the model did not account for this failure, a difference was inevitable. Overall, Figure 7.3 shows when the tested crash structures crushed progressively, the simulation and physical quasi–static crush tests were in good correlation (i.e. for the first 100 mm of displacement).

Note that the quasi–static simulations, Figure 7.3, were crushed to a displacement of 200 mm in all instances as the level of instability in the simulations was less

than seen in the physical tests. When instability occurred in the physical tests, they were halted hence the displacements of the test results do not extend beyond 170 mm.

7.2.2 Dynamic

The single, double and triple core sandwich material behaviour was predicted well by the simulations in dynamic (crash) tests, Figure 7.5. The displacements of the folds as well as the peak and trough heights were close to the tested values, but the secondary peak seen in the test was not predicted, as was the case in the quasi–static crushing.

Even though in dynamic (crash) tests, steel skin failure became more prevalent in the double and triple core variants, peak and trough placements in the simulations did not alter significantly from the test data. This is because the crash structures underwent mostly progressive crushing. When significant failure occurred, it was towards the end of the individual fold production; hence, the force response was not significantly altered.

The triple core Steelite exhibited the most prevalent failure of the steel skin when impacted. Since the simulations did not account for failure, the folding seen in the structure is rather idealised, Figure 7.4 – images 1 & 2. However, up until failure there is a good correlation in deformation between the models as shown by comparing Figure 7.4 – 1 & 3. Figure 7.4 – images 2 & 4 show where the simulation (lacking failure prediction) did not compare to the test result; the anterior face of the impacted crash structure failed through thickness, Figure 7.4 – 4, circle), and the failure of the flanges when bent through 180°, Figure 7.4 – 4, dashed circle.

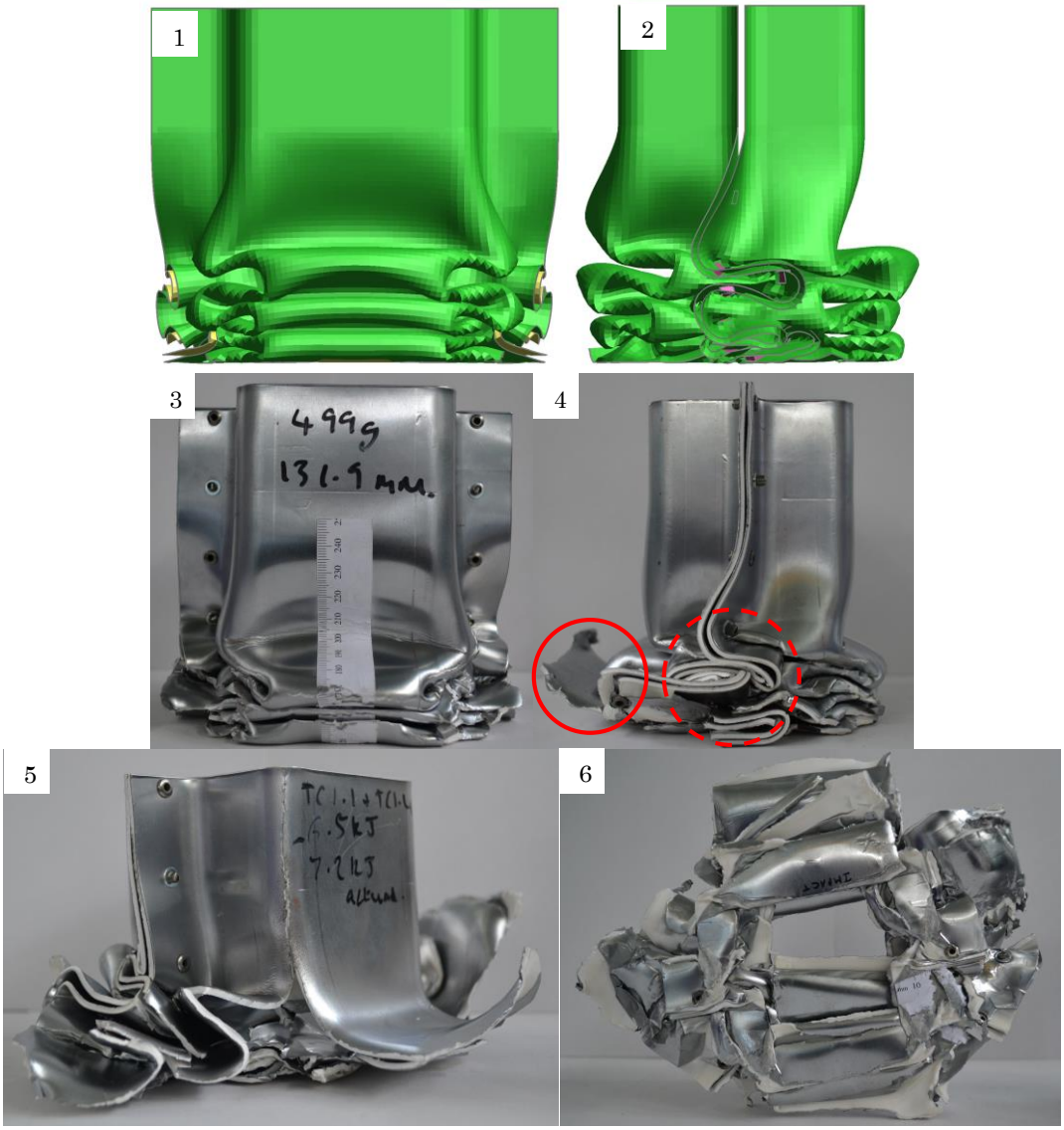

Figure 7.4 – 1 and 2 – LS–DYNA simulations of the impacted triple core Steelite (anterior and lateral views respectively). 3 and 4 – views of Steelite triple core crash structures (anterior and lateral views respectively), failure in the material when drop tested is highlighted by the red circles. 5 and 6 – Triple core Steelite crash structure which underwent catastrophic failure. 6 – underside of the triple core Steelite crash structure, significant failure of the sandwich materials through thickness can be clearly seen.

For the dynamic (crash) tests, the impact energy was matched to the test condition, therefore, if the mean crush force is under–predicted, by definition the displacement of simulation will be less than the physical test and *vice versa.*

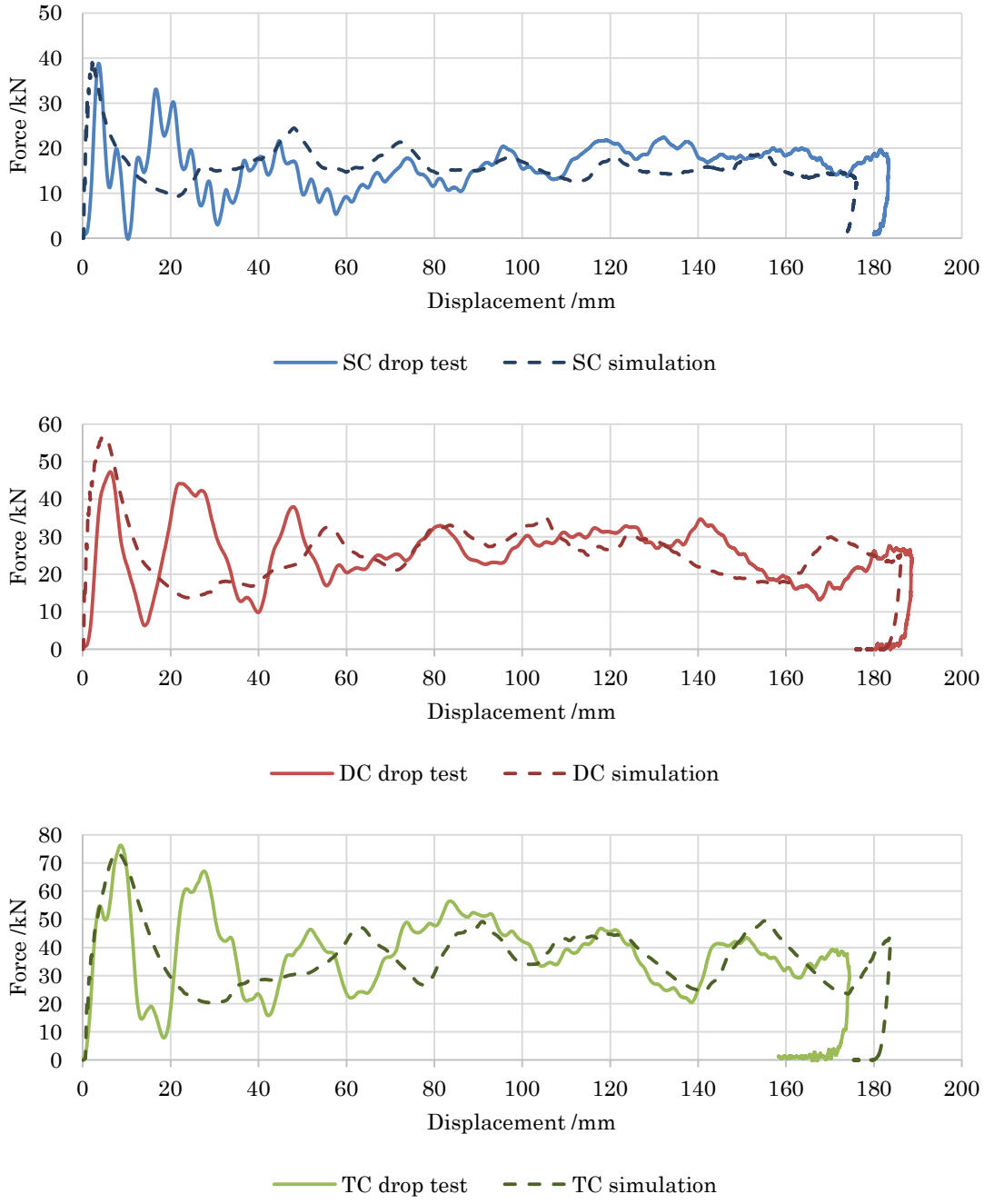

Figure 7.5 – Steelite dynamic (crash) test simulations (dashed), from top to bottom single, double and triple core respectively, compared to physical tests (solid).

7.2.3 Discussion

Table 7.2 shows the mean crush force difference between both quasi–static and dynamic tests for all thicknesses of the Steelite sandwich material. The quasi–static tests produced a consistently higher force; however, with increasing core

thickness the values became closer to the test results, Table 7.2. Dynamically the mean crush force varied both above and below the tested values.

Table 7.2 – Comparison of FEA results to physical tests for the Steelite sandwich materials in all three thicknesses. Bracketed values are physical test results.

Thickness	Mean crush force /kN		Percentage difference	
	Quasi–static	Dynamic	Quasi–static	Dynamic
Single core	10.3 (9.6)	16.4 (15.6)	+7.8%	+5.0%
Double core	17.0 (15.9)	25.9 (26.5)	+7.0%	–2.2%
Triple core	23.9 (22.8)	37.2 (37.5)	+4.9%	–0.8%

The over–stiff behaviour in the FEA quasi–static mean crush force compared to the physical test result is hypothesised to be due to the variability in the sandwich materials and in the crash structure production processes. Leading to a variation from the idealised crash structure simulated.

Since the top hats were press brake bent, there was variability in their geometry, which meant they had to be clamped to the correct shape for joining. The sandwich materials were also modelled with a nominal thickness. However, the variation in sandwich material thickness was up to an order of magnitude greater than rolled steel or aluminium sheet material (1–3% of total thickness for sandwich materials, in comparison to < 0.5% for monolithic metals). This variability was not accounted for in the simulations. Hence, the simulations were idealised, and did not account for many of the differences in comparison to the physical tests, which had manually produced materials and crash structures.

Instability in the crash structure during the physical tests, Figure 7.3 occurred with the single core Steelite. The simulation was displaced to 200 mm whereas, in the physical tests instability occurred before this point, hence increasing the force towards the end of the test resulted in the tests being aborted prematurely. Additionally, the triple core tests showed failure (rivet pull–out) of the spot–joints (blind rivets) in testing, which was not simulated in the model.

The triple core quasi–static simulations showed a decrease in mean crush force prediction in comparison to the single and double core results. This is hypothesised to have been the initial failure in the steel skin on the outer surface of the bent corners (discussed in Chapter 3), as well as the failure of the steel skin during testing. This led to a reduced bending strength of the sandwich, leading to a reduction in the mean crush force.

The dynamic results, Table 7.2, did not show the same trend of consistently over–predicting the mean crush force. The Cowper–Symonds strain rate hardening parameters were defined for the single core material and were then applied to the double and triple core variants (described in Chapter 6 – Modelling methodology). The simulated response for these materials was lower than the test response. The trend in the results suggests the double and triple core materials absorbed more energy than the simulations predicted.

This discrepancy in the double and triple core results absorbing more energy than the simulations predicted can be theorised to be due to the large amount of failure seen in the double and triple core variants. Quasi–statically, failure of the skin reduced the bending strength but a progressive crushing response remained. Dynamically, when failure occurred, energy had already been absorbed through progressive crushing. The energy absorption mechanisms then became mixed–mode, both progressive crushing and progressive failure aiding in energy absorption. The progressive failure increased the energy absorption, which was not predicted by the LS–DYNA simulations.

7.3 0.3 mm Electrolytically chrome coated (ECCS) sandwich

7.3.1 Quasi–static

Quasi–statically, the ECCS crash structures exhibited wrinkling (long and short folds) in the corners, with conventional plastic hinges across the faces. Figure 7.6 – image 1 shows the single core ECCS where wrinkling was not as dominant, the simulation predicted the folding well, Figure 7.6 – image 3. Figure 7.6 – image 2 shows the double core response where considerable wrinkling in the corners was exhibited, this also occurred in the triple core variant (not shown since response was similar to the double core). The simulation did not predict the wrinkling in the corners, hence the simulation was again idealised, Figure 7.6 – image 4. The wrinkling (long and short folds) seemed to interrupt the folding in the double core ECCS sandwich crash structure; however, the structure still folded in the progressive manner.

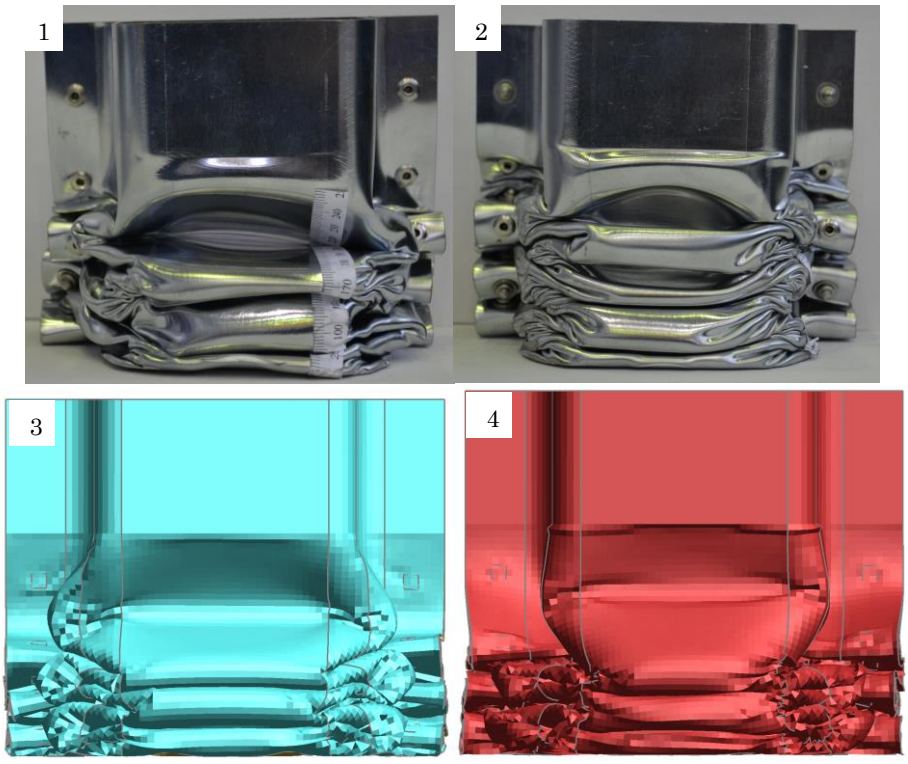

Figure 7.6 – 1 – ECCS SC and 2 – ECCS DC with wrinkling in the corners. 3 and 4 – respective simulations which did not predict the wrinkling behaviour.

A second discrepancy observed was the number of folds produced by the crash structure. The tested sandwich materials producing four folds instead of the three predicted. As opposed to being incorrect modelling of the crash structure this can be theorised to be due to the initiator in the crash structure not being modelled correctly. The initiator used was the same size as the monolithic crash structures since they were the same geometry. However, the sandwich material was observed to fracture at the point of bending of the initiator when tested. This lead to a fold being produced at the point of this failure. Once the material had folded over in the first fold on the anterior face, the crash structure folded normally. This was put forward as the case since the posterior face of the crash structure did not exhibit an additional fold to follow the one on the anterior face, as would be observed in conventional asymmetric collapse.

Figure 7.7 shows the force–displacement plots for the quasi–static crush tests in the simulations compared to the physical tests. The displacement at the peak force in the simulations, Figure 7.7 – dashed, was consistently around the 20 mm mark. In the physical tests, Figure 7.7 – solid, the first fold was completed after 10 mm, the point at where the initiator was set. A predominantly flat response was seen in the progressive crushing region of the physical tests, which was not portrayed in the simulations. This is most likely due to the continual wrinkling of the corners obscuring any potential force oscillations.

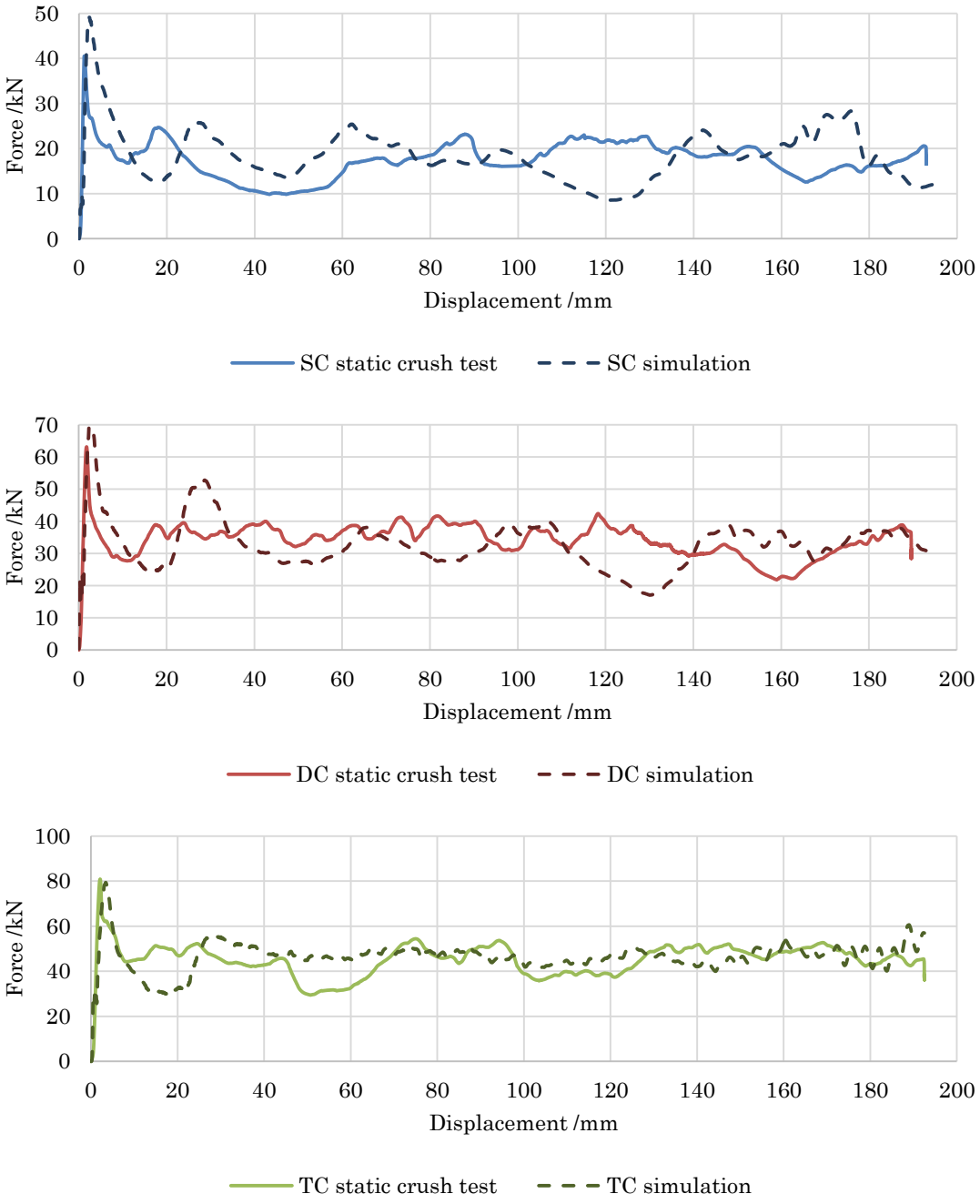

Figure 7.7 – ECCS quasi–static crush test simulations (dashed), from top to bottom single, double and triple core respectively, compared to physical tests (solid).

7.3.2 Dynamic

Dynamically, conventional asymmetric collapse was dominant in all three thicknesses, Figure 7.8 – images 1 & 2 shows the single and double core. The wrinkling observed quasi–statically was not as dominant dynamically, suggesting the wrinkling was caused by instabilities not present when impacted at higher

velocities. Again, four folds were seen as opposed to the three folds predicted, most likely due to the same reason as that in the quasi–static tests.

The single core ECCS, Figure 7.8 – image 1, showed irregularity in the folding most likely caused by the low thickness to width ratio for the crash structure, as well as the variability in the formed shape of the top hats. The simulation showed a more idealised folding, Figure 7.8 – image 1. The double and triple core crash structures exhibited more regular folding and were modelled well, double core is shown in Figure 7.8 – image 2 and compared to image 4.

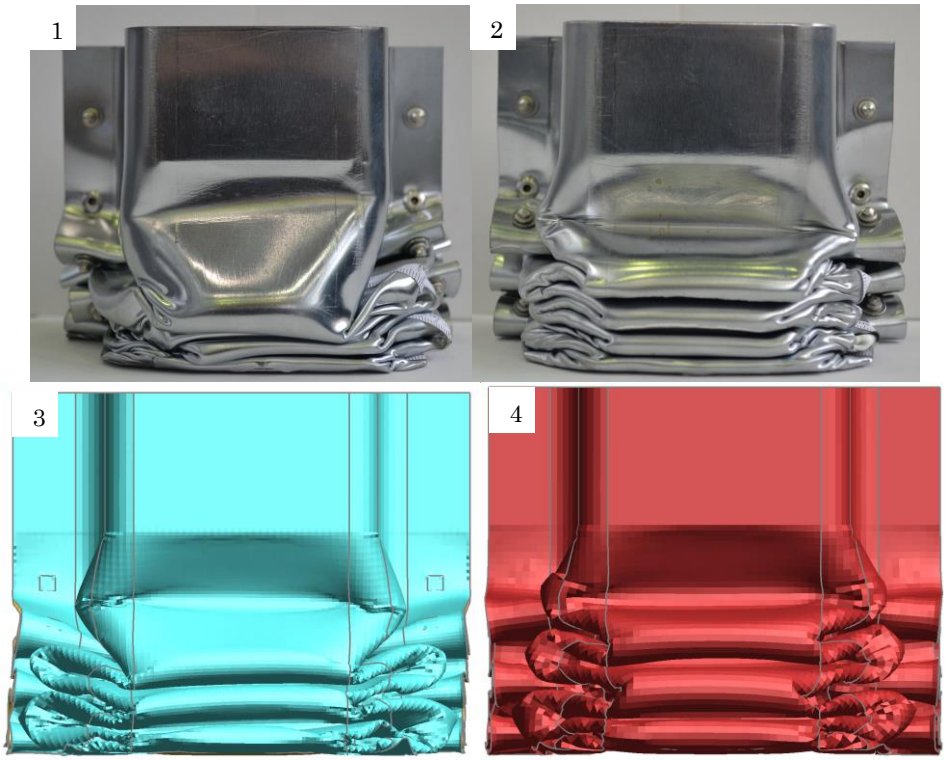

Figure 7.8 – Single (image 1) and double (image 2) core drop tested crash structures and the simulated response (images 3 & 4 respectively).

The force–displacements plots showed the oscillatory behaviour, Figure 7.9 – solid, predicted by the simulations, Figure 7.9 – dashed. The simulations predicted only three folds; however, Figure 7.9 shows the first two folds in the physical tests coincided with the first fold in the simulations. This confirms the theory suggested

in the quasi–static results that the first fold was due to the initiator production. After the peak force, a good correlation in fold placement was observed.

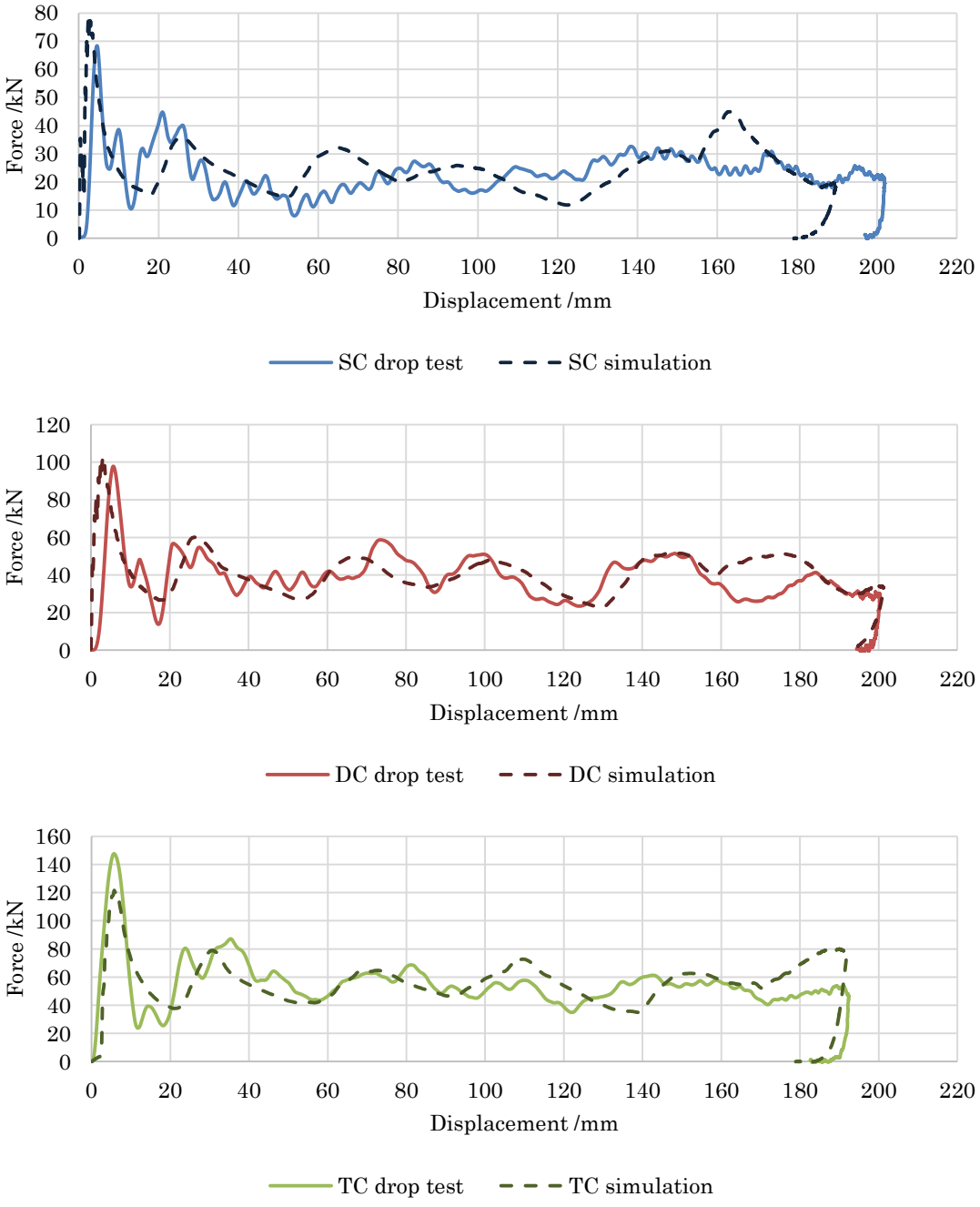

Figure 7.9 – ECCS dynamic (crash) test simulations (dashed), from top to bottom single, double and triple core respectively, compared to physical tests (solid).

7.3.3 Discussion

The comparison of the mean crush force between the simulations and the physical tests are summarised in Table 7.3.

Table 7.3 – Comparison of FEA results to physical tests for the ECCS sandwich materials in all three thicknesses. Bracketed values are physical test results.

Thickness	Mean crush force /kN		Percentage difference	
	Quasi–static	Dynamic	Quasi–static	Dynamic
Single core	18.4 (17.4)	25.4 (23.8)	+5.6%	+6.4%
Double core	32.7 (34.7)	41.6 (40.0)	–6.0%	+3.9%
Triple core	46.8 (45.3)	57.2 (55.1)	+3.2%	+3.7%

The results were in reasonable agreement with the physical tests, being within ± 6% in all circumstances. The result for the double core quasi–static crush was unexpectedly higher than the simulation predicted, presumably due to the wrinkling in the corners. The increase in mean crush force from single to double core in the Steelite was 60%, whereas the single to double core increase in the ECCS sandwich was 100%. This suggests that the physical test result was greater than it should be, as a similar increase in mean crush force would be expected when increasing the core thickness from single core to double core.

The trend seen in the Steelite sandwich materials (Section 7.2) was also seen here, where the simulated dynamic mean crush force decreased with increasing the core thickness with respect to the test value. However, in the ECCS sandwich materials, the simulated value was greater than the test value in all thicknesses. The lack of catastrophic failure in the ECCS materials (as was seen in the triple core Steelite) can account for this. It was hypothesised the failure through thickness of the entire Steelite triple core sandwich increased the energy absorption in the sandwich, since the energy absorption mode changed to progressive failure. Whereas, in the ECCS triple core sandwich, failure of the skin was common, and failure through thickness occurred, however, not to the extent seen in the Steelite triple core sandwich. Hence, the overall energy absorption mode was still progressive crushing and not progressive failure.

7.4 0.5 mm DP600 sandwich (DPSW)

7.4.1 Quasi–static and Dynamic

The press brake bent single hat geometry (77 mm × 58.5 mm) is not discussed since no quasi–static tests were performed and no repeat results were produced dynamically. Therefore, only physical test results for the stamp–formed geometry were used to compare to the FEA simulations.

The quasi–static and dynamic results in the physical testing were visually similar, hence only the dynamic crash deformation is shown, Figure 7.10 – image 1, this is compared to the dynamic test result, Figure 7.10 – image 2.

The small radius folds characteristic of the DPSW stamp–formed crash structure was seen in the simulations, Figure 7.10 – image 1. However, the folds were difficult to visualise in comparison to the physical test, Figure 7.10 – image 2, the small fold radius in the physical tests was not well portrayed kinematically by the 2 mm element size. Hence, there was the potential that a refined mesh (1 mm) would improve the folding since a finer mesh would have more elements to portray the fold; however, this was not found to be the case.

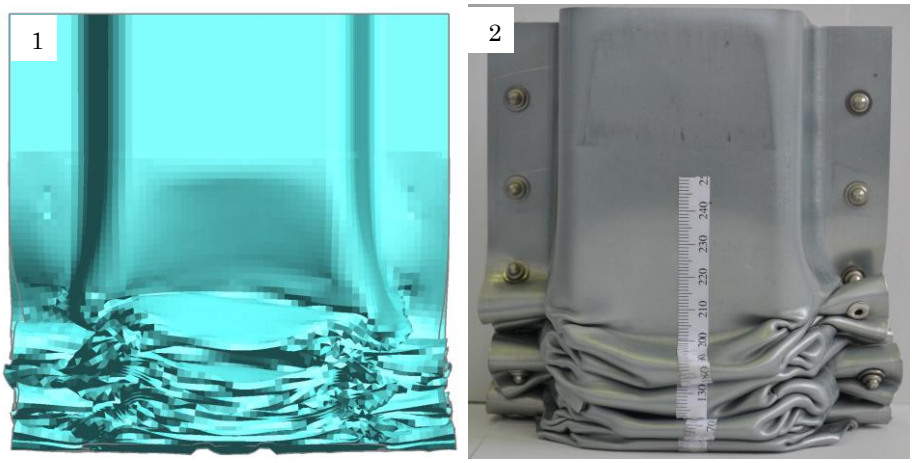

Figure 7.10 – Comparison of deformed geometry of DPSW stamp–formed simulation (image 1) to physical impact test (image 2).

The force–displacement plots for the quasi–static and dynamic tests, Figure 7.11, show the results are predicted well. The oscillatory force seen in the monolithic metals were again not observed in the DP600 sandwich materials. The LS–DYNA simulation predicted the large number of smaller folds in the stamp–formed crash structures. The peak force in the simulation was greater in displacement than the physical tests as was seen previously (Section 7.2 and 7.3). However, the important property is the progressive crushing force response; this was seen to be in good agreement to the physical tests, particularly the drop (dynamic) tests, where there was reasonable correlation between the force oscillations.

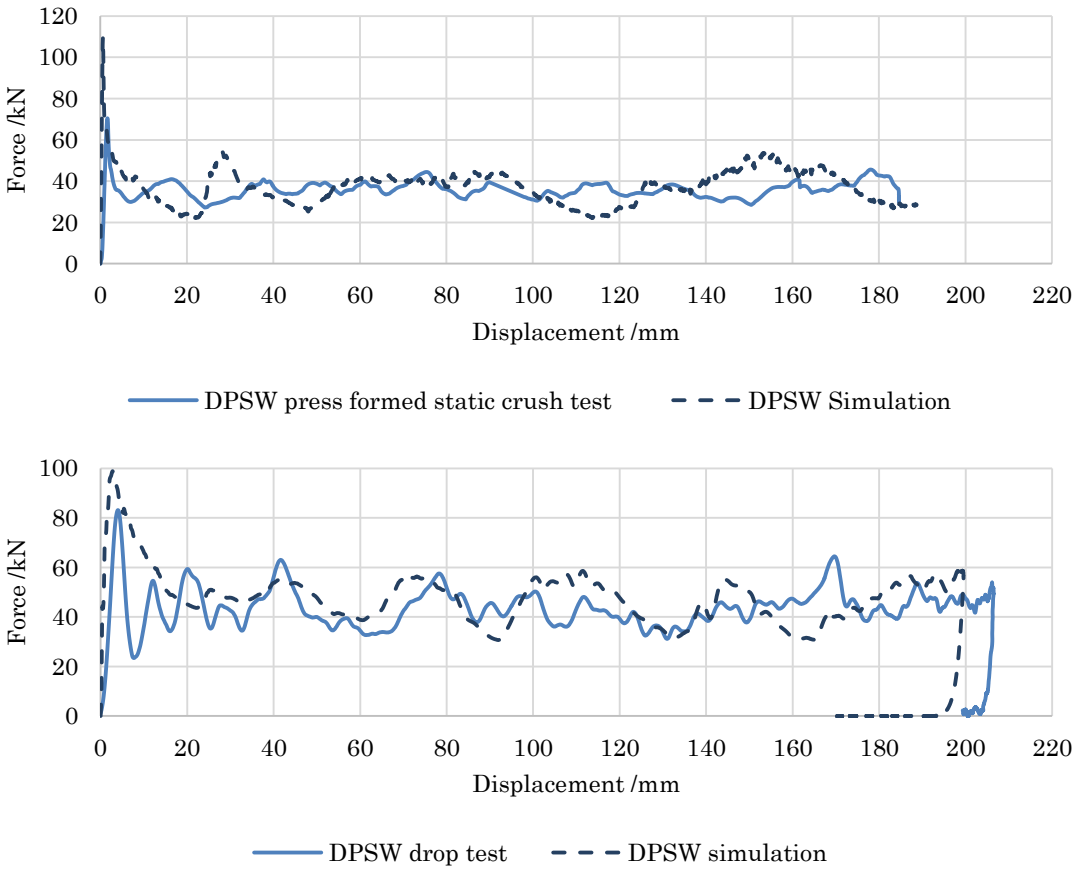

Figure 7.11 – DP600 sandwich (DPSW) quasi–static crush and dynamic (crash) test simulations (dashed) compared to physical tests (solid). Top is the quasi–static crush result and bottom is the dynamic (crash) result.

7.4.2 Discussion

Table 7.4 shows the quasi–static and dynamic results for the stamp–formed geometry. The drop tests, which showed significant delamination failure, had a mean crush force of 36.7 kN (see Chapter 5). The physical test results where delamination was not deemed to have occurred had a mean crush force of 48.4 kN, therefore this was used as the mean crush force target for the simulations. The simulation result quasi–statically was within 2.2% of the test result, however dynamically, the result was 7.6% greater than the test value.

Table 7.4 – Comparison of FEA results to physical tests for the DP600 sandwich materials in both geometries. Bracketed values are physical test results.

Thickness	Mean crush force /kN		Percentage difference	
	Quasi–static	Dynamic	Quasi–static	Dynamic
1.7 mm	36.9 (36.1)	48.4 (45.0)	+2.2%	+7.6%

There are three suggested reasons for the larger discrepancy in the dynamic result. The first is the difference in the peak forces in the simulation compared to the test, which was greater in the simulation than the test result and extended over a displacement of 15 mm, which contributed to increased energy absorption of the simulation. Second, the use of generic Tata Steel DP600 strain rate sensitivity data may have also been a factor; the DP600 physically tested potentially had a different strain rate sensitivity, since after sandwich production the steel was observed to have bake hardened when tensile tested (discussed in Chapter 3). Finally, the DP600 sandwich material suffered from low adhesive strength. Therefore, the modelling assumption of a perfect adhesive bond may not be suitable in this instance.

7.5 Summary

Chapter 6 detailed the methodology used to simulate the MPM sandwich material in quasi–static crush and dynamic (crash) scenarios. The literature was inconclusive about how to best model MPM sandwich materials. Therefore, various methods were attempted and a viable solution found with the use of a single shell element model. The final model used a single shell element to model the sandwich, with the fully–integrated (Type 16) element formulation, and one integration per layer of material (hence three through the total thickness of the sandwich). The *PART_COMPOSITE model was used, with laminated shell theory (LST) accounting for the reduced stiffness of the polymer core correctly by the use of *MAT_114. If LST was not used (*MAT_24) the result was visually over–stiff, the fold radius being greater, and the crushing force over–predicted by 32%.

It was determined that the parameters which monolithic materials adhere to, suit MPM sandwich modelling. The most important was the mesh element size. The mesh element size was set to 2 mm × 2 mm, as this produced a visually accurate portrayal of the fold wavelengths in most cases whilst also having an acceptable computation time.

It was noteworthy that the deformation of MPM sandwich materials exhibited smaller radius folds than monolithic metals. In most instances, the folds were large enough to allow the 2 mm elements to model them successfully. However, a wrinkling phenomenon seen in the corners of the ECCS sandwich materials was not modelled, and refining the mesh further did not capture this high frequency feature.

Forming strains and strain rate sensitivity were considered, the latter only ignored for the monolithic aluminium alloys. The spot–joints were positioned correctly,

however, each joint was modelled using a solid element. Failure of the joint was not considered since it did not occur frequently, hence was not detrimental to the performance of the crash structure. Additionally, when failure of a spot–joint did occur in reality it was due to its ejection from the constrained sandwich material, not due to lack of joint strength. It was assumed that at this point there was no reduction in the load carrying capacity of the structure.

The monolithic material results showed the correct deformation, and the mean crush force results were close to the test values, within 5.2%.

All steel–polypropylene–steel sandwich materials folding behaviour were predicted well by the *PART_COMPOSITE model. The mean crush force was generally over–predicted quasi–statically, in all cases by no more than 8%. Dynamically, the mean crush force was over–predicted for the single core, but the double and triple core were under–predicted. This was theorised to be due to these thicker sandwich materials exhibiting multiple failure modes, both progressive crushing as expected and progressive failure as seen in fibre–reinforced composite materials (see Chapter 2 for more details), which increased the energy absorbed by the crash structure, but was not accounted for in the simulations.

The ECCS sandwich materials were modelled aptly, the deformation was idealised, but the fold placement was in reasonable agreement with the test results, after a discrepancy with the first two folds. Quasi–statically, the wrinkling in the corners was not predicted, but this did not affect the energy absorption performance significantly. Dynamically, the energy absorption was predicted within 6.4% and was consistently over–predicted owing to the simulation modelling a perfect scenario without skin failure or adhesive failure.

The modelling of the DPSW sandwich confirmed the geometry of the crash structure altered the folding of the sandwich material to produce multiple smaller

folds. This was not seen in the larger press brake bent geometry and the LS–DYNA model predicted both configurations with good agreement. This showed the potential that geometry of the crash structure significantly alters the folding behaviour of the MPM sandwich material. Although the geometry is known to effect the crushing response of a crash structure, the extent seen in the DP600 sandwich material was not witnessed in monolithic aluminium (see Chapter 5).

From the comparison of the testing to the simulations, it can be seen that accounting for failure of the materials is imperative if the use of thicker cores and thinner skin steels is performed. However, for more conservative sandwich panels (thicker skins and thinner cores), modelling of failure may not be required to determine a performance gain.

Concerning modelling of failure of the adhesive, if the material exhibits a strong adhesive bond (and most likely a cohesive failure) the potential to ignore the bond and assume perfect attachment between core and skin material would be acceptable. However, the potential for strain rate dependency in the failure of the adhesive would mean that even if cohesive failure was seen when testing the bond strength, adhesive failure or delamination might occur dynamically. Hence, modelling of the bond may be required.

The physical test and simulation comparison showed that when failure of the adhesive (delamination) occurred the performance drop was significant, with a >30% reduction in mean crush force in some instances. However, this was only observed in the DP600 sandwich materials. This highlights a limitation of the single shell element model, since it cannot model delamination, which can be seen to significantly effect the mean crush force.

In all circumstances, the behaviour at initial impact was not correctly modelled. The simulations suggested the peak force would occur over 20 mm for the model

initiator, which had the same nominal depth as the actual initiator. However, in the physical tests the peak force generally occurred over a smaller displacement. The reason for this was most likely the plastic deformation, thinning and failure of the steel skin in the initiated region of the sandwich. Since the peak force prediction was not the focus of the work this was deemed to be acceptable.

Overall, three scenarios have been identified from the comparison of results from the comparison of the physical test results and the simulations:

- The first is where there is little to no delamination failure occurs in the sandwich and little to no failure occurs in the steel skins due to excessive straining of the steel. This scenario was modelled well by the *PART_COMPOSITE method using *MAT_114, since the progressive crushing (asymmetric folding) was the only method of collapse and energy absorption.
- The second is where failure occurs in the skin of the steel however, the crash structure collapses under progressive crush. This occurs when the strain in bending exceeds the strain to failure and the bending strength decreases, thereby reducing the energy absorbed by the crash structure. The failure of the skin is not modelled, therefore the simulation over–predicts the performance of the material.
- The third scenario is where failure occurs through thickness of the entire sandwich. Initially progressive crushing occurs, failure of one steel skin occurs, however folding still occurs, therefore, the remainder of the sandwich fails through thickness, through both steel skins and the polypropylene core. Failure through thickness changes the method of collapse to progressive failure. The progressive failure is not modelled, hence the simulation under–predicts the energy absorbed by the material.

8 Performance prediction

The ability to predict the mean crush force from a known sandwich construction or conversely devise a sandwich construction for a given mean crush force target is of utmost importance for practical applications. This chapter seeks to develop a solution to predict the energy absorption of steel–polypropylene–steel sandwich materials *via* the use of an analytical solution. The analytical solution is based on a model in the literature originally formulated for monolithic metals. The analytical solution was validated using finite element analysis simulations in LS–DYNA. This was made possible by the good agreement between the physical testing and finite element simulations seen in this thesis.

Figure 8.1 shows the advantage of an analytical solution. Physical testing is a labour intensive process which takes considerable time to achieve a solution. The use of validated FEA allows the prediction of performance of any sandwich construction, provided there is confidence in the simulation process. The limitation in this instance is usually computational expense. An analytical solution however, can provide any result requested with very little computing power. Hence is an advantage, particularly to an engineer making material choices. This methodology allows the reverse process of this thesis to taken in the future, to design sandwich constructions for axial energy absorption applications.

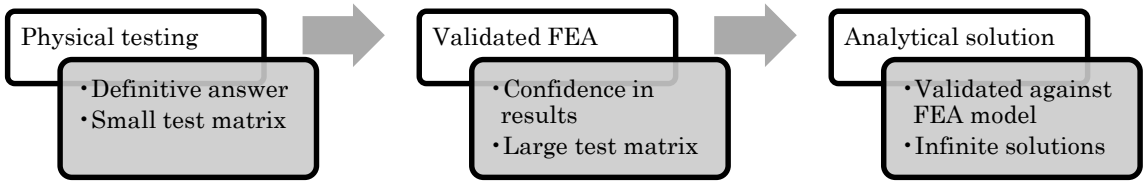

Figure 8.1 – Schematic process showing the potential for analytical solution.

8.1 LS–DYNA simulations for validation

The finite element model defined in Chapter 6 – Modelling methodology was used to validate the analytical model discussed in this chapter. The *PART_COMPOSITE model using laminated shell theory was found to be in good agreement with the physically tested steel–polypropylene–steel sandwich crash structures (Chapter 7 – Results comparison).

A full–factorial experiment was performed in LS–DYNA, varying both the skin and core thickness. For each test a mean crush force and specific energy absorption result was produced. This array of simulations allows visualisation of the trend in the energy absorption (mean crush force) of sandwich materials when changing the skin and core thickness independently.

The *PART_COMPOSITE model portrayed the deformation of the sandwich materials accurately provided no significant failure of the skin occurred. Failure of the skin would lead to a change in energy absorption mode from progressive crushing to progressive failure (discussed in Chapter 7), for the simulations in this chapter this was ignored. In order to simplify the simulation of multiple sandwich constructions, modelling of the strains in the corners was removed. This allowed only the properties of the material to be considered in the result and not external factors such as forming strains. This meant the energy absorption and mean crush force values are lower than when physically tested, since tested crash structures must be formed to shape.

The geometry chosen was the single hat and backplate press brake bent geometry (detailed in Chapter 3 – Materials and methods). Limits were imposed on the minimum and maximum thickness of the steel skin and polypropylene core. These

limits narrowed the range of simulations and also produced sandwich constructions in the energy range for automotive crash structures. The limits were:

- 0.2 – 0.6 mm steel skin thickness (0.1 mm increments)
- 0.5 – 2.5 mm polypropylene core thickness (0.1 mm increments)

This resulted in an experimental matrix of 5 × 21 combinations, producing in total 105 outcomes, which were all modelled. All three steel skin materials physically tested were simulated. In other words, 105 different sandwich material constructions were simulated for three different skin materials (total of 315 distinct constructions) using finite element analysis (FEA).

8.2 Analytical solution for axial energy absorption

The analytical model of the axial crash energy absorber has been researched since the 1960s [1] and particularly concerning automotive applications since the 1970s [2]–[4]. White and Jones [5] have provided a summary of different methods of predicting the performance of metallic axial crash energy absorbers and the advancement of the solution since its inception.

The folding modes of monolithic metal crash structures have been comprehensively researched, and an analytical solution produced, Equation 8.1. The current widely accepted solution assumes the top hat and backplate crash structure consists of four elements, which collapse in the asymmetric form, shown in Figure 8.2.

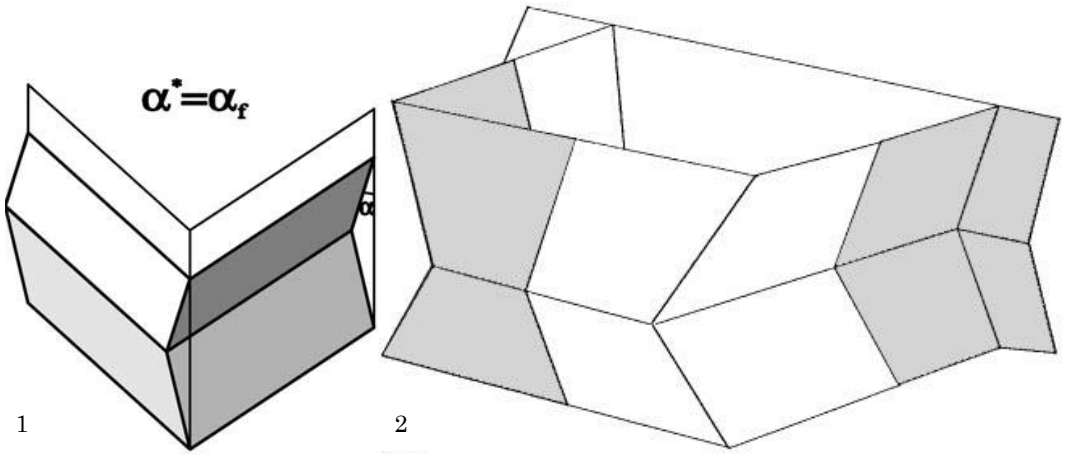

Figure 8.2 – Image 1 – The single asymmetric collapse element [6]. Image 2 – Four collapse elements producing the top hat and backplate crash structure geometry [5].

The analytical solution has been proven over a large body of testing of differing steel and aluminium alloy grades, crash structure geometries and thicknesses [5], [7]–[10]. However, prior to the work presented in this thesis, data for MPM sandwich materials did not exist.

$$P_m = 32.88 \cdot M_o \cdot \left(\frac{p}{T}\right)^{1/3} \cdot \left\{1 + \left(1.33 \cdot \frac{V}{p \cdot D}\right)^{1/q}\right\} \qquad \text{Equation 8.1}$$

Where,

P_m = Mean crush force (N)

M_o = Plastic bending moment (N.m)

T = Overall material thickness (m)

p = Effective width of crash structure (m)

V = Impact velocity ($m.s^{-1}$)

D = Cowper–Symonds coefficient (s^{-1})

q = Cowper–Symonds exponent

$\left\{1 + \left(1.33 \cdot \frac{V}{p \cdot D}\right)^{1/q}\right\}$ = Dynamic to Static stress ratio

In the case of quasi–static crush, the equation is simplified (Equation 8.2):

$$P_m = 32.88 \cdot M_o \cdot \left(\frac{p}{T}\right)^{1/3} \qquad \text{Equation 8.2}$$

The solution defines both the collapse mode in terms of geometry by accounting for the cross–section of the crash structure and thickness of the material. Second, the analytical model accounts for the material properties *via* the plastic bending moment and the Cowper–Symonds strain rate sensitivity parameters.

The most important factor in the analytical solution is the plastic bending moment, which defines the degree of resistance the material has towards progressive crushing deformation. For monolithic metals, the plastic bending moment is defined in Equation 8.3.

$$M_{o,monolithic} = \frac{\sigma_o \cdot T^2}{4}$$ Equation 8.3

Where,

$M_{o,monolithic}$ = Plastic bending moment (N.m)

σ_o = Flow stress of material (Pa)

T = Thickness of material (m)

The flow stress is the stress which the material attains on average through the deformed crash structure. The flow stress is calculated as a proportion of the materials' ultimate tensile strength (UTS) as suggested by DiPaolo *et al.* [11]. For stainless steel crash structures quasi–statically tested the value was shown to be between 90% and 95% of the UTS.

The flow stress can be seen to be different for the steel grades, not based on strength instead on the hardening rate of the material. Consider Figure 8.3, where three different steel grades shown. The two mild steel grades (Steelite and ECCS) exhibit a low plastic modulus since they have low UTS to yield stress ratio, as well as a strain to UTS of around 0.2 strains. Whereas the DP600 steel has a much steeper gradient of plastic modulus, the UTS to yield stress ratio is higher and the strain at UTS is lower at 0.15 strains.

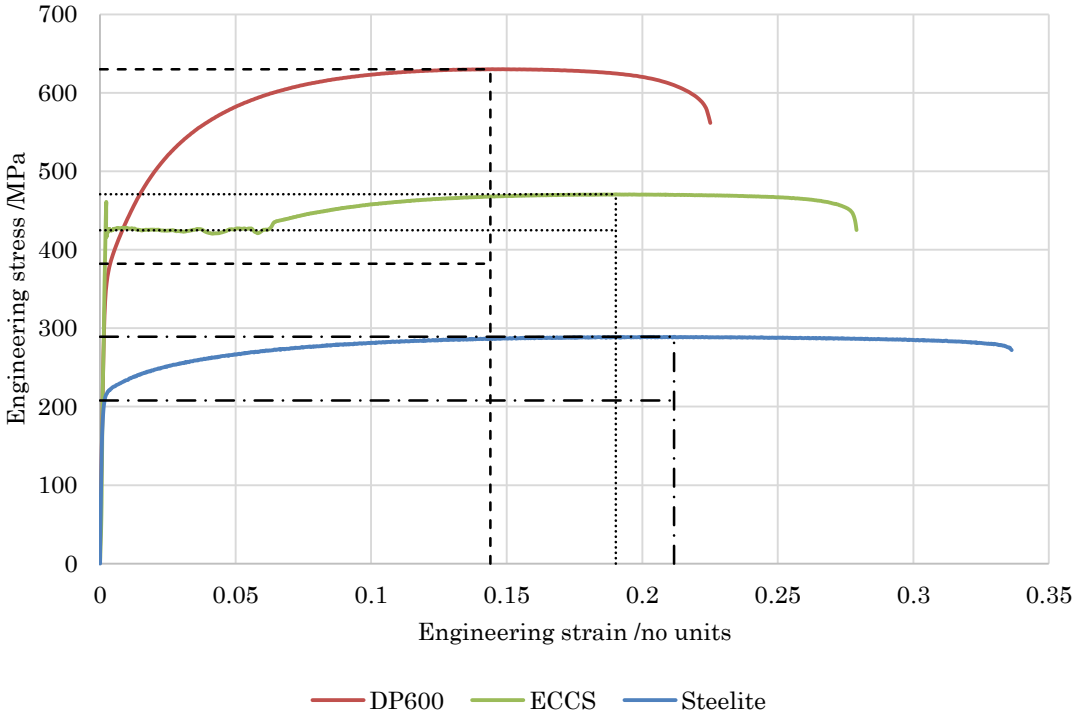

Figure 8.3 – Flow stress of the three steel grades used to model the MPM sandwich materials.

8.2.1 Monolithic material model

The applicability of the analytical solution was confirmed on monolithic metals. The results for the steel and aluminium alloys physically tested in Chapter 5 (DP600, AA5754 and AC300–T61) were used for this validation. However, the physical test results included forming effects which the analytical solution cannot account for. The analytical solution was therefore validated against the FEA results. The FEA simulations were previously validated against the physical testing, and found to be within ± 5% (Chapter 7).

Figure 8.4 plots the mean crush force *versus* the thickness of the material in the crash structure using both the analytical solution (solid line) and the finite element prediction (dashed line). Both methods of prediction follow the same trend, a parabolic relationship (Equation 8.1).

Figure 8.4 shows that the analytical solution over–predicted the mean crush force result consistently in comparison to the FEA result. The mean crush force over–

prediction was due to the flow stress term in Equation 8.3 being defined as the ultimate tensile strength. How the flow stress is defined is important since Equation 8.3 calculates that the AA5754 and AC300–T61 alloys absorb nearly the same energy since their UTS values are similar (241.9 MPa and 246.7 MPa respectively), however from Figure 8.4 this can be seen to not be the case. A scale factor was sought in order to quantify the difference between the analytical solution and the finite element analysis prediction. This scale factor was produced by minimising the residual sum of square error between the analytical solution and the finite element solution values.

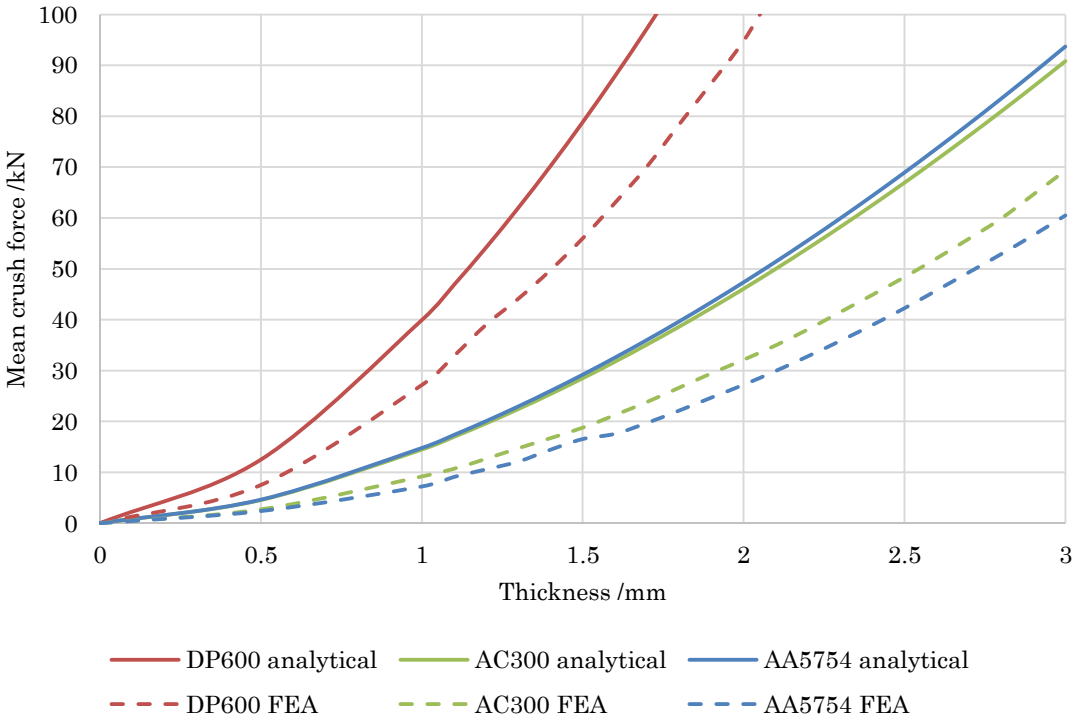

Figure 8.4 – Prediction of performance of crash structures at any given thickness in three monolithic materials. The dashed lines show the finite element analysis solution. The solid line shows the prediction of the analytical solutions; the correction factor has not been applied to the results.

For the DP600 steel, a scale factor of 0.735 was determined. For AA5754, the value was 0.607 and for AC300–T61 aluminium alloy, this factor was determined to be 0.727. The scaled analytical model is compared to the FEA values in Figure 8.5, it can be seen that the use of a constant correction factor is not ideal, however, for

this purpose is adequate. The reason for this is thicker the material, the lower the average stress experienced by the metal, which for increased accuracy should be accounted for.

A knowledge of the properties of the metals (steel and aluminium alloys) helps explain the difference in scale factors observed. As deformation of a crash structure is geometry dependent, it can be assumed that, regardless of the material, the strain experienced by the material is similar for a given thickness. The plastic flow curve of the DP600 steel and the AC300–T61 alloys are similar, albeit at different strength range. Whereas the discontinuous yielding observed by AA5754 means it remains at a lower stress for more of its deformation, hence the lower scale factor value.

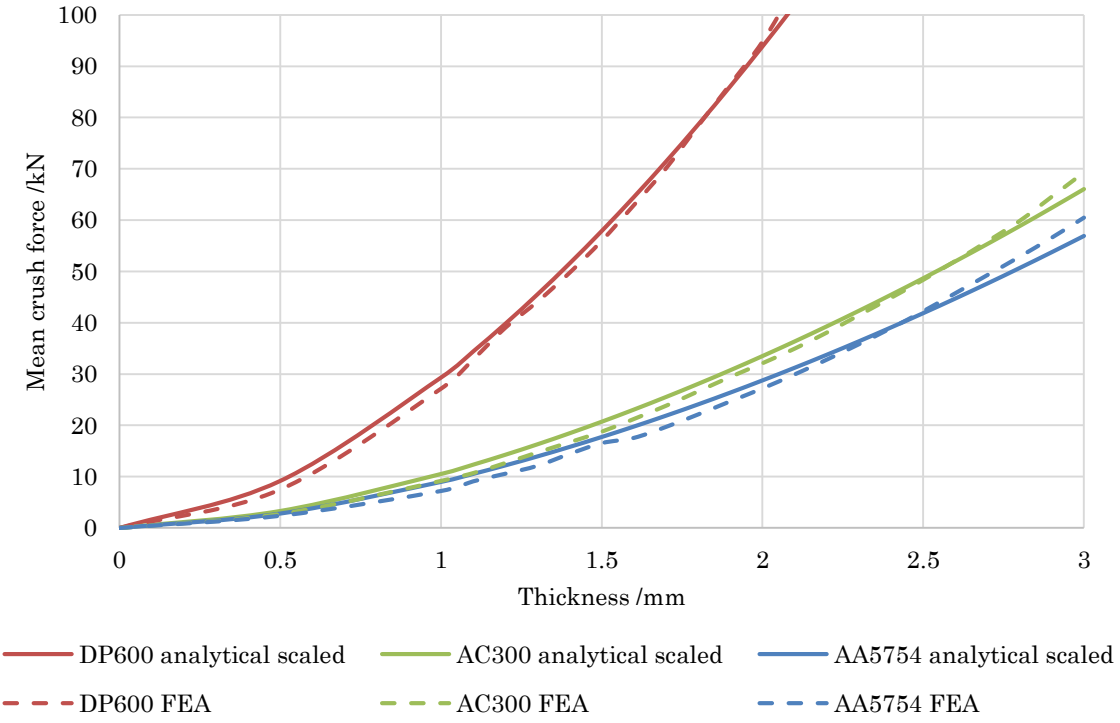

Figure 8.5 – Analytical solution with correction factor compared to the finite element analysis solution.

The analytical solution can be seen to be within ± 3% (mean crush force) of the FEA result, once corrected with the linear scale factor (Table 8.1).

Table 8.1 – Comparison of the analytical prediction *versus* physical test result.

		FEA	Analytical	Analytical with scale factor	Percentage difference
	Thickness /mm	MCF /kN	MCF /kN	MCF /kN	MCF
DP600	1.6	62.9	70.2	64.5	2.6%
AA5754	2.5	42.3	50.3	41.9	–1.0%
AC300–T61	2.5	48.4	58.4	48.7	–0.6%

The analytical solution was therefore, determined to be appropriate and applicable to illustrate the trend in the mean crush force of monolithic metal crash structures. This further supports the observations previously reported by many authors [5], [7]–[10].

8.2.2 Sandwich material model

The same process used to model the monolithic materials was used for the MPM sandwich materials. Analytical solutions were developed for the three grades of steel tested in Chapter 5 (Steelite, ECCS and DP600).

For the representation of sandwich materials, the plastic bending moment term in the analytical solution required modification. The remaining terms deal with the deformation of the crash structure, which for the MPM sandwich materials were found to be similar to the monolithic metals (discussed in Chapter 5), and hence kept the same.

The plastic bending moment for sandwich materials in axial collapse has been considered previously [12] and two solutions provided; an upper bound and a lower bound. The lower bound solution is the worst–case scenario, where the core itself is ignored and only the thickness of steel in the sandwich is considered. The plastic bending moment in this case is defined in Equation 8.4.

$$M_{o,lower\ bound} = \frac{1}{2} \cdot \sigma_o \cdot {t_f}^2 \qquad \text{Equation 8.4}$$

Where,

σ_o = Flow stress of steel skin (Pa)

t_f = Steel skin thickness (m)

The upper bound describes the perfect sandwich material, where the core is assumed to have infinite shear stress. The plastic bending moment in this instance is defined in Equation 8.5. [12], [13]

$$M_{o,upper\ bound} = \left(\left(t_c + t_f\right) \cdot \sigma_f \cdot t_f\right) + \frac{1}{4} \cdot \left(\sigma_c \cdot {t_c}^2\right) \qquad \text{Equation 8.5}$$

Where,

t_c = Core thickness (m)

t_f = Skin thickness (m)

σ_f = Flow stress of steel skin (Pa)

σ_c = Flow stress of polymer core (Pa)

Currently, accurately determining the plastic bending moment of a sandwich material is problematic. It is analytically difficult to define the effect of shear on the core, as it is dependent on many factors including the skin material strength and thickness, the core material strength and thickness and the level of strain imparted on the material. Hence, the current best practice is to determine the plastic bending moment from test results [12]. Therefore, this was also the method used in this instance.

Additionally, the flow stress also affects the plastic bending moment (discussed in Section 8.2.1). In monolithic steel, it was seen to be 73.5% of the UTS. For simplicity and since the steel in the MPM sandwich materials experiences greater strain, the flow stress was assumed to reach the UTS in the steel skin. The increased stress in the skin is due to the properties of sandwich materials; the skin being further away from the neutral axis and is significantly thinner.

To ascertain where the plastic bending moment of the steel–polypropylene–steel sandwich materials is in respect to the upper and lower bounds, the two plastic bending moment theories (Equation 8.4 and Equation 8.5) were compared to the full–factorial LS–DYNA simulation (see Figure 8.6). For simplicity, only the 0.4 mm steel skin ECCS sandwich material is shown.

It can be seen that the lower bound equation is not appropriate for a steel–polypropylene–steel sandwich material, Figure 8.6 – red. The mean crush force decreases with increasing core thickness, since the model ignores the thickness of the core and treats the two steel skins as acting independently. The upper bound equation does predict the trend in behaviour well, Figure 8.6 – blue. However, as expected the upper bound equation showed a higher result than the simulation, Figure 8.6 – green.

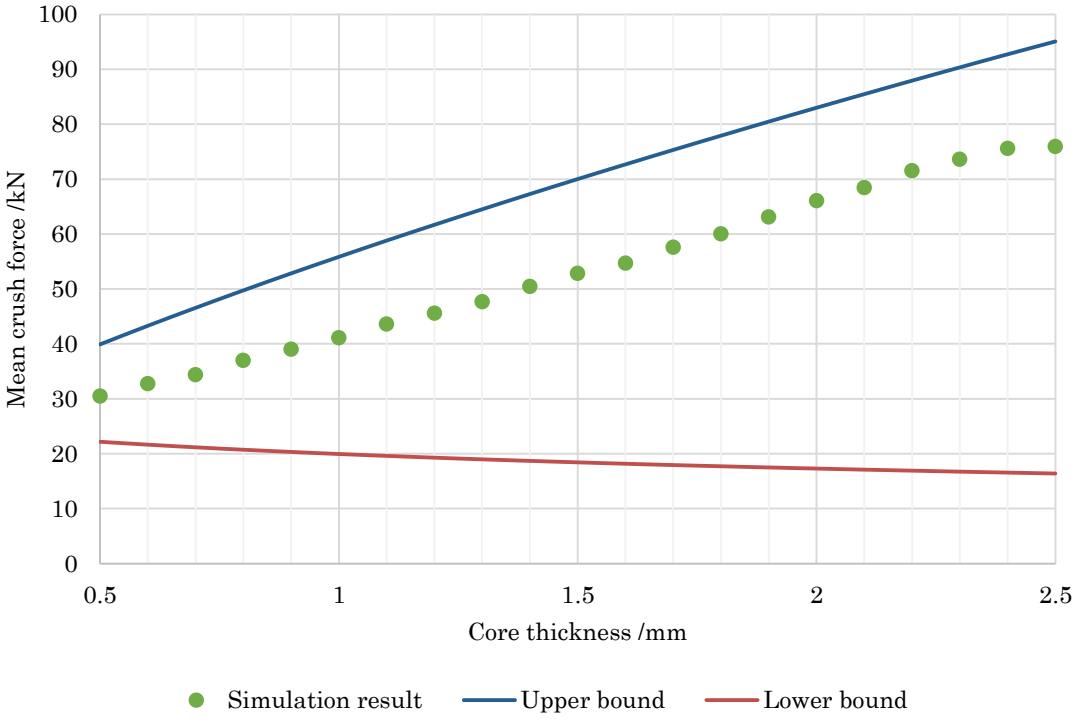

Figure 8.6 – Plastic bending moment comparison for the lower and upper bound approximations *versus* the simulated response in LS–DYNA. Skin thickness is fixed to 0.4 mm and the core thickness varied between 0.5 and 2.5 mm in all three cases.

8.2.3 Plastic bending moment correction factor, βσ

Figure 8.6 showed the upper bound plastic bending moment (Equation 8.5) gave an over–stiff response. This could be due to three reasons; the first is the flow stress, which was discussed in Section 8.2.2. The second reason is the lack of shear consideration in the core [13]. The third is the strain rate in the polypropylene core, this was assumed to be the same as the steel skins. However, due to the low strength of the polypropylene core, the strength of the polypropylene core can be assumed to be negligible. Since determining the effects of these separately was out of scope for the project, the terms were combined into a single correction factor.

As mentioned previously, a scale factor was applied to the monolithic metal results (Section 8.2.1) to account for the over–prediction of the flow stress in the analytical solution. This same process was performed for the steel–polypropylene–steel sandwich materials.

The correction factor for the steel–polypropylene–steel sandwich materials (denoted β_o) is a scalar multiplier. The correction factors per skin material were determined by minimising the residual sum of square errors between the analytical solution result and the simulation results and are shown in Table 8.2.

Table 8.2 – Correction factors calculated for the three sandwich materials tested (Steelite, ECCS and DP600).

Steel grade in sandwich material	Correction factor, $\beta\sigma$
Steelite	0.762
ECCS	0.731
DP600	0.595

The difference between these values can be explained by the hardening profile of the metals (shown in Figure 8.3). The plastic flow properties of the Steelite and ECCS skins are similar, exhibiting relatively high yield strength in comparison to the UTS. Additionally, the strain at which the steel reaches the UTS is similar for the Steelite and ECCS (around 0.2 strains) steels and much lower for the DP600 (less than 0.15 strains). Hence, the plastic modulus up to UTS has a steeper gradient for the DP600 than for the Steelite and ECCS steels.

The overall equation used for the modelling of steel–polypropylene–steel is therefore, as shown in Equation 8.6:

$$P_m = \beta_\sigma \cdot 32.88 \cdot M_o \cdot \left(\frac{p}{T}\right)^{1/3} \cdot \left\{1 + \left(1.33 \cdot \frac{V}{p \cdot D}\right)^{1/q}\right\} \quad \text{Equation 8.6}$$

Where,

$$M_o = \left(\left(t_c + t_f\right) \cdot \sigma_f \cdot t_f\right) + \frac{1}{4} \cdot \left(\sigma_c \cdot {t_c}^2\right) \quad \text{Equation 8.5}$$

$$\sigma_f = \sigma_{UTS,f} \quad \text{Equation 8.7}$$

$$\sigma_c = \sigma_{UTS,c} \quad \text{Equation 8.8}$$

$\sigma_{UTS,f}$ = Ultimate tensile strength of the skin /MPa

$\sigma_{UTS,c}$ = Ultimate tensile strength of the core /MPa

β_{σ} = Plastic bending moment correction factor

8.3 Results of the analytical solution and full–factorial simulation

The results of the full–factorial FEA simulations and the analytical solution are compared in this section. The analytical solution (Equation 8.6) has the proposed scalar correction factor, β_o, (see Table 8.2) applied from this point forward.

Due to the similarity in response between all three grades of steel–polypropylene–steel sandwich materials (Steelite, ECCS and DP600), the results will be represented by the ECCS sandwich materials, as the ECCS steel skin has the highest dynamic strength. Identical trends were found for the other two steel skins, however, with lower mean crush force values. The DP600 sandwich result was only marginally lower than the ECCS sandwich result due the greater strain rate sensitivity of the ECCS steel skin material.

8.3.1 Mean crush force

Figure 8.7 shows a plot of mean crush force *versus* polypropylene core thickness for the ECCS sandwich materials. The dashed lines show the analytical solution, while the plotted points represent the results obtained from the LS–DYNA simulations. Figure 8.8 shows a plot of mean crush force *versus* steel skin thickness; again the dashed lines represent the analytical solution, whilst the plotted points are the results from the LS–DYNA simulations.

Note that Figure 8.7 (influence of core thickness) shows all 105 FEA simulation results (5 curves of 21 points). Whereas for clarity, Figure 8.8 (influence of skin thickness) shows a reduced dataset (5 curves of 5 points instead of 21 curves of 5 points). This does not influence the results, as the same relationship between skin thickness and mean crush force was observed in all cases. The overall trend for increasing both the thickness of the core and skin is the same, the mean crush force increased. The analytical solution showed a good fit to the FEA results.

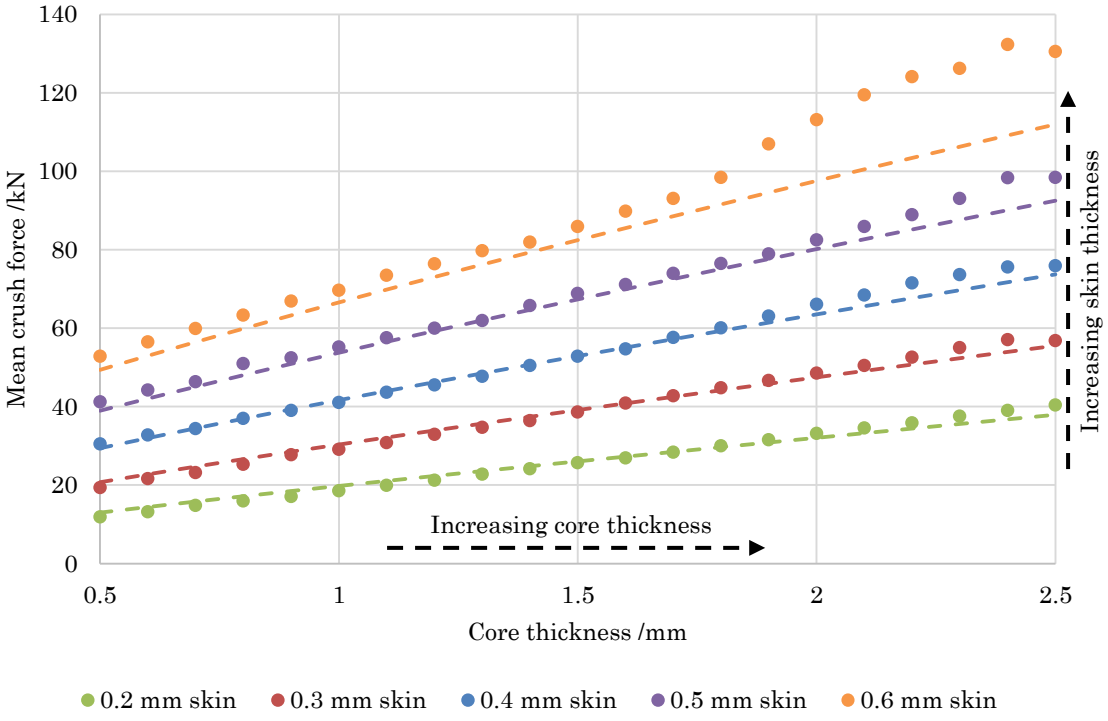

Figure 8.7 – Mean crush force *versus* core thickness for the ECCS sandwich material. Each line represents a fixed skin thickness. Dotted – LS–DYNA full–factorial experiment. Dashed – Analytical solution.

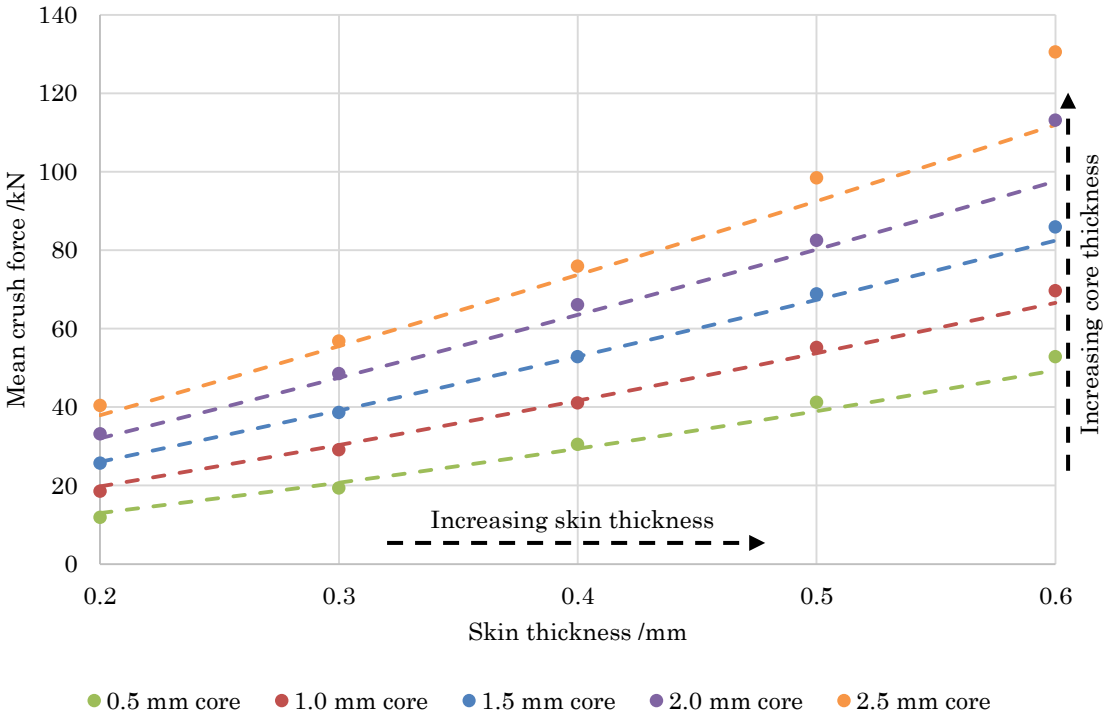

Figure 8.8 – Mean crush force *versus* skin thickness for the ECCS sandwich material. Each line represents a fixed core thickness. Dotted – LS–DYNA full–factorial experiment. Dashed – Analytical solution.

8.3.1.1 Trend in mean crush force results

The full–factorial experimental design and separation of the plots, Figure 8.7 and Figure 8.8, allowed the effects of the core and skin thickness to be considered independently. Portraying the analytical solution in the same manner allowed for facile comparison.

As would be expected, an increase in either the skin or core thickness was accompanied by an increase in the mean crush force for steel–polypropylene–steel sandwich materials, Figure 8.7 and Figure 8.8.

The analytical solution showed a parabolic relationship of the mean crush force with the core thickness, however, with a decreasing gradient or negative x^2 coefficient, Figure 8.7 – dashed. This relationship could not be inferred from the FEA results, Figure 8.7 – dotted; where a linear relationship was determined. The linearity of the FEA results is due to the natural variability in the FEA results and the analytical solution's parabolic relationship having only a small rate of change (the x^2 term coefficient is small in comparison to the x term coefficient). Hence, a straight–line relationship was also a suitable assumption.

Conversely, increasing the skin thickness produced a parabolic fit with an increasing gradient or positive x^2 coefficient, both in the analytical solution, Figure 8.8 – dashed and the FEA model, Figure 8.8 – dotted.

The correlation between the analytical solution and the FEA result is good but warrants further discussion. From Figure 8.7 and Figure 8.8 it was observed that the FEA results at the lower end of the spectrum (0.2 mm, 0.3 mm and 0.4 mm steel skins) were in better agreement with the analytical model than the 0.5 mm and 0.6 mm steel skin results. This was confirmed using in Table 8.3 and Table 8.4, where it can be seen that the average residual value between the

analytical solution and the simulation are in close proximity to one another with the exception of the 0.5 mm and 0.6 mm skins and the 2.0 mm and 2.5 mm cores. The reason for the deviation in the 0.5 mm and 0.6 mm steel skin sandwich materials was theorised to be the single shell element model incorrectly predicting the behaviour of thicker sandwich materials. With 0.5 or 0.6 mm skins and over 2.0 mm of polypropylene core, the assumption that the crash structure may be modelled as a thin shell is not as robust as with thinner skins and cores. The solution to this would be to use either solids or a combination of solids and shells to model the sandwich material (previously discussed in Chapter 3). However, this will mean significantly increased computational expense.

Table 8.3 – Correlation between the analytical solution and the finite element model in Figure 8.7.

	Average residual /kN
0.2 mm skin	1.1
0.3 mm skin	1.2
0.4 mm skin	1.3
0.5 mm skin	2.4
0.6 mm skin	8.7

Table 8.4 – Correlation between the analytical solution and the finite element model in Figure 8.8.

	Average residual /kN
0.5 mm core	0.8
1.0 mm core	0.6
1.5 mm core	0.5
2.0 mm core	1.6
2.5 mm core	2.1

8.3.2 Specific energy absorption results

The specific energy absorption (SEA) was plotted against core and skin thickness to quantify their relationship, Figure 8.9 and Figure 8.10. Similar to the relationship with mean crush force, a parabolic relationship was observed, since the energy absorbed and the mean crush force are analogous. The result showed a decreasing rate of increase in the SEA with increasing thickness (either skin or core).

The same trend for the thicker skins (0.5 mm and 0.6 mm) as seen in the mean crush force plots, Figure 8.7 and Figure 8.8, was also seen in the SEA plots, Figure 8.9 and Figure 8.10. The analytical solution and the simulations results still have an acceptable fit.

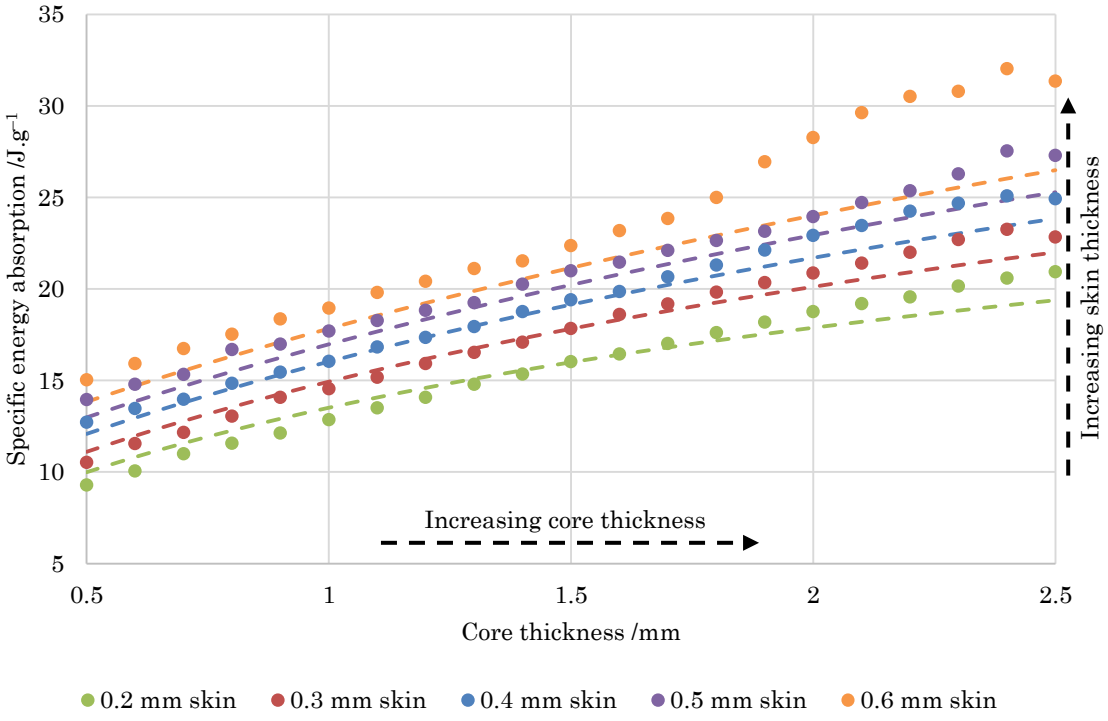

Figure 8.9 – SEA *versus* core thickness for the ECCS sandwich material. Each line is of fixed skin thickness. Dotted – LS–DYNA full–factorial experiment. Dashed – Analytical solution.

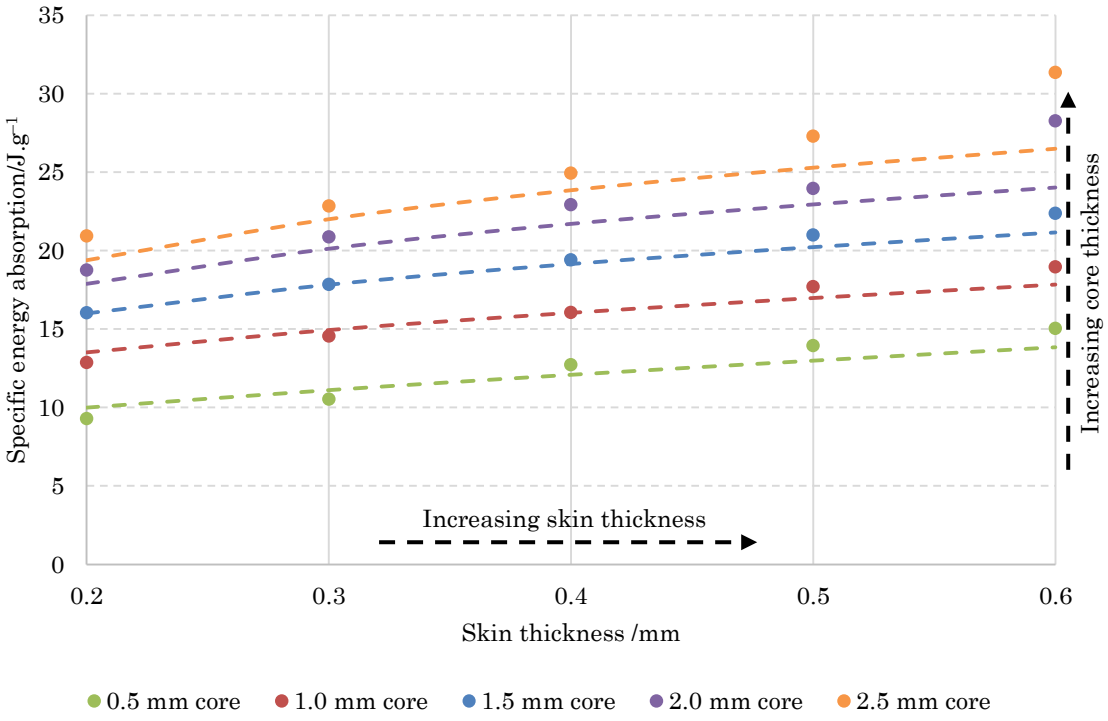

Figure 8.10 – SEA *versus* skin thickness for the ECCS sandwich material. Each line is of fixed core thickness. Dotted – LS–DYNA full–factorial experiment. Dashed – Analytical solution.

8.3.2.1 3D plot

The most important feature of the SEA is the difference in its response when increasing either the skin or the core thickness. From Figure 8.11 it can be seen that the increase in core thickness leads to a more significant increase in the SEA than an increase in the skin thickness. The surface is shaded with the mass of the crash structure, this shows more clearly the effect on the specific energy absorption of increasing the core thickness. This is indeed the function of the sandwich material; however, this confirms it is upheld in the case of the axial energy absorbing crash structure.

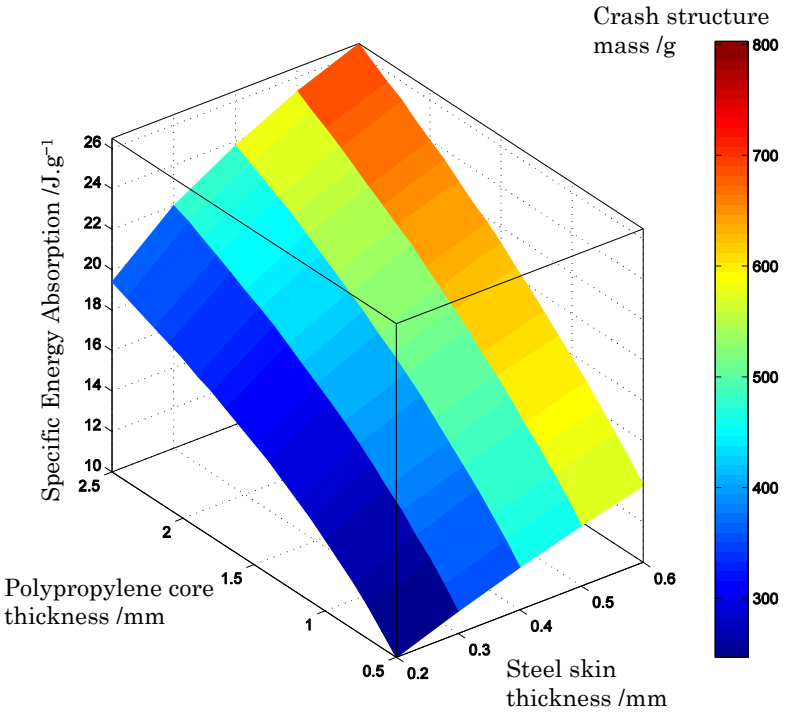

Figure 8.11 – 3D plot of SEA *versus* core and skin thickness. Surface is shaded with the mass of the crash structure.

8.4 Conclusion

This chapter proposed a general analytical solution for the crash performance of MPM sandwich materials. This analytical solution was compared a finite element analysis based full–factorial experiment. The intention of this chapter was to produce an analytical solution to predict the mean crush force (or energy absorption) of a crash structure of known construction. This ability is of particular interest to facilitate their adoption by industry.

In a previous chapter, physical testing of the material validated the finite element solution, and showed FEA was able to predict the behaviour of steel–polypropylene–steel. In this chapter, the effects of shear on the core were ignored in the analytical solution; instead a linear scale factor (β_o) was used to fit to the finite element values. This proved to be successful; the FEA results and the analytical solution with the scale factor applied were in good agreement. However, the finite element model was found to be less accurate for the thickest skins and polymer cores (0.5 mm and 0.6 mm steel skins and over 2.0 mm of polypropylene core). This was attributed to the thickness of the sandwich not being accurately modelled by a shell element.

The scale factor to correct the performance of the sandwich material for the analytical solution was not consistent for the different steel skins. This further suggests that the flow stress of the steel also has to be considered, since higher strength steels do not attain the same proportion of their ultimate tensile strength as lower strength steels. A scale factor between 0.6 and 0.75 is suggested as being appropriate for steel–polypropylene–steel sandwich materials; where, the correction factor, β_o is determined by the plastic flow properties of the steel.

Increasing steel or core thickness produced an increase in the mean crush force. The core thickness alone produced a linear increase in mean crush force. The skin thickness on the other hand, showed a parabolic relationship with mean crush force, the conventional response for monolithic metals.

The sensitivity of specific energy absorption to core thickness was found to be greater than for skin thickness. Hence, greater gains in specific energy absorption can be gained from increasing the core thickness compared to skin thickness.

8.4.1 Industrial significance for crash structure performance

The analytical solution presented in this chapter highlights where on the spectrum steel–polypropylene–steel sandwich materials lie in comparison to monolithic steel and aluminium alloys, in terms of energy absorption in automotive crash structures. Figure 8.12 plots the specific energy absorption (SEA) *versus* the energy absorbed by the crash structure. All results are those from the analytical solution, both for the monolithic metals and the sandwich materials.

The ECCS sandwich material results shown are obtained for a 70:30 ratio of core to skin thickness (determined in Chapter 5). Up to this ratio, little failure was observed in the steel skins of the sandwich. This ratio also governs the density of the sandwich materials; hence, they are all the same, at 2992 $kg.m^{-3}$, compared to aluminium alloys, which have a density circa 2700 $kg.m^{-3}$.

It is notable that at any energy target, both low and high strength aluminium alloys, Figure 8.12 – blue and green exhibit a greater specific energy absorption than the DP600 steel, Figure 8.12 – red. Therefore, the mass of an aluminium (AA5754 or AC300–T61) crash structure will always be less than that of an equivalent performance monolithic DP600 steel crash structure. The sandwich material crash structure, Figure 8.12 – orange dashed, produced a near identical

performance to monolithic AC300–T61 aluminium and far exceeded the high strength DP600 steel.

Therefore, with an increase in the strength of the steel used in the sandwich, or the acceptance of some steel skin failure in the sandwich, it would be possible to produce a steel–polypropylene–steel sandwich material which could match the performance of a high strength aluminium alloy such as AC300–T61. Additionally, the steel–polypropylene–steel sandwich material will always outperform the base metal used for the skins.

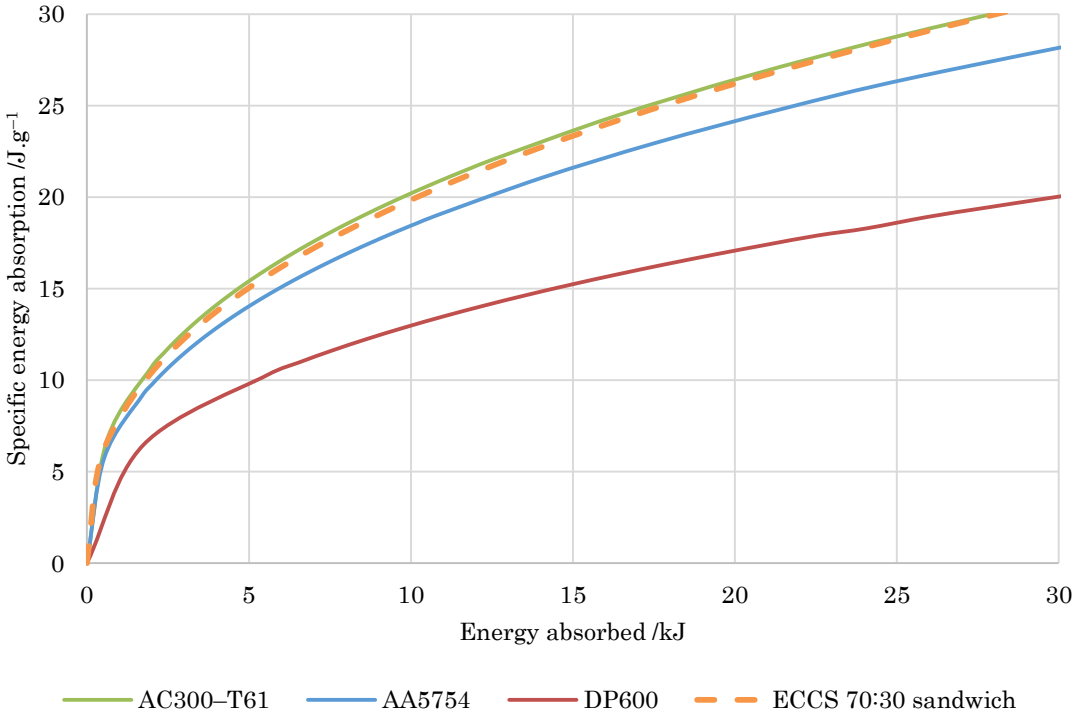

Figure 8.12 – Specific energy absorption *versus* the energy absorbed by the crash structure, for monolithic metal crash structures and sandwich materials of core to skin thickness ratio of 70:30.

8.5 References

[1] J. M. Alexander, "An approximate analysis of the collapse of thin cylindrical shells under axial loading," *Q. J. Mech. Appl. Math.*, vol. 13, no. 1, pp. 10–15, 1960.

[2] T. Ohkubo, K. Shirasawa, and Y. Akamatsu, "Mean Crushing Strength of Closed-Hat Section Members," *Trans. Soc. Automot. Eng. Japan*, no. 740040, 1974.

[3] N. Aya and K. Takahashi, "Energy absorbing characteristics of vehicle body structure," *Trans. Soc. Automot. Eng. Japan*, no. 746009, 1974.

[4] M. Tani and A. Funahashi, "Energy Absorption by the Plastic Deformation of Body Structural Members," *Soc. Automot. Eng. Tech. Pap.*, no. 780368, 1978.

[5] M. D. White, N. Jones, and W. Abramowicz, "A theoretical analysis for the quasi-static axial crushing of top-hat and double-hat thin-walled sections," *Int. J. Mech. Sci.*, vol. 41, no. 2, pp. 209–233, 1999.

[6] W. Abramowicz, "Thin-walled structures as impact energy absorbers," *Thin-Walled Struct.*, vol. 41, no. 2–3, pp. 91–107, 2003.

[7] W. Abramowicz and T. Wierzbicki, "Axial crushing of foam-filled columns," *Int. J. Mech. Sci.*, vol. 30, no. 3–4, pp. 263–271, 1988.

[8] W. Abramowicz and N. Jones, "Dynamic axial crushing of circular tubes," *Int. J. Impact Eng.*, vol. 2, no. 3, pp. 263–281, 1984.

[9] A. Najafi and M. Rais-Rohani, "Mechanics of axial plastic collapse in multi-cell, multi-corner crush tubes," *Thin-Walled Struct.*, vol. 49, no. 1, pp. 1–12, 2011.

[10] V. Tarigopula, M. Langseth, O. S. Hopperstad, and A. H. Clausen, "Axial crushing of thin-walled high-strength steel sections," *Int. J. Impact Eng.*, vol. 32, no. 5, pp. 847–882, May 2006.

[11] B. DiPaolo, P. Monteiro, and R. Gronsky, "Quasi-static axial crush response of a thin-wall, stainless steel box component," *Int. J. Solids Struct.*, vol. 41, no. 14, pp. 3707–3733, Jul. 2004.

[12] D. Mohr and T. Wierzbicki, "Crushing of soft-core sandwich profiles: experiments and analysis," *Int. J. Mech. Sci.*, vol. 45, no. 2, pp. 253–271, 2003.

[13] D. Mohr and T. Wierzbicki, "On the Crashworthiness of Shear-Rigid Sandwich Structures," *J. Appl. Mech.*, vol. 73, no. 4, pp. 633–641, 2006.

9 Conclusions and Further Work

9.1 Conclusions

The aim of the project has been to perform fundamental research into the performance of metal–polymer–metal (MPM) sandwich materials as automotive axial impact energy absorbers. With the trend in the automotive industry to reduce vehicle mass, this research is of high importance in both academic and industrial circles so that under–pinning knowledge is gained, allowing uptake of MPM materials. In this thesis, steel–polypropylene–steel sandwich materials were chosen to represent MPM materials. Three grades of steel were used, a low strength and low thickness Steelite (0.15 mm) skin, an intermediate strength and intermediate thickness ECCS skin (0.3 mm) and a high strength and high thickness DP600 skin (0.5 mm). The core in all instances was polypropylene, in 0.7 mm increments, up to a maximum of 2.1 mm.

9.1.1 Literature review

The literature review showed the opportunity for research around the use of MPM materials for energy absorbers. The majority of research in the field of impact energy absorption is focussed on the use of either fibre–reinforced composite materials or monolithic metals with complex multi–corner geometries for the reduction of crash structure mass. However, these methods are currently of limited use, since they are not readily producible in the high volumes required for the automotive sector. Additionally, the lack of confidence in the performance prediction of fibre–reinforced composite materials and the complexity of joining them to the rest of a conventional body–in–white are the main hindrances to the adoption of these materials. Currently, research in the field of MPM sandwich

materials is predominantly concerned with automotive skin panels and forming applications.

9.1.2 Manufacture of sandwich materials

The manufacturing methods for the MPM sandwich materials were detailed in Chapter 3 – Materials and methods . Two of the three sandwich materials (Steelite and ECCS grades) were successfully produced in three thicknesses. The zinc coated DP600 steel however, proved difficult to bond to therefore, only one thickness was produced. Crash structures were produced using press brake bending in most instances; however, heated press forming was also used to alleviate the problems of the DP600 steel's low adhesive bond strength in the MPM sandwich material. Monolithic material crash structures (1.6 mm DP600, 2.5 mm AA5754 and 2.5 mm AC300–T61) were also produced for benchmarking purposes. The joining method for the sandwich materials was the blind rivet; self–pierced rivets were also attempted and found to be suitable, however only tested on the DP600 sandwich (due to the suitable skin thickness). Monolithic metals were joined using their conventional process in industry, namely resistance spot welding for steel and self–pierced riveting for aluminium alloys.

9.1.3 Quasi–static and Dynamic testing

Crash structures were quasi–statically (crush) tested and dynamically (drop) tested in order to assess the differences in performance of the materials at high and low strain rates, and to provide data for finite element validation.

The monolithic metal crash structures exhibited the same folding and force response when tested quasi–statically and dynamically, and the mean crush force exhibited at most a 9% increase dynamically (DP600). This showed that high strength steels and aluminium alloys have little strain rate sensitivity, and their

performance does not differ significantly in crash applications in comparison to quasi–static tests.

The predominant mode of deformation for the MPM sandwich materials was progressive crushing as per monolithic metals, both quasi–statically and dynamically. However, the Steelite sandwich materials (single, double and triple core) also exhibited some unstable collapse, though this is most likely due to the geometry rather than the sandwich material, since double hat monolithic materials also exhibit unstable collapse modes. Increasing the core thickness increased the likelihood of steel skin failure (exhibited particularly in double and triple core Steelite and ECCS sandwich materials). In the case of the triple core Steelite a change in deformation mode was observed in the dynamic tests. The sandwich was observed to fail through thickness, which led to a change in the energy absorption mode to progressive failure, akin to fibre–reinforced composite materials.

The thicker ECCS sandwich (0.3 mm steel skins) also exhibited failure of the steel skin in the double and particularly triple core variants. The triple core ECCS sandwich did not fail through thickness as was seen in the triple core Steelite sandwich materials owing to the increase in steel thickness. Though, it was noted that at the points of failure of the steel skin, delamination of the sandwich was observed. This suggests that there is a strain rate dependency to the adhesive strength, since in static peel tests, cohesive failure was the only observed mode of sandwich failure.

DP600 (0.5 mm steel skins) sandwich testing was limited; only two crash structures were tested in the same geometry as the ECCS sandwich materials. However, they exhibited a similar progressive crushing behaviour. In the press–formed geometry, an increased number of smaller radius folds was seen.

Suggesting, sandwich materials may be more affected by crash structure geometry than monolithic metals.

A limiting ratio of core to skin thickness was also deduced from the testing, this was 70% core thickness to 30% skin thickness, in order that failure of the skin steel was not significant. Minimising the amount of steel skin failure in turn reduces the chance of through thickness failure in the entire sandwich, which therefore reduces the risk of progressive failure occurring. This is advantageous since the progressive crushing energy absorption mode is a more predictable response.

A static to dynamic ratio of the mean crush force was also defined from the quasi–static and dynamic tests. This static to dynamic ratio was higher in all the sandwich materials variants than observed in the three monolithic metals tested. The low strength Steelite sandwich materials showed a minimum 60% increase in energy absorption dynamically for all thicknesses. This is an unprecedented increase in energy absorption, which has not been previously reported in the literature for monolithic metals. The remainder of the sandwich materials exhibited static to dynamic increases between 15% and 37%.

A comparison to a monolithic metal was only possible with DP600 steel, since it was tested both in monolithic and sandwich forms. Achieving a 9% increase in the mean crush force (dynamically over quasi–statically) as a monolithic metal and a 25% increase in sandwich form. This difference is hypothesised to be a greater strain imparted in the thinner steel of the sandwich, hence the dynamic stress reached by the metal is higher. Second, the strain rate sensitivity of the polymer core may also be a factor in the energy absorption increase. Strain rate sensitivity of polymers such as polypropylene has been shown to be proportionally more significant than metals, not only increasing the material's yield and ultimate strength but also the elastic modulus.

9.1.4 FEA model – Single shell element

Finite element modelling was used to simulate the behaviour and predict the performance of the steel–polypropylene–steel sandwich and monolithic materials. This model was then validated against the physical test results. The model employed a single shell element, with laminated shell theory to account for the shear behaviour of the core. The single shell element model predicts the deformation modes of the sandwich well however, it is rather idealised. The single shell element model was unable to account for failure of either the individual layers of the sandwich or the delamination of the metal from the polymer. However, when comparing to the physical testing, in most instances this was not seen to be lead to any significant discrepancies. Overall, the FEA model was determined to over predict the result by no more than 8% for the sandwich materials. For the monolithic metals, the use of a single shell element model and conventional through thickness shear behaviour in the FEA simulations exhibited good agreement with the physical test results being between –5.2% and +1.4%.

9.1.5 Performance prediction

An array of 105 discrete sandwich material constructions were simulated using the single shell element model in LS–DYNA.

An analytical solution from the literature based on the asymmetric collapse deformation of monolithic metals was modified to predict the energy absorption of MPM sandwich materials; assuming they underwent similar deformation. This was a fair assumption, since the physical testing predominantly showed asymmetric collapse modes. The analytical solution was fitted to the simulation results using a linear scale factor. The comparison suggests an analytical solution based on sandwich bending theory is able to predict the performance of sandwich materials in axial energy absorbers.

The results showed that steel–polypropylene–steel sandwich materials are able to achieve a similar specific energy absorption performance as high strength aluminium alloys (AC300–T61) when limited to a sandwich thickness ratio of 70% core to 30% steel. The analytical solution results also suggest around 35% mass reduction for a steel–polypropylene–steel sandwich material over monolithic DP600.

9.1.6 Contribution to knowledge

This thesis has examined the applicability of steel–polypropylene–steel sandwich materials for the role of axial energy absorbers, an application previously undescribed in the literature. The results show that MPM sandwich materials can be accurately predicted and highlight potential for their use in automotive applications. The work has discovered that the deformation modes in the steel–polypropylene–steel sandwich mimic the monolithic metal crash structure, however, with smaller fold radii, hypothesised to be due to shear in the polypropylene core. Whilst it could not be categorically defined that increasing the core thickness increased the radius of the folds in the structure, it was observed in most instances. The MPM sandwich material crash structures tested did not show the same level of increased variability over monolithic materials. Whilst this may be due to the variability in the sandwich material (due to its manual production), it will may be due in part to the local wrinkling behaviour of sandwich materials already seen in the literature.

From the physical testing, the effect of core thickness for a fixed skin thickness is also defined and confirmed using the finite element analysis. The physical tests showed a linear relationship between increasing core thickness and mean crush force. Further, the effectiveness of increasing the core thickness on the specific energy absorption was identified. The testing also showed an unprecedented >60%

increase in energy absorption from quasi–static to dynamic tests for all three thicknesses of Steelite sandwich material, a level not seen in monolithic metal crash structures. This also alluded to an increased strain rate sensitivity of steel in MPM sandwich materials over the monolithic steel, a property which has been suggested in the literature for tensile tests but unknown in axial crash deformation.

The testing demonstrates the potential for the crushing mode to change from a desirable progressive crushing mode to an undesirable and difficult to predict progressive failure, this occurred with a 7:1 core to thickness ratio (triple core Steelite), though failure of the steel skin is seen in most circumstances. A 70%:30% ratio of thickness for the polypropylene core to steel skin is shown to minimise steel skin failure, i.e. the individual steel skin thickness should be no less than 15% of the total sandwich thickness. The analytical solution suggests this ratio could give the MPM sandwich a similar specific energy absorption to high strength aluminium alloys.

The thesis also shows the single shell element model with laminated shell theory can be used in LS–DYNA to predict the performance of the steel–polypropylene–steel sandwich materials. However, there is a potential thickness limit for which the model is applicable for the single hat and backplate crash structure considered; further research would be required to increase the confidence in the model. The single shell element model was accurate to within +8% of the physical test results.

An analytical solution fitted the LS–DYNA single shell element model well and showed increasing the core thickness is more effective at increasing the specific energy absorption than increasing the skin thickness. As well as the potential for steel–polypropylene–steel sandwich materials to equal the performance of high strength aluminium alloys.

9.1.7 Limitations of this research

The biggest limitation of the work was the differing geometries used in testing, the reasons being difficulties in manufacture and the minimum energy requirement of the drop tower; hence, the original intention to compare differing materials at the same geometry was not possible.

Different thicknesses of steel skins used were of different grades, which meant two variables were changed at once, preventing straightforward comparison. Furthermore, the use of blind rivets to assemble the sandwich material crash structures was non–ideal in a production sense. Although blind rivets performed as required, an automotive solution would be required for production use. A joining solution for sandwich materials in the automotive body–in–white was out of scope for this project.

A final limitation was the different sandwich material production methods. The Steelite and ECCS skins had chrome coated surfaces. The Steelite skin was industrially pre–applied with adhesive, the adhesive was applied manually on the ECCS skin. The DP600 steel required phosphate conversion coating of its galvanised surface to improve the adhesion properties. Nevertheless, the different steels had different adhesive bond strengths, which lead to another variability in the testing.

9.2 Further Work

The work conducted in this PhD raises further questions which require answering in order to ensure the applicability of MPM sandwich materials for axial energy absorbers, therefore, recommendations for further work are presented here.

9.2.1 Sandwich material production

This thesis has raised questions about the bond strength requirements for MPM sandwich materials.

A full study on the effect of the bond strength is required to ascertain the bond strength requirement for a given sandwich construction, in order for the sandwich to withstand forming and crash deformation. This would also define the most strenuous task for the adhesive; during forming or crash deformation.

Since delamination was seen in the ECCS sandwich materials when crash tested which was not seen when static peel testing was performed, there is potential that the adhesive failure mechanism is strain rate dependent. A study of the failure mechanisms of MORAD–M801 adhesive quasi–statically and dynamically is required to ascertain whether there are differences in the failure mechanisms due to strain rate. This would also include testing in different loading conditions (shear, tension, bending, compression and combinations of such), as the loading experienced by the adhesive is purely tensile.

9.2.2 Further testing

To confirm the theoretical analysis in Chapter 8 – Performance prediction, testing of a single steel grade at different thicknesses is required, as well as testing different grades of steel at the same thickness. Therefore, validating the steel's strength effect on the sandwich performance.

The 70:30 thickness ratio for polymer core to steel skin thickness suggested in the thesis requires confirming. The testing carried out in thesis was limited, hence the 70:30 ratio test should be applied across a range of thicknesses to allow the assertion to be thoroughly examined.

9.2.3 Finite Element Analysis

Simulation of the deformation of MPM sandwich materials during forming is required to account for the forming effects in crash structure modelling. This also allows the production of a strain map across the formed corner, showing the maximum strain imparted on the metal, hence confirming how much elongation or strain capacity is remaining in the material.

The analytical solution showed the characteristics of the plastic flow of the steel skin are important in plastic bending moment of the sandwich material and hence the energy absorption of the crash structure. Therefore, additional analyses of material properties such as the yield strength and plastic flow properties of the steel skin material would allow the improvement of the energy absorption potential of the sandwich material.

9.2.3.1 Sensitivity analyses

Sensitivity analyses on the variations in both rolled steel sheet and produced sandwich materials are required to comprehend how small changes in these properties effect the performance of the sandwich materials. The properties which should be considered are the steel skin thickness variability in production, the strength variability of rolled steel sheet and the total thickness of the manufactured sandwich materials.

9.2.4 Polymer core properties

A study on effect of the strength and elastic modulus of the polymer core would confirm its effects on the sandwich material performance. In this thesis, classical mechanics was applied to the sandwich construction and the strength of the polymer was found to be of little importance. However, if the strength and stiffness particularly dynamically, of the polymer could be increased with little weight penalty, it would be interesting to understand the effect of this on the performance of the material.

For automotive applications, temperature dependent strength decrease of the polymer needs to be considered. Vehicle body–in–whites undergo high temperature paint curing (around 200°C), therefore, the effect of this high temperature needs to be accounted for. Hence, a study on the required polymer melting point temperature will also need to be performed, as well as the effect of re–heating on the adhesive strength.

9.2.5 Steel skin properties and flow stress

A study on the effect of the steel skin properties such as yield and ultimate strength as well as the strain rate sensitivity of the metal, would confirm the properties required to optimise the performance of MPM sandwich materials.

9.2.6 Joining

For the adoption of MPM sandwich materials into the automotive body–in–white they must be readily joinable with either monolithic metals or to themselves. Therefore, defining parameters for joining of sandwich materials using self–pierced rivets are important. Additionally, other metals of joining MPM sandwich materials should also be considered, such as clinching, welding and brazing.

9.2.7 Use of other metals

Different metals were not considered for the skin material of the sandwich, although they are plausible. Classical mechanics suggests that lower density metals are not as effective in a sandwich construction as higher density metals. The higher strength of higher density metals such as steel make them relatively more effective in the sandwich form with regards to stiffness or energy absorption. In comparison, low density/low strength aluminium and magnesium alloys are relatively less effective since the low density core is relatively denser when placed in a sandwich. An interesting construction would therefore be the use of titanium as the skin metal, due to its high modulus and high strength, although at considerable cost.

9.2.8 Structural test cases

This thesis only considered the axial energy absorption capacity of MPM sandwich materials, there are however other load cases of interest. 3 and 4 point bending both quasi–statically and dynamically are of interest for automotive components.

The fatigue performance of MPM sandwich materials as the material and in a structure would be of interest. Polymers exhibit long fatigue life, whereas a lower steel skin thickness would decrease the fatigue life since the stress experienced by the metal would increase. Additionally the fatigue performance of the adhesive in combination with these two effects would be complex.

Oblique impacting of the crash structure would also be of interest due to the requirement of automotive crash structures to absorb energy from multiple directions. This requirement is also a necessity in other energy absorbing fields, such as rail locomotives which must overcome oblique loads to prevent locomotives over–riding one another, particularly on passenger trains.

An important feature of the axial energy absorption of automotive crash structures is the peak load for an uninitiated crash structure, since this defines the peak acceleration experiences by vehicle occupants. Therefore, quasi–static and dynamic peak impact force measurement would be of interest to compare to monolithic metal crash structures.